CRANFIELD UNIVERSITY

YONGLIANG YAN

OXY-FUEL AND CHEMICAL-LOOPING COMBUSTION FOR A LOW-CARBON FUTURE

SCHOOL OF WATER, ENERGY AND ENVIRONMENT
PhD in Energy and Power

PhD
Academic Year: 2017 - 2020

Supervisor: Dr Peter T. Clough
Associate Supervisors: Prof. Vasilije Manovic and Prof. Edward J. Anthony

September 2020

CRANFIELD UNIVERSITY

SCHOOL OF WATER, ENERGY AND ENVIRONMENT
PhD in Energy and Power

PhD

Academic Year 2017 - 2020

YONGLIANG YAN

OXY-FUEL AND CHEMICAL-LOOPING COMBUSTION FOR A LOW-CARBON FUTURE

Supervisor: Dr Peter T. Clough
Associate Supervisors: Prof. Vasilije Manovic and Prof. Edward J. Anthony
September 2020

This thesis is submitted in partial fulfilment of the requirements for the degree of PhD

© Cranfield University 2020. All rights reserved. No part of this publication may be reproduced without the written permission of the copyright owner.

Abstract

This thesis is focused on investigating the potential of oxy-fuel and chemical-looping combustion (CLC) for carbon capture, and their integration with sorbent enhanced steam methane reforming (SE-SMR) for low-carbon hydrogen production. Oxy-fuel combustion converts a fuel within a mixture of O_2/CO_2 instead of air, while CLC converts a fuel by reduction of a metal oxide. In both cases, the resulting flue gas is free of N_2, and consist of only CO_2 and steam, and the steam can easily be condensed out. With the use of biomass as the fuel feedstock for the oxy-fuel combustion and CLC, negative CO_2 emissions can be achieved for power and heat generation.

Oxy-fuel combustion is also a likely route to decarbonise the calcination of limestone, as used in the calcium looping and SE-SMR processes. SE-SMR combines the conventional steam methane reforming with calcium looping (CaL), which utilises CO_2 sorbents (e.g. CaO) to capture the CO_2 produced during the SMR process and shifts the equilibrium of the reforming and water-gas shift reactions in favour of more H_2 production according to Le Chatelier's principle.

Three main areas of work were conducted within this thesis, which includes 1) a detailed investigation into the effects of various parameters on the reaction kinetics of air and oxy-fuel combustion of woody biomass in a lab-scale fluidised-bed reactor; 2) applying machine learning in estimating the performance of oxygen carriers in chemical-looping processes; and 3) thermodynamic and techno-economic assessment of the integration of SE-SMR with oxy-fuel and chemical-looping combustion for low-carbon hydrogen production.

Firstly, combustion rates of the biomass and its char were measured by a lab-scale fluidised-bed reactor. The shirking core model was used to simulate the char conversion during the experiments and under combustion mechanisms. Then, a novel approach that uses machine learning to efficiently screen the suitable oxygen carrier materials for CLC has been proposed. Lastly, the integration of oxy-fuel and CLC within the calciner of SE-SMR has been simulated in the Aspen Plus to understand their thermodynamic limitations and optimal

operating conditions. Moreover, a detailed techno-economic analysis of the proposed configurations has been conducted to investigate their feasibility for a large-scare low-carbon hydrogen production.

The obtained combustion kinetics and characteristics of air- and oxy-fuel combustion of biomass can provide useful information for retrofit and design of boilers. The framework of applying machine learning in oxygen carriers is expected to accelerate the finding and designing cost-effective oxygen carriers for large-scale CLC. The results of techno-economic analysis of the integration of oxy-fuel combustion and CLC with SE-SMR indicate that it is competitive with conventional steam methane reforming (SMR) with carbon capture and storage (CCS).

Keywords:

Carbon capture and storage, hydrogen production, negative emissions, machine learning, high-temperature solid-looping, techno-economic analysis.

Acknowledgements

Firstly, I would like to express my sincere gratitude to my supervisors, Dr Peter Clough, Prof. Vasilije Manovic, and Prof. Ben Anthony for their patience, motivation and continuous support of my PhD study. I would like to thank Ben for introducing me to the world of high-temperature solid-looping and his valuable suggestions and guidance which will serve me in good stead for my career. I would also like to thank Peter for passing his experimental knowledge and experience to me, and giving me the opportunity to teach master students, and involve me in other research projects, which has been an invaluable experience to me. I am immensely grateful to Vasilije for the scientific discussions and inspirations during my PhD project. I would also like to express my gratitude to my PhD progress reviewers, Prof. Fred Coulon and Dr Stuart Wagland, who have provided many useful suggestions and guidance for delivering my PhD project on time.

I would like to express immense appreciation to Prof Tobias Mattisson and Dr Patrick Moldenhauer at Chalmers University of Technology, Sweden, for supervising me when conducting joint research on machine learning for oxygen carriers, as well as the funding from Erasmus+ scheme and Chalmers Energy Area of Advances. I have gained a significant amount of useful knowledge and come up with many new research ideas for chemical-looping during this six months visiting. I would also like to thank all the current and previous staff and students at Energy technology, Chalmers University of Technology for their assistance and support in my life at Chalmers and research while there. In particular, I would like to thank Prof. Bo Leckner, Prof Anders Lyngfelt, Prof Henrik Leion and Dr Carl Linderholm for many valuable scientific discussions.

I would like to thank Dr Sanjay Mukherjee, Dr Ke Wang, Serap Ozmen, Paula Nkulikiyinka, Dr Fatih Gulec, Jianrui Zha and Jude Odianosen Asibor for their assistance in the lab and useful discussions throughout my PhD. It has been a wonderful journey working with you in the same research group. I would also like to thank Dhinesh Thanganadar for his friendship when working together on the HyPER project.

I would like to say thank you to all the past and present members of Energy and Power theme and wider department community. I would like to thank all the technicians in building 43a: Peter, Euan, Robert and Howard. Without your support, I couldn't complete my tests so effectively. I would also like to thank Sam Skears and Dr Gill Drew for their administrative support for my PhD application and submission.

Last, but not least, I wish to thank my mother, Mrs Shumei Tang, my father, Mr Guojun Yan and other family members for their love, patience and support throughout my life. Finally, to my girlfriend, Xinyue (Karry) Yang, thank you for your love, accompany, encouragement and support during my PhD.

“No amount of experimentation can ever prove me right; a single experiment can prove me wrong.”

-Albert Einstein

“An engineering science aims to organise the design principles used in engineering practice into a discipline and thus to exhibit the similarities between different areas of engineering practice and to emphasise the power of fundamental concepts. In short, an engineering science is predominated by theoretical analysis and very often uses the tool of advanced mathematics.”

-Xuesen Qian

“Essentially, all models are wrong, but some are useful.”

- George E.P. Box (Box, G. E. P., & Draper, N. R. (1987). Wiley series in probability and mathematical statistics. Empirical model-building and response surfaces. John Wiley & Sons.)

List of Publications

Published papers presented in this thesis:

Chapter 3:

Y. Yan, P.T. Clough, E.J. Anthony, Investigation of the apparent kinetics of air and oxy-fuel biomass combustion in a spouted fluidised-bed reactor, Chem. Eng. Res. Des. (2019). **(IF = 3.4)**

Chapter 5:

Y. Yan, T. Mattisson, P. Moldenhauer, E.J. Anthony, P.T. Clough, Applying machine learning algorithms in estimating the performance of heterogeneous, multi-component materials as oxygen carriers for chemical-looping processes, Chem. Eng. J. 387 (2020) 124072. **(IF = 10.7)**

Chapter 6:

Y. Yan, D. Thanganadar, P.T. Clough, S. Mukherjee, K. Patchigolla, V. Manovic, E.J. Anthony, Process simulation of blue hydrogen production by upgraded sorption enhanced steam methane reforming (SE-SMR) processes, Energy Convers. Manag. 2 (2020) 1–36. **(IF = 8.2)**

Chapter 7:

Y. Yan, V. Manovic, E.J. Anthony, P.T. Clough, Techno-economic analysis of low-carbon hydrogen production by sorption enhanced steam methane reforming (SE-SMR) processes, Energy Convers. Manag. 226 (2020) 113530. **(IF =8.2)**

Submitted and unpublished manuscripts:

Chapter 4:

Y. Yan, P.T. Clough, V. Manovic, E.J. Anthony, Investigation of air and oxy-fuel combustion kinetics of wood char in a fluidised-bed reactor. (Plan to submit to Fuel)

The author has also contributed to other publications not directly related to the subject of the thesis:

Y. Yan, K. Wang, P.T. Clough, E.J. Anthony, Developments in calcium/chemical looping and metal oxide redox cycles for high-temperature thermochemical energy storage: A review, Fuel Process. Technol. 199 (2020) 106280. **(IF = 5.0)**

Y. Yan, T.N. Borhani, P.T. Clough, Chapter 14. Machine Learning Applications in Chemical Engineering, in: The Royal Society of Chemistry, 2020: pp. 340–371. doi:10.1039/9781839160233-00340.

P. Nkulikiyinka, **Y. Yan**, F. Güleç, P.T. Clough, V. Manovic, Application of machine learning to develop a soft-sensor model for the prediction of sorption enhanced steam methane reforming products (Submitted to Energy and AI)

Declaration

I declare that this thesis is an original report of my research, which has been written by myself and has not been submitted for any other degree or professional qualification.

My contribution and those of the other authors to the collaborative work have been explicitly indicated in the text below and acknowledgements. All the co-authors and publishers allow me to use the joint publications in my thesis.

Paper 1: Investigation of the apparent kinetics of air and oxy-fuel biomass combustion in a spouted fluidised-bed reactor, Chem. Eng. Res. Des. (2019). (Link to Chapter 3)

Nature of contribution:

Yongliang Yan: Conceptualization, Methodology, Software, Validation, Investigation, Formal analysis, Data curation, Visualization, Writing - original draft.

Peter T. Clough: Project administration, Funding acquisition, Supervision, Visualization, Writing - review & editing.

Edward J. Anthony: Project administration, Funding acquisition, Supervision, Visualization, Writing - review & editing.

Paper 2: Applying machine learning algorithms in estimating the performance of heterogeneous, multi-component materials as oxygen carriers for chemical-looping processes, Chem. Eng. J. 387 (2020) 124072. (Link to Chapter 5)

Natural of contribution:

Yongliang Yan: Conceptualization, Methodology, Software, Validation, Investigation, Formal analysis, Data curation, Visualization, Writing - original draft.

Peter T. Clough: Project administration, Funding acquisition, Supervision, Visualization, Writing - review & editing.

Edward J. Anthony: Supervision, Visualization, Writing - review & editing.

Tobias Mattisson: Project administration, Funding acquisition, Supervision, Writing - review & editing.

Patrick Moldenhauer: Supervision, Writing - review & editing.

Paper 3: Process simulation of blue hydrogen production by upgraded sorption enhanced steam methane reforming (SE-SMR) processes, Energy Convers. Manag. 2 (2020) 1–36. (Link to Chapter 6)

Natural of contribution:

Yongliang Yan: Conceptualization, Methodology, Software, Validation, Investigation, Formal analysis, Data curation, Visualization, Writing - original draft.

Dhinesh Thanganadar: Conceptualization, Methodology, Software, Validation, Investigation, Software, Validation, Investigation, Formal analysis, Data curation, Writing - original draft.

Peter T. Clough: Project administration, Funding acquisition, Supervision, Visualization, Writing - review & editing.

Edward J. Anthony: Supervision, Visualization, Writing - review & editing.

Vasilije Manovic: Supervision, Visualization, Writing - review & editing.

Sanjay Mukherjee: Writing - review & editing.

Kumar Patchigolla: Writing - review & editing.

Manuscript 1: Techno-economic analysis of low-carbon hydrogen production by sorption enhanced steam methane reforming (SE-SMR) processes (Link to Chapter 7)

Natural of contribution:

Yongliang Yan: Conceptualization, Methodology, Software, Validation, Investigation, Formal analysis, Data curation, Visualization, Writing - original draft.

Peter T. Clough: Project administration, Funding acquisition, Supervision, Visualization, Writing - review & editing.

Edward J. Anthony: Supervision, Visualization, Writing - review & editing.

Vasilije Manovic: Supervision, Visualization, Writing - review & editing.

ELSEVIER[1]:

“Theses and dissertations which contain embedded PJAs (Published Journal Articles) as part of the formal submission can be posted publicly by the awarding institution with DOI links back to the formal publications on ScienceDirect”

[1] ELSEVIER https://www.elsevier.com/about/policies/sharing (accessed August 5, 2020).

Table of Contents

Abstract iii
Acknowledgements v
List of Publications viii
Declaration x
List of Figures xvi
List of Tables xxi
List of Equations xxiii
List of Abbreviations 1
1 Introduction 3
1.1 Background 3
1.2 Project Aims and Objectives 6
1.3 Thesis Outline 7
1.4 References 9
2 Literature Review 12
2.1 Carbon Capture and Storage (CCS) 12
2.2 Blue Hydrogen Production 17
2.3 Machine Learning in CCS 19
2.4 References 25
3 Investigation of the Apparent Kinetics of Air and Oxy-Fuel Biomass Combustion 33
3.1 Introduction 34
3.2 Materials and Methods 36
3.2.1 Materials 36
3.2.2 Experimental Setup 37
3.2.3 Standard Operating Procedure 38
3.3 Results and Discussion 40
3.3.1 Reaction Rates 40
3.3.2 Order of Reaction 42
3.3.3 Activation Energies 43
3.3.4 Shrinking Core Model Validation 44
3.3.5 Discussion 48
3.4 Conclusions 49
3.5 References 50
4 Kinetic Study of Wood Char Combustion under O_2/N_2 and O_2/CO_2 in a Bubbling Fluidised-bed Reactor 54
4.1 Introduction 55
4.2 Experimental 58
4.2.1 Experimental apparatus 58
4.2.2 Materials 60
4.2.3 Experimental procedure 60

4.2.4 Data evaluation 61
4.3 Results and discussion 63
4.3.1 Reaction kinetics of char combustion 63
4.3.2 Order of reaction and activation energies 66
4.3.3 Shrinking core model validation 67
4.3.4 Discussion 68
4.4 Conclusions 70
4.5 References 71
5 Applying Machine Learning Algorithms in Estimating the Performance of Heterogeneous, Multi-component Materials as Oxygen Carriers for Chemical-looping Processes 75
5.1 Introduction 76
5.2 Methodology 80
5.2.1 Materials 80
5.2.2 Experimental Investigation 80
5.3 Results and Discussion 86
5.3.1 Performance of the Trained Neural Networks 86
5.3.2 Confirmation of Model Robustness Using Unseen Data 87
5.3.3 Sensitivity Analysis 90
5.3.4 Fe/Mn Content in Manganese Ores 91
5.3.5 Discussion 92
5.4 Summary and Conclusions 95
5.5 References 96
6 Process Simulations of Blue Hydrogen Production by Upgraded Sorption Enhanced Steam Methane Reforming (SE-SMR) Processes 103
6.1 Introduction 104
6.2 Process Configuration and Simulation 107
6.2.1 Process Configuration 107
6.2.2 Process Simulation 111
6.2.3 Performance Evaluation 114
6.3 Results and Discussion 115
6.3.1 Thermodynamic Analysis 115
6.3.2 Discussion 126
6.4 Conclusions 130
6.5 References 131
7 Techno-economic Analysis of Low-carbon Hydrogen Production by Sorption Enhanced Steam Methane Reforming (SE-SMR) Processes 138
7.1 Introduction 139
7.2 Methodology 142
7.2.1 Process Description of Different SE-SMR Configurations 142
7.2.2 Process Simulation 146
7.2.3 Economic Evaluation 150

7.3 Results and Discussion 154
7.3.1 Technical Performance 154
7.3.2 Economic Analysis 156
7.4 Conclusions 165
7.5 References 166
8 Conclusions and Recommendations for Future Work 174
8.1 General Conclusions 174
8.2 Recommendations for Future Work 177
Appendices 179
Appendix A Biomass Combustion Kinetics Measurement using a Fluidised-bed Reactor 179
Appendix B Applying Machine Learning Algorithms in Estimating the Performance of Heterogeneous, Multi-component Materials as Oxygen Carriers for Chemical-looping Processes 187
Appendix C Process Simulations of Blue Hydrogen Production by Upgraded Sorption Enhanced Steam Methane Reforming (SE-SMR) Processes 197

List of Figures

Figure 1-1 Global CO_2 emissions reductions by technology area: Reference Technology Scenario (RTS) to 2DS [6]..... 4

Figure 1-2 Global CO_2 emissions reductions by technology area and scenario B2DS [6] 4

Figure 1-3 Structure and linkage of each project in this thesis 8

Figure 2-1 Current and potential components of the low-carbon hydrogen system [16] 18

Figure 2-2 Classification and applications of machine learning [32] 20

Figure 2-3 Artificial neural network used to predict the thermodynamic performance of calcium looping for CO_2 capture [57]. 24

Figure 3-1 Process flow diagram of the spouted fluidised-bed reactor and ancillary equipment..... 38

Figure 3-2 Rate of biomass combustion in 10-40 vol% O_2. At conditions of 973 K, U/U_{mf} = 3, 0.02 g (±2%) biomass, and 1 bar(a))..... 40

Figure 3-3 Rate of CO_2 production vs. temperature and O2 concentration for the air combustion tests..... 41

Figure 3-4 Rate of CO_2 production *vs.* temperature and O_2 concentration for the oxy-fuel combustion tests 41

Figure 3-5 ln(*r*) *vs.* ln[O_2] in air combustion tests. At conditions of 923-1073 K, 20-35 vol% O_2, 0.02 g (±2%) sample, U/U_{mf} = 3, and 1 bar(a). The error bars show the standard deviation between three repeats. 42

Figure 3-6 ln(*r*) *vs.* ln[O_2] in oxy-fuel combustion tests. At conditions of 923-1073 K, 20-35 vol% O_2, 0.02 g (±2%) sample, U/U_{mf} = 3, and 1 bar(a). The error bars show standard deviation between three repeats 43

Figure 3-7 Comparison of experimental results and model predictions at 25 vol% O_2, bed temperature 923-1073 K under air combustion of wood. (Points: experimental results. Solid lines: shrinking core model predictions)..... 45

Figure 3-8 Comparison of experimental results and model predictions at 25 vol% O2, bed temperature 923-1073 K under oxy-fuel combustion of wood. (Points: experimental results. Solid lines: shrinking core model predictions). 45

Figure 3-9 Comparison of experimental results and model predictions at 20-35 vol% O_2, bed temperature 923 K under air combustion of wood. (Points: experimental results. Solid lines: shrinking core model predictions)..... 46

Figure 3-10 Comparison of experimental results and model predictions at 20-35 vol% O_2, bed temperature 923 K under oxy-fuel combustion of wood. (Points: experimental results. Solid lines: shrinking core model predictions)..... 46

Figure 4-1 Schematic diagram of the bubbling fluidised-bed reactor..... 59

Figure 4-2 The evolution of CO_2 and CO concentrations in the flue gas during the combustion of wood char in 20 vol. % O_2/ 80 vol. % N_2 and 20 vol. % O_2/ 80 vol. % CO_2 at a bed temperature of 923 K..... 63

Figure 4-3 Typical reaction rates of CO_2 and CO during three different particle sizes of wood char combustion at bed temperature of 923 K, 20 % O_2 / 80 % N_2..... 64

Figure 4-4 ln [r] against ln [O_2] at conditions of 923 and 1023 K, 5-30 vol.% O_2 with the balance of N_2 ((a)) and CO_2 ((b)). The error bars represent the standard deviation between three repeats..... 66

Figure 4-5 Comparison of experimental results and model predictions of wood char combustion in O_2/N_2 with the oxygen concentration from 5 to 30 % at the bed temperatures of 923, 973, 1023, 1073 and 1123 K. (Points: experimental results. Solid lines: shrinking core model predictions)..... 68

Figure 4-6 Comparison of experimental results and model predictions of wood char combustion in O_2/CO_2 with the oxygen concentration from 5 to 30 % at the bed temperatures of 923, 973, 1023, 1073 and 1123 K. (Points: experimental results. Solid lines: shrinking core model predictions)..... 68

Figure 4-7 Gas concentrations of wood char combustion at 923 K (a) 20 % O_2/ 80 % N_2, (b) 20 % O_2/ 80 % CO_2..... 69

Figure 5-1 Workflow of developing a machine-learning model for oxygen carriers in the chemical-looping process. 83

Figure 5-2 Proposed neural networks structure to predict the reactivity of manganese ores in the chemical-looping process..... 86

Figure 5-3 Experimental and predicted reactivity and oxygen release of manganese ores as oxygen carriers at bed temperature 900 °C- (a) trainlm single hidden-layer (14-input ANNs)and (b) trainlm two hidden-layer (14-input ANNs) (c) trainlm single hidden-layer (7 and 4-input ANNs) (d) trainlm two hidden-layer (7 and 4-input ANNs)..... 88

Figure 5-4 (a) Predictions of stacked neural network (14-13-3) trained with trainbr with 95% confidence intervals on unseen data; (b) Predictions of stacked neural network (14-8-3) trained with trainlm with 95% confidence intervals on unseen data; (c) Predictions of stacked neural network (14-7-12-3) trained with trainlm with 95% confidence intervals on unseen data..... 89

Figure 5-5 The predicted performance of reactivity with methane and syngas with 95% confidence intervals with the change in BET surface area, attrition index, and Fe and Mn content of an averaged ore..... 91

Figure 5-6 The predicted effects of varied Fe/Mn mass ratio of manganese ore EC on its oxygen release and reactivity with methane and syngas. 92

Figure 6-1 Flow diagrams of different simulated sorption enhanced steam methane reforming processes with CO_2 capture. CAL: sorbent regenerator (calciner), COM: combustor SE-SMR: sorption enhanced steam methane reformer, HX: heat exchanger, WR: water removal, PSA: pressure swing absorption unit, FR: fuel reactor, AR: air reactor, ASU: air separation unit. 108

Figure 6-2 Options of heat integration between the air reactor and calciner .. 110

Figure 6-3 Process performance for different reforming temperatures. (a) Case 1 SE-SMR, (b) Case 2 SE-SMR+PSAOG, (c) Case 3 CLC+SE-SMR, (d) Case 4 CLC+SE-SMR+PSAOG, (e) Case 5 SE-SMR+Oxy-fuel combustion, (f) Case 6 SE-SMR+H_2 recycle 117

Figure 6-4 Process performance for different reforming pressures. (a) Case 1 SE-SMR, (b) Case 2 SE-SMR+PSAOG, (c) Case 3 CLC+SE-SMR, (d) Case 4 CLC+SE-SMR+PSAOG, (e) Case 5 SE-SMR+Oxy-fuel Combustion, (f) Case 6 SE-SMR+H_2 Recycle. 121

Figure 6-5 Process performance for different S/C ratios. (a) Case 1 SE-SMR, (b) Case 2 SE-SMR+PSAOG, (c) Case 3 CLC+SE-SMR, (d) Case 4 CLC+SE-SMR+PSAOG, (e) Case 5 SE-SMR+Oxy-fuel Combustion, (f) Case 6 SE-SMR+H_2 Recycle. 124

Figure 6-6 Effect of NiO and Fe_2O_3/fuel on performance of FR in Case 4..... 125

Figure 6-7 Comparison of proposed SE-SMR+PSA+CLC with the reported steam methane reforming processes in literature: SMR+PSA [17], ATR+PSA+MDEA [56,57], SMR+MEA+PSA [58], CLC+SMR+PSA [39], SE-SMR+Oxy-fuel [59], CLC+SE-SMR [26], SE-CL-SMR [60]..... 130

Figure 7-1 Simplified process flow diagram of case 1A and B 143

Figure 7-2 Simplified process flow diagram of case 2A & B 144

Figure 7-3 Simplified process flow diagram of case 3A and B 146

Figure 7-4 Split of total capital costs of SE-SMR hydrogen plants 159

Figure 7-5 Split of the variable operating costs of SE-SMR hydrogen plants . 160

Figure 7-6 Distribution of different costs of levelised cost of hydrogen for different SE-SMR processes 162

Figure 7-7 Sensitivity analyses a) TDCC vs LCOH, b) Discount rate vs LCOH, c) Fuel costs vs LCOH, d) CO_2 storage costs vs LCOH, e) Operating capacity factor vs LCOH, f) Net efficiency vs LCOH. 164

Figure 7-8 Cumulative discounted cash flow of SE-SMR plants under different hydrogen selling price..... 165

Figure_Apx A-1 The ratio of oxygen outlet and inlet concentrations plotted against the mass of fuel at conditions of 923K, 25 vol% O_2/75 vol% N_2, U/U_{mf} = 3, and 1 bar (a). 180

Figure_Apx A-2 'Step' increases of CO_2 concentration. 181

Figure_Apx A-3 Measured response for ‘step’ increases of CO_2. 181

Figure_Apx A-4 Measured gas concentrations during the blank tests and an oxy-fuel test. At conditions of 973 K; 30 vol.% O_2/65 vol.% CO_2/5 vol% N_2, U/U_{mf} = 3, 0.02 g (±2%) biomass and 1 bar(a). 182

Figure_Apx A-5 Measured and corrected CO_2 concentration from oxy-fuel combustion. At conditions of 973 K, 30 vol% O_2/65 vol% CO_2/5 vol% N_2, U/U_{mf} = 3, 0.02 g (±2%) biomass and 1 bar(a). 183

Figure_Apx A-6 Raw measured data (left) and time-shifted data (right) of direct-measured gas concentration. At conditions of 1023 K, 35 vol% O_2/65 vol% N_2, U/U_{mf} = 3, 0.02 g (±2%) biomass, and 1 bar(a). 183

Figure_Apx A-7 Compensation of the effects of mass added on measured rate of reaction. At conditions of 923K, 25 vol% O_2/75 vol% N_2, U/U_{mf} = 3, and 1 bar(a). 185

Figure_Apx B-1. Pearson linear correlation factor of each inputs to the O_2 release rate of manganese ores 188

Figure_Apx B-2 Pearson linear correlation factor of each inputs to the reactivity with CH_4 of manganese ores 188

Figure_Apx B-3 Pearson linear correlation factor of each inputs to the reactivity with syngas of manganese ores 189

Figure_Apx B-4 Feature selection using neighbourhood component analysis for regression for reducing the inputs of ANNs 189

Figure_Apx B-5 Mean absolute error (MAE) of single hidden layer neural networks (14 inputs) with different number of neurons and trained with three different learning algorithms, trainlm, trainbr and trainbfg. 190

Figure_Apx B-6 Mean absolute error (MAE) of two-hidden layers neural networks (14 inputs) with different number of neurons using the algorithm *trainlm*. 190

Figure_Apx B-7 Experimental and predicted reactivity and O_2 release of manganese ores as oxygen carriers (*trainbr* single hidden-layer) at bed temperature 900 °C. 194

Figure_Apx B-8 Experimental and predicted reactivity and O_2 release of manganese ores as oxygen carriers (*trainbr* two hidden-layer) at bed temperature 900 °C. 195

Figure_Apx B-9 Experimental and predicted reactivity and O_2 release of manganese ores as oxygen carriers (*trainbfg* single hidden-layer) at bed temperature 900 °C. 195

Figure_Apx B-10 Experimental and predicted reactivity and O_2 release of manganese ores as oxygen carriers (*trainbfg* two hidden-layer) at bed temperature 900 °C. 195

Figure_Apx B-11 (a) Predictions of stacked neural network (7-24-2) trained with *trainbr* with 95% confidence intervals on unseen data; (b) Predictions of stacked neural network (7-7-2) trained with *trainlm* with 95% confidence intervals on unseen data; (c) Predictions of stacked neural network (7-4-9-2) trained with *trainlm* with 95% confidence intervals on unseen data. 196

Figure_Apx C-1. Flowsheet of SE-SMR 197

Figure_Apx C-2 Flowsheet of SE-SMR+PSA 197

Figure_Apx C-3 Flowsheet of SE-SMR+CLC 198

Figure_Apx C-4 Flowsheet of SE-SMR+PSA+CLC 198

Figure_Apx C-5 Flowsheet of SE-SMR+Oxy-fuel combustion 198

Figure_Apx C-6 Flowsheet of SE-SMR+H_2 recycle 199

List of Tables

Table 2-1 Overview of different carbon capture technologies [4.11]..... 14

Table 2-2 Comparison of different carbon capture technologies [3,4,12,13] 16

Table 2-3 Description of common machine learning algorithms and terms [43,44] 21

Table 3-1 Proximate and ultimate analyses of biomass sample..... 36

Table 3-2 Shrinking core model and experimental observed rate constants. Experiments varying bed temperature were conducted at a constant O_2 concentration of 25 vol%, and experiments varying oxygen concentrations were conducted at 923 K..... 47

Table 4-1 Ultimate analysis of wood char sample. 60

Table 4-2 Overview of corrected rates of char combustion at O_2/N_2 and O_2/CO_2 with different bed temperatures 65

Table 4-3 Kinetic parameters of wood char combustion..... 66

Table 5-1 Elemental compositions and physical properties of the manganese ores 84

Table 6-1 Design assumptions used for developing the process flowsheet models in Aspen Plus..... 112

Table 6-2 The performance of SE-SMR+PSA+CLC with different oxygen carriers. (Reformer operated at 600 °C, 25 bar and S/C = 5). 126

Table 6-3 Optimal design space for each SE-SMR process. 128

Table 7-1 Main parameters and assumptions for process simulation in Aspen plus 149

Table 7-2 Parameters and assumptions for economic analysis 152

Table 7-3 Technical performance indicators of SE-SMR H_2 production plants 155

Table 7-4 Main results of economic analysis of SE-SMR hydrogen plants 156

Table_Apx A-1 Operating conditions used in tests..... 179

Table_Apx A-2 Overview of measured rates of air and oxy-fuel combustion of biomass and measured recovery of carbon. Here the average rate of CO_2 production is used as a proxy for the rate of combustion. 184

Table_Apx B-1. Name of the manganese ores investigated in this work..... 187

Table_Apx B-2. Topology and performance of the trained neural networks with all 14 inputs. 191

Table_Apx B-3 Topology and performance of the reduced 7-input trained neural networks 192

List of Equations

(3-1)..... 44
(3-2)..... 44
(3-3)..... 44
(4-1)..... 61
(4-2)..... 61
(4-3)..... 61
(4-4)..... 62
(4-5)..... 62
(4-6)..... 62
(4-7)..... 62
(4-8)..... 62
(4-9)..... 67
(4-10)..... 67
(5-1)..... 76
(5-2)..... 77
(5-3)..... 77
(5-4)..... 77
(5-5)..... 81
(5-6)..... 81
(5-7)..... 81
(5-8)..... 81
(6-1)..... 108
(6-2)..... 110
(6-3)..... 110
(6-4)..... 110
(6-5)..... 110
(6-6)..... 114
(6-7)..... 114

(6-8)..... 115
(6-9)..... 115
(7-1)..... 144
(7-2)..... 145
(7-3)..... 145
(7-4)..... 145
(7-5)..... 145
(7-6)..... 145
(7-7)..... 145
(7-8)..... 145
(7-9)..... 150
(7-10)..... 150
(7-11)..... 150
(7-12)..... 151
(7-13)..... 151
(7-14)..... 151
(7-15)..... 151
(7-16)..... 152

List of Abbreviations

2DS	2 °C Scenario
AI	Artificial Intelligence
ANNs	Artificial neural network models
AR	Air reactor
ASU	Air separation unit
ATR	Autothermal Reforming
ATR +GHR	Autothermal Reforming with Gas Heated Reformer
B2DS	Beyond 2 °C Scenario
BECCS	Bio-energy with carbon capture and storage
BFGS	Broyden–Fletcher–Goldfarb–Shanno
CAL	Calciner
CCA	Cost of CO_2 avoided
CCR	Cost of CO_2 removal
CCS	Carbon capture and storage
CEPI	Chemical engineering plant cost index
CF	Capacity factor
CFB	circulating fluidised-bed
CLC	Chemical-looping combustion
CLG	Chemical-looping gasification
CLOU	Chemical-looping with oxygen uncoupling
CLR	Chemical-looping reforming
DAQ	Data acquisition
DEA	Diethanolamine
DTR	Drop tube reactor
EFR	Entrained-flow reactor
FBR	Fluidised-bed reactor
FC	Fuel costs
FCF	Fixed charge factor
FOM	Fixed operating and maintenance costs
FR	Fuel reactor
GHG	greenhouse gas
HR	Heat rate

HRSG	Heat recovery steam generator
ITC	International Test Centre
LCOH	Levelised cost of hydrogen
LHV	Lower heating value
MA-CLR	Membrane assisted chemical looping reforming
MAE	Mean absolute error
MDEA	Methyldiethanolamine
MEA	Monoethanolamine
MFB	Micro fluidised bed
MFCs	Mass flow controllers
ML	Machine learning
MOFs	Metal-organic frameworks
NCF_n	Net cash flow in year n
NPV	Net present value
OCAC	Oxygen-carrier-aided combustion
PCA	Principal component analysis
PID	Proportional-integral-derivative
PSA	Pressure swing adsorption
PSAOG	Pressure Swing Adsorption Off Gas
RMSE	Root mean square error
RTS	Reference Technology Scenario
SE-SMR	Sorption enhanced steam methane reforming
SMR	Steam methane reforming
SR-CLC	Steam reforming with chemical-looping combustion
SVMs	Support vector machines
TDCC	Total direct capital cost
TEA	Triethanolamine
TGA	Thermogravimetric analysis
TRL	Technology readiness level
TOC	Total overnight capital costs
VOM	Variable operating and maintenance costs

1 Introduction

1.1 Background

The results from multiple independently-recorded datasets indicate that the climate is warming. The average global temperature during the 2009-2018 decade increased by 0.93±0.07 °C compared to that of the pre-industrial period (1850-1900), and the surface temperature is continuously increasing by ~0.2 °C per decade [1,2]. The Fifth Assessment Report (AR5) by the Intergovernmental Panel on Climate Change (IPCC) [3] emphasised that it is extremely likely that more than half of the observed increase in global average surface temperature from 1951 to 2010 was caused by the anthropogenic increase in greenhouse gas (GHG) concentrations (predominantly CO_2). The impacts of climate change are already evident worldwide with wild fires, droughts, and rising global mean sea level. Hence, it is urgent to reduce CO_2 emissions to the atmosphere to mitigate the ensuing climate breakdown.

Power generation is the largest CO_2 emissions driver, which together with transportation accounted for over two thirds of global CO_2 emissions in 2018, reaching a historical high of 33.5 Gt CO_2 [4]. To decarbonise power and industry, Carbon Capture and Storage (CCS) has been recognised as a vital and proven technology which needs to be rapidly deployed at scale. It is estimated that CCS could contribute 14% and 32% of global CO_2 cumulative emissions reductions in realising the goals in 2 °C Scenario (2DS) and Beyond 2 °C Scenario (B2DS), respectively, as **Figure 1-1** and **Figure 1-2** shown.

CCS prevents most CO_2 from being emitted to the atmosphere. It consists a set of processes for the separation of CO_2 from industrial and energy-related sources, compressing it for transportation and then injecting it deep into geological storage locations and long-term isolation from the atmosphere. CCS technologies can be generally classified into four categories [5]:

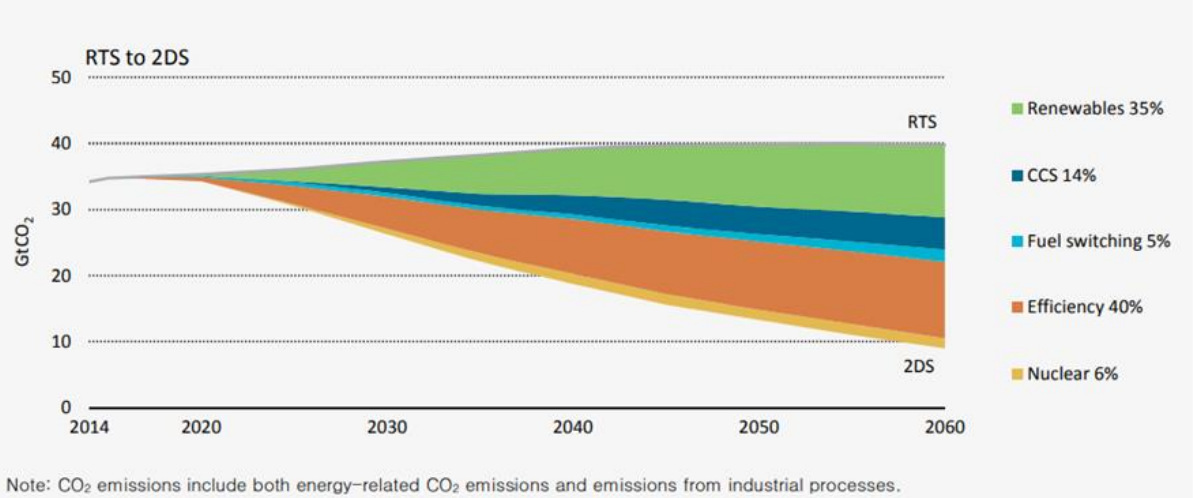

Figure 1-1 Global CO_2 emissions reductions by technology area: Reference Technology Scenario (RTS) to 2DS [6].

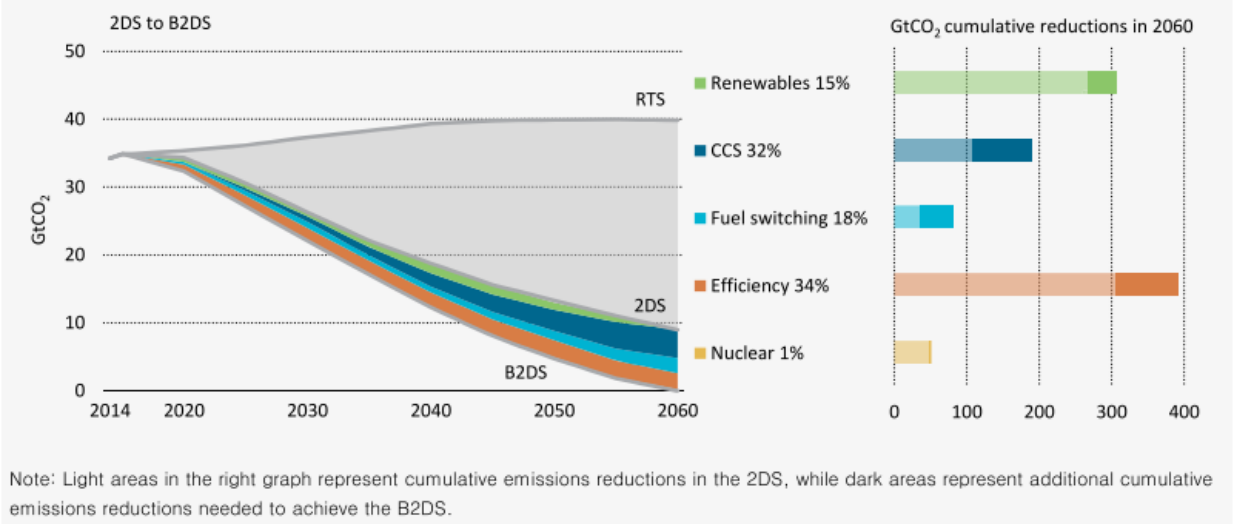

Figure 1-2 Global CO_2 emissions reductions by technology area and scenario B2DS [6]

- **Pre-combustion:**

  This technology involves the process of partial oxidisation of fossil fuels or biomass in steam and oxygen/air under high temperature and pressure to produce a mixture of gases, which typically include CO, CO_2, CH_4 and H_2. This gas mixture is further converted to a H_2 and CO_2-rich gas mixture via the water-gas shift reaction. Then, the CO_2 can be efficiently separated and the H_2 can be supplied for end uses such as hydrogen turbines, fuel cells or as a chemical feedstock.

- **Post-combustion:**

In this process, CO_2 is removed from the flue gases of power plants and other large CO_2 emissions sources by the means of chemical and physical sorption. Amine scrubbing is a well-developed technology for CO_2 removal used in natural gas processing for decades, which has been also applied in two commercial-scale post-combustion capture coal-fired power plants, Boundary Dam and Petra Nova (Reverse shutdown due to current worldwide economic situation). There is the potential to retrofit the existing energy and industrial processes with post-combustion capture systems.

- **Oxy-fuel combustion:**
  This technology burns fuel in a mixture of pure O_2 and recycled CO_2 instead of air. Then, the CO_2 is easily separated from the flue gases, which primarily consists of CO_2 and H_2O. The first generation of oxy-fuel combustion technology uses an air separation unit to separate the oxygen from air, which increases the capital cost and energy penalty significantly.
- **Chemical-looping combustion (CLC):**
  To overcome the issue of high capital cost and energy penalty, the next generation of CO_2 capture technology - chemical-looping combustion - can separate the oxygen from air by means of oxygen carriers and pass this oxygen to the fuel, which results in CO_2 separation and power and heat generation at a low cost and with lower energy penalties.

In addition, CCS can be integrated with low-carbon or carbon-neutral bioenergy, which is usually referred to as BECCS, to achieve negative emissions and limit global warming to below 2 °C [7]. Oxy-fuel combustion and CLC of biomass are two emerging BECCS technologies to achieve negative CO_2 emissions [8–10]. The current technology readiness level (TRL) of oxy-fuel and chemical-looping combustion of biomass is estimated at 6-7 and respectively, and the cost of CO_2 captured for these two technologies is calculated to be approximately £155/tCO_2 and £145/tCO_2 respectively, which is more economically feasible than that for biomass power plants with amine scrubbing system or bioenergy with integrated gasification combined cycle (IGCC) [11].

Although oxy-fuel and chemical-looping combustion of biomass are two promising technologies for negative CO_2 emissions, there are still several key challenges required to address to deploy these technologies at scale. For oxy-fuel combustion of biomass in circulating fluidised beds, better understanding of the boiler heat balance, heat transfer mechanisms, furnace hydrodynamics, and the mechanical and chemical mechanisms of the process is required [12,13]. For the chemical-looping combustion of biomass, the current pure and mixed oxygen carriers are expensive. It is necessary to screen the low-cost and suitable oxygen carrier materials for the process, which have high reactivity with fuels and air, long lifetime, low health risk and environmental impacts, as well as low-cost [14]. Besides, oxy-fuel and chemical-looping combustion of biomass are not only suitable for low-carbon power generation, but also can be integrated with current dominant nature gas reforming process for blue hydrogen production [15–17]. Hydrogen is a versatile feedstock that is widely used in oil refining, ammonia synthesis and the production of many other chemicals, and the low-carbon hydrogen is also an attractive energy carrier that will play a crucial role in in future global energy transitions [18].

1.2 Project Aims and Objectives

The general aim of this research is to address some of the issues in applying oxy-fuel and chemical-looping combustion for a low-carbon future and broaden the knowledge with regards to applying machine learning in CCS. Hence, there are three linked aims involved in this PhD project and the objectives are described as follows:

Aim 1: Investigate the air- and oxy-fuel combustion kinetics of biomass in a fluidised-bed reactor.

> **Objective 1a:** Design and retrofit a lab-scale fluidised-bed reactor that can be operated to measure the reaction kinetics of biomass combustion.
>
> **Objective 1b:** Analyse the experimental data to calculate the reaction order and activation energies.

Objective 1c: Compare and discuss the differences of air and oxy-fuel combustion of biomass in terms of reaction kinetics.

Objective 1d: Apply kinetic models to explore the combustion reaction mechanisms.

Aim 2: Harness the power of machine learning for oxygen carrying materials development in chemical-looping combustion (CLC).

Objective 2a: Create the database of oxygen carriers for chemical-looping processes.

Objective 2b: Develop a fast tool to design and screen optimal oxygen carrying materials.

Objective 2c: Build the workflow in applying machine learning in oxygen carriers developments.

Aim 3: Evaluate the potential and performance of integration of sorption enhanced steam methane reforming (SE-SMR) with oxy-fuel and CLC for blue hydrogen production.

Objective 3a: Simulate a set of SE-SMR process configurations with rigorous heat integration with oxy-fuel combustion and CLC in Aspen Plus.

Objective 3b: Analyse the technical and economic potential of different SE-SMR configurations for blue hydrogen production.

1.3 Thesis Outline

The structure of this research and linkages of each part of the project are illustrated in **Figure 1-3.**

The thesis outline is described as follows:

Chapter 1 - This chapter presents the background, aims and objectives of this project, as well as an overview of the novelty and linkages between publications and project outputs.

Chapter 2 - This chapter presents a general literature review on CCS, blue hydrogen production and machine learning in CCS to review the current scientific knowledge and experience from previous research, and identify the future research direction and gaps in the research.

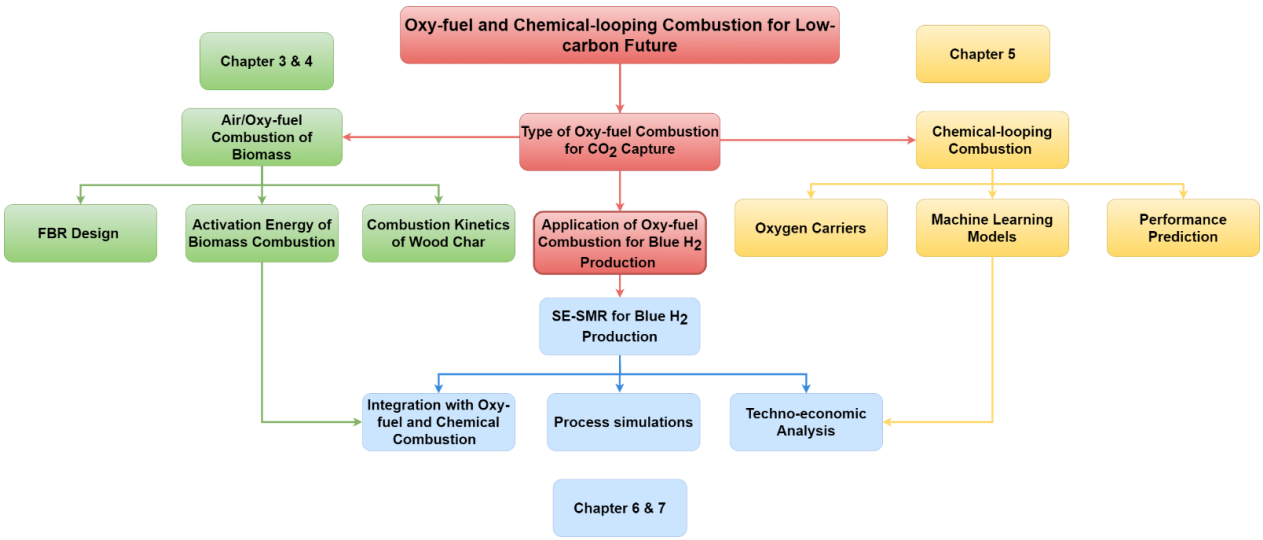

Figure 1-3 Structure and linkage of each project in this thesis

Chapter 3 - This chapter is published work (Published in DOI: https://doi.org/10.1016/j.cherd.2019.10.043) on experimental investigation of air and oxy-fuel combustion kinetics of biomass. A bench-scale spouted fluidised-bed reactor was used to investigate the combustion kinetics of pulverised woody biomass under air and oxy-fuel atmospheres.

Chapter 4 – This chapter presents an experimental investigation of kinetics of wood char combustion in different O_2/N_2 and O_2/CO_2 atmospheres. A lab-scale bubbling fluidised-bed reactor with a rapid analyser for CO and CO_2 was used to investigate the kinetics of biomass char combustion under O_2/N_2 and O_2/CO_2 atmospheres. O_2 inlet concentrations were varied from 5 to 30 vol.% and bed temperatures were in the range of 923 to 1123 K. The biomass char was obtained from the pyrolysis of wood pellet at a bed temperature of 823 K in N_2 and CO_2, respectively.

Chapter 5 - This chapter (Published in Chemical engineering journal, DOI: https://doi.org/10.1016/j.cej.2020.124072) introduces a novel approach, which uses machine learning techniques to estimate the performance of

heterogeneous, multi-component materials as oxygen carriers for chemical-looping. Artificial neural networks that can predict the reactivity of manganese ores as oxygen carriers for CLC/CLOU are used as an example to illustrate the feasibility of applying ML in the development of oxygen-carrier materials.

Chapter 6 - This chapter (DOI: https://doi.org/10.1016/j.enconman.2020.113144) evaluates the potential performance and provides a comprehensive investigation of six new process configurations for SE-SMR integrated with pressure swing adsorption, an iron-based CLC, and oxyfuel combustion for low-carbon and high-purity hydrogen production, which is to understand the thermodynamic limitations of achieving the maximum cold gas efficiency and net efficiency whilst simultaneously capturing the greatest quantity of CO_2 from the production process.

Chapter 7 - This chapter (DOI: https://doi.org/10.1016/j.enconman.2020.113530) presents a preliminary techno-economic assessment of the SE-SMR process integrated with oxy-fuel combustion, chemical-looping combustion and a biomass-fired calciner for low-carbon (blue) and carbon-negative hydrogen production. The thermodynamic and economic performance of the proposed cases are evaluated in terms of the net efficiency, CO_2 capture efficiency, levelised cost of hydrogen (LCOH), CO_2 avoided and removal cost, and is compared with that of SMR and chemical-looping reforming (CLR) with CCS.

Chapter 8 - This chapter provides a summary of the conclusions and discusses the contributions to knowledge and recommendations for future research.

1.4 References

[1] IPCC. Climate Change 2014 Synthesis Report Summary for Policymakers. IPCC 5th Assess Rep 2014:1–31.

[2] Masson-Delmotte V, Zhai P, Pörtner HO, Roberts D, Skea J, Shukla PR, et al. Summary for Policymakers. In: Global Warming of 1.5°C. An IPCC Special Report on the impacts of global warming of 1.5°C above pre-industrial levels and related global greenhouse gas emission pathways, in the context of strengthening the global response to. 2018.

[3] IPCC. IPCC CLIMATE CHANGE 2013 Climate Change 2013. 2013. doi:10.1017/CBO9781107415324.Summary.

[4] Energy Agency I. Statistics report CO_2 Emissions from Fuel Combustion. 2020.

[5] Bui M, Adjiman CS, Bardow A, Anthony EJ, Boston A, Brown S, et al. Carbon capture and storage (CCS): The way forward. Energy Environ Sci 2018;11:1062–176. doi:10.1039/c7ee02342a.

[6] Energy Agency I. Energy Technology Perspectives 2017 Catalysing Energy Technology Transformations INTERNATIONAL ENERGY AGENCY. 2017.

[7] Fuss S, Canadell JG, Peters GP, Tavoni M, Andrew RM, Ciais P, et al. COMMENTARY: Betting on negative emissions. Nat Clim Chang 2014;4:850–3. doi:10.1038/nclimate2392.

[8] Gładysz P, Ziebik A. Environmental analysis of bio-CCS in an integrated oxy-fuel combustion power plant with CO_2 transport and storage. Biomass and Bioenergy 2016;85:109–18. doi:10.1016/j.biombioe.2015.12.008.

[9] Mattison T. Negative emissions of carbon dioxide through chemical-looping combustion (CLC) and gasification (CLG) using oxygen carriers based on manganese and iron n.d. doi:10.1007/s11027-019-09860-x.

[10] Rydén M, Lyngfelt A, Langørgen O, Larring Y, Brink A, Teir S, et al. Negative CO_2 Emissions with Chemical-Looping Combustion of Biomass - A Nordic Energy Research Flagship Project. Energy Procedia, vol. 114, Elsevier Ltd; 2017, p. 6074–82. doi:10.1016/j.egypro.2017.03.1744.

[11] Bhave A, Taylor RHS, Fennell P, Livingston WR, Shah N, Dowell N Mac, et al. Screening and techno-economic assessment of biomass-based power generation with CCS technologies to meet 2050 CO_2 targets. Appl Energy 2017;190:481–9. doi:10.1016/j.apenergy.2016.12.120.

[12] Seddighi S, Clough PT, Anthony EJ, Hughes RW, Lu P. Scale-up challenges and opportunities for carbon capture by oxy-fuel circulating fluidized beds. Appl Energy 2018;232:527–42. doi:10.1016/J.APENERGY.2018.09.167.

[13] Zhu Q. Developments in fluidised bed combustion technology. 2013.

[14] Lyngfelt A. Oxygen Carriers for Chemical Looping Combustion - 4000 h of Operational Experience. Oil Gas Sci Technol 2011;66:161–72. doi:10.2516/ogst/2010038.

[15] Khojasteh Salkuyeh Y, Saville BA, MacLean HL. Techno-economic analysis and life cycle assessment of hydrogen production from natural gas using current and emerging technologies. Int J Hydrogen Energy 2017;42:18894–909. doi:10.1016/j.ijhydene.2017.05.219.

[16] Yan Y, Thanganadar D, Clough PT, Mukherjee S, Patchigolla K, Manovic V, et al. Process simulations of blue hydrogen production by upgraded sorption enhanced steam methane reforming (SE-SMR) processes. Energy Convers Manag 2020;222:113144. doi:10.1016/j.enconman.2020.113144.

[17] Ochoa-Fernández E, Haugen G, Zhao T, Rønning M, Aartun I, Børresen B, et al. Process design simulation of H2 production by sorption enhanced steam methane reforming: Evaluation of potential CO_2 acceptors. Green Chem., vol. 9, Royal Society of Chemistry; 2007, p. 654–62. doi:10.1039/b614270b.

[18] IEA. The Future of Hydrogen. 2019. doi:10.1787/1e0514c4-en.

2 Literature Review

2.1 Carbon Capture and Storage (CCS)

The concerns about global warming and climate change, which arise from the accumulation of CO_2 in the atmosphere, have triggered global efforts to reduce the amount of CO_2 released into the atmosphere. With the implementation of the Kyoto protocol [1] and the Paris agreement [2], it is urgent to develop appropriate technologies to reduce carbon dioxide emissions from the use of energy.

Many authors and organisations have suggested different approaches for different countries to mitigate global warming and climate change, including [3,4]:

- Energy efficiency improvements and energy conservation promotion.
- The switch to reduced carbon-intensity fuels, such as natural gas.
- Utilization of renewable energy sources or nuclear power.
- Reduction of non-CO_2 greenhouse gas emissions.
- CCS.

CCS is a technology that involves the separation of CO_2 from industrial and energy-related sources, transportation of that CO_2 to a storage location and long-term isolation from the atmosphere, which is considered to play a key role in effectively reducing carbon dioxide emissions worldwide [3]. The global modelling efforts by IPCC and IEA have illustrated that CCS technologies play an important role to reduce carbon dioxide emission as well as it is the least-cost pathway to realise a 2 °C scenario. It would be 138% more costly to reach 450 parts per million (ppm) carbon dioxide equivalent by 2100 without CCS [5].

In terms of capture approaches, the CCS technologies can be divided into three main types: 1) Pre-combustion capture, 2) Post-combustion capture, and 3) Oxy-fuel combustion. The related capture technologies and applications have been well defined, explained and reviewed by many authors [6,7], and are illustrated in **Table 2-1**. While, a comparison of the different carbon capture technologies based on the review of related papers is shown in **Table 2-2**. According to the database of large-scale-CCS facilities from the official website of the Global CCS Institute, it reports that CCS facilities are proved to be operated successfully for

more than 40 years. There are currently 37 large-scale CCS facilities running or under construction across the world which have the potential to prevent the release of 40.3 million tonnes CO_2 per annum (Mtpa) [8]. There are nine large-scale CCS projects for power generation, which apply pre-combustion, oxy-fuel combustion, and post-combustion capture technologies. Only two of them are in operation- Boundary Dam Carbon Capture and Storage (Canada) and Petra Nova Carbon Capture (USA), which both apply the post-combustion capture technology (Amine-scrubbing). Most of the current large-scale CCS projects are operated in industrial processes separating CO_2 as indicated in **Table 2-2**. The CCS database of Global CCS Institute reports that there has been significant development of CCS this decade in the Canada, United States, China, Japan, the Middle East and Europe. Nonetheless, the current capacity of CCS is still at a low level, especially for applying in electricity and heat generation, which produced 41% global CO_2 emissions in 2018 [9]. IEA states in their projections that it would require the capture and storage of nearly 4,000 million tonnes of CO_2 per annum in 2040, around 100 times of annual CO_2 capture capacity by the end of 2019 to meet a 2 °C scenario [5,10].

The five-year plan of Accelerating CCS by the Global CCS Institute suggests that if CCS is to make a noticeable contribution to the reduction of CO_2 emissions, it is obvious that a significant increase in new commercial-scale CCS projects is required. It also notes that several actions should be taken before the application of CCS, including: improving the efficiency, increasing funding and policy support and dealing with the potential challenges together [7]. In this section, we only provide a general overview of the status of CCS. The detailed literature review of oxy-fuel combustion of coal and biomass can be found in sections 3.1 and 4.1.

Table 2-1 Overview of different carbon capture technologies [4.11]

Capture technology	Separation technology		Current TRL
Post-combustion	Absorption by chemical solvents	Amine-based solvent, e.g. monoethanolamide (MEA), diethanolamine (DEA), and hindered amine (KS-1).	Commercial
		Alkaline solvents, e.g. NaOH and $Ca(OH)_2$.	Pilot plant
		Ionic liquids.	Proof of concept
	Adsorption by solid sorbents	Amine-based solid sorbents.	Demonstration
		Alkali earth metal-based solid sorbents, e.g. $CaCO_3$.	Demonstration
		Alkali metal carbonate solid	Demonstration
		Sorbents, Na_2CO_3 and K_2CO_3.	Demonstration
	Membrane separation	Porous organic frameworks-polymers.	Commercial Refinement request
		Polymeric membranes, e.g. polymeric gas permeation membranes.	Pilot plant

		Inorganic membranes, e.g. zeolites.	Proof of concept
		Hybrid membranes.	Proof of concept
	Cryogenic separation	Cryogenic separation.	Commercial Refinement request
	Pressure/ vacuum swing adsorption	Zeolites. Active carbon.	Demonstration
Oxy-fuel-combustion	Separation of oxygen from air	Oxy-fuel process, chemical looping combustion, and chemical looping reforming	Pilot plant
Pre-combustion	Absorption by chemical solvents	Amine-based solvent, e.g. monoethanolamine (MEA)	Commercial
	Adsorption by physical solvents	Selexol, rectisol	Proof of concept
	Adsorption by porous organic frameworks	• Porous organic frameworks members	Commercial Refinement request

Table 2-2 Comparison of different carbon capture technologies [3,4,12,13]

Capture Technology	Advantages	Disadvantages	Cost of CO_2 capture $/t$CO_2$ (Pulverised coal-fired plants)	Thermal efficiency %LHV
Post-combustion	Mature technologies are available to retrofit into current plants.	Low capture efficiency; High-energy penalty; the low pressure of produced CO_2.	34	34.8
Pre-combustion	High CO_2 concentration, high CO_2 sorption efficiency; fully developed technology in some industrial area.	Application mainly to new plants; Barriers to the commercial application; Cost of equipment; Extra space for supporting systems.	27	31.5
Oxy-fuel combustion	High CO_2 absorption efficiency; reduce the size of the boiler; mature air separation technology.	High-efficiency drop and energy penalty of Air separation unit (ASU) and compression and purification unit (CPU).	36	35.4

2.2 Blue Hydrogen Production

Hydrogen is a versatile chemical. It is not only widely used in oil refining, ammonia and other chemicals production, but also has significant potential to help tackle various critical energy challenges in decarbonising transport and residential sectors, as well as power and industrial sectors. The dominant hydrogen production technology is steam methane reforming (SMR), which accounts for 76% of global H_2 production [14]. Despite huge efforts to produce affordable "green" hydrogen (carbon-zero) by solar energy, wind energy and bioenergy, SMR remains the most economic and efficient technology for large-scale H_2 production [15]. **Figure 2-1** illustrates the current and potential components of the low-carbon hydrogen system.

It is worth noting that current hydrogen production contributes 2% of annual global CO_2 emissions [14], which will increase with the increase in hydrogen demand if no CCS technologies are applied to its production. To reduce the CO_2 emissions from fossil derived hydrogen production, CCS is required to be integrated to decarbonise the process, and such hydrogen is referred to as blue hydrogen.

A series of studies have been conducted to investigate the feasibility as well thermodynamic and economic performance of natural gas reforming integrated with different CO_2 capture technologies mentioned in section 2.1. Salkuyeh et al. [16] evaluated techno-economic performance of hydrogen production from SMR and autothermal reforming (ATR) with amine capture units, syngas chemical reforming and chemical reforming. Spallina et al. [18,19] analysed and compared the CLC + SMR with membrane assisted chemical looping reforming (MA-CLR) for low-carbon H_2 production, and the results indicated a better techno-economic performance than the conventional SMR integrated with a MDEA unit and H_2 firing in the furnace.

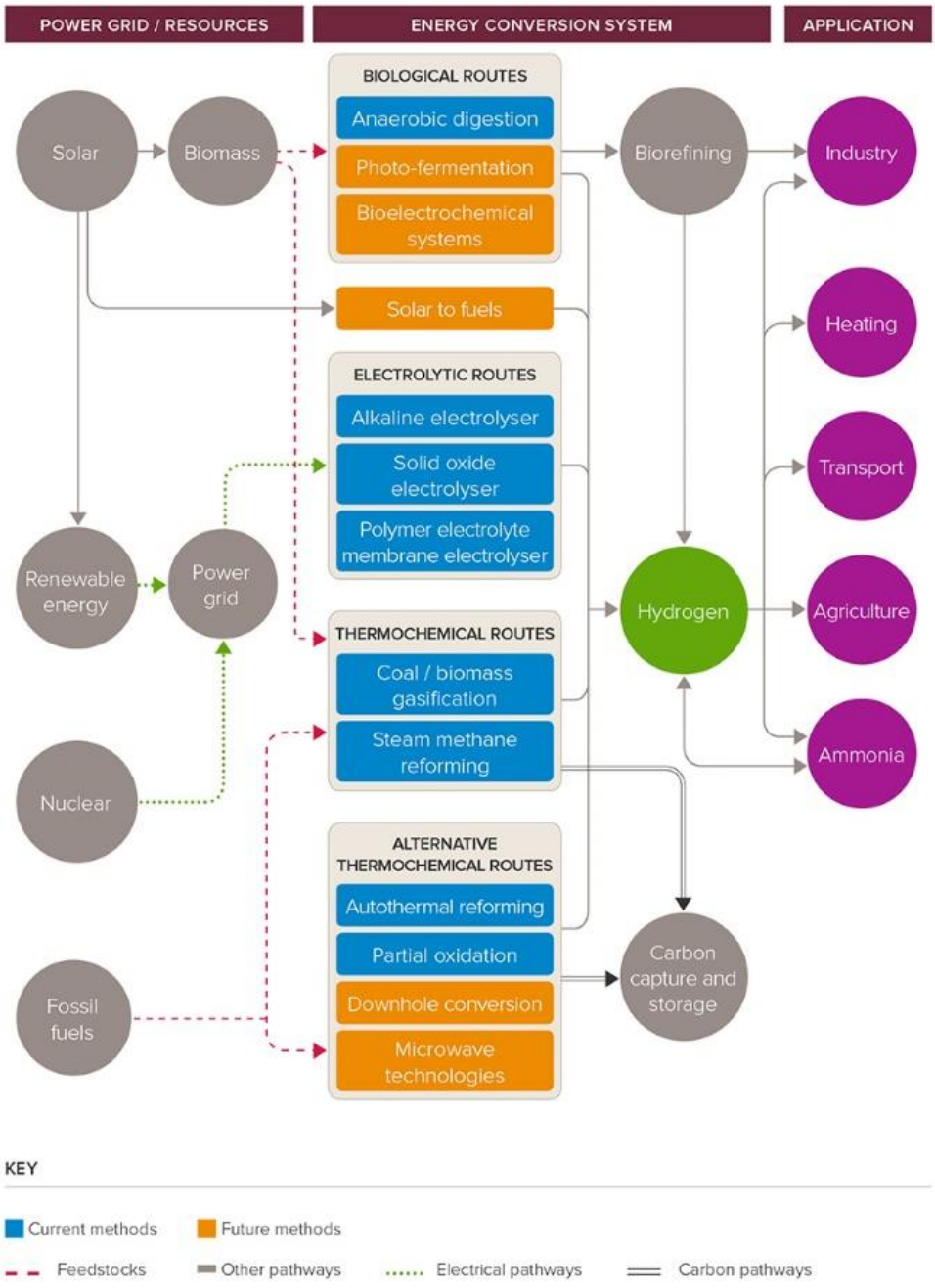

Figure 2-1 Current and potential components of the low-carbon hydrogen system [16]

Besides SMR and ATR with amine based CO_2 capture or integrated CLC as well as MA-CLR, another emerging method is to use the sorption enhanced steam methane (SE-SMR), which involves an in-situ CO_2 capture process where the hydrocarbon fuel is reacted with steam in the presence of a CO_2 sorbent (e.g. CaO) and a reforming catalyst to produce decarbonised H_2 production [20]. Compared to the conventional SMR process, SE-SMR can achieve high yields of

H_2 (~95%, dry basis) at relatively low reaction temperatures (650 °C), without the need for multiple shift reactors and significant subsequent purification steps [20,21]. Recent progress has been made to investigate different sorbents with Ni catalyst as well as Ni-CaO combined sorbent–catalyst materials under the multiple SE-SMR/regeneration cycles in a packed bed or a fluidised-bed [22-27].

Although most of the process CO_2 can be captured by the sorbents in the reformer during SE-SMR process, some CO_2 emissions will occur from the regeneration of the sorbents and the need for providing heat to generate the steam. Therefore, oxy-fuel combustion or other CO_2 capture processes are required to be integrated with SE-SMR process. The integration of these additional processes as well as their thermodynamic performance, operating conditions and economic performance should be evaluated before scale-up. A detailed literature review of these areas presented in sections 6.1 and 7.1.

2.3 Machine Learning in CCS

Machine learning (ML) is an application of artificial intelligence (AI) that can deal with the question of how to develop computers that improve automatically through experience [28]. It has been well developed in past two decades and successfully applied in retail, medical diagnosis, image recognition, speech recognition, robot control and other sectors [28,29]. **Figure 2-2** illustrates the types and applications of machine learning. It can be divided into three categories: Supervised learning, which develops classification and regression predictive models based on both input and output data; Unsupervised learning searches for the hidden patterns or intrinsic structures in the input data without labelled responses; Reinforcement learning is a learning method that interacts with environment by generating actions and discovering errors or rewards [30,31]. A brief description of common machine learning algorithms is presented in the **Table 2-3**.

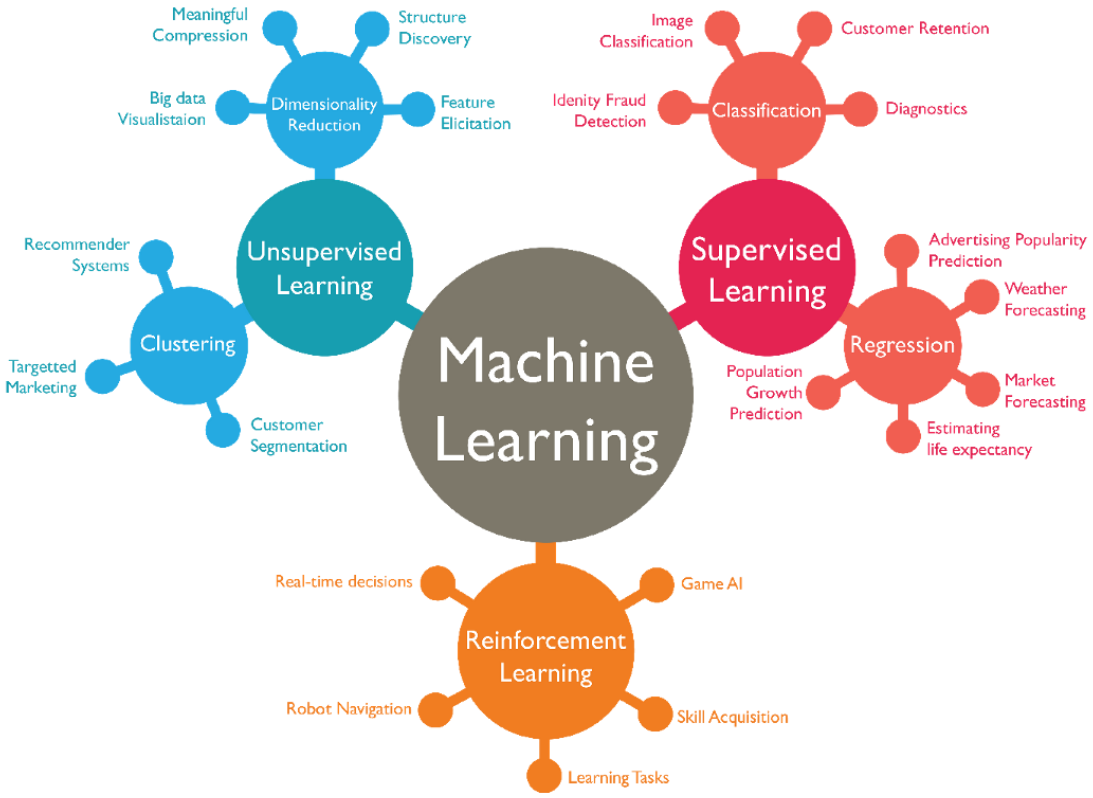

Figure 2-2 Classification and applications of machine learning [32]

Machine learning as a powerful data-driven tool can also play a crucial role in energy and chemical engineering to gain useful insights and understanding of data in order to improve process efficiency and reduce costs and testing time [33-36]. The cross-disciplinary nature of CCS, combining engineering with geology, economics, law and politics, generates a large amount of data during over the past two decades' intensive research, which also provides a huge potential to apply machine learning to accelerate the development of CCS. For CO_2 capture and utilisation, machine learning can be potentially applied for process control, modelling and optimisation of different carbon capture processes; materials selections and development; and as a machine learning based estimator. For CO_2 transport and storage, it can be used for flow monitoring, selection of storage reservoir and sites [37-39], geological CO_2 sequestration monitoring, and prediction of leaks or to identify states of subsurface stresses [40-42]. Here, only the literature on machine learning for CO_2 capture is reviewed.

Table 2-3 Description of common machine learning algorithms and terms [43,44]

Algorithm Name	Type	Description
Artificial neural networks (ANN)	Classification, regression and clustering	ANN inspired by the biological neural networks of the human brain, are made up of input, hidden and output layers as well as a number of parallel-interconnected neurons in each layer. It can be trained to recognise patterns, classify data, and predict future events.
Support vector machines (SVMs)	Classification and regression	SVM applies supervised learning algorithms to search for a hyperplane in high-dimensional space for classification and regression analysis.
Navie Bayes	Classification	Navie Bayes is a classification method that applies the Bayesian theorem, which updates the prior knowledge of an event with the independent probability of each feature that can affect the event.
Decision tree	Classification and regression	This method is highly interpretable classification or regression model that divides values of data features into branches at decision nodes until a final decision output is made.
Random forest	Classification and regression	This method is established on the decision tree to improve the accuracy significantly. It can generate many simple decision trees and uses a ‘majority vote’ to decide on which label to return.

Linear regression	Regression	This method searches for a way to correlate each feature to the output to help predict future values.
K-means clustering	Clustering	This method divides the data into several groups that each contains data with similar characteristics.
Gaussian mixture model	Clustering	A Gaussian mixture model is a probabilistic model that assumes all the data points are generated from a mixture of a finite number of Gaussian distributions with unknown parameters.
Hierarchical clustering	Clustering	This method separates clusters along a hierarchical tree to form a classification system.
Principal component analysis (PCA)	Dimension reduction	PCA reduces the dimensionality of the data by projecting each data point onto only the first few principle components to obtain lower-dimensional data while preserving as much as the data's variation as possible.

ANN was first investigated to model and predict the outputs of amine based CO_2 capture process. Sipöcz et al [45] used simulation data of an amine based CO_2 capture plant as training data to develop ANN model, and the results indicated that trained ANN models were useful for fast simulation of complex steady state process with very high accuracy compared to the rigorous model. Zhou et al [46] used ANN modelling combined with sensitivity analysis and neuro-fuzzy modelling methods, which were trained by the 3-year operational data collected from an amine-based post combustion CO_2 capture process system at the International Test Centre (ITC) of CO_2 Capture located in Regina, Saskatchewan, Canada. The results showed that the neuro-fuzzy modelling technique could

achieve higher accuracy in predicting the CO_2 production rate than the ANN with sensitivity analysis [46]. Later on, Li et al. [47] proposed that Bootstrap aggregated ANN models can provide more accurate predictions and confidence bounds for the predictions in modelling and optimisation of the post-combustion CO_2 capture process.

ANN is also applied as a descriptor-based cheminformatics model for predicting CO_2 solubility in physical solvents in the form of mole fraction with the inputs of organic structural and bond information, thermodynamic properties, and experimental conditions, and the results indicate that the machine learning model can be used to estimate the performance of CO_2 absorbents and to optimise their experimental operating conditions [48].

Venkatraman and Alsberg [49] investigated the application of different machine learning algorithms (partial least squares regression, conditional inference trees and random forests) to predict CO_2 solubility of ionic liquid based on its structure properties for CO_2 capture.

There are also a set of studies that uses different machine learning with molecular simulation in process optimisation and properties prediction of metal-organic frameworks (MOFs) for CO_2 capture [50-55]. Pai et al. [56] developed fast and robust surrogate models using different supervised machine learning algorithms to predict the key parameters such as purity, recovery, energy and productivity in a vacuum swing adsorption process for CO_2 capture. The results showed that Gaussian process regression-based surrogate models had the best performance in outputs predictions, and it can reduce the computational load significantly more than that of traditional detailed models [56].

For calcium looping, oxy-fuel and chemical-looping combustion for CO_2 capture, there is still a significant potential to applying machine learning for process modelling and optimisation, performance predictions and materials design, but largely this hasn't been investigated. Hanak and Manovic [57] developed an ANN model to predict the thermodynamic performance of calcium looping process for CO_2 capture (**Figure 2-3**), and used it for the stochastic economic assessments.

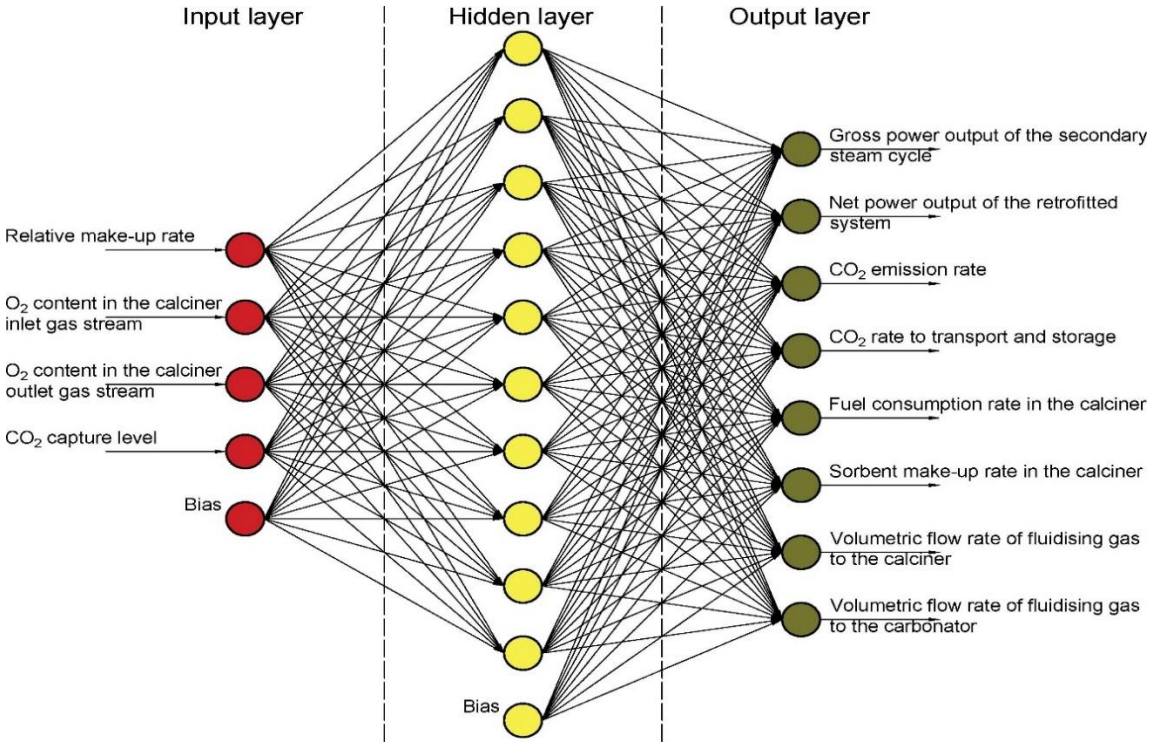

Figure 2-3 Artificial neural network used to predict the thermodynamic performance of calcium looping for CO_2 capture [57].

Zhu et al. [58] investigated the use of ANN models to predict the combustion rate of coal and char, which can provide fast and accurate estimation of combustion rate of different coals without using complex kinetics modelling. This approach was also applied for kinetic parameters prediction of oxy-fuel combustion of different solid fuels, which can achieve high accuracy in prediction compared to that of experimental results [59-61].

To conclude, it is urgent to develop cost-effective CCS technologies to mitigate the global warming. There is a lack of knowledge in the kinetic parameters and reaction mechanisms of oxy-fuel combustion of biomass in the fluidised-bed, which is important for design and retrofitting fluidised-bed boilers. Although, AI and machine learning is versatile, there is no enough work to harness the power of machine learning in oxygen carrying materials developments for chemical-looping processes, especially for heterogeneous, multi-component materials. SE-SMR is emerging technology for blue hydrogen production, but it is required to optimise its system integration to realise 100% CO_2 capture. The integration of

CLC or oxy-fuel combustion with SE-SMR can provide nearly 100% CO_2 capture, but their optimal operating windows and economic potential should be further investigated.

2.4 References

[1] Springer U. The market for tradable GHG permits under the Kyoto Protocol: A survey of model studies. Energy Econ 2003;25:527–51. doi:10.1016/S0140-9883(02)00103-2.

[2] Hulme M. 1.5 °C and climate research after the Paris Agreement. Nat Clim Chang 2016;6:222–4. doi:10.1038/nclimate2939.

[3] Carbon Dioxide Capture and Storage — IPCC. https://www.ipcc.ch/report/carbon-dioxide-capture-and-storage/.

[4] Leung DYC, Caramanna G, Maroto-Valer MM. An overview of current status of carbon dioxide capture and storage technologies. Renew Sustain Energy Rev 2014;39:426–43. doi:10.1016/j.rser.2014.07.093.

[5] The Global Status of CCS | 2016 “Time To Accelerate” 2016:1–28.

[6] Bui M, Adjiman CS, Bardow A, Anthony EJ, Boston A, Brown S, et al. Carbon capture and storage (CCS): The way forward. Energy Environ Sci 2018;11:1062–176. doi:10.1039/c7ee02342a.

[7] Boot-Handford ME, Abanades JC, Anthony EJ, Blunt MJ, Brandani S, Mac Dowell N, et al. Carbon capture and storage update. Energy Environ Sci 2014;7:130–89. doi:10.1039/c3ee42350f.

[8] Global CCS Insitute. The Global Status of CCS | 2016 SUMMARY REPORT 1. 2016. doi:10.1021/ie050569e.

[9] IEA. CO_2 Emissions from Fuel Combustion 2016. Oecd/Iea 2016:1–155. doi:10.1787/co2_fuel-2016-en.

[10] IEA. Energy Technology Perspectives 2016. Iea 2016:14. doi:10.1787/energy_tech-2014-en.

[11] Cuéllar-Franca RM, Azapagic A. Carbon capture, storage and utilisation technologies: A critical analysis and comparison of their life cycle environmental impacts. J CO_2 Util 2015;9:82–102. doi:10.1016/j.jcou.2014.12.001.

[12] IEAGHG. CO_2 Capture As a Factor in Power Station Investment. Energy 2006;19. doi:2006/8.

[13] Figueroa JD, Fout T, Plasynski S, McIlvried H, Srivastava RD. Advances in CO_2 capture technology-The U.S. Department of Energy's Carbon Sequestration Program. Int J Green Gas Control 2008;2:9–20. doi:10.1016/S1750-5836(07)00094-1.

[14] IEA. The Future of Hydrogen. 2019. doi:10.1787/1e0514c4-en.

[15] Stenberg V, Rydén M, Mattisson T, Lyngfelt A. Exploring novel hydrogen production processes by integration of steam methane reforming with chemical-looping combustion (CLC-SMR) and oxygen carrier aided combustion (OCAC-SMR). Int J Greenh Gas Control 2018;74:28–39. doi:10.1016/J.IJGGC.2018.01.008.

[16] The Royal Society. Options for producing low-carbon hydrogen at scale. Policy Briefing.

[17] Salkuyeh YK, Saville BA, MacLean HL. Techno-economic analysis and life cycle assessment of hydrogen production from different biomass gasification processes. Int J Hydrogen Energy 2018;43:9514–28. doi:10.1016/j.ijhydene.2018.04.024.

[18] Spallina V, Shams A, Battistella A, Gallucci F, Annaland MVS. Chemical Looping Technologies for H_2 Production with CO_2 Capture: Thermodynamic Assessment and Economic Comparison. Energy Procedia, vol. 114, Elsevier Ltd; 2017, p. 419–28. doi:10.1016/j.egypro.2017.03.1184.

[19] Spallina V, Pandolfo D, Battistella A, Romano MC, Van Sint Annaland M, Gallucci F. Techno-economic assessment of membrane assisted fluidized bed reactors for pure H_2 production with CO_2 capture. Energy Convers Manag 2016;120:257–73. doi:10.1016/j.enconman.2016.04.073.

[20] Clough PT, Boot-Handford ME, Zheng L, Zhang Z, Fennell PS. Hydrogen production by sorption enhanced steam reforming (SESR) of biomass in a fluidised-bed reactor using combined multifunctional particles. Materials (Basel) 2018;11. doi:10.3390/ma11050859.

[21] Broda M, Manovic V, Imtiaz Q, Kierzkowska AM, Anthony EJ, Müller CR. High-purity hydrogen via the sorption-enhanced steam methane reforming reaction over a synthetic CaO-based sorbent and a Ni catalyst. Environ Sci Technol 2013;47:6007–14. doi:10.1021/es305113p.

[22] Johnsen K, Ryu HJ, Grace JR, Lim CJ. Sorption-enhanced steam reforming of methane in a fluidized bed reactor with dolomite as CO_2-acceptor. Chem Eng Sci 2006;61:1195–202. doi:10.1016/j.ces.2005.08.022.

[23] García-Lario AL, Aznar M, Martinez I, Grasa GS, Murillo R. Experimental study of the application of a NiO/$NiAl_2O_4$ catalyst and a CaO-based synthetic sorbent on the Sorption Enhanced Reforming process. Int J Hydrogen Energy 2015;40:219–32. doi:10.1016/j.ijhydene.2014.10.033.

[24] Arstad B, Prostak J, Blom R. Continuous hydrogen production by sorption enhanced steam methane reforming (SE-SMR) in a circulating fluidized bed reactor: Sorbent to catalyst ratio dependencies. Chem Eng J 2012;189–190:413–21. doi:10.1016/j.cej.2012.02.057.

[25] Li ZS, Cai NS, Yang JB. Continuous production of hydrogen from sorption-enhanced steam methane reforming in two parallel fixed-bed reactors operated in a cyclic manner. Ind Eng Chem Res 2006;45:8788–93. doi:10.1021/ie061010x.

[26] Di Giuliano A, Gallucci K, Kazi SS, Giancaterino F, Di Carlo A, Courson C, et al. Development of Ni- and CaO-based mono- and bi-functional catalyst and sorbent materials for Sorption Enhanced Steam Methane Reforming: Performance over 200 cycles and attrition tests. Fuel Process Technol 2019;195:106160. doi:10.1016/j.fuproc.2019.106160.

[27] Di Felice L, Kazi SS, Sørby MH, Martinez I, Grasa G, Maury D, et al. Combined sorbent and catalyst material for sorption enhanced reforming of

methane under cyclic regeneration in presence of H_2O and CO_2. Fuel Process Technol 2019;183:35–47. doi:10.1016/j.fuproc.2018.10.012.

[28] Jordan MI, Mitchell TM. Machine learning: Trends, perspectives, and prospects. Science 2015;349:255–60. doi:10.1126/science.aaa8415.

[29] Gu GH, Noh J, Kim I, Jung Y. Machine learning for renewable energy materials. J Mater Chem A 2019;7:17096–117. doi:10.1039/c9ta02356a.

[30] Machine Learning in MATLAB - MATLAB & Simulink - MathWorks India https://in.mathworks.com/help/stats/machine-learning-in-matlab.html?w.mathworks.com (accessed August 26, 2020).

[31] What is Machine Learning? A definition - Expert System https://expertsystem.com/machine-learning-definition/ (accessed August 26, 2020).

[32] Machine Learning Algorithms In Layman's Terms, Part 1 | by Audrey Lorberfeld | Towards Data Science. https://towardsdatascience.com/machine-learning-algorithms-in-laymans-terms-part-1-d0368d769a7b (accessed August 25, 2020).

[33] Narciso DAC, Martins FG. Application of machine learning tools for energy efficiency in industry: A review. Energy Reports 2020;6:1181–99. doi:10.1016/j.egyr.2020.04.035.

[34] Cheng L, Yu T. A new generation of AI: A review and perspective on machine learning technologies applied to smart energy and electric power systems. Int J Energy Res 2019;43:1928–73. doi:10.1002/er.4333.

[35] Ghoddusi H, Creamer GG, Rafizadeh N. Machine learning in energy economics and finance: A review. Energy Econ 2019;81:709–27. doi:10.1016/j.eneco.2019.05.006.

[36] Yan Y, Borhani TN, Clough PT. Chapter 14. Machine Learning Applications in Chemical Engineering, The Royal Society of Chemistry; 2020, p. 340–71. doi:10.1039/9781839160233-00340.

[37] You J, Ampomah W, Kutsienyo EJ, Sun Q, Balch RS, Aggrey WN, et al. Assessment of enhanced oil recovery and CO_2 storage capacity using machine learning and optimization framework. Soc. Pet. Eng. - SPE Eur. Featur. 81st EAGE Conf. Exhib. 2019, Society of Petroleum Engineers; 2019. doi:10.2118/195490-MS.

[38] Romdhane A, Bunting S, Anyosa S, Eidsvik J, Bergmo AnouarRomdhane P. A machine learning based monitoring framework for CO_2 storage EGU-2020

[39] Shao D, Yan Y, Zhang W, Sun S, Sun C, Xu L. Dynamic measurement of gas volume fraction in a CO_2 pipeline through capacitive sensing and data driven modelling. Int J Greenh Gas Control 2020;94:102950. doi:10.1016/j.ijggc.2019.102950.

[40] Ahmadi MA, Kashiwao T, Rozyn J, Bahadori A. Accurate prediction of properties of carbon dioxide for carbon capture and sequestration operations. Pet Sci Technol 2016;34:97–103. doi:10.1080/10916466.2015.1107847.

[41] Lin Y, Harp DR, Chen B, Pawar R, Lin Y, Harp DR, et al. Geologic Carbon Sequestration Leakage Detection: A Physics-Guided Machine Learning Approach. AGUFM 2017;2017:IN13B-0062.

[42] De Lima RP, Lin Y. Geophysical data integration and machine learning for multi-target leakage estimation in geologic carbon sequestration. SEG Int. Expo. Annu. Meet. 2019, Society of Exploration Geophysicists; 2020, p. 2333–7. doi:10.1190/segam2019-3215405.1.

[43] Sakura S. Machine learning Algorithms and where they are used? https://techsavvypriya.wordpress.com/2019/12/19/machine-learning-algorithms-and-where-they-are-used/ (accessed August 31, 2020).

[44] Fit Data with a Shallow Neural Network - MATLAB & Simulink https://www.mathworks.com/help/deeplearning/gs/fit-data-with-a-neural-network.html (accessed March 20, 2019).

[45] Sipöcz N, Tobiesen FA, Assadi M. The use of Artificial Neural Network models for CO_2 capture plants. Appl Energy 2011;88:2368–76. doi:10.1016/j.apenergy.2011.01.013.

[46] Zhou Q, Wu Y, Chan CW, Tontiwachwuthikul P. Modeling of the carbon dioxide capture process system using machine intelligence approaches. Eng Appl Artif Intell 2011;24:673–85. doi:10.1016/j.engappai.2011.01.003.

[47] Li F, Zhang J, Oko E, Wang M. Modelling of a post-combustion CO_2 capture process using neural networks. Fuel 2015;151:156–63. doi:10.1016/j.fuel.2015.02.038.

[48] Li H, Yan D, Zhang Z, Lichtfouse E. Prediction of CO_2 absorption by physical solvents using a chemoinformatics-based machine learning model. Environ Chem Lett 2019;17:1397–404. doi:10.1007/s10311-019-00874-0.

[49] Venkatraman V, Alsberg BK. Predicting CO_2 capture of ionic liquids using machine learning. J CO_2 Util 2017;21:162–8. doi:10.1016/j.jcou.2017.06.012.

[50] Burns TD, Pai KN, Subraveti SG, Collins SP, Krykunov M, Rajendran A, et al. Prediction of MOF Performance in Vacuum Swing Adsorption Systems for Post-combustion CO_2 Capture Based on Integrated Molecular Simulations, Process Optimizations, and Machine Learning Models. Environ Sci Technol 2020;54:4536–44. doi:10.1021/acs.est.9b07407.

[51] Dureckova H, Krykunov M, Aghaji MZ, Woo TK. Robust machine learning models for predicting high CO_2 working capacity and CO_2/H_2 selectivity of gas adsorption in metal organic frameworks for pre-combustion carbon capture. J Phys Chem C 2019;123:4133–9. doi:10.1021/acs.jpcc.8b10644.

[52] Deng X, Yang W, Li S, Liang H, Shi Z, Qiao Z. Large-scale screening and machine learning to predict the computation-ready, experimental metal-organic frameworks for CO_2 capture from air. Appl Sci 2020;10. doi:10.3390/app10020569.

[53] Subraveti SG, Li Z, Prasad V, Rajendran A. Machine Learning-Based Multiobjective Optimization of Pressure Swing Adsorption. Ind Eng Chem Res 2019; 58:20412–22. doi:10.1021/acs.iecr.9b04173.

[54] Anderson R, Rodgers J, Argueta E, Biong A, Gómez-Gualdrón DA. Role of Pore Chemistry and Topology in the CO_2 Capture Capabilities of MOFs: From Molecular Simulation to Machine Learning. Chem Mater 2018;30:6325–37. doi:10.1021/acs.chemmater.8b02257.

[55] Fernandez M, Boyd PG, Daff TD, Aghaji MZ, Woo TK. Rapid and accurate machine learning recognition of high performing metal organic frameworks for CO_2 capture. J Phys Chem Lett 2014;5:3056–60. doi:10.1021/jz501331m.

[56] Pai KN, Prasad V, Rajendran A. Experimentally validated machine learning frameworks for accelerated prediction of cyclic steady state and optimization of pressure swing adsorption processes. Sep Purif Technol 2020;241:116651. doi:10.1016/j.seppur.2020.116651.

[57] Hanak DP, Manovic V. Economic feasibility of calcium looping under uncertainty. Appl Energy 2017;208:691–702. doi:10.1016/J.APENERGY.2017.09.078.

[58] Q. Zhu, J.M. Jones, A. Williams KMT. The predictions of coal-char combustion rate using an artificial neural. Fuel 1999;78:1755–62.

[59] Sunphorka S, Chalermsinsuwan B, Piumsomboon P. Application of artificial neural network for kinetic parameters prediction of biomass oxidation from biomass properties. J Energy Inst 2017;90:51–61. doi:10.1016/j.joei.2015.10.007.

[60] Xie C, Liu J, Zhang X, Xie W, Sun J, Chang K, et al. Co-combustion thermal conversion characteristics of textile dyeing sludge and pomelo peel using TGA and artificial neural networks. Appl Energy 2018;212:786–95. doi:10.1016/j.apenergy.2017.12.084.

[61] Chen J, Xie C, Liu J, He Y, Xie W, Zhang X, et al. Co-combustion of sewage sludge and coffee grounds under increased O_2/CO_2 atmospheres:

Thermodynamic characteristics, kinetics and artificial neural network modelling. Bioresour Technol 2018;250:230–8. doi:10.1016/j.biortech.2017.11.031.

3 Investigation of the Apparent Kinetics of Air and Oxy-Fuel Biomass Combustion

Yongliang Yan, Peter T. Clough, Edward J. Anthony

Energy and Power Theme, Cranfield University, Cranfield, Bedfordshire, MK43 0AL, UK

Submitted on 18th April 2019. Accepted on 28th October 2019.

Published in Chemical Engineering Research and Design 153 (2020) 276-283

DOI: https://doi.org/10.1016/j.cherd.2019.10.043

Abstract

A bench-scale spouted fluidised-bed reactor was used to investigate the combustion kinetics of pulverised woody biomass under air and oxy-fuel atmospheres. Bed temperatures were in the range of 923-1073 K and O_2 concentrations were varied from 20-35 vol%. The activation energies and apparent orders of reaction were calculated for air and oxy-fuel combustion by means of an n^{th} order Arrhenius equation approach. Results indicated that the apparent order of reaction for both air and oxy-fuel combustion was approximately zero. The activation energies were calculated assuming a zero-order reaction mechanism and were averaged over all oxygen concentrations for air and oxy-fuel combustion and found to be 18.95 kJ/mol and 26.93 kJ/mol, respectively. The rate of combustion under oxy-fuel conditions was, on average, 37.5% higher compared to air combustion. The shrinking core model with a reaction-controlled step was found to accurately represent the biomass combustion reactions under both air and oxy-fuel conditions.

Keywords

Combustion; Kinetics; Biomass; Oxy-fuel; Spouted fluidised bed; Carbon capture and storage

3.1 Introduction

Carbon capture and storage (CCS) is a significant technology to reduce the environmental burden of fossil fuel use [1]. More recently, the combination of Bio-Energy with CCS (BECCS) has drawn global attention in the context of greenhouse gas (GHG) emissions reduction [2]. Oxy-fuel combustion is a promising technology with a Technology Readiness Level (TRL) of 7-8 for carbon capture from power generation and industry [3]. In particular, fluidised bed (FB) is one of the more promising technologies that can apply an oxy-fuel based approach, which has the benefits of fuel flexibility, low SO_x and NO_x emissions, and a reduced energy penalty. Burning biomass under oxy-fuel conditions provides the option of CO_2-negative emissions as well as offering other advantages such as improving ignition and burnout performance and reducing the pollutant emissions when co-firing with coal [4]. Biomass with oxy-fuel combustion technology is a potential BECCS technology.

However, there are significant differences between coal and biomass with respect to combustion kinetics and, hence, design and operation of a boiler [3,5,6]. Therefore, it is necessary to study the kinetics of the air and oxy-fuel combustion of biomass before deploying BECCS at a large scale. The derived and calculated kinetic parameters from an experimental study can be used for computational fluid dynamics calculations, to help design and optimise commercial-scale boilers for air and oxy-fuel combustion of biomass [7].

The kinetics study of solid fuels is conducted in a range of equipment, including: the thermogravimetric analyser (TGA) [8,9], drop-tube reactor (DTR) [10,11], entrained-flow reactor (EFR) [12], wire-mesh reactor (WMR) [13], and fluidised-bed reactors (FBR) [17-17].

TGA kinetic analysis allows direct measurement of sample mass, with high repeatability. However, the low heating rates and the effects of the heat and mass transfer influence the accuracy of the experimental results and are generally regarded as problematic when determining intrinsic kinetic parameters [13,14]. EFR and WMR by contrast, have complicated measurement and analysis and require a skilled operator which limits their application [15]. Aside from these

techniques, other researchers [14,15] have proposed using a bench-scale fluidised-bed reactor (FBR) with a fast-response gas analyser to investigate the kinetics of char combustion. This method can provide homogeneous temperature and bulk gas composition, high heating rates (around 10^4 K/s), sufficient residence time, flexible temperature and gas compositions and an approximate carbon mass balance [13,18,19]. However, this method relies on any reaction of the sample being inferred by measuring the gas composition rather than directly measuring the weight change of the sample itself, thus opening itself up to errors. It is also difficult to extract and quench fuel samples during a combustion experiment to permit the analysis of morphology and composition evolution, which are possible for EFR and DTR [13,18].

Bews *et al.* first determined the kinetic parameters and reaction mechanism of the combustion of graphite using a small FBR [20]. Subsequently, Fennell *et al.* (2009) further developed this method to study the kinetics of burning of coal char in a FBR with a fast-response gas analyser of CO/CO_2 [12,21]. More recently, Haustein *et al.* also used a small-scale FBR with Fourier Transform Infrared (FTIR) spectroscopy to study the kinetic parameters of char combustion and gasification [21]. Similarly, Gövert *et al.* measured and compared the kinetic parameters of coal char combustion and gasification under air/oxy-fuel combustion using the same reactor and noted that the reaction of char in air was faster than in oxy-fuel atmosphere, and that there is no significant difference in activation energies in air and oxy-fuel combustion [14]. Generally, it has been found that the results obtained through FBRs can be comparable to those obtained from EFRs and TGAs, once the minimisation of mixing effects and fast analysers are employed [14,15,18].

Compared with the existing kinetic studies of coal char combustion for FBR, there is a dearth of literature regarding air and oxy-fuel combustion of biomass when employing a FBR. Much of the previous work has focused on the kinetically-controlled oxidation reaction of char in different oxidising gases [14,15,21,22]. The apparent kinetics of air and oxy-fuel combustion of raw biomass by the FBR method and the effects of devolatilisation and volatile matter combustion on the

kinetics measurement of char have not been well investigated. In this work, a bench-scale spouted fluidised-bed reactor operating in bubbling fluidisation mode with a fast-response multi-gas analyser has been used to investigate the apparent kinetics of air and oxy-fuel combustion of woody biomass with the aim of exploring the effects of devolatilisation and volatile matter combustion on the overall kinetics of biomass combustion.

3.2 Materials and Methods

3.2.1 Materials

Here, ECOTEK wood pellets were ground, with a pestle and mortar, and sieved to a particle size fraction of 300-425 μm, and then stored in sealed sample containers. The proximate analysis of the pulverised wood was conducted with a TGA 8000 (Perkin Elmer) using the method reported in [23], which was proven to yield similar results to those obtained from the ASTM standard method. The ultimate analysis of the fuel sample was measured by a Vario EL III Elemental Analyser. The proximate and ultimate analyses of the biomass are given in **Table 3-1**.

For the bed material, silica sand (bulk density = 2600 kg/m^3, rounded to sub-rounded in shape, supplied by David Ball Group Plc.) and sieved to a size fraction of 425-500 μm, was used. For the fluidising gases, CO_2, O_2 and N_2 (supplied by BOC UK) of respective purities 99.8%, 99.5% and 99.998%, were used in these experiments.

Table 3-1 Proximate and ultimate analyses of biomass sample

Proximate analysis (wt%, as received)		Ultimate analysis (wt%, as received)	
Moisture	4.97	C	47.91
Volatile matter	78.30	H	6.70
Fixed carbon	14.93	N	0.12
Ash content	1.79	S	0.04

O (by difference)	45.27

3.2.2 Experimental Setup

A process flow diagram of the bench-scale spouted fluidised reactor and ancillary equipment is shown in **Figure 3-1**. A quartz liner (240 mm in length, 26 mm O.D., supplied by Soham Scientific, Cambridge, UK) was placed inside the main body of the reactor and was made of a cylindrical section with a conical frustum at the base (8 mm I.D.). The reactor was heated by electrical resistance heating and its temperature was measured by K-type thermocouples on the outer wall of the reactor and inside the bed's quartz liner. The reactor shell was constructed of Incoloy 800HT (supplied by Special Metals, UK) and had a total length of 500 mm, an outer diameter of 31.8 mm and a wall thickness of 2.9 mm.

The reactor was designed to facilitate the addition of solid fuels through a U-bend and pressurised batch feeding system. The U-bend and gas supply tubes after the mass flow controls were wrapped with heating tapes and heated to 105 °C in order to preheat the gas and fuels before entering the reactor. Superwool insulating blanket (supplied by RS Components Ltd, UK) was utilised to minimise heat loss.

Three mass flow controllers (MFCs) (Bronkhorst EL-FLOW model F-201CV) controlled the gas flow rate of N_2, CO_2 and O_2. All the MFCs can be controlled by a computer *via* a dynamic data exchange field bus based on RS485 technology (Bronkhorst Flow BUS) to realise automatic control of the flow in the various gas transport lines and simulate different gas mixtures at the gas mixing point.

Finally, a series of gas filters was installed to clean the flue gas leaving the reactor, particularly to remove fine particulate matter and moisture. A portion of the gas was then diverted to the ADC multi-gas analyser (MGA 3000, ADC Ltd., UK), and the remaining gases were sent to the exhaust gas ventilation system. The analyser measured the concentrations of O_2, CO and CO_2 from the flue gas and the measurement ranges of these gases were 0-40 vol%, 0-20 vol% and 0-100 vol%, respectively, and their intrinsic accuracy was ±1% of the measured value. The humidity content in the flue gas was measured with a relative humidity

probe (Vaisala HUMICAP HMT330). An Agilent VEE process controller and data recording system was used for this work; data were passed to this system from data acquisition (DAQ) cards (RedLab USB-1208FS, Meilhaus Electronic).

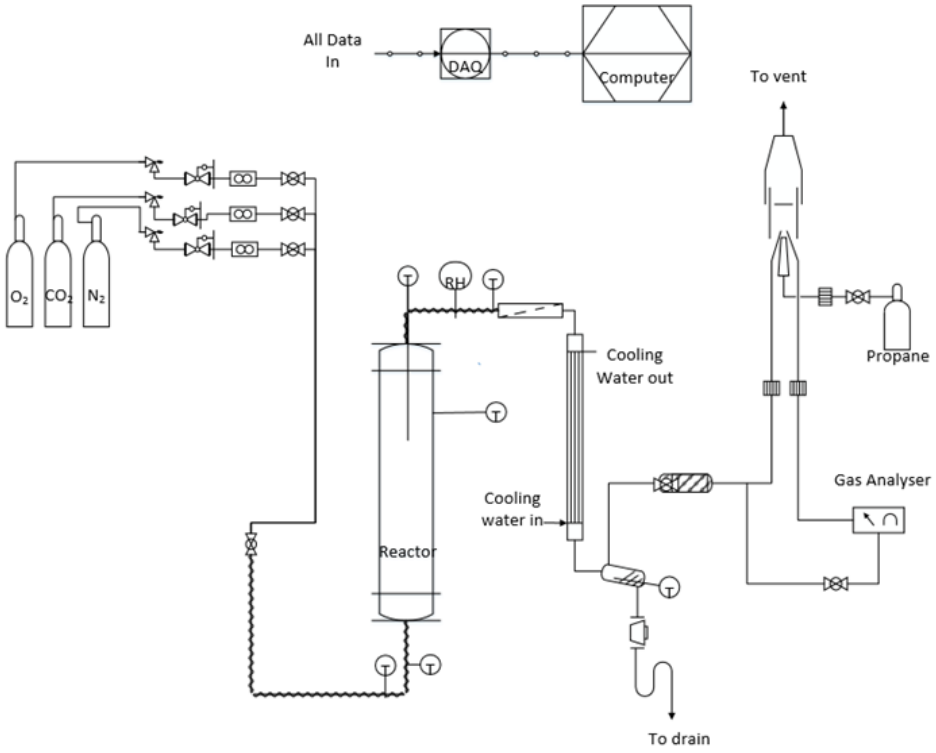

Figure 3-1 Process flow diagram of the spouted fluidised-bed reactor and ancillary equipment

3.2.3 Standard Operating Procedure

The experiments were conducted at atmospheric pressure in a temperature range of 923-1073 K. Typically, 15 g of silica sand (425-500 µm) was added into the reactor when the reactor reached the desired temperature and had a uniform gas concentration. The oxygen concentration in the air and oxy-fuel combustion tests was varied from 20 vol% to 35 vol% and balanced with N_2 and CO_2, respectively. A small amount of N_2 (5 vol%) was added to each of the oxy-fuel tests to ensure an accurate mass balance could be achieved; it was assumed that the N_2 was inert in these combustion tests. The detailed operation conditions are shown in **Table_Apx A-1**. (See Appendix A).

The minimum fluidisation velocity (U_{mf}) was calculated using the Wen and Yu correlation (Wen and Yu, 1966). To ensure sufficiently vigorous bubbling fluidisation and to improve the gas-solid mixing inside the reactor, a ratio of fluidisation velocity (U) to minimum fluidisation velocity (U/U_{mf}) of ~3 was employed. Fuel sample masses of 0.02 g (±2%) were injected into the reactor *via* the pressurised feeding system, once the bed temperature and gas concentrations were at steady state. An assessment of the correct sample mass was made, the data from which is presented in the Appendix A; the aim was to select the smallest mass which presented a readable signal relative to the background noise level of the analyser and was closest in observed rate to the assumed intrinsic rate of the smallest sample mass. As the amount of silica sand was much greater than that of the injected fuel sample, this ensured good heat transfer between bed material and injected fuel sample allowing the fuel to rapidly achieve similar temperatures. Furthermore, a high cross-flow factor (See Appendix A for more details) was calculated for this system, which indicated that the gas concentration in the bubble phase and particle phase were nearly the same, and there was a high degree of mixing within the bed. Each test was repeated three times at each set of conditions, and a blank test (no biomass sample only inert gas (N_2) added during feeding) was repeated before and after every sample injection, which was used to indicate whether the sample was fully injected into the reactor, and to quantify the effects of sample injection on the measured gas concentrations ((See Appendix A for more details). Any blank test where the hold-up prevented 100% of the sample from being completely introduced into the reactor, was repeated after cleaning the valve and sample hopper. In addition, the average carbon recovery based on CO_2 was calculated for each condition to ensure elutriation of the fuel samples was minimised. To achieve the real-time measured gas concentration, it is necessary to consider the response time of the test rig. In this work, the deconvolution of the measured gas concentration was dealt with a published method by [15]. The response time of this test rig was calculated to be around 2.29 s and the details of calculation can be found in the Appendix A.

3.3 Results and Discussion

3.3.1 Reaction Rates

The dynamic response of the gas analysers measured concentrations, caused pressurised sample injection, were corrected to obtain the actual rate of gas production (further detail is supplied in the Appendix A, **Figure_Apx A-4**-**Figure_Apx A-6**). The peak rates of biomass combustion were assumed approximately equivalent to the initial rate of reaction. During some initial tests it was found that, below 20 vol% O_2, the rate of CO production exceeded that of CO_2 production (Figure **3-2**), due to sub-stoichiometric conditions leading to incomplete combustion; therefore, the data at 10 vol% O_2 were excluded from the analysed data set. The O_2 concentration was varied from 20-35 vol% at intervals of 5 vol% for both air and oxy-fuel combustion tests. The combustion rates for air and oxy-fuel combustion for pulverised wood and recovery of carbon are summarised in **Table_Apx A-2** (See Appendix A).

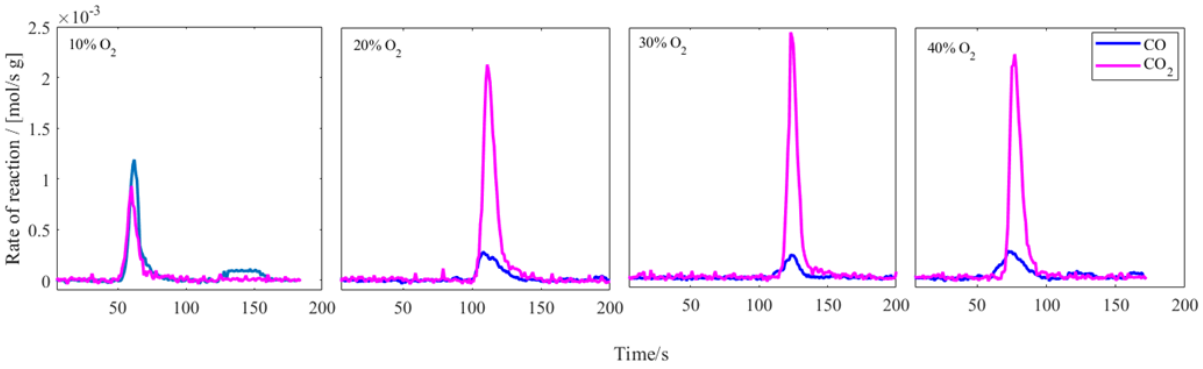

Figure 3-2 Rate of biomass combustion in 10-40 vol% O_2. At conditions of 973 K, U/U_{mf} = 3, 0.02 g (±2%) biomass, and 1 bar(a))

Figure 3-3 and **Figure 3-4** give the rates of CO_2 production *vs.* bed temperature and oxygen concentration, both of which indicate that the rates of CO_2 production increase with the increase of the bed temperature. The measured rate with different sample weights at conditions of 823 K, 25 vol% O_2/75 vol% N_2, U/U_{mf} = 3, and 1 bar(a) are compared in **Figure_Apx A-7** in the Appendix A. It is clearly shown that the sample mass added had no effect on the rate of reaction, for sample masses greater than 0.02 g. The sample mass was selected to maximise the signal to noise ratio and use a little sample as possible in order to minimise

intraparticle diffusion effects which could hamper the rate of reaction. Comparing the rates of air and oxy-fuel combustion at the same bed temperature and oxygen concentration shows that the rate of oxy-fuel combustion is about 20-30% larger than that of air combustion, which is opposite to the results reported for air and oxy-fuel combustion of coal char [14]. It is also worth pointing out that carbon balance for oxy-fuel combustion is higher than that of the air combustion of raw woody biomass when the bed temperature is over 923 K, which means that the burnout rate of fuel could be improved when switching from air to oxy-fuel combustion at those conditions. The average carbon recovery for both air and oxy-fuel combustion of biomass was approximately 80%, without considering the CO and CH_4 produced, which indicates there was negligible particle elutriation.

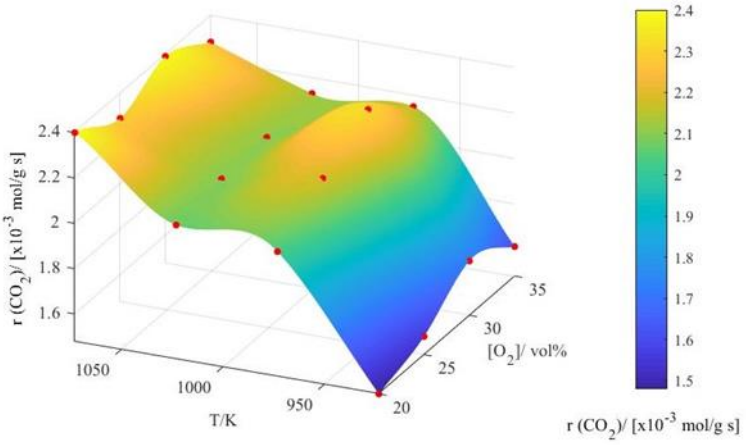

Figure 3-3 Rate of CO_2 production vs. temperature and O2 concentration for the air combustion tests

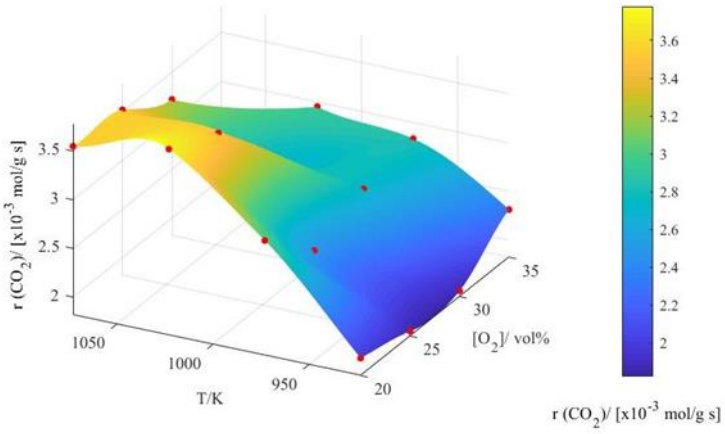

Figure 3-4 Rate of CO_2 production *vs.* temperature and O_2 concentration for the oxy-fuel combustion tests

3.3.2 Order of Reaction

The combustion process can be described by the rate equation $r = k[O_2]^n$ [15], where r is the rate of combustion, k is the rate constant, $[O_2]$ is the molar concentration of oxygen, and n is the reaction order.

In air combustion conditions, the apparent order of reaction obtained here is approximately zero (see **Figure 3-5**). It was found, at all temperatures investigated, that the rate of biomass combustion was not influenced by an increase in oxygen concentration from 20 to 35 vol%. This zero-order trend was also seen in the oxy-fuel combustion tests (**Figure 3-6**) at the lower bed temperatures (923-973 K), but at the higher bed temperatures (1023-1073 K) the order of was found to be -0.4, which appears to be caused by errors in the CO_2 concentration measurement at oxygen concentrations close to the maximum range of the analyser (40 vol%).

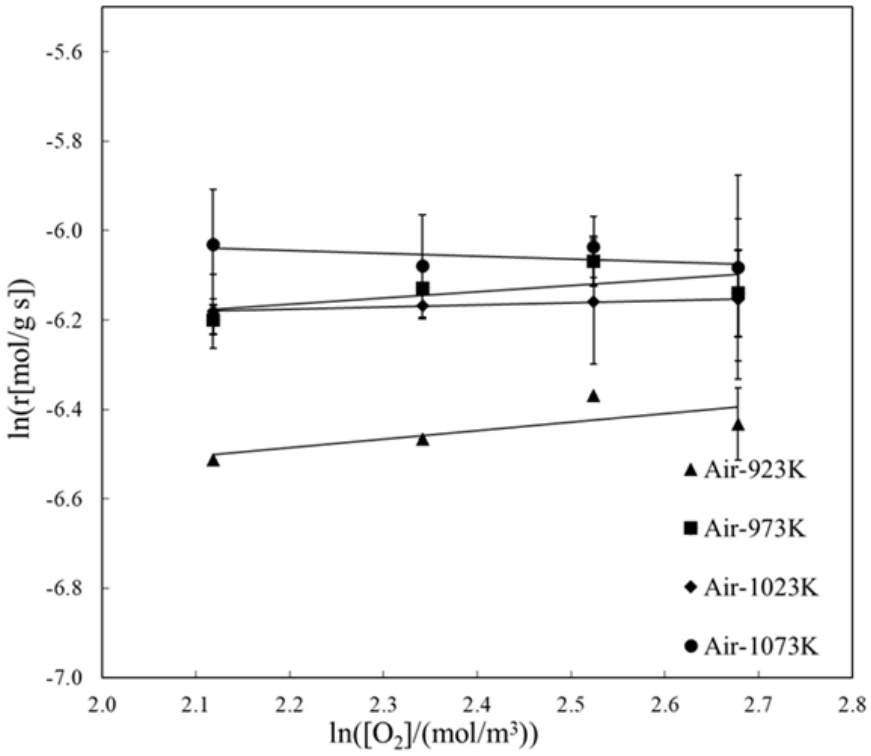

Figure 3-5 ln(r) *vs.* ln$[O_2]$ in air combustion tests. At conditions of 923-1073 K, 20-35 vol% O_2, 0.02 g (±2%) sample, U/U_{mf} = 3, and 1 bar(a). The error bars show the standard deviation between three repeats.

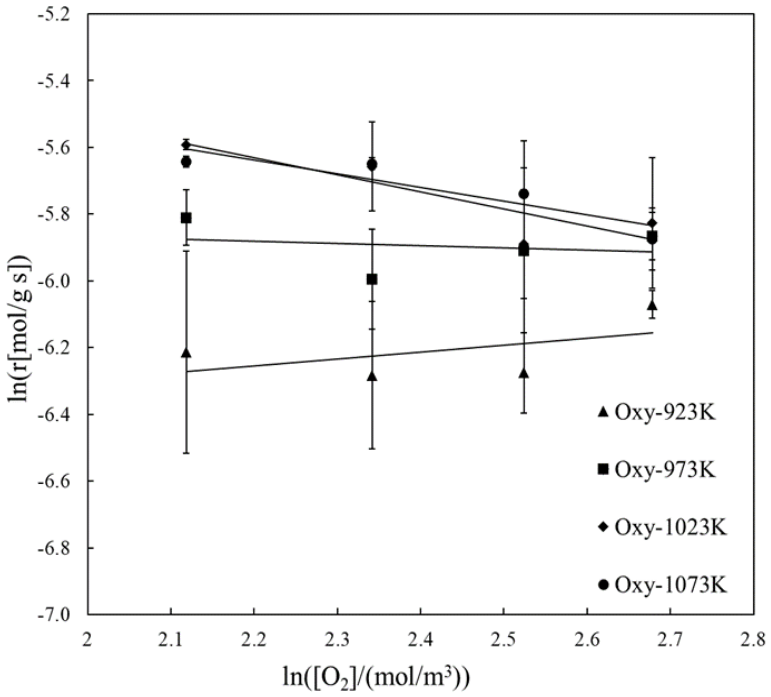

Figure 3-6 ln(*r*) *vs.* ln[O_2] in oxy-fuel combustion tests. At conditions of 923-1073 K, 20-35 vol% O_2, 0.02 g (±2%) sample, U/U_{mf} = 3, and 1 bar(a). The error bars show standard deviation between three repeats

3.3.3 Activation Energies

The activation energies and pre-exponential factors under air and oxy-fuel combustion were derived using the Arrhenius equation. The rate constants, *k,* were calculated over the 20-35 vol% O_2 range and across the bed temperature range of 923-1073 K under air and oxy-fuel combustion conditions. The average activation energy (Ea) for air combustion was found to be 18.95 kJ/mol and 26.93 kJ/mol for oxy-fuel combustion. This trend is in agreement with the work of Li *et al.* [26].

It should also be noted that both activation energies in this test are about one-third of previous activation energies of coal or biomass char combustion found in the literature [14,15,27,28], likely because of measured rates of CO_2 from both volatile and char combustion. This, therefore, represents the apparent activation energy of biomass combustion instead of the intrinsic activation energy of volatile combustion or char combustion.

3.3.4 Shrinking Core Model Validation

The shrinking unreacted core model has been fitted to the data for fuel carbon conversion to CO_2, in order to identify the likely mechanisms for combustion. The process of biomass combustion was simplified, as **Equation. (3-1)**:

$$C_{(s)} + O_{2\,(g)} \rightarrow CO_{2\,(g)} \quad \textbf{(3-1)}$$

In this process, oxygen first diffuses through the gas film surrounding the fuel particle and then reacts at its surface. The produced CO_2 then diffuses back through the product ash layer and fresh O_2 diffuses in through the product layer. External film and ash layer diffusion can be assumed to be negligible here, because of the relatively high fluidisation velocity (U/U_{mf} = 3). The rate of mass transfer of oxygen to the exterior of the spherical fuel particles is calculated to be approximately 4.5×10^{-7} mol/g s, which is far less than the measured reaction rate (1.48×10^{-3} at 973 K in air conditions). The conversion and dimensionless time equations for a reaction-controlled shrinking unreacted core model on a spherical particle are as follows:

$$\frac{t}{\tau} = 1 - (1 - X)^{1/3} \quad \textbf{(3-2)}$$

$$\tau = \frac{\rho\, Rp}{b\, ks\, C_{Ag}} \quad \textbf{(3-3)}$$

where t is the instantaneous reaction time point, τ is the total reaction time, X is the fuel conversion, b is the stoichiometric coefficient, C_{Ag} is the concentration of A in bulk gas, ρ is the molar density of the particle, Rp is the radius of the particle, and ks is the reaction rate constant.

Fitting the experimental data to this model involved minimising the sum of the squared errors between the experimental and modelled conversions, whilst adjusting the value of the rate constant, *ks*. The fitting was carried out up to the final experimental C-to-CO_2 conversion value. The conversion-time data obtained from the shrinking core model were compared with the experimental results, as shown in **Figure 3-7** to **Figure 3-10**. It was found that the reaction-controlled shrinking core model prediction closely matched the experimental results, with

the largest deviations occurring at the lowest levels of conversion. This difference at the initial phase of reaction appears to be caused by external mass transport smoothing effects in the tubing post-reactor. The experiments with the lowest carbon conversions were probably governed by other factors: incomplete combustion or more likely fine particles elutriating from the reactor before fully reacting.

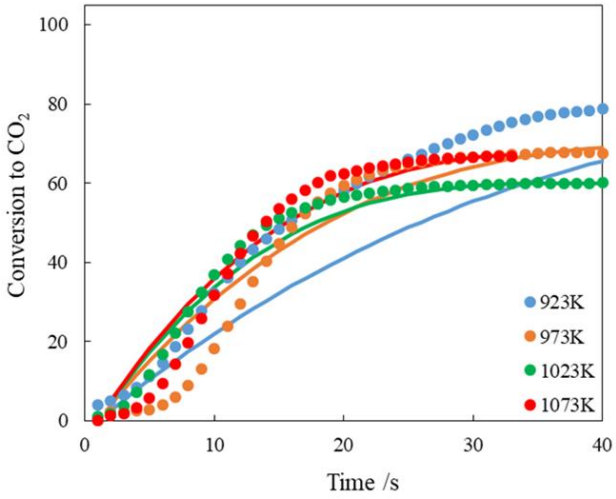

Figure 3-7 Comparison of experimental results and model predictions at 25 vol% O_2, bed temperature 923-1073 K under air combustion of wood. (Points: experimental results. Solid lines: shrinking core model predictions)

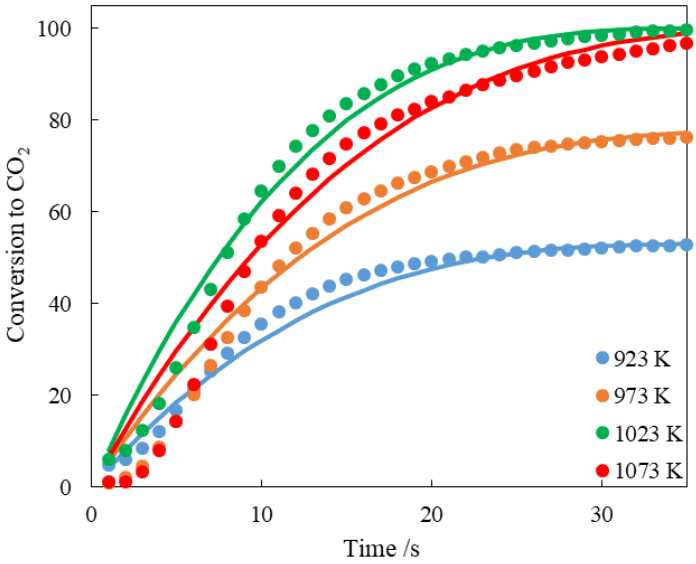

Figure 3-8 Comparison of experimental results and model predictions at 25 vol% O2, bed temperature 923-1073 K under oxy-fuel combustion of wood. (Points: experimental results. Solid lines: shrinking core model predictions).

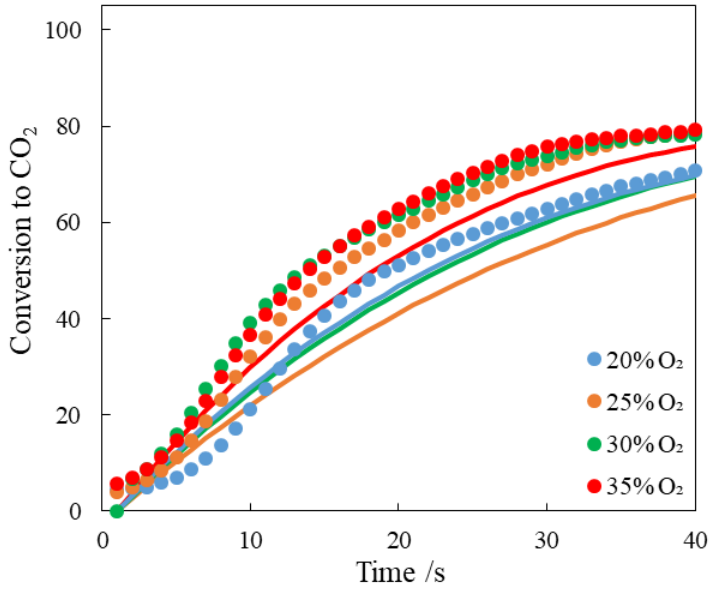

Figure 3-9 Comparison of experimental results and model predictions at 20-35 vol% O_2, bed temperature 923 K under air combustion of wood. (Points: experimental results. Solid lines: shrinking core model predictions)

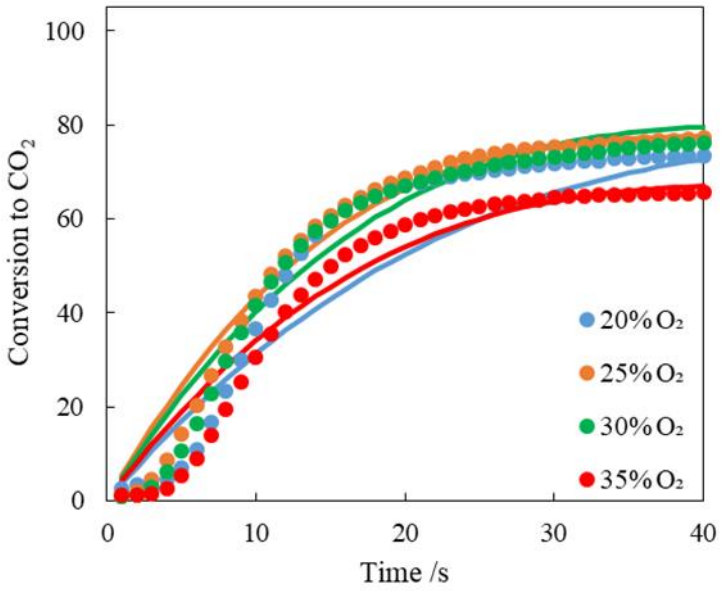

Figure 3-10 Comparison of experimental results and model predictions at 20-35 vol% O_2, bed temperature 923 K under oxy-fuel combustion of wood. (Points: experimental results. Solid lines: shrinking core model predictions)

Table 3-2 presents the reaction rate constants determined by the shrinking core model. These have similar trends to those measured from the experimental tests, having an average difference of 50%. This difference was primarily due to the experimental data in the initial portion of the reaction, which have a marked

inflection. Again, this difference was likely a result of the tubing length post-reactor causing a smoothing effect on the data; additionally, the numerical method of removing the blank feed from the data may have impacted the data. Furthermore, the shrinking core model to fit the experimental data by **Equation.** (3-1**)** neglected more complicated reactions that occur simultaneously due to the presence of other chemical species in the fuel, such as hydrogen, oxygen, nitrogen, sulphur and moisture. The combustion process is probably also slightly affected by ash layer diffusion effects.

Table 3-2 Shrinking core model and experimental observed rate constants. Experiments varying bed temperature were conducted at a constant O_2 concentration of 25 vol%, and experiments varying oxygen concentrations were conducted at 923 K

	***k*exp (m/s)**		***ks* (m/s)**	
Bed temperature (K)	Air	Oxy-fuel	Air	Oxy-fuel
923	0.074	0.093	0.044	0.102
973	0.109	0.124	0.079	0.097
1023	0.105	0.174	0.115	0.118
1073	0.114	0.176	0.314	0.100
Oxygen concentration (%)	Air	Oxy-fuel	Air	Oxy-fuel
20	0.074	0.150	0.069	0.082
25	0.074	0.093	0.044	0.102
30	0.086	0.136	0.042	0.071
35	0.080	0.141	0.044	0.061

3.3.5 Discussion

In this work, the apparent kinetics of air and oxy-fuel combustion of raw biomass were calculated by measuring the rate of gas concentration change. It was found that the activation energy of biomass combustion in this work was about one-third that for wood char combustion found in previous work [8]. The different chemical and physical properties (due to the presence of volatile hemicellulose and cellulose) and different combustion process can explain the difference between the woody biomass and its char.

Raw biomass contains a larger amount of volatile matter (78.3 wt%) than that of char (15.0 wt%), which when added to a hot reactor, quickly devolatilises and begins to combust in the gaseous phase, enhancing the char oxidation reactions. In addition, the particle size and surface of biomass char are also different from the raw biomass due to the devolatilisation and swelling in the char generation process [14,27]. A decrease in volatile matter content of biomass fuels reduces its reactivity, which was demonstrated by Li *et al*. [27], who showed that the reactivity of biomass decreases with the increase of degree of torrefaction.

Another reason for the lower apparent activation energy for biomass combustion relative to char combustion found in this work is the different reaction processes between biomass and char. The process of biomass combustion consists of heating and drying, devolatilisation, volatile matter combustion, and char combustion. Previous work, measuring the kinetics of char combustion using a FBR found that the reaction was controlled predominantly by the kinetics of the oxidation reactions (120 kJ/mol) and secondly by the oxygen diffusion control (60 kJ/mol) [15,20]. In this work, when the biomass was injected into the reactor, the process of devolatilisation and volatile matter combustion overlapped with the char combustion. The measured CO_2 cannot differentiate whether CO_2/CO came from char combustion or from volatile matter combustion. Instead, it describes the total production of CO and CO_2 from both the volatile matter and char combustion. This method was also used by Shan *et al.* [29], who investigated biomass combustion behaviour using a visualisation method. It was observed that there were two separate processes for volatile matter and char combustion

for biomass and the duration of those processes is based on the fixed carbon-to-volatile matter mass ratio of the biomass [29,30]. It was also concluded that the devolatilisation and volatile matter combustion not only influenced the time to complete burnout, but also had a large impact on the measured biomass combustion kinetics by the FBR method.

The reaction-controlled shrinking core model was able to fit the experimental data relatively well; however, the calculated reaction rate constants tended to be slightly lower than those obtained from the experimental data due to the complex biomass combustion processes and the assumptions made in fitting the model to the data (considered only fuel carbon to CO_2 reactions).

3.4 Conclusions

The air and oxy-fuel combustion reactions of raw woody biomass have been investigated in a bench-scale, spouted fluidised-bed reactor. Combustion experiments were conducted under the different oxygen concentrations (20-35 vol%), and across a range of bed temperatures (923-1073 K). The shrinking core model was fitted to the carbon conversion data and well represented the reaction kinetics observed, with the largest deviation occurring in the initial stages of combustion.

The experimental results indicate that the measured rate of oxy-fuel combustion is higher (~37.5%) than that of air combustion under the same conditions. The apparent orders of reaction for air and oxy-fuel combustion of biomass in the spouted fluidised-bed reactor were found to be approximately zero. The activation energies for air and oxy-fuel combustion of biomass were found to be 18.95 kJ/mol and 26.93 kJ/mol, respectively. Comparing those with previous work, the activation energy of raw woody biomass combustion in this work is less than that of wood char combustion. This can be explained by the fact that the devolatilisation and volatile combustion of woody biomass overlap the char combustion. Therefore, the measured CO_2 rate indicates the apparent kinetics of woody biomass combustion—it cannot represent the corrected reaction rates of any process.

The issue of pressurised sample injection on the accurate measurement of CO_2 concentration was resolved by factoring in the effects of blank (no sample) injections. Ideally, the apparent kinetics of air and oxy-fuel combustion of biomass should be measured using biomass char in the spouted fluidised-bed reactor with the advantages of high heating rates, and minimised heat and mass transfer resistances.

3.5 References

[1] Bui M, Adjiman CS, Bardow A, Anthony EJ, Boston A, Brown S, et al. Carbon capture and storage (CCS): The way forward. Energy Environ Sci 2018;11:1062–176. doi:10.1039/c7ee02342a.

[2] Sher F, Pans MA, Sun C, Snape C, Liu H. Oxy-fuel combustion study of biomass fuels in a 20 kWth fluidized bed combustor. Fuel 2018;215:778–86. doi:10.1016/j.fuel.2017.11.039.

[3] Seddighi S, Clough PT, Anthony EJ, Hughes RW, Lu P. Scale-up challenges and opportunities for carbon capture by oxy-fuel circulating fluidized beds. Appl Energy 2018;232:527–42. doi:10.1016/j.apenergy.2018.09.167.

[4] Duan L, Duan Y, Zhao C, Anthony EJ. NO emission during co-firing coal and biomass in an oxy-fuel circulating fluidized bed combustor. Fuel 2015;150:8–13. doi:10.1016/j.fuel.2015.01.110.

[5] Zhu Q. Developments in fluidised bed combustion technology. IEA. 2013.

[6] Varol M, Symonds R, Anthony EJ, Lu D, Jia L, Tan Y. Emissions from Co-firing Lignite and Biomass in an Oxy-fired CFBC. Fuel Process Technol 2018;173:126–33. doi:10.1016/j.fuproc.2018.01.002.

[7] Gil MV, Riaza J, Álvarez L, Pevida C, Pis JJ, Rubiera F. Kinetic models for the oxy-fuel combustion of coal and coal/biomass blend chars obtained in N_2 and CO_2 atmospheres. Energy 2012; 48:510–8. doi:10.1016/J.ENERGY.2012.10.033.

[8] Wang X, Hu Z, Deng S, Wang Y, Tan H. Kinetics investigation on the combustion of biochar in O_2/CO_2 atmosphere. Environ Prog Sustain Energy 2015. doi:10.1002/ep.12063.

[9] Liu H. Combustion of Coal Chars in O_2/CO_2 and O_2/N_2 Mixtures: A Comparative Study with Non-isothermal Thermogravimetric Analyzer (TGA) Tests , Energy Fuels 2009. doi:10.1021/ef9002928.

[10] Tolvanen H, Raiko R. An experimental study and numerical modelling of combusting two coal chars in a drop-tube reactor: A comparison between N_2/O_2, CO_2/O_2, and $N_2/CO_2/O_2$ atmospheres. Fuel 2014;124:190–201. doi:10.1016/J.FUEL.2014.01.103.

[11] Tolvanen H, Keipi T, Raiko R. A study on raw, torrefied, and steam-exploded wood: Fine grinding, drop-tube reactor combustion tests in N_2/O_2 and CO_2/O_2 atmospheres, particle geometry analysis, and numerical kinetics modeling. Fuel 2016;176:153–64. doi:10.1016/j.fuel.2016.02.071.

[12] Álvarez L, Gharebaghi M, Pourkashanian M, Williams A, Riaza J, Pevida C, et al. CFD modelling of oxy-coal combustion in an entrained flow reactor. Fuel Process Technol 2011;92:1489–97. doi:10.1016/j.fuproc.2011.03.010.

[13] Kim GM, Kim JP, Lisandy KY, Jeon CH. Experimental model development of oxygen-enriched combustion kinetics on porous coal char and non-porous graphite. Energies 2017;10. doi:10.3390/en10091436.

[14] Gövert B, Pielsticker S, Kreitzberg T, Habermehl M, Hatzfeld O, Kneer R. Measurement of reaction rates for pulverized fuel combustion in air and oxyfuel atmosphere using a novel fluidized bed reactor setup. Fuel 2017;201:81–92. doi:10.1016/j.fuel.2017.03.009.

[15] Fennell PS, Dennis JS, Hayhurst AN. The order with respect to oxygen and the activation energy for the burning of an anthracitic char in O_2 in a fluidised bed, as measured using a rapid analyser for CO and CO_2. Proc Combust Inst 2009;32 II:2051–8. doi:10.1016/j.proci.2008.06.097.

[16] Fennell PS, Kadchha S, Lee H-Y, Dennis JS, Hayhurst AN. The measurement of the rate of burning of different coal chars in an electrically heated fluidised bed of sand. Chem Eng Sci 2007;62:608–18. doi:10.1016/J.CES.2006.09.024.

[17] Fennell PS, Hayhurst AN, Dennis JS, Kadchha S, Lee HY. The kinetics of oxidation of chars from three different coals, as measured in fluidized beds. Proc. 18th Int. Conf. Fluid. Bed Combust. 2005, vol. 2005, ASME; 2005, p. 881–94. doi:10.1115/FBC2005-78073.

[18] Mueller A, Haustein HD, Stoesser P, Kreitzberg T, Kneer R, Kolb T. Gasification Kinetics of Biomass-and Fossil-Based Fuels: Comparison Study Using Fluidized Bed and Thermogravimetric Analysis, Energy Fuels 2015. doi:10.1021/acs.energyfuels.5b01123.

[19] Li J, Paul MC, Younger PL, Watson I, Hossain M, Welch S. Characterization of biomass combustion at high temperatures based on an upgraded single particle model. Appl Energy 2015;156:749–55. doi:10.1016/j.apenergy.2015.04.027.

[20] Bews IM, Hayhurst AN, Richardson SM, Taylor SG. The Order, Arrhenius Parameters, and Mechanism of the Reaction Between Gaseous Oxygen and Solid Carbon, Combust. Flame, 124 (2001), pp. 231-245

[21] Haustein HD, Kreitzberg T, Gövert B, Massmeyer A, Kneer R. Establishment of kinetic parameters of particle reaction from a well-stirred fluidized bed reactor. Fuel 2015;158:263–9. doi:10.1016/J.FUEL.2015.05.038.

[22] Morin M, Pécate S, Hémati M. Kinetic study of biomass char combustion in a low temperature fluidized bed reactor. Chem Eng J 2018;331:265–77. doi:10.1016/J.CEJ.2017.08.063.

[23] Cai J, He Y, Yu X, Banks SW, Yang Y, Zhang X, et al. Review of physicochemical properties and analytical characterization of lignocellulosic biomass. Renew Sustain Energy Rev 2017;76:309–22. doi:10.1016/j.rser.2017.03.072.

[24] Wen CY, Yu YH. A generalized method for predicting the minimum fluidization velocity. AIChE J 1966;12:610–2. doi:10.1002/aic.690120343.

[25] Clough PT, Boot-Handford ME, Zheng L, Zhang Z, Fennell PS. Hydrogen production by sorption enhanced steam reforming (SESR) of biomass in a fluidised-bed reactor using combined multifunctional particles. Materials (Basel) 2018;11. doi:10.3390/ma11050859.

[26] Li L, Duan L, Tong S, Anthony EJ. Combustion characteristics of lignite char in a fluidized bed under O_2/N_2, O_2/CO_2 and O_2/H_2O atmospheres. Fuel Process Technol 2019;186:8–17. doi:10.1016/j.fuproc.2018.12.007.

[27] Li J, Bonvicini G, Tognotti L, Yang W, Blasiak W. High-temperature rapid devolatilization of biomasses with varying degrees of torrefaction. Fuel 2014;122:261–9. doi:10.1016/j.fuel.2014.01.012.

[28] Yurdakul Yorulmaz S, Atimtay AT. Investigation of combustion kinetics of treated and untreated waste wood samples with thermogravimetric analysis. Fuel Process Technol 2009;90:939–46. doi:10.1016/j.fuproc.2009.02.010.

[29] Shan L, Kong M, Bennet TD, Sarroza AC, Eastwick C, Sun D, et al. Biomass and Bioenergy Studies on combustion behaviours of single biomass particles using a visualization method. Biomass and Bioenergy 2018;109:54–60. doi:10.1016/j.biombioe.2017.12.008.

[30] Bai X, Lu G, Bennet T, Sarroza A, Eastwick C, Liu H, et al. Combustion behavior profiling of single pulverized coal particles in a drop tube furnace through high-speed imaging and image analysis. Exp Therm Fluid Sci 2017;85:322–30. doi:10.1016/j.expthermflusci.2017.03.018.

4 Kinetic Study of Wood Char Combustion under O_2/N_2 and O_2/CO_2 in a Bubbling Fluidised-bed Reactor

Yongliang Yan, Peter T. Clough, Vasilije Manovic, Edward J. Anthony

Energy and Power Theme, Cranfield University, Cranfield, Bedfordshire, MK43 0AL, UK

Draft, propose to submit to Fuel

Abstract

A lab-scale bubbling fluidised-bed reactor with a rapid analyser for CO and CO_2 was used to investigate the kinetics of biomass char combustion under O_2/N_2 and O_2/CO_2 atmospheres. O_2 inlet concentrations were varied from 5 to 30 vol.% and bed temperatures were in the range of 923 to 1123 K. The biomass char was obtained from the pyrolysis of wood pellet at bed temperature of 823 K in N_2 and CO_2, respectively. The order of char combustion was calculated based on the rate equation, which was 0.41 (R^2= 0.84) for char combustion under O_2/N_2 and 0.44 (R^2= 0.95) for char combustion under O_2/CO_2. The activation energies for char combustion under O_2/N_2 and O_2/CO_2 at the oxygen concentration of 20% were calculated by an n^{th} order Arrhenius equation approach, which were 20.03 (R^2= 0.90) and 26.58 (R^2= 0.91) kJ/mol, respectively. The rates of char combustion in O_2/N_2 and O_2/CO_2 atmospheres were both improved by the increase in oxygen concentration and bed temperature. At the same condition, the rate of char combustion in O_2/CO_2 was 13 % points in average higher than that of char combustion in O_2/N_2, which can be explained by the increase in pore size, volume and surface area of char derived from CO_2. The predictions of reaction-controlled shrinking core model give a good agreement in the experimental results of carbon conversion during the char combustion at the both conditions. The experimental results indicated that more CO was produced during the char combustion in O_2/CO_2 than that in O_2/N_2, even at higher oxygen concentration and lower bed temperature. This suggests that char-CO_2 gasification should be considered during the retrofit current fluidised-bed boilers and design new oxy-fuel biomass fluidised-bed combustion boilers.

Keywords

Char combustion, kinetics, bubbling fluidised-bed, oxy-fuel combustion, carbon capture and storage

4.1 Introduction

Carbon capture and storage (CCS) is a vital technology to reduce the CO_2 emissions across the industry and power, and it is the least-cost pathway to realise the 2 °C climate change goal [22,23]. Recently, the combination of Bio-Energy with CCS (BECCS) has attracted global attention in the context of net-negative greenhouse gas (GHG) emissions to limit the global warming below 2 °C [24]. Oxy-fuel combustion is one of the most developed CCS technologies with a Technology Readiness Level (TRL) 7-8 [12,25], and the use of biomass in the oxy-fuel combustion is potential option to realise the negative CO_2 emissions.

In particular, circulating fluidised-bed (CFB) is one of the more favourable technologies that can been applied for oxy-fuel combustion, which has the advantages of fuel flexibility, low NO_x emissions, better sulphur removal and higher net efficiency [26,27]. An intensive research has been conducted on oxy-fuel combustion of coal and co-firing of coal and biomass to accelerate their deployment in a large-scale [12,28–30]. But it is should be emphasised that there are drastic differences in combustion characteristics and behaviours between coal and biomass, and hence it is necessary to be considered in design and operation of a boiler [13]. The combustion kinetics of char are key parameters that can be experimental investigated to design and optimise a boiler [31,32]. Thus, it is necessary to investigate the reaction kinetics and mechanism of biomass char under the O_2/N_2 and O_2/CO_2 before deploying the oxy-fuel combustion biomass in a large scale or retrofitting the conventional boilers to oxy-fired boilers.

Liu [33] investigated the combustion kinetics of two chars derived from bituminous and anthracite coal under the O_2/N_2 and O_2/CO_2 conditions in a thermogravimetric analyser (TGA), and the results indicated that activation energies for these two chars were 138.03 and 127.83 kJ/mol respectively and the reaction order was approximately first-order. However, the low heating rates and the effects of the heat and mass transfer of TGA have restricted its further

application to measure intrinsic kinetics of char combustion at higher temperatures [34]. The lab-scale fluidised-bed reactor (FBR), which has the advantages of high heating rates, homogeneous temperature, bulk gas composition, sufficient residence time and flexible temperature and gas compositions, has been applied to the measurement of reaction kinetics of gas-solids for various solid fuels [32,34–40]. Fennell et al. [41] illustrated the measurement of the rate of burning an anthracitic char in a fluidised bed with rapid analyser for CO and CO_2, and the results indicated the oxidation of an anthracitic char was first-order reaction in O_2 between 700 and 900 °C and the activation energy was well agreed with the literature data. Scala [36] proposed a new experimental technique to measure the CO/CO_2 production ratio at the surface of spherical char particles from a low-attrition bituminous coal at 850 °C and low oxygen concentration between 0.1 and 2.0% and results showed that the carbon was mostly oxidised to CO_2 within the particle boundary layer under the under the experimental conditions investigated. Later, Haustein et al. [42] used the lab-scale fluidised-bed reactor with the Fourier Transform Infrared (FTIR) spectroscopy to study the kinetic parameters of char combustion and gasification. Fang et al. [34] compared the kinetics of the coal char from the micro fluidised bed (MFB) with mass spectrometer and TGA, and the results indicated that the kinetics measured by MFB were more accurate than that of TGA at high temperatures. Li e al. [43] investigated the combustion characteristic of light char in a FBR under O_2/N_2, O_2/CO_2, and O_2/H_2O atmospheres, and found that the calculation results for the activation energy based on the shrinking core model of different atmospheres were O_2/CO_2 (28.96 kJ/mol) > O_2/H_2O (26.11 kJ/mol) > O_2/N_2 (23.31 kJ/mol), and the char-gasification cannot be ignored in both O_2/CO_2, and O_2/H_2O. Wang et al. [32] studied the combustion characteristics and kinetics of bituminous char particles in a FBR under simulated fluidised-bed combustor conditions at low oxygen concentrations (4 to 10%), and the results suggested that the effect of char-CO_2 gasification on the char conversion should be taken into account at the highest bed temperatures and largest particle diameters.

For the biomass char combustion kinetics, especially under the O_2/CO_2 condition, few literature has been reported to use FBR to measure their combustion kinetics.

Henrich et al. [44] measured the combustion and gasification kinetics of pyrolysis chars from waste and biomass in a FBR. Salatino et al. [45] investigated the the effects of carbon attrition and fines post combustion on fixed carbon conversion in fluidised-bed combustion of a biomass char. Morin et al. [46] investigated the kinetic parameters of biomass char combustion by FBR method at low temperature with the oxygen partial pressure ranging from 5065 to 21273 Pa, and results indicated the Volumetric Model well-represented experimental data and the FBR method could avoid the effects of both diffusional effects and oxidation of CO in the stagnant zone within the crucible in TGA. Yan et al. [47] investigated the apparent kinetics of air and oxy-fuel combustion of woody biomass in a spout fluidised-bed reactor, and concluded that the reaction was approximately zeroth order with respect to O_2 concentration under both air and oxy-fuel conditions, and the activation energies for air and oxy-fuel combustion of woody biomass were lower than that of wood char combustion due to the fact that the effects of the devolatilisation and volatile combustion of woody biomass overlapped its char combustion. It is also worth noting that most of the researchers used the char derived from the fast pyrolysis of coal and biomass under the N_2 atmosphere for oxy-fuel combustion tests. This might be an important factor to influence the accuracy of oxy-fuel combustion kinetics of char measurement. In the practical oxy-fuel combustion of coal or biomass condition, the char is derived from the pyrolysis of coal or biomass under the CO_2 environment, and the char under this condition has the larger surface area, pore diameter, and pore volume than that of char derived from pyrolysis of coal or biomass under the N_2 condition [48,49].

The aim of this work is to investigate the combustion and kinetic characteristics of biomass char in a lab-scale bubbling fluidised-bed reactor under the different O_2/CO_2 and O_2/N_2 atmospheres with the bed temperatures from 650 to 850 °C. The biomass char used in this work is obtained from the fast pyrolysis of woody biomass under N_2 and CO_2 respectively. The effects of O_2 concentration, bed temperature, and char particle size on the measurements of reaction kinetics have been evaluated. Furthermore, the shrinking core model is applied to model the char conversion during the tests. The results obtained in this study will provide

useful information for design and operation of the oxy-fuel combustion of biomass in a fluidised-bed combustor.

4.2 Experimental

4.2.1 Experimental apparatus

A lab-scale bubbling fluidised-bed reactor (**Figure 4-1**) was used for conducting the experiments in this work. It was retrofitted from a spout fluidised bed reactor, which was previously intended for investigation of combustion of woody biomass [31]. The reactor shell was built from Incoloy Alloy 800HT (supplied by Special Metals, UK) and had a total length of 450 mm, an outer diameter of 32 mm and a wall thickness of 2 mm. A quartz liner (278 mm in length, 26 mm O.D., supplied by Cambridge Glassblowing Ltd) that was made of a cylindrical section with a conical frustum at the base (8 mm I.D.) was placed in the reactor shell. A glass frit with a pore size between 0.16 and 0.25 mm was located at the bottom of the cylindrical section of the quartz liner, acting both supporter and distributor of the bed materials. The reactor was heated by electrical resistance heating, and its temperature was monitored by K-type thermocouples placed in bed materials and outer wall and continuously controlled by a proportional-integral-derivative (PID) controller. Superwool insulating blanket (supplied by RS Components Ltd, UK) was covered the reactor shell as well as gas pre-heating area to reduce heat loss.

Mass flow controllers (MFCs) supplied by Bronkhorst (UK) Ltd were used to control the volumetric flow rate of N_2, CO_2, and O_2 at ambient temperature. All the MFCs can be controlled by a computer through the communication with the Bronkhorst Flow Bus to adjust the volumetric flow rate of each gas transport lines and simulate different gas mixtures at the gas mixing point. The pressure of all the inlet gases to the MFCs was set to 1 barg, which can be measured by the pressure gauge in each gas transport lines before the MFCs, and adjusted by the pressure regulators after the pressure gauges.

A pressurised batch feeding system that consists of ball valves, pressure gauges and ¼ tube was designed to inject the char samples to the surface or the bubbles of the fluidising bed materials. The pressure of the batch feeding system was set around 0.4 to 0.6 barg higher than the pressure inside the reactor to ensure the

char sample can be completely and fast injected into the bed materials. The injection time was less than 0.1 s, and hence the decomposition of the char was negligible.

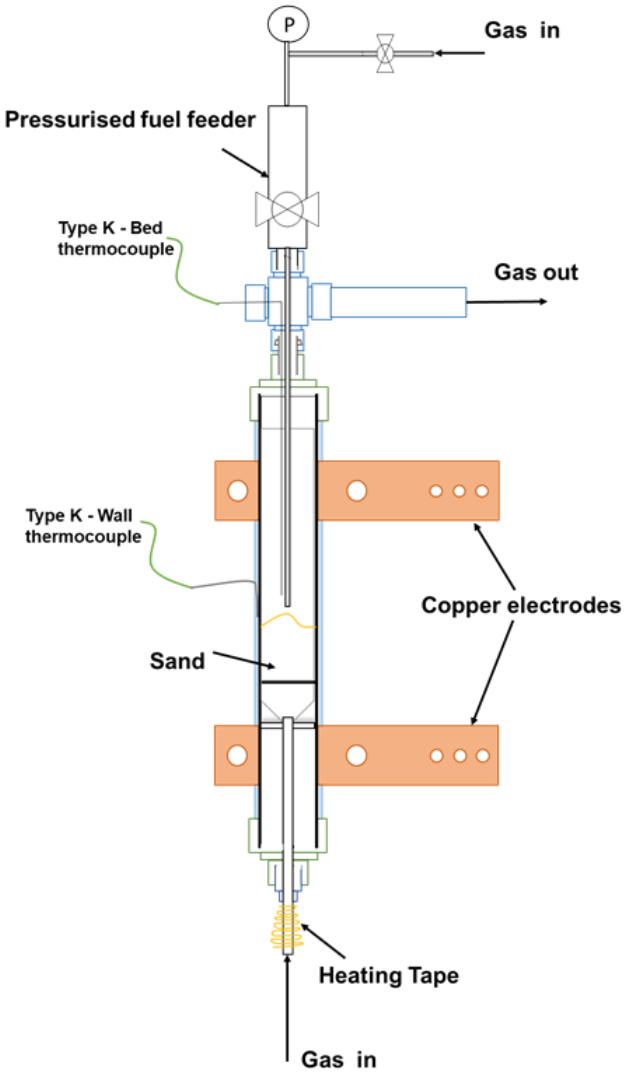

Figure 4-1 Schematic diagram of the bubbling fluidised-bed reactor

The flue gas after the fluidised-bed reactor was firstly clean and dried by a series of gas filters, and then a portion of the flue gas was analysed by the ADC infrared multi-gas analyser (MGA 3000, ADC Ltd., UK) to detect the concentrations of O_2, CO, and CO_2, and the remaining gases were sent to the exhaust gas ventilation system. Their measurement ranges were 0-40 vol.%, 0-20 vol.% and 0-100 vol.%, respectively, with the rated accuracy in ±1% of the measured value. An operator interface developed in Agilent VEE^{TM} was used to realise the online

process control, and the data processed by the data acquisition (DAQ) cards (RedLab USB-1208FS, Meilhaus Electronic) was stored in the computer for further analysis.

4.2.2 Materials

Wood pellets reported in [47] was used to produce the char particles in this work. The char particles were produced from the pyrolysis of raw wood pellets in the FBR at bed temperature 823 K with N_2 and CO_2, respectively. The pyrolysis time was 40 min to ensure that the volatiles were released from the wood pellets, and the char practices were cooled to room temperature under the N_2 or CO_2. The flue gas during the pyrolysis of wood pellets went to the flaring system to burn off the combustible gases before going to the venting system. Then the char particles were ground, with a pestle and mortar, and sieved to a particle size fraction of 65-125 μm. The ultimate analysis of the char sample derived from N_2 and CO_2 was measured by a Vario EL III Elemental Analyser and shown in **Table 4-1**. Silica sand (bulk density = 2600 kg/m^3, diameter: 425−500 μm, supplied by David Ball Group Plc.) was used as the bed material with an unexpanded bed height of 50 mm. All the gases (CO_2, O_2 and N_2) supplied by BOC UK with purities over 99.5% were used in these experiments.

Table 4-1 Ultimate analysis of wood char sample.

Ultimate analysis (wt%, as received)		
	Char –N_2	Char –CO_2
C	84.57	75.94
H	3.96	3.19
N	0.31	0.14
O (by difference)	11.17	20.73

4.2.3 Experimental procedure

The combustion experiments were conducted in O_2/N_2 and O_2/CO_2 atmospheres with the inlet oxygen concentrations of 5, 10, 15, 20, 25 and 30 vol. % at the bed temperatures of 923 and 1023 K. At the bed temperatures 973, 1073 and 1123

K, the char combustion tests were performed in O_2/N_2 and O_2/CO_2 atmospheres with the inlet oxygen concentrations of 20 vol. %. 10 g silica sand was supported on a glass frit inside the quartz liner and fluidised by a mixture of O_2/N_2 or O_2/CO_2 with the total flowrate of 45 ml/s NTP, giving a ratio of fluidisation velocity (U) to minimum fluidisation velocity (U_{mf}) between 5.5 and 7.5 to ensure sufficiently vigorous bubbling fluidisation and well gas-solid mixing inside the reactor. In each test, 0.01 g char particles was injected into the surface or the bubbles of the fluidising bed materials when the desired experimental conditions were reached, and the flue gases were analysed by the ADC infrared multi-gas analyser. To ensure the accuracy of measurements, each test was repeated 3 times and the gas analyser was calibrated before the daily tests. A blank test was repeated before and after each char combustion test to indicate whether the char particles were completely injected into the reactor and quantify the pressurised char injection on the measurement of gas concentrations. The combustion temperature of the injected char particles was considered as same as the bed temperature because the amount of silica sand was much greater than that of the injected char particles, and this provided good heat transfer between bed material and char particles, allowing the char particles to rapidly achieve similar temperatures.

4.2.4 Data evaluation

The CO and CO_2 are considered as the main products during the reaction of wood char particles with O_2 in different O_2/N_2 and O_2/CO_2 conditions with different bed temperatures. The reactions involved in char combustion under O_2/N_2 and O_2/CO_2 atmospheres can be described as following [40,46]:

$$C + O_2 = CO_2 \quad \textbf{(4-1)}$$

$$C + CO_2 = 2\ CO \quad \textbf{(4-2)}$$

$$2\ CO + O_2 = 2\ CO_2 \quad \textbf{(4-3)}$$

Figure 4-2 shows one of the measurements of CO_2 and CO during char combustion at the O_2/N_2 and O_2/CO_2 condition. It should be noted that these measurements of CO and CO_2 are measured in the freeboard of the fluidised

bed, and thus it requires the deconvolution of the measured gas concentration to obtain the real instantaneous concentrations of CO_2 and CO within the particulate phases. The method published in [41] was applied to calculate the real instantaneous concentrations of CO_2 and CO within the particulate phases (Eq. (4-4)).

$$C_{tCO_2/CO} = C_{mCO_2/CO} + \tau_{bed} \frac{dC_{mCO_2/CO}}{dt} \quad \textbf{(4-4)}$$

Where $C_{tCO_2/CO}$ is the instantaneous concentrations of CO_2/CO, $C_{mCO_2/CO}$ is the measured concentrations of CO_2/CO and τ_{bed} is the response time of the bed (4.5 s).

Molar rates of CO and CO_2 production per unit mass of char injected were calculated by the Eq. (4--5) and Eq. (4-6), respectively. The sum of the peak rates of CO and CO_2 production were assumed to be the initial rates (r), and it can be used for Eq.(4-7) to derive the reaction order n.

$$\mathrm{r_{CO}} = (\frac{\mathrm{Q}}{\mathrm{V_m}} \times \mathrm{X_{CO}})/\mathrm{m} \quad \textbf{(4-5)}$$

$$\mathrm{r_{CO_2}} = (\frac{\mathrm{Q}}{\mathrm{V_m}} \times \mathrm{X_{CO_2}})/\mathrm{m} \quad \textbf{(4-6)}$$

$$\mathrm{r} = \mathrm{k}[\mathrm{O_2}]^{\mathrm{n}} \quad \textbf{(4-7)}$$

Herein, Q is the inlet volumetric flow rate of reactor; V_m is the molar volume of idea gas under the standard conditions; m is the weight of injected char particles; k is rate constant; and $\mathrm{X_{CO}}$ and $\mathrm{X_{CO_2}}$ are the molar fractions of CO and CO_2, which can be converted from the $C_{tCO_2/CO}$.

The carbon balance ratio ($\mathrm{X_C}$) was calculated by Eq.(4-8) to evaluate the reliability of each char combustion test. The tests of which carbon balance ratio has over 0.7 were selected for further analysis.

$$\mathrm{X_C} = \int_0^{\infty} 12\mathrm{m}(\mathrm{r_{CO}} + \mathrm{r_{CO_2}})/\mathrm{m_C} dt \quad \textbf{(4-8)}$$

Herein, $\mathrm{m_C}$ represents the weight of carbon in injected char particles.

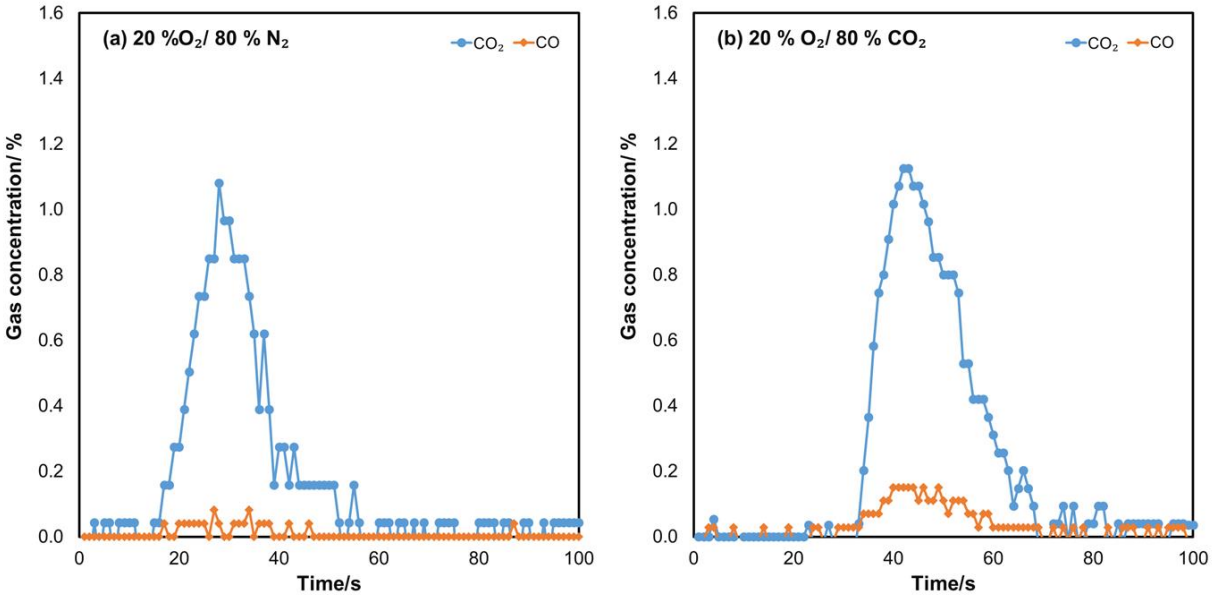

Figure 4-2 The evolution of CO_2 and CO concentrations in the flue gas during the combustion of wood char in 20 vol. % O_2/ 80 vol. % N_2 and 20 vol. % O_2/ 80 vol. % CO_2 at a bed temperature of 923 K.

4.3 Results and discussion

4.3.1 Reaction kinetics of char combustion

In order to ensure the char combustion is controlled by the intrinsic kinetics of reaction between O_2 and char, it is necessary to use the small char particles in this test and the selected size of char particles cannot be elutriated during the fluidisation of sand. **Figure 4-3** indicates the reaction rates of CO_2 and CO production during three different groups of size of wood char combustion at bed temperature of 923 K, 20 % O_2 / 80 % N_2. It can be found that the maximum reaction rate is similar for all three char particle sizes. However, there is a huge elutriation of char particles and more CO produced in **(a)** due to the lower residence time. When the char particle size is over 125 μm, the peak rates of CO_2 production are hold for several seconds then dropping to zero, which is because of fragmentation and combustion of large char particles. Thus, it can be concluded that 65-125 μm is the optimal particle size for this char combustion test, which could a sharp rate of CO_2 production under the kinetically controlled reaction (**(b)**).

The actual rate of char combustion was derived from the measured changes in CO and CO_2 concentrations with the correction of gases mixing inside the reactor. The sum of the maximum rates of CO and CO_2 production were assumed to be the initial rates of char combustion. **Table 4-2** summaries the averaged rates of char combustion together with their carbon balance ratio at O_2/N_2 and O_2/CO_2 with bed temperature of 923, 973, 1023, 1073 and 1123 K. It can be observed that the rates of char combustion increase with the increase of oxygen concentration and bed temperatures at both O_2/N_2 and O_2/CO_2 atmospheres. Moreover, the rate of char combustion are improved by the average of 13 % points from O_2/N_2 to O_2/CO_2 atmospheres with the same oxygen concentration and bed temperatures.

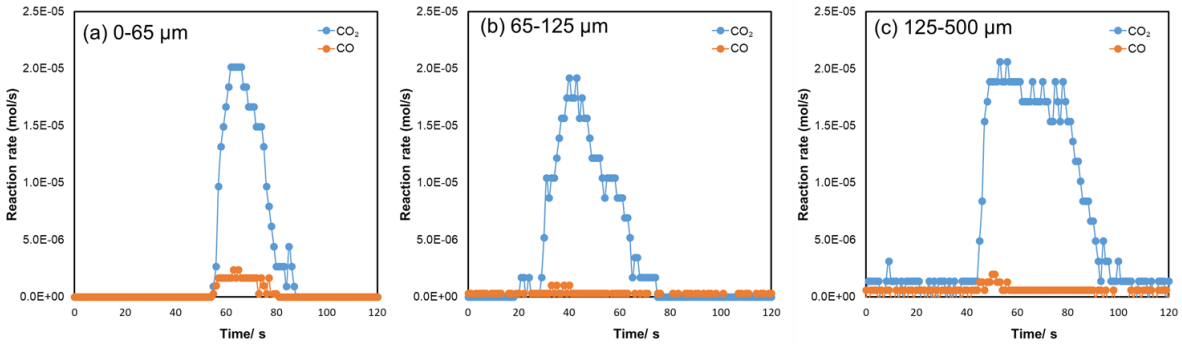

Figure 4-3 Typical reaction rates of CO_2 and CO during three different particle sizes of wood char combustion at bed temperature of 923 K, 20 % O_2 / 80 % N_2.

Table 4-2 Overview of corrected rates of char combustion at O_2/N_2 and O_2/CO_2 with different bed temperatures

	Temperature (K)	O_2 concentration (vol. %)	Average rate of char combustion ($\times 10^{-3}$ mol/g s)	Standard deviation $\sigma(r)$ (%)	Average carbon conversion (%)	Standard deviation σ (%)
Air combustion	923	5	1.63	0.05	0.86	6.07
		10	2.92	0.02	0.82	7.29
		15	2.80	0.02	0.78	5.69
		20	2.89	0.05	0.83	0.96
		25	3.23	0.02	0.88	3.13
		30	3.75	0.03	0.99	9.88
	973	20	3.87	0.05	0.77	6.98
	1023	5	2.46	0.05	1.04	12.13
		10	3.52	0.02	0.99	6.80
		15	4.66	0.02	0.86	4.55
		20	4.21	0.02	0.88	4.90
		25	5.03	0.04	0.85	2.02
		30	5.27	0.09	0.91	5.75
	1073	20	4.58	0.03	0.77	4.05
	1123	20	4.74	0.02	0.83	0.50
Oxy-fuel combustion	923	5	1.70	0.03	0.70	7.09
		10	2.71	0.01	0.78	7.13
		15	2.88	0.02	0.75	4.87
		20	3.22	0.03	0.77	4.58
		25	3.43	0.02	0.83	2.31
		30	4.34	0.03	0.88	12.30
	973	20	4.45	0.05	0.74	2.18
	1023	5	3.09	0.04	0.72	8.43
		10	4.25	0.07	0.82	8.09
		15	4.55	0.04	0.88	6.36
		20	5.38	0.01	0.84	2.10
		25	5.55	0.01	0.81	5.95
		30	5.89	0.07	0.90	16.49
	1073	20	5.50	0.04	0.81	4.86
	1123	20	6.18	0.12	0.82	7.43

4.3.2 Order of reaction and activation energies

The apparent order of reaction was obtained from the plot of ln [r] against ln [O_2] at bed temperatures of 923 and 1023 K, and the gradient indicates the order of reaction as **Figure 4-4** shown. The averaged order of char combustion at O_2/N_2 and O_2/CO_2 is 0.41 (R^2 = 0.84) and 0.44 (R^2 = 0.95), respectively.

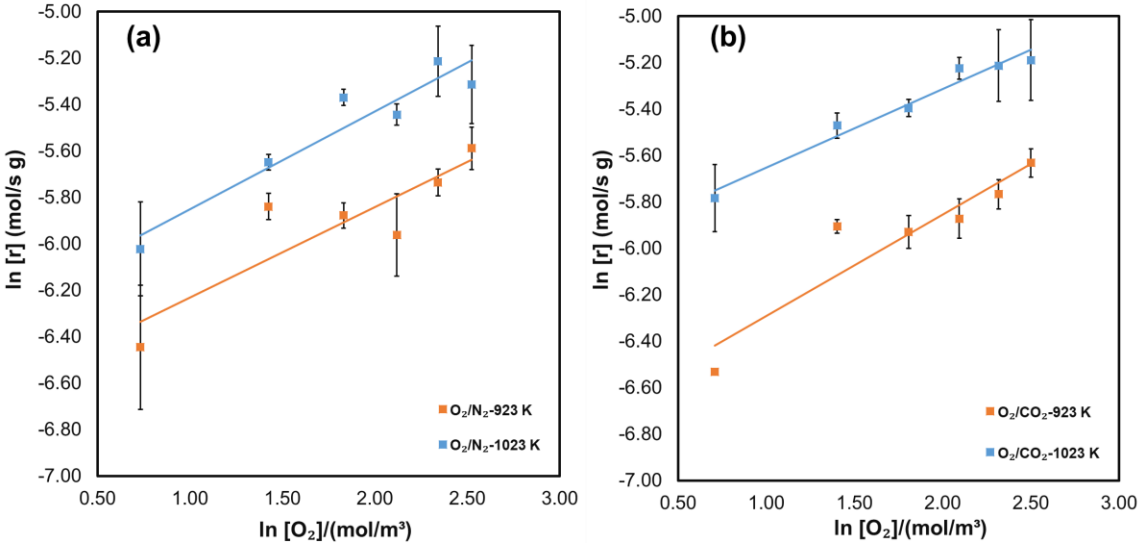

Figure 4-4 ln [r] against ln [O_2] at conditions of 923 and 1023 K, 5-30 vol.% O_2 with the balance of N_2 ((a)) and CO_2 ((b)). The error bars represent the standard deviation between three repeats.

The activation energies and pre-exponential factors of wood char combustion under the O_2/N_2 and O_2/CO_2 were calculated by the Arrhenius equation. The rate constants, *k,* were calculated at the 20 vol. % O_2 and across the bed temperature range of 923-1123 K. The results of activation energy (Ea) and pre-exponential factor (A) is shown in **Table 4-3.** The activation energy of char combustion at 20 % O_2/ 80 % N_2 is 32.7% points lower than that of char combustion at 20 % O_2/ 80 % CO_2, which means the reactivity of char under the O_2/N_2 is higher than that of char under the O_2/CO_2.

Table 4-3 Kinetic parameters of wood char combustion

Conditions	Ea (kJ/mol)	Pre-exponential factor A (s^{-1})	R^2
20 % O_2/ 80 % N_2	20.03	8.52 x 10^3	0.90
20 % O_2/ 80 % CO_2	26.58	2.10 x 10^4	0.91

4.3.3 Shrinking core model validation

The shrinking core model is widely applied to simulate the process of char combustion and has been demonstrated by many researchers [32,43,50–52]. In this work, the maximum rate of mass transfer of O_2 to the exterior of the spherical char particles was calculated to be 1.5×10^{-7} and 9.0×10^{-8} mol/g s in 20 vol. % O_2/ 80 vol. % N_2 and 20 vol. % O_2/ 80 vol. % CO_2 at bed temperature of 923 K. These were significantly higher than their chemical reaction rates (6.0×10^{-20} and 6.6×10^{-20} mol/g s), which suggests that the oxidisation of char in this work was controlled by its intrinsic kinetics. Thus, the conversion and dimensionless time equations for for a reaction-controlled shrinking unreacted core model illustrated as Eq. (9) and (10) has been used to fit with the experimental data of char carbon conversion to CO_2/CO.

$$\frac{t}{\tau} = 1 - (1 - X)^{1/3} \quad \textbf{(4-9)}$$

$$\tau = \frac{\rho\ Rp}{b\ ks\ C_{Ag}} \quad \textbf{(4-10)}$$

Herein, *t* is the instantaneous reaction time point, *τ* is the total conversion time, *X* is the char conversion, *b* is the stoichiometric coefficient, C_{Ag} is the concentration of A in bulk gas, *ρ* is the molar density of the particle, *Rp* is the radius of the particle, and *ks* is the reaction rate constant.

To fit with the experimental data with this model, it is required to obtain the optimal value of rate constant (k_s) by minimising the sum of the squared errors between the experimental and predicted char conversions. **Figure 4-5** and **Figure 4-6** present the comparison of all the experimental results with the shrinking core model predictions. It can be summarised that the reaction-controlled shrinking model predictions are well agreed with the experimental results.

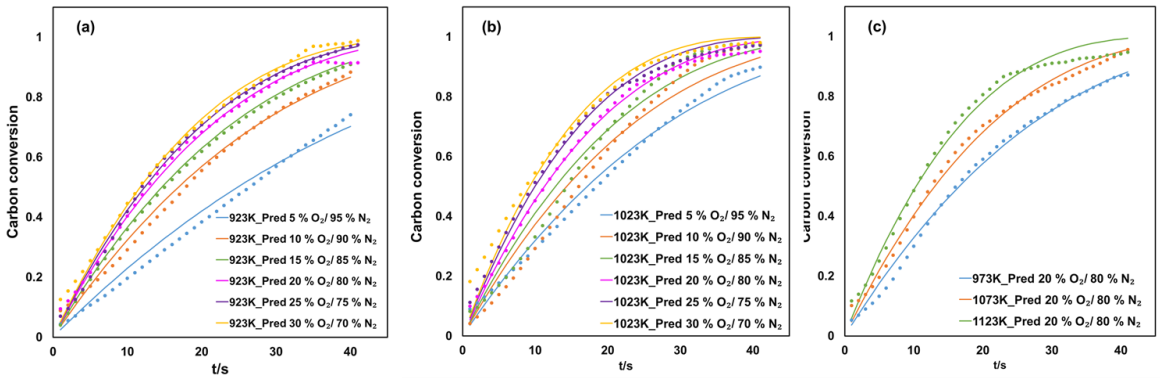

Figure 4-5 Comparison of experimental results and model predictions of wood char combustion in O_2/N_2 with the oxygen concentration from 5 to 30 % at the bed temperatures of 923, 973, 1023, 1073 and 1123 K. (Points: experimental results. Solid lines: shrinking core model predictions)

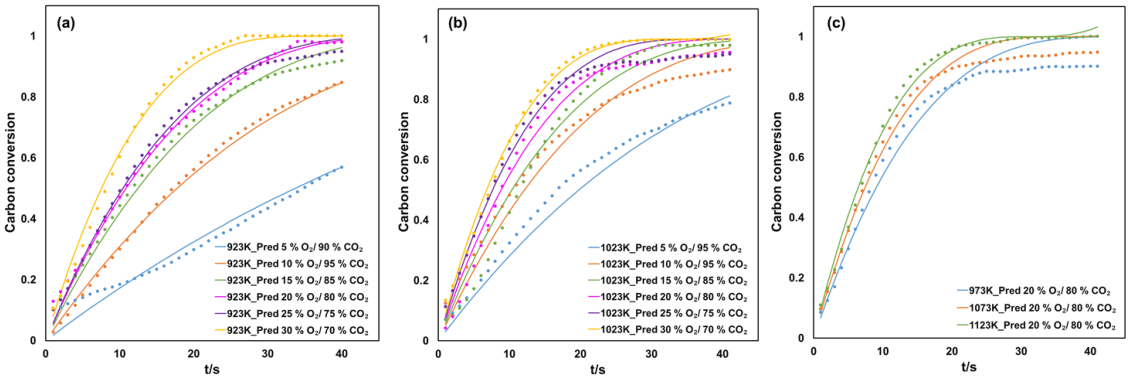

Figure 4-6 Comparison of experimental results and model predictions of wood char combustion in O_2/CO_2 with the oxygen concentration from 5 to 30 % at the bed temperatures of 923, 973, 1023, 1073 and 1123 K. (Points: experimental results. Solid lines: shrinking core model predictions)

4.3.4 Discussion

The potential reaction mechanism of char combustion under the O_2/N_2 is that oxygen first diffuses from the bulk phase through the boundary layer and then reacts at its surface to form CO_2 and CO, followed by the oxidation of CO with the fresh diffused oxygen. Then the produced CO_2 is realised from the product ash layer. For char combustion under the O_2/CO_2, not only the oxygen, but also the CO_2 reacts at the char surface via the Boudouard reaction to produce CO, and then the CO can be oxidised by the diffused oxygen or the oxygen in the freeboard of fluidised bed to generate CO_2. **Figure 4-7** presents the evolution of CO and CO_2 concentrations during the char combustion under the 20 % O_2/ 80 %

N_2 and 20 % O_2/ 80 % CO_2 at 923 K. It indicates that more CO is produced during char combustion under the O_2/CO_2 than the same conditions under the O_2/N_2. Moreover, the CO produced from the char-CO_2 gasification cannot been completely oxidised to CO_2 even at the oxygen concentration 30% at bed temperature of 923 K. This is due to the design of the current reactor that does not have enough freeboard to provide sufficient residence time and oxygen to fully convert the CO to CO_2. It is recommended that the effect of char-CO_2 gasification during the char combustion under the O_2/CO_2 cannot be negligible, and it should be considered to retrofit the current fluidised-bed combustors and design of new oxy-fuel biomass combustors.

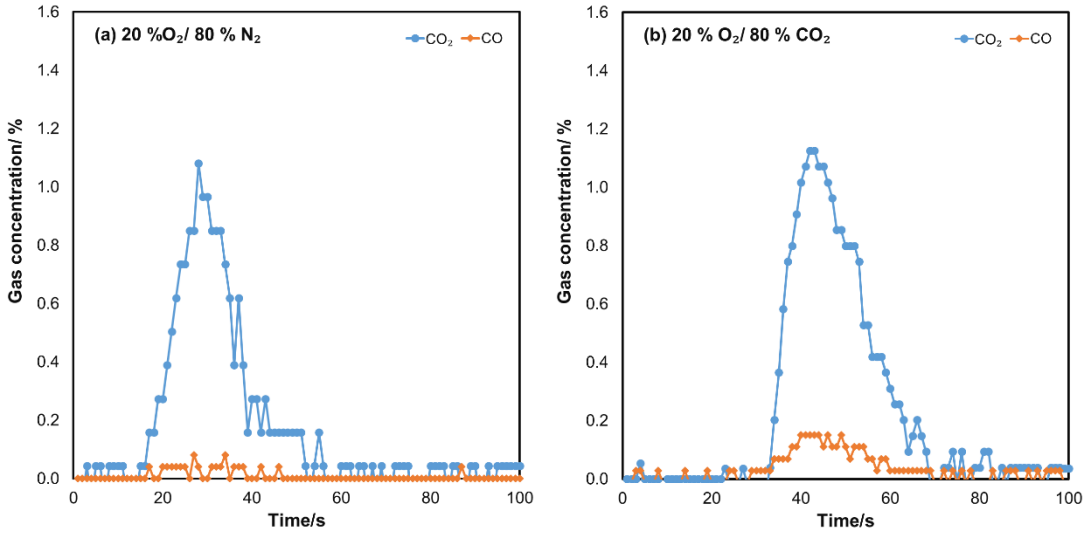

Figure 4-7 Gas concentrations of wood char combustion at 923 K (a) 20 % O_2/ 80 % N_2, (b) 20 % O_2/ 80 % CO_2

In this work, the measured kinetics of char combustion in O_2/CO_2 are about 13 % points higher than that of char combustion in O_2/N_2 as illustrated in **Table 4-2**, which is opposite to the conclusions of many researchers that rates of char conversion are higher in O_2/N_2 than that in O_2/CO_2 [32,43,53]. The reason why the rates of char combustion are higher in O_2/N_2 than that in O_2/CO_2 is due to the lower O_2 diffusion rate in CO_2 than that in N_2 [32,53]. However, it is worth noting that the char particles used for combustion tests in O_2/N_2 and O_2/CO_2 were derived only the pyrolysis of their parent coal or biomass, which have the similar physicochemical properties. Hence, O_2 diffusion rate is key factor to decide the rate of char combustion. Nevertheless, if their char are derived from N_2 and CO_2,

respectively in the practical air and oxy-fuel combustion of biomass. Many studies [48,49,54] indicate that the char derived from the CO_2 has the larger surface area, pore diameter, and pore volume than that of char derived from pyrolysis of coal or biomass under the N_2 condition. This can be explained why the rates of char combustion in O_2/CO_2 is higher than that in O_2/N_2 in this work. Although, the theoretical O_2 diffusion rate is lower in CO_2 than that in N_2, the higher values in pore size, volume and surface area of char derived from CO_2 can enhance the O_2 diffusion rate from its surface to the core, and hence the kinetics of char combustion haven been improved.

4.4 Conclusions

Experimental investigation of characteristic of wood char and its combustion kinetics under O_2/N_2 and O_2/CO_2 was carried out in a lab-scale bubbling fluidised-bed reactor with fast-response gas analyser. The wood char was obtained from pyrolysis of wood pellet at bed temperature 823 K with N_2 and CO_2, respectively. The experimental results show that the corrected rates of char combustion in O_2/CO_2 are about 13% points higher than that in O_2/N_2 at the same temperature. The apparent order of reaction is 0.41 (R^2= 0.84) for char combustion under O_2/N_2 and 0.44 (R^2= 0.95) for char combustion under O_2/CO_2. The activation energies for char combustion under O_2/N_2 and O_2/CO_2 at the oxygen concentration of 20% were calculated to be 20.03 (R^2= 0.90) and 26.58 (R^2= 0.91) kJ/mol, respectively. The reaction-controlled shrinking core model can well predict the experimental results of carbon conversion during the char combustion under both conditions.

The rates of char combustion under O_2/N_2 and O_2/CO_2 conditions are both improved with the increase of the oxygen concentration and bed temperature. In the same condition, more CO generated during the char combustion in O_2/CO_2, even at the oxygen concentration of 30% and bed temperature of 923 K. This suggests that the impact of char-CO_2 gasification is not negligible for the retrofit of current fluidised-bed biomass boilers as well as design of new oxy-fuel biomass combustion fluidised-bed boilers.

Acknowledgements

YYL would like to acknowledge the financial support from the Cranfield University Energy and Power research bursary, and the assistance from Serap Ozmen and Paula Nkulikiyinka for the char production.

4.5 References

[1] Page B. the Global Status of Ccs | 2016 “Time To Accelerate” 2016:1–28.

[2] Global CCS Institute. The Global Status of CCS: 2017 2017:43.

[3] Bui M, Fajardy M, Mac Dowell N. Bio-Energy with CCS (BECCS) performance evaluation: Efficiency enhancement and emissions reduction. Appl Energy 2017;195:289–302. doi:10.1016/j.apenergy.2017.03.063.

[4] Seddighi S, Clough PT, Anthony EJ, Hughes RW, Lu P. Scale-up challenges and opportunities for carbon capture by oxy-fuel circulating fluidized beds. Appl Energy 2018;232:527–42. doi:10.1016/j.apenergy.2018.09.167.

[5] Nemitallah MA, Habib MA, Badr HM, Said SA, Jamal A, Ben-Mansour R, et al. Oxy-fuel combustion technology: current status, applications, and trends. Int J Energy Res 2017;41:1670–708. doi:10.1002/er.3722.

[6] Pang L, Shao Y, Zhong W, Liu H, Jiang P. Experimental Investigation of Oxy-coal Combustion in a 15 kWth Pressurized Fluidized Bed Combustor. Energy and Fuels 2019;33:1694–703. doi:10.1021/acs.energyfuels.8b02654.

[7] Li W, Li S, Ren Q, Tan L, Li H, Liu J, et al. Study of oxy-fuel coal combustion in a 0.1 MWth circulating fluidized bed at high oxygen concentrations. Energy and Fuels 2014;28:1249–54. doi:10.1021/ef4020422.

[8] Stanger R, Wall T, Spörl R, Paneru M, Grathwohl S, Weidmann M, et al. Oxyfuel combustion for CO2 capture in power plants. Int J Greenh Gas Control 2015;40:55–125. doi:10.1016/j.ijggc.2015.06.010.

[9] Wall T, Liu Y, Spero C, Elliott L, Khare S, Rathnam R, et al. An overview on oxyfuel coal combustion-State of the art research and technology development. Chem Eng Res Des 2009;87:1003–16. doi:10.1016/j.cherd.2009.02.005.

[10] Singh RI, Kumar R. Current status and experimental investigation of oxy-fired fluidized bed. Renew Sustain Energy Rev 2016;61:398–420. doi:10.1016/j.rser.2016.04.021.

[11] Zhu Q. Developments in fluidised bed combustion technology. 2013.

[12] Yan Y, Clough PT, Anthony EJ. Investigation of the apparent kinetics of air and oxy-fuel biomass combustion in a spout fluidised-bed reactor. Chem Eng Res Des 2020;153:276–83. doi:10.1016/j.cherd.2019.10.043.

[13] Wang W, Bu C, Gómez-Barea A, Leckner B, Wang X, Zhang J, et al. O_2/CO_2 and O_2/N_2 combustion of bituminous char particles in a bubbling fluidized bed under simulated combustor conditions. Chem Eng J 2018;336:74–81. doi:10.1016/j.cej.2017.11.027.

[14] Liu H. Combustion of coal chars in O_2/CO_2 and O_2/N_2 mixtures: A comparative study with non-isothermal thermogravimetric analyzer (TGA) tests. Energy and Fuels 2009;23:4278–85. doi:10.1021/ef9002928.

[15] Fang Y, Zou R, Luo G, Chen J, Li Z, Mao Z, et al. Kinetic Study on Coal Char Combustion in a Microfluidized Bed. Energy and Fuels 2017;31:3243–52. doi:10.1021/acs.energyfuels.6b03137.

[16] Dennis JS, Lambert RJ, Milne AJ, Scott SA, Hayhurst AN. The kinetics of combustion of chars derived from sewage sludge. Fuel 2005;84:117–26. doi:10.1016/j.fuel.2004.08.020.

[17] Scala F. A new technique for the measurement of the product CO/CO_2 ratio at the surface of char particles burning in a fluidized bed. Proc Combust Inst 2009;32 II:2021–7. doi:10.1016/j.proci.2008.06.047.

[18] Fennell PS, Kadchha S, Lee H-Y, Dennis JS, Hayhurst AN. The measurement of the rate of burning of different coal chars in an electrically heated fluidised bed of sand. Chem Eng Sci 2007;62:608–18. doi:10.1016/J.CES.2006.09.024.

[19] Chirone R, Salatino P, Scala F, Solimene R, Urciuolo M. Fluidized bed combustion of pelletized biomass and waste-derived fuels. Combust Flame 2008;155:21–36. doi:10.1016/j.combustflame.2008.05.013.

[20] Gövert B, Pielsticker S, Kreitzberg T, Habermehl M, Hatzfeld O, Kneer R. Measurement of reaction rates for pulverized fuel combustion in air and oxyfuel atmosphere using a novel fluidized bed reactor setup. Fuel 2017;201:81–92. doi:10.1016/j.fuel.2017.03.009.

[21] Scala F, Chirone R. Combustion of Single Coal Char Particles under Fluidized Bed Oxyfiring Conditions. Ind Eng Chem Res 2010;49:11029–36. doi:10.1021/ie100537a.

[22] Fennell PS, Dennis JS, Hayhurst AN. The order with respect to oxygen and the activation energy for the burning of an anthracitic char in O_2 in a fluidised bed, as measured using a rapid analyser for CO and CO_2. Proc Combust Inst 2009;32 II:2051–8. doi:10.1016/j.proci.2008.06.097.

[23] Haustein HD, Kreitzberg T, Gövert B, Massmeyer A, Kneer R. Establishment of kinetic parameters of particle reaction from a well-stirred fluidized bed reactor. Fuel 2015;158:263–9. doi:10.1016/J.FUEL.2015.05.038.

[24] Li L, Duan L, Tong S, Anthony EJ. Combustion characteristics of lignite char in a fluidized bed under O_2/N_2, O_2/CO_2 and O_2/H_2O atmospheres. Fuel Process Technol 2019;186:8–17. doi:10.1016/j.fuproc.2018.12.007.

[25] Henrich E, Bürkle S, Meza-Renken ZI, Rumpel S. Combustion and gasification kinetics of pyrolysis chars from waste and biomass. J Anal Appl Pyrolysis 1999;49:221–41. doi:10.1016/S0165-2370(98)00119-3.

[26] Salatino P, Scala F, Chirone R. Fluidized-bed combustion of a biomass char: The influence of carbon attrition and fines postcombustion on fixed carbon conversion. Symp. Combust., vol. 27, Elsevier; 1998, p. 3103–10. doi:10.1016/S0082-0784(98)80172-0.

[27] Morin M, Pécate S, Hémati M. Kinetic study of biomass char combustion in a low temperature fluidized bed reactor. Chem Eng J 2018;331:265–77. doi:10.1016/j.cej.2017.08.063.

[28] Yan Y, Clough PT, Anthony EJ. Investigation of the apparent kinetics of air and oxy-fuel biomass combustion in a spout fluidised-bed reactor. Chem Eng Res Des 2020;153. doi:10.1016/j.cherd.2019.10.043.

[29] Luo Y, Ben H, Wu Z, Nie K, Han G, Jiang W. Impact of CO_2 on pyrolysis products of bituminous coal and platanus sawdust. Polymers (Basel) 2019;11:1–12. doi:10.3390/polym11081370.

[30] Shen Y, Ma D, Ge X. CO2-looping in biomass pyrolysis or gasification. Sustain Energy Fuels 2017;1:1700–29. doi:10.1039/c7se00279c.

[31] Gil MV, Riaza J, Álvarez L, Pevida C, Pis JJ, Rubiera F. Kinetic models for the oxy-fuel combustion of coal and coal/biomass blend chars obtained in N2 and CO_2 atmospheres. Energy 2012;48:510–8. doi:10.1016/J.ENERGY.2012.10.033.

[32] Manovic V, Komatina M, Oka S. Modeling the temperature in coal char particle during fluidized bed combustion. Fuel 2008;87:905–14. doi:10.1016/j.fuel.2007.05.020.

[33] Sadhukhan AK, Gupta P, Saha RK. Analysis of the dynamics of coal char combustion with ignition and extinction phenomena: Shrinking core model. Int J Chem Kinet 2008;40:569–82. doi:10.1002/kin.20343.

[34] Bu C, Gómez-Barea A, Chen X, Leckner B, Liu D, Pallarès D, et al. Effect of CO_2 on oxy-fuel combustion of coal-char particles in a fluidized bed: Modeling and comparison with the conventional mode of combustion. Appl Energy 2016;177:247–59. doi:10.1016/j.apenergy.2016.05.108.

[35] Naredi P, Pisupati S. Effect of CO_2 during coal pyrolysis and char burnout in oxy-coal combustion. Energy and Fuels 2011;25:2452–9. doi:10.1021/ef20019

5 Applying Machine Learning Algorithms in Estimating the Performance of Heterogeneous, Multi-component Materials as Oxygen Carriers for Chemical-looping Processes

Yongliang Yan[a,b], Tobias Mattisson[b], Patrick Moldenhauer[b], Edward J. Anthony[a], Peter T. Clough[a]

[a] Energy and Power Theme, School of Water, Energy and Environment, Cranfield University, Cranfield, Bedfordshire, MK43 0AL, UK.

[b] Division of Energy Technology, Department of Space, Earth and Environment, Chalmers University of Technology, 412 96 Gothenburg, Sweden.

DOI: https://doi.org/10.1016/j.cej.2020.124072

Abstract

Heterogeneous, multi-component materials such as industrial tailings or by-products, along with naturally occurring materials, such as ores, have been intensively investigated as candidate oxygen carriers for chemical-looping processes. However, these materials have highly variable compositions, and this strongly influences their chemical-looping performance. Here, using machine learning techniques, we estimate the performance of heterogeneous, multi-component materials as oxygen carriers for chemical-looping. Experimental data for 19 manganese ores chosen as potential chemical-looping oxygen carriers were used to create a so-called training database. This database has been used to train several supervised artificial neural network models (ANN), which were used to predict the reactivity of the oxygen carriers with different fuels and the oxygen transfer capacity with only the knowledge of reactor bed temperature, elemental composition, and mechanical properties of the manganese ores. This novel approach explores ways of dealing with the training dataset, learning algorithms and topology of ANN models to achieve enhanced prediction precision. Stacked neural networks with a bootstrap resampling technique have been applied to achieve high precision and robustness on new input data, and the confidence intervals were used to assess the precision of these predictions. The

current results indicate that the best trained ANNs can produce highly accurate predictions for both the training database and the unseen data with the high coefficient of determination (R^2 = 0.94) and low mean absolute error (MAE = 0.057). We envision that the application of these ANNs and other machine learning algorithms will accelerate the development of oxygen carrying materials for a range of chemical-looping applications and offer a rapid screening tool for new potential oxygen carriers.

Keywords

Machine learning, artificial neural network, manganese ores, oxygen-carrier materials, chemical-looping.

5.1 Introduction

Chemical-looping combustion (CLC) and chemical-looping with oxygen uncoupling (CLOU) are state-of-the-art methods for heat and power production, which can achieve CO_2 separation at low cost and with very low energy penalties [1]. The chemical-looping process is carried out in a dual fluidised-bed reactor system, where the oxygen is transported from an air reactor to a fuel reactor by means of an oxygen carrier [2]. The chemical-looping concept can also be integrated with steam reforming (SR-CLC) for H_2 production or operated under partial oxidation for chemical-looping gasification (CLG) and reforming (CLR) to generate a syngas [3-7]. Furthermore, CLC can be implemented in current fluidised bed boilers through oxygen-carrier-aided combustion (OCAC), which partially or completely replaces bed materials with oxygen-carrier materials to enhance the combustion process [8,9].

In CLC, the fuel, here idealised as a pure hydrocarbon (C_nH_{2m}), is oxidised by the oxygen carrier, here denoted as a metal oxide (M_yO_x) to produce CO_2 and steam [1,10] according to the following global reaction scheme:

$$(2n+m)\mathrm{M_yO_x} + \mathrm{C_nH_{2m}} \rightarrow (2n+m)\mathrm{M_yO_{x-1}} + m\mathrm{H_2O} + n\mathrm{CO_2} \quad \textbf{(5-1)}$$

Subsequently, the reduced oxygen carrier particles are reoxidised by air as shown in **Equation (5-2)**.

$$\mathbf{M_yO_{x-1} + 1/2O_2 \rightarrow M_yO_x} \quad \textbf{(5-2)}$$

For CLOU, gaseous oxygen is released from the oxygen carrier, **Equation (5-3)**, and thereafter, the fuel reacts with the gas-phase oxygen as in normal combustion processes to produce CO_2 and H_2O through **Equation (5-4)**, allowing easy separation of CO_2 by condensing the steam. The reduced oxygen carrier is regenerated by **Equation (5-2)** in the air reactor [1].

$$\mathrm{M_yO_x \rightarrow M_yO_{x-1} + 1/2O_2} \quad \textbf{(5-3)}$$

$$\left(n + \frac{1}{2}m\right)\mathrm{O_2} + \mathrm{C_nH_{2m}} \rightarrow m\mathrm{H_2O} + n\mathrm{CO_2} \quad \textbf{(5-4)}$$

Over the last two decades, extensive research has been conducted on the chemical-looping process focused on reactor design, oxygen-carrier materials development and continuous operation testing [11]. Currently, the overall technology readiness level (TRL) for CLC is estimated as TRL 6, and well over a 1000 materials based on Ni, Cu, Fe, Mn, Co, as well as other mixed oxides and inexpensive materials, have been investigated at different research institutes, e.g., ICB-CSIC in Zaragoza, Vienna University of Technology, Technical University Darmstadt, Ohio State University, University of Utah, Southeast University in Nanjing, and Chalmers University of Technology in Gothenburg among others [3,12,13]. In addition, a range of materials have been successfully tested in long-term, continuous operation in CLC facilities from 0.3 kW_{th} to 1 MW_{th} worldwide [11,14].

A key barrier to chemical-looping technologies development is the selection of the optimal oxygen-carrier materials according to the criteria of cost, availability, reactivity, oxygen transfer capacity as well as stability over a large number of reduction/oxidation cycles [3,15,16]. Many reviews are available, which provide a detailed summary of experience and knowledge related to CLC oxygen carrying [3,10,14,16-18].

Besides the investigation of pure and synthetic metal oxides for oxygen carrying materials, ores and industrial products as oxygen carriers have attracted great interest due to their low cost and availability, especially where they offer sufficient

reactivity for use with solid fuels. Leion et al. [19,20] conducted a series of tests to identify suitable candidates as oxygen carrying materials for CLC based on Fe- and Mn-containing ores as well as industrial products in a bench-scale, batch fluidised bed reactor. Later on, researchers studied the feasibility of using Norwegian industrial tailings as well as minerals and ores as the oxygen carrying materials for CLC. The results indicated that manganese ores represent a promising candidate for use in CLC processes [15]. The high reactivity seen with Mn-based materials may be explained by the propensity of such materials to release oxygen to the gas phase, or having CLOU properties. Arjmand et al. [21] evaluated six different manganese ores as oxygen carrier for CLC of solid fuels. Sundqvist et al. [22,23] invested the reactivity of 19 different manganese ores with methane and syngas, as well as their oxygen uncoupling behaviour in a batch, fluidised-bed reactor. The results indicated that some of these manganese ores exhibited high reactivity with different gaseous fuels, had lower attrition rates and low cost; and in summary, they were promising candidates for CLC processes. In addition, many ores and industrial products, such as iron ores, ilmenite, manganese ores and slags, have been tested in continuous CLC operation processes and show promising behaviour [24-31].

Unfortunately, such ores and industrial products have highly variable compositions, and contain heterogeneous, multi-component phases and, hence, their performance may vary significantly. For Mn ores, this may be particularly true, as it is well known that common impurities affect the thermodynamics to a large extent. Therefore, some researchers have suggested that extensive investigation on heterogeneous, multi-component materials may be necessary to determine if they are suitable for chemical-looping [19].

Given the versatility of Artificial Intelligence (AI), various areas, such as games, automation, medical and process control, have begun to apply AI to achieve improved performance, prediction of unmeasured parameters, or pattern recognition [32]. Machine learning (ML), which can be classified into supervised, unsupervised and reinforcement learning, is part of the wider spectrum of AI technology that applies statistical techniques to allow models to progressively improve performance [33]. Artificial neural networks (ANNs) are one of the most

widely applied machine learning approaches. Inspired by the learning behaviour of the human brain, ANNs have been widely applied in various applications, including control, robotics, pattern recognition, forecasting, medicine, power systems, manufacturing, optimisation, signal processing, and social/psychological science [34,35]. ANNs can act as a “black box” that can generate the desired output given a set of input data, and they can learn from the historical data and are able to deal with different disciplines for tasks such as prediction, classification, and pattern recognition [36,37].

Recently, ANN has been used in carbon capture technologies, mainly focused on the process modelling and control of amine-based post-combustion technology [38-41]. In terms of carbon capture materials, some researchers proposed using large-scale computational screening to aid the experimental investigation to discover novel materials for calcium looping and chemical-looping [42,43]. However, to the best of our knowledge, ANNs or other machine learning algorithms have not been applied to the area of oxygen carriers for chemical-looping processes. To develop the next generation of chemical-looping materials and reduce the time and cost of material development, it is necessary to evaluate whether data-driven ML algorithms can allow us to exploit valuable information contained in historical experimental data to assist the design and manufacture of optimal oxygen carriers. Further, for complex natural oxygen carriers, the multi-element, multi-phase environment makes it very difficult to predict behaviour using traditional chemical characterisation, and here data-driven approaches could be of significant use for determining important parameters, and provide guidance for what to search for in natural systems.

In this work, we explore the potential application of ML algorithms in estimating the performance of heterogeneous, multi-component materials as oxygen carriers for chemical-looping processes. Feedforward backpropagation artificial neural networks that can predict the reactivity of manganese ores as oxygen carriers for CLC/CLOU are used as an example to illustrate the feasibility of applying ML in the development of oxygen-carrier materials. The experimental data of different manganese ores in CLC/CLOU under a bench-scale, batch fluidised-bed reactor have been used as the datasets to develop the ANN models,

and then the performance of the trained ANN for estimation of the reactivity of manganese ores as oxygen carriers has been discussed.

5.2 Methodology

5.2.1 Materials

In this work, 19 manganese ores from various suppliers around the world were analysed. These ores were first calcined in air at 950 °C for 24 h in a box furnace, and then crushed and sieved to a particle size fraction of 125-180 µm. Their elemental compositions were analysed and determined by ICP-SFMS (Inductively-Coupled Plasma – Sector Field Mass Spectrometry). The results of elemental compositions and physical properties such as attrition index, crushing strength and BET surface area are shown in **Table 5-1**. It is clear that the ores contain a significant fraction of metals and semi-metals in addition to manganese. For instance, enhanced levels of Fe, Si, Ca and Mg, all components which can affect CLC behaviour, are present.

5.2.2 Experimental Investigation

The experimental investigations with the manganese ores were conducted in a batch fluidised-bed reactor. A quartz liner (820 mm long, 22 mm I.D.) was placed inside the main body of the reactor and a porous quartz plate, the gas distributor, was located 370 mm from the bottom. The reactor was heated with an electrical furnace and the fluidisation of particles was monitored by the pressure fluctuations over the reactor. Gases controlled by mass flow controllers were injected from the bottom of the reactor to enable fluidisation of the particles. From the outlet of the reactor, the exhaust gases were sent to a cooler to remove the moisture from the gas stream. Subsequently, the volumetric flow and gas composition of the dry gas stream were analysed with a Rosemount NGA 2000 multi-component gas analyser, where concentrations of CH_4, CO, CO_2 and O_2 were measured.

The performance of the manganese ores was assessed with regard to their oxygen release and reactivity towards methane and syngas (50 % CO in H_2) at three temperatures (900 °C, 950 °C and 1000 °C). Additional tests for their performance with syngas were conducted at bed temperature of 850 °C. The CO_2

yield from syngas and methane conversion are given in **Equation (5-5)** and **(5-6)**, respectively. A schematic description of the experimental system and more details of the experimental investigation can be found elsewhere [22.23,44].

$$\gamma_{CO} = \frac{P_{CO_2}}{P_{CO} + P_{CO_2}} \quad \textbf{(5-5)}$$

$$\gamma_{CH_4} = \frac{P_{CO_2}}{P_{CO} + P_{CO_2} + P_{CH_4}} \quad \textbf{(5-6)}$$

5.2.2.1 Estimation of Reactivity of Manganese Ores Using the Artificial Neural Network

5.2.2.2 Background of Artificial Neural Network

Artificial neural networks are composed of input, hidden and output layers as well as a number of parallel-interconnected neurons in each layer. The input data are received by the neurons of the input layer and the output of each input neuron feeds into the neurons of a hidden layer. Then their output is transferred either through more hidden layers or directly to the output layer to achieve the results or predictions. With the tuning of activation functions by adjusting the weight and bias vectors between the neurons in each layer, the prediction performance can be enhanced. The above process of single-layer networks can be expressed by the following equation:

$$y_n = f\left(\sum_{i=1}^{n} x_n w_i^n + b_i^n\right) \quad \textbf{(5-7)}$$

Herein, y_n are the output signals of the current layer and input signals of neurons of the next layer; x_n are the input signals of the network; $w_i^n$and b_i^n are the values of weights and biases between the neurons, respectively. f is the activation function, where a sigmoid function is usually applied, as shown in **Equation (5-8)**.

$$\boldsymbol{f_{(x)} = \frac{1}{1 + e^{-x}}} \quad \textbf{(5-8)}$$

The ability of the ANN model to learn and generalise the relationship of practical and complex non-linear processes has developed as a powerful tool to predict

the properties and performance in material science [45-51]. The application of ANNs in estimation of the performance of heterogeneous, multi-component materials as oxygen carriers for chemical-looping process ought to provide a cost-effective approach to predict the performance and aid the design of oxygen carriers for chemical-looping. In this work, we consider the general workflow in developing a machine learning model to predict the performance of the oxygen carriers and the potential method to aid the design of the oxygen-carrying materials, as illustrated in **Figure 5-1**. In the following sections, we will illustrate how to utilise the ANN model trained by the experimental data to predict the reactivity of manganese ores as oxygen carrying materials in CLC/CLOU.

5.2.2.3 Database

A database that consists of the physical and chemical properties, experimental conditions, reactivity with fuels and oxygen release rates has been established based on previous work [22,23]. From here, one must decide the input and output parameters of the ANNs, and generate the training database from the experimental data. As mentioned earlier, it is well established for manganese ores that the oxygen release behaviour and reactivity with fuels are dependent on the type of the ore, and their properties including elemental compositions, attrition rate, crushing strength and surface area, and experimental investigation conditions (temperature, pressure, flow rate and fuel type). Therefore, fourteen parameters, including the mass concentration of the elements Mn, Fe, Si, Al, Ti, Ca, K, Mg, Na and P, bed temperature, attrition index, crushing strength and BET surface area of the fresh materials, have been considered as inputs of the training database.

For the output parameters, the reactivity with syngas, methane and the oxygen release to the gas phase were selected, as they are the most valuable parameters to evaluate the performance and determine whether they are suitable for chemical-looping.

A linear correlation analysis and feature selection by neighbourhood component analysis for regression was performed to select the most important inputs (termed ‘feature’) out of the 14 possible inputs by calculating the absolute values of

Pearson Correlation Coefficients (PCC) (This data is available in the Figure_Apx B-1 to Figure_Apx B-3 in the Appendix B) and feature weights (Figure_Apx B-4 in the Appendix B). In this case, the PCC value of 0.5-1 implies a strong linear correlation, whereas 0 indicates a weak linear correlation. For the feature weights analysis, an unimportant input would have a feature weighting close to zero. Based on these analyses, we selected seven out of the initially considered 14 inputs for the reactivity predictions and four out of 14 inputs for oxygen release rate predictions. The seven inputs chosen were bed temperature, crushing strength, and elemental compositions of Al, Ti, P, Si, and K. It is interesting to note that the reactivity with syngas and methane was not found to be highly correlated with the main constituent parts of the ores – Mn and Fe. The four chosen inputs for oxygen releasing rate predictor were bed temperature, and elemental compositions of Fe, Mn, and Si. These reduced input models were compared against ANN models that utilised all 14 inputs, which were able to predict the oxygen release rate and reactivity simultaneously.

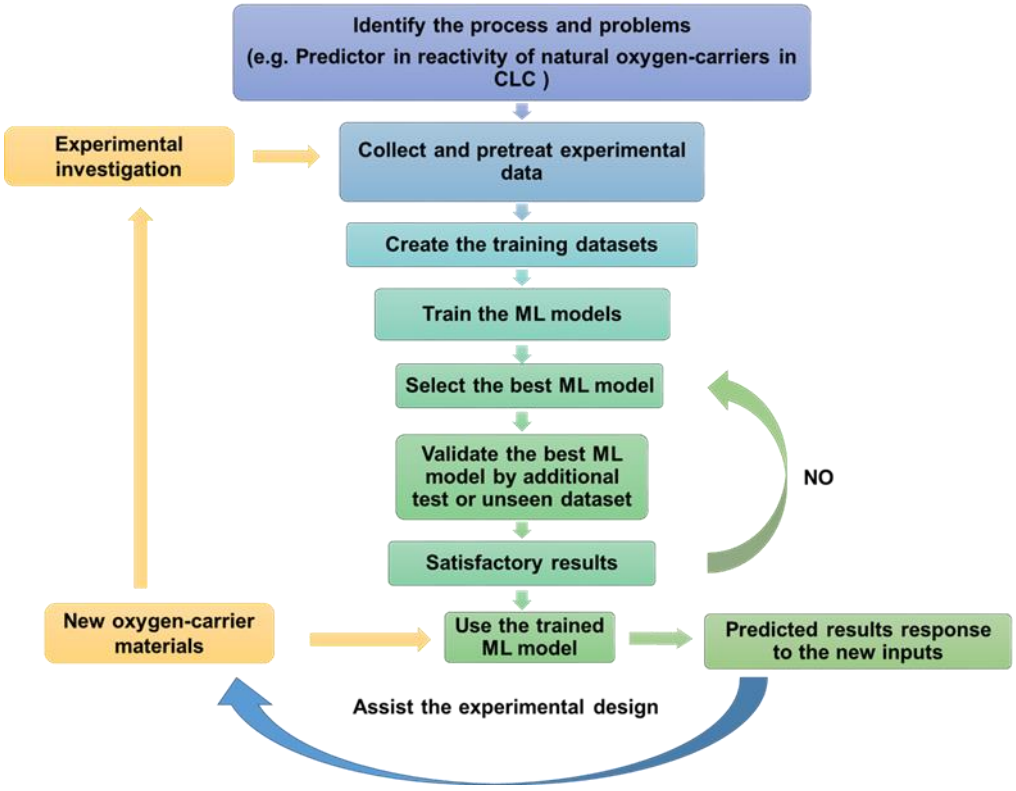

Figure 5-1 Workflow of developing a machine-learning model for oxygen carriers in the chemical-looping process.

Table 5-1 Elemental compositions and physical properties of the manganese ores

Composition (wt.%) and properties	EB	EC	AN	AC	SB	SA	GZ	SC	BR	EG	GL	MT	NCH	SL	SAB	SAA	UMK	TS	HM
Mn	32.42	11.53	35.31	34.59	54.76	52.60	18.01	46.11	58.36	50.44	34.59	15.85	42.51	36.75	46.83	38.91	61.97	42.51	53.32
Fe	21.70	51.80	11.90	10.50	16.10	9.10	28.70	5.18	3.57	10.50	5.88	35.70	11.90	4.13	11.90	16.10	3.85	5.39	7.00
Si	4.67	4.57	7.00	6.53	3.17	3.92	7.47	3.73	0.93	0.89	2.85	6.07	1.59	3.03	2.15	1.73	0.93	4.43	1.73
Al	1.22	1.27	1.64	1.69	0.17	2.49	7.41	3.39	1.91	0.32	0.12	1.64	0.22	0.19	0.19	0.26	2.06	0.20	4.55
Ti	0.08	0.07	0.08	0.08	0.01	0.12	0.72	0.23	0.11	0.02	0.01	0.06	0.03	0.01	0.02	0.01	0.10	0.02	0.14
Ca	1.71	0.86	9.29	12.86	2.43	0.93	0.20	1.86	0.14	1.43	8.57	0.59	6.21	8.57	5.93	3.93	0.17	10.71	0.07
K	0.46	0.27	0.21	0.32	0.07	1.08	0.24	1.00	0.61	0.12	0.07	0.34	0.07	0.33	0.07	0.07	0.59	0.17	1.08
Mg	0.84	0.39	3.96	3.54	0.37	0.22	0.56	0.25	0.34	0.96	2.22	0.11	0.60	1.80	0.72	0.41	0.34	2.34	0.07
Na	0.38	0.30	0.07	0.07	0.04	0.21	0.04	0.05	0.04	0.38	0.04	0.04	0.04	0.15	0.04	0.14	0.04	0.08	0.04
P	0.13	0.10	0.06	0.06	0.03	0.10	0.10	0.10	0.06	0.06	0.02	0.04	0.04	0.02	0.04	0.04	0.06	0.02	0.13
Attrition (wt%/h)	3.59	4.07	1.99	4.51	1.29	1.21	2.88	1.37	2.80	4.60	4.30	6.10	2.40	4.30	2.40	2.20	4.90	3.20	8.40
Crushing strength (N)	1.90	1.70	2.80	2.20	3.20	3.40	2.40	3.20	1.90	3.70	4.50	1.80	3.80	3.70	4.70	4.30	4.20	2.60	2.00
BET (m^2/g)	16.40	0.39	0.14	0.61	0.28	0.11	1.46	0.10	1.20	0.75	1.10	1.20	0.86	6.10	0.41	1.20	12.00	0.70	1.40

EB = Elwaleed Grade B, EC = Elwaleed Grade C, AN = Autlan Nodules, AC = Autlan Carbonate, SB = Sibelco Braunite, SA = SinAus, GZ = Guizhou, SC = Sibelco Calcined, BR = Brazilian (Buritirama), EG = Egyptian, GL = Gloria, MT = Metmin, NCH = Nchwaning, SL = Slovakian, SAB = South Africa B, SAA = South Africa A, UMK = United Manganese of Kalahari, TS = Tshipi, HM = Eramet HM

The abbreviations of each of the ores investigated are summarised in **Table_Apx B-1** of the Appendix B. In addition, the experimental data of the reactivity with syngas of 19 different ores at bed temperature 850 °C were selected as an unseen dataset, which was not included in the original training database and only used to assess the performance and robustness of the trained ANNs.

5.2.2.4 Optimising Artificial Neural Network Models

Once the original training database (171 input-output pairs) was established, the next step was to design and train the ANN models. In this work, MATLAB was used to develop the feedforward ANN models. Three training functions designated as *trainlm, trainbr* and *trainbfg* have been selected to train the multi-layer neural networks. *Trainlm* is a popular fast backpropagation algorithm that updates the weight and bias values according to Levenberg-Marquardt optimisation in supervised learning ANNs. *Trainbr* is the Bayesian regularisation backpropagation algorithm, which minimises a combination of squared errors and weights, and then decides the correct combination to achieve a more generalised neural network. *Trainbfg* is the Broyden–Fletcher–Goldfarb–Shanno (BFGS) quasi-Newton backpropagation algorithm that updates weights and biases according to the BFGS quasi-Newton method. To improve the ANNs generalisation and avoid overfitting, the original training database is randomly divided into different datasets and an “early stopping” mechanism has been applied in the training algorithms. For the *trainlm* and *trainbfg* algorithms, the input data was randomly divided into a training set (70%), validation set (15%) and test set (15%). For the the *trainbr* algorithm, 80% of the dataset was used for training and 20% to the test set for ANNs. No validation set was used for the *trainbr* algorithm because *trainbr* has its own form of validation built into the algorithm. It is also worth noting that the input data of the training database was normalised to values between 0 and 1, before training the ANNs, to prevent any unintended bias occurring in the training data.

It is a complex task to decide the topology (number of neurons and hidden layers) of the ANN and to train the ANN. In order to achieve the optimal ANN model to predict the reactivity of manganese ores, several MATLAB scripts were developed to decide the topology of the ANN. The performances of the ANNs were evaluated by the minimum value of the mean absolute error (MAE) and the highest value of the coefficient of determination (R^2). Single and double hidden layer ANNs were investigated. The single hidden layer ANNs with the number of neurons from one to

twenty-five, and two hidden layers ANNs (number of neurons: first hidden layer from one to twenty-five, and second hidden layer from one to thirty-five) were trained and validated with the three training functions. The random number seed was reset at the beginning of each new number of hidden neuron trials. The trained ANNs are then further assessed by the unseen dataset to investigate their performance and robustness to new inputs. The architecture of ANN with two hidden layers is shown in **Figure 5-2**.

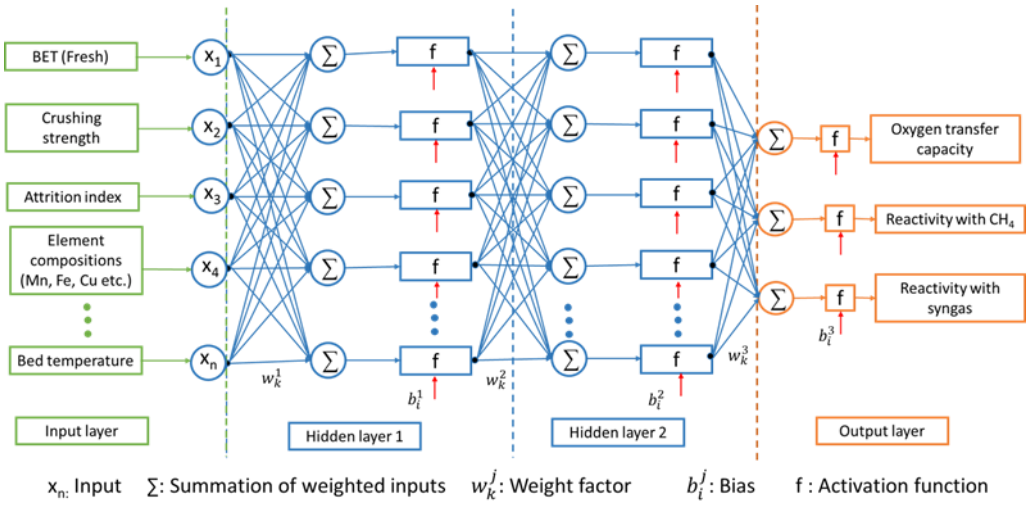

Figure 5-2 Proposed neural networks structure to predict the reactivity of manganese ores in the chemical-looping process.

5.3 Results and Discussion

5.3.1 Performance of the Trained Neural Networks

The prediction performance of the trained neural networks was evaluated by the root mean square error (RMSE), the mean absolute error (MAE) and the coefficient of determination (R^2). Lower values of RMSE and MAE, along with higher values of R^2 indicated better-fitting ANN models. The proposed ANN structures with different training algorithms were trained by the original training database. The performances of proposed ANNs were varied with the number of neurons in each hidden layer as shown in **Figure_Apx B-5** and **Figure_Apx B-6**. Only the single hidden layer neural networks with *trainbr* indicated that the MAE of the ANN decreased when increasing the number of neurons. This is because *trainbr* not only checks the performance of the model, but also determines how large the weights are, and this results in this training method producing more generalised ANN models. Therefore, it is necessary to try different structures of ANNs to optimise the ANN models. Once optimised ANN models

were obtained with different hidden layers and number of neurons, the results showed that the data predicted by the ANN models fitted the experimental results well. The performance of the trained neural networks with different topologies and training functions are shown in **Table_Apx B-2** (14-inputs) and **Table_Apx B-3** (7-inputs) in the Appendix B. The performance of the trained neural networks with the functions *trainlm* and *trainbfg* increased with increasing number of hidden layers, whereas performance with the function *trainbr* was not improved by increasing the number of hidden layers. Furthermore, the reduced input models did not improve the performance of trained ANNs, this is likely due to the strong correlating features not being able to represent all the information within the experimental training data. By only utilising the strongest correlating features, the weak correlating features are excluded and their minor, but important, impact on the final predictions is lost. The authors also suggest that these weaker correlating features are an important part of the dataset that enable the production of a generalised model. **Figure 5-3** presents a comparison of experimental and predicted data by *trainlm* with different optimised numbers of neurons in the hidden layers at a bed temperature of 900 °C with different numbers of inputs. Further comparisons of the ANN predicted data with the experimental results is presented in **Figure_Apx B-7** to **Figure_Apx B-10** in the Appendix B.

5.3.2 Confirmation of Model Robustness Using Unseen Data

Another important requirement for the ANN models is that they should not only accurately predict data within the training, validation and testing database but also provide a high prediction accuracy and robustness with new data that was not included within the training database. As previously mentioned, the selected ANNs were utilised to predict the reactivity of manganese ores with syngas at a bed temperature of 850 °C, which formed an unseen dataset to confirm the robustness and generality of the optimised ANNs. In addition, the performance of single optimised ANNs was compared with the stacked ANNs, which combine the results of 50 different ANNs with the same structure and different initial weights and biases. In the case of the performance on the unseen data, the stacked ANNs increased the prediction accuracy significantly over that of the single ANNs. The single hidden layer stacked ANNs trained with *trainbr* achieved the closest match with the experimental data on both the

training database and unseen data. Nevertheless, the increase of the number of hidden layers for the stacked ANNs reduces the prediction accuracy on unseen data.

When applying the trained ANNs to predict the results of unseen data, it is necessary to give a confidence interval for the prediction, since closely agreeing results do not automatically mean high precision of the predictions. It can be concluded that based on the data presented in the two-hidden-layer ANNs trained with *trainbr* (14-5-21-3) had the second best performance on the training database, but its stacked ANNs had the worst performance on unseen data, likely caused by overfitting of the ANNs. The network has memorised the relationship of the training dataset, but it has not learned to generalise under new situations. In this work, the bootstrap resampling technique was used to calculate the confidence intervals of predictions of stacked ANNs on unseen data through the function *bootci* in MATLAB, which computes the 95% bootstrap confidence interval based on the estimated standard error of predictions.

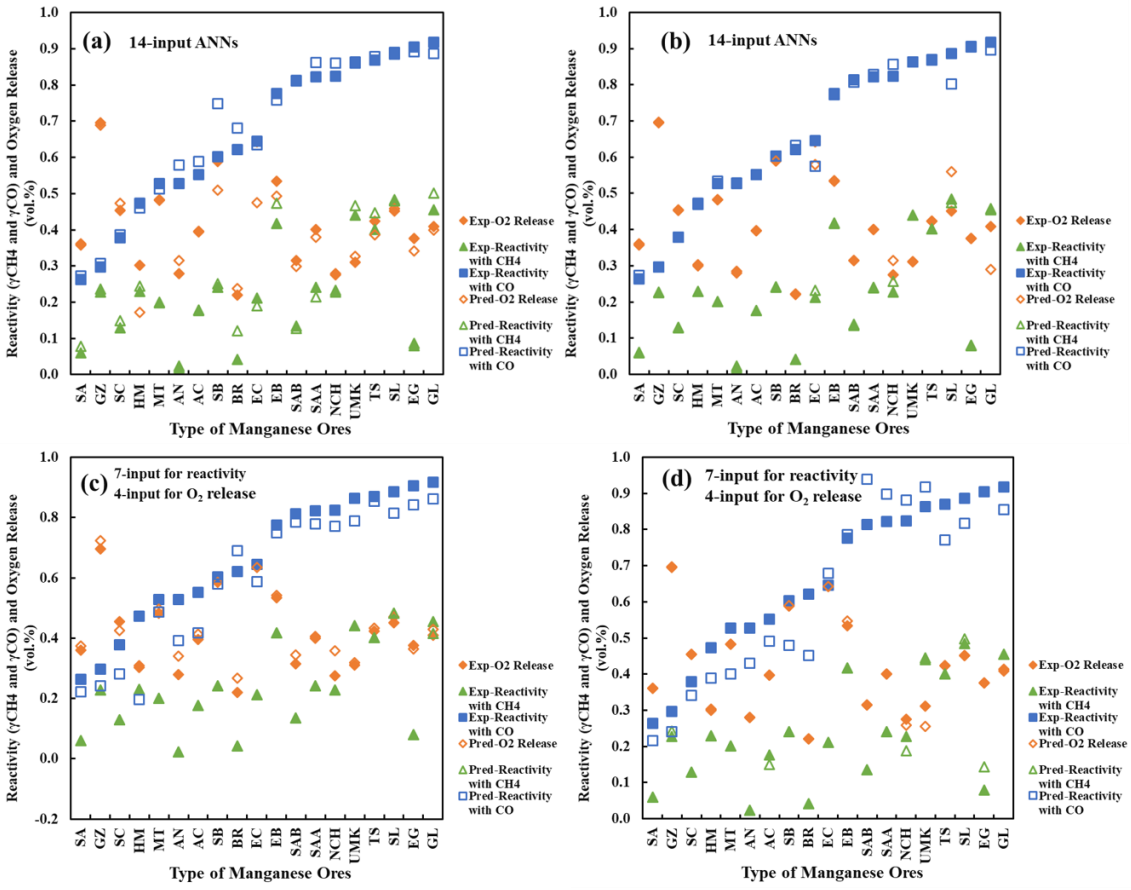

Figure 5-3 Experimental and predicted reactivity and oxygen release of manganese ores as oxygen carriers at bed temperature 900 °C- (a) trainlm single hidden-layer (14-input ANNs)and (b) trainlm two hidden-layer (14-input ANNs) (c) trainlm single hidden-layer (7 and 4-input ANNs) (d) trainlm two hidden-layer (7 and 4-input ANNs).

This is presented as error bars in **Figures 5-4**, which show the top three stacked ANNs on reactivity predictions of unseen data with the 95% confidence intervals. In general, the predictions of these three ANNs on unseen data are in good agreement with the experimental data, although there were some discrepancies in the AC, AN, and BR manganese ores. This may arise from the fact that most highly correlated input features (identified in the reduced order models) were similar in value but different experimental results were found. There may have been experimental or analytical inaccuracies, or some other material property not captured in the training dataset that could identify the cause of this discrepancy. The average difference between the experimental data and predictions of these three stacked ANNs on the unseen data was 14.7% in **Figure 5-4** (a), 15.2% in **Figure 5-4** (b) and 18.0% in **Figure 5-4** (c). Compared with the reduced order 7-input ANNs (MAE = 0.064 and R^2=0.92, **Figure_Apx B-11** in the Appendix B), the 14-input ANNs (MAE = 0.057 and R^2=0.94) presented a much higher accuracy and robustness to the unseen data.

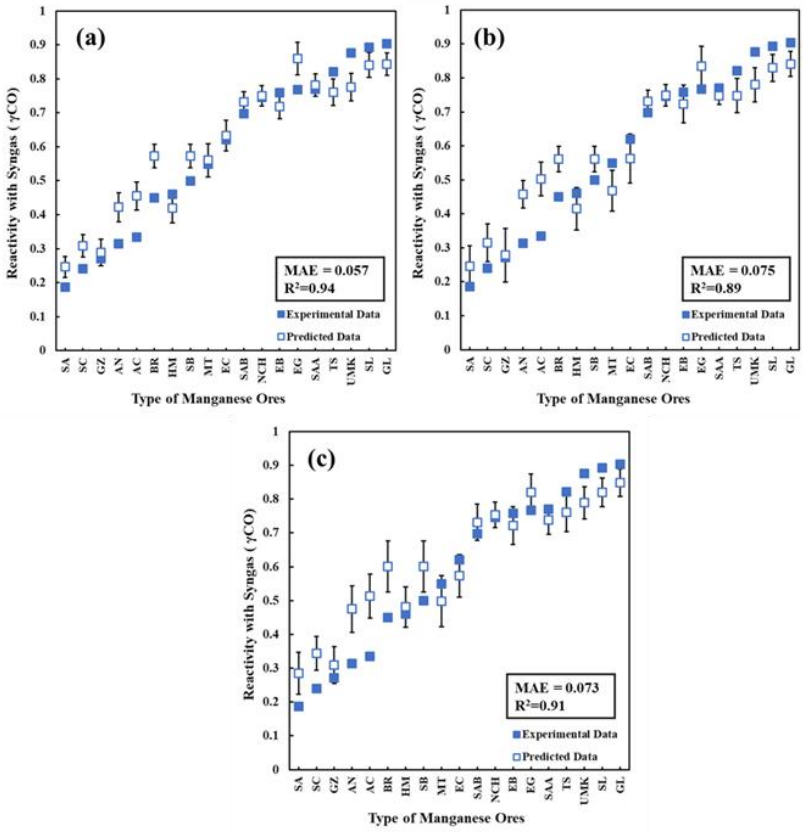

Figure 5-4 (a) Predictions of stacked neural network (14-13-3) trained with trainbr with 95% confidence intervals on unseen data; (b) Predictions of stacked neural network (14-8-3) trained with trainlm with 95% confidence intervals on unseen data; (c) Predictions of stacked neural network (14-7-12-3) trained with trainlm with 95% confidence intervals on unseen data.

5.3.3 Sensitivity Analysis

Besides using the trained ANNs to predict the reactivity of manganese ores with different fuels, they can also be used to estimate the potential effect of changing input values on the expected outputs, i.e. a predictive sensitivity analysis. We have selected four input parameters: Fe content, Mn content, BET surface area, and attrition index. Using the average value of each input parameter of all the ores as a baseline, a new dataset was created by varying these parameters by up to ±50% relative to the normalised inputs. The highest performing stacked ANN model (14-13-3 with *trainbr*) was used to undertake the sensitivity analysis, data from which is shown as **Figure 5-5.** The results from the ANN model, suggest that the BET surface area and attrition index have little to no effect on predicted reactivity and oxygen release. While, the reactivity with methane showed little effect from increasing Fe contents, the Mn content did appear to negatively affect the reactivity with syngas and CH_4. A marginally positive effect on CH_4 reactivity was noticed from increasing the Fe content, BET surface area and attrition index. Oxygen release was found to increase with an increasing Fe and Mn contents and to a lesser extent with increasing BET surface area and attrition index. This analysis suggests that researchers should focus on more the chemical composition of synthetic oxygen carriers rather than simply aiming for a high surface area or high crushing strength material. Similarly, researchers using natural ores should select materials primarily based on their chemical composition (Fe and Mn content and other minor elemental species) rather than their physical characteristics. However, it should be noted that there is likely a minimum cut-off value for BET surface area and attrition index, below which material are unsuitable for use in chemical-looping reactions.

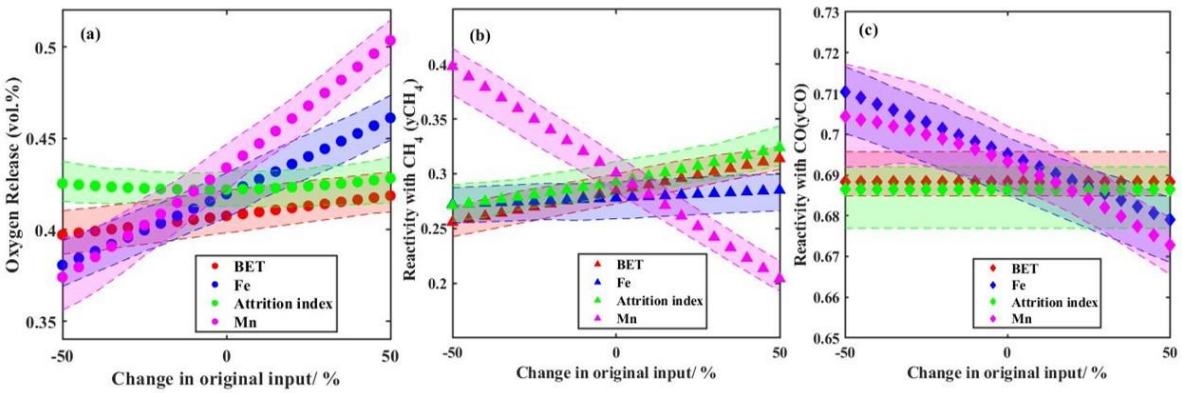

Figure 5-5 The predicted performance of reactivity with methane and syngas with 95% confidence intervals with the change in BET surface area, attrition index, and Fe and Mn content of an averaged ore.

5.3.4 Fe/Mn Content in Manganese Ores

In the experimental investigations [55,56], it was observed that the higher the Fe/Mn ratio the greater the oxygen release and methane conversion. Using this knowledge, we can demonstrate the effect of different Fe/Mn mass ratios on the oxygen release and reactivity with different fuels by artificially modifying of the input values of Fe for the EC ore using the trained ANNs. The EC ore has the highest mass concentration of Fe (normalised input 1) and the lowest mass concentration of Mn (normalised input 0) than any other ores investigated in this work and so offers a good starting point ore to vary the Fe/Mn from.

The new dataset has been generated by only modifying the normalised input of Fe content of the EC ore from 0 to 1 at 0.1 intervals, and thus different Fe/Mn mass ratios were achieved. The ANN model with the lowest MAE and R^2 determination coefficient has been applied to predict the performance of the new dataset of modified EC ores. **Figure 5-6** shows oxygen release rate and reactivity with different fuels of modified versions of EC ore where the Fe/Mn ratio was varied from 0.3 to 4.5. The results indicate that both oxygen release rate and reactivity with methane improved with higher ratios of Fe/Mn while the effects on reactivity with syngas are relatively small. This highlights the fact that it may be possible to synthetically increase the Fe/Mn ratio of some manganese ores/oxygen carriers to achieve enhanced performance.

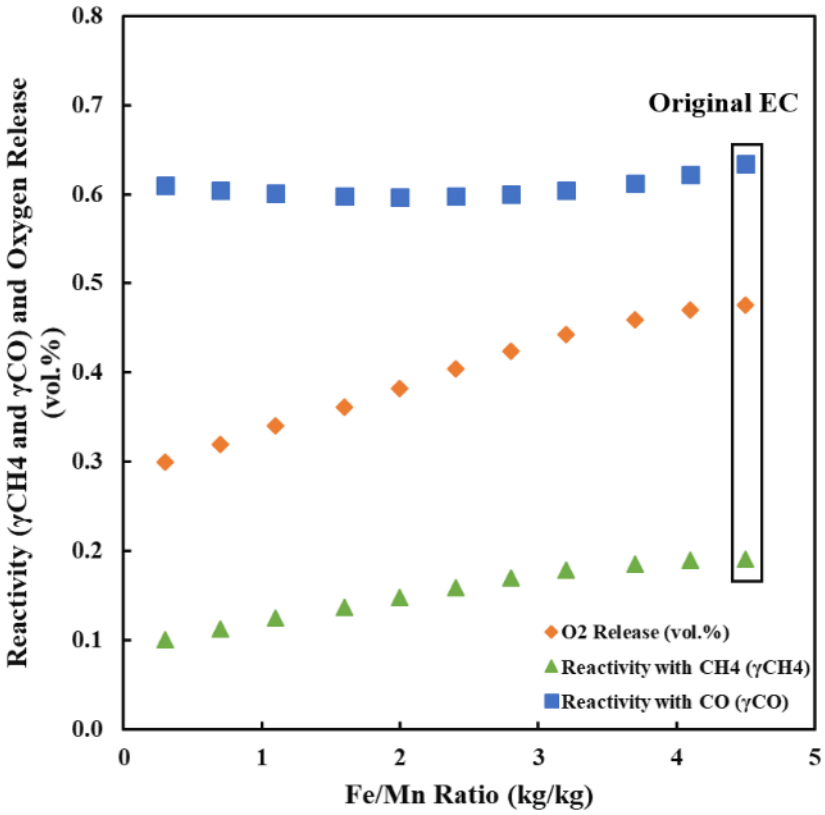

Figure 5-6 The predicted effects of varied Fe/Mn mass ratio of manganese ore EC on its oxygen release and reactivity with methane and syngas.

5.3.5 Discussion

Oxygen carrying materials have been largely investigated experimentally, however there been has limited work on investigation of the oxygen carriers by applying ML algorithms. In this work, it is shown that ANNs can be utilised as a prediction tool to estimate the reactivity of different manganese ores with different fuels for chemical-looping.

It is worth noting that ANNs are a data-driven method and the accuracy and robustness of ANNs is largely influenced by the availability of reliable training data and therefore the precision of these predictions is only ever as good as the initial experimental training data. It is generally assumed that a large amount of good experimental data is readily available for oxygen carriers in chemical-looping due to the numerous studies that have been carried out and consequently the extensive number of publications on oxygen carrying materials for the chemical-looping processes. In practice however, it is problematic to collect a large amount of data on oxygen carriers

for the chemical-looping processes to establish a training database. The main reason for this is that different experimental apparatuses (such as the thermogravimetric analysers, and fixed- and fluidised- bed reactors) are used, leading to very different results due to intra-particle mass transfer limitations [52], and the same oxygen carriers may exhibit a different performance in different reactors. Also, different researchers may define reactivity of oxygen carriers in different ways; for instance, some researchers evaluate the reactivity of oxygen carriers based on the oxygen carrier conversion, while others use the CO_2 yield to indicate the reactivity of oxygen carriers with different fuels [57]. These reasons made it impractical to combine data from multiple literature sources into a single dataset.

In this work, we have used the experimental data, gathered at Chalmers University of Technology, of different manganese ores from different mines around the world, which cover a broad range of ores, to form the training data for ANNs. It was feasible to implement ANNs to discover the relationships between the input features and the outputs, and the most optimally performing ANNs were able act as predictor to estimate the likely performance of new manganese ores. Although the size of the training database relative to the number of inputs was relatively small, i.e. 171:14, several methods were employed to ensure that the model minimised overfitting and maintained its generality. For instance, 1) the data was normalised and randomly divided into a training dataset, 2) different training algorithms were applied to study the generality of the models, 3) a cross-validation based on the early stopping mechanism was used, and 4) stacked neural networks were adopted to prevent overfitting of the ANNs.

In addition to this, we have compared the results of the ANNs with 14 inputs with reduced-input ANNs where only the most important and highest correlating features were used as inputs. These features were selected based on a Pearson correlation and feature selection analysis. Upon comparison, the results indicated that the reduced-input models did not improve the robustness or accuracy of ANNs. We explain the reason for this is because the physical and chemical properties of manganese ores are complex and reducing the number of input variables of the ANNs will ignore some relatively minor, but important, features relevant to the oxygen carriers' performance. It should be mentioned that ANNs have been successfully

applied elsewhere with limited datasets, of similar scale to ours, to predict the performance and properties in materials science [54-56].

Stacked ANNs with bootstrap resampling technology was applied to show the confidence bounds of the model predictions on unseen data and indicated that the selected ANNs have high prediction efficiency for both the new dataset and training dataset. These results indicate that it is feasible to implement ANN or other ML techniques to assist in investigating the reactivity of oxygen-carrying materials and designing new oxygen carriers as illustrated in **Figure 5-1**. ML can potentially spot links in datasets that would otherwise be missed and could lead to new materials being selectively designed and manufactured with desired properties or characteristics. Similar to the predictive sensitive analysis of the selected inputs and the analysis of the impact of Fe/Mn ratio on the performance of manganese ores in chemical-looping processes, other effects such as varied inputs on the predicted results can be estimated. This can potentially provide useful information for optimisation and synthesis of oxygen-carrying materials.

In this work, an analysis of the different weights for the different inputs (see **Figure 5-2**) rendered complex correlations: the magnitude of the weights of an input throughout the layers (three weights for double-hidden-layers ANNs) can change in comparison to the weights of other inputs. For example, when only comparing the first layer, the weight of the input (e.g., temperature) is larger than that of the other input node weights. However, according to the second layer, the input (e.g., elemental concentration of magnesium) has the highest weighting. This creates complex interlinked connections and as a result the weights change dynamically throughout the layers. Consequently, no general conclusions regarding the importance of the different inputs can be deduced based on the weights and biases produced by the ANN training algorithms. More research is required on producing an explainable ANN for non-classification datasets. We have investigated the potential effect of changing some of the input values on the expected outputs, and it can be seen that the inputs of Fe and Mn have more effects on the predicted data, which is also observed in tests of various manganese ores [22,44].

The ANNs developed in this work were focused on the experimental investigation of manganese ores as oxygen carriers for CLC and CLOU in a batch, lab-scale, fluidised

bed reactor. Because of this, these models may have some experimental testing bias and therefore as the results are not based on empirical or intrinsic data, they may not accurately estimate the performance of the same oxygen carrier ore in a different testing facility. Furthermore, the important parameters of oxygen carriers, such as lifetime and long-term performance of oxygen carriers, were not considered in these ANNs but should be investigated in the future. The issue related to prediction accuracy of material properties based on physics-chemical descriptors is also faced by other applications on ML in chemistry and chemical engineering. For instance, Skoraczyński et al. [57] indicated that the current descriptors is insufficient to predict the outcomes of organic reactions, and the new fundamental chemical descriptors should be developed to improve the performance of ML models. This is also the reason why the predictive sensitive analysis of the inputs shows that chemical compositions (Fe and Mn) of ores have larger impacts than their physical parameters (BET surface area and attrition index). The quantity and quality of the training dataset play a significant role in the performance of the ANN models and what useful information we can extract from the data. The performance data of the manganese ores in a variety of different reactors would be a useful addition to the dataset to aid the development of ANNs that can predict the performance of manganese ores as oxygen carriers for a variety of different applications, for instance, OCAC, CLR, CLG, CLC and CLOU.

5.4 Summary and Conclusions

In this work, we demonstrated an approach to predict the reactivity of manganese ores as oxygen-carrying materials in chemical-looping processes using machine learning (ML) algorithms named artificial neural networks (ANNs). We illustrate and discuss several methods such as different training algorithms, optimal topology and stacked ANNs with bootstrap techniques to prevent the overfitting with small datasets. We showed that trained ANNs can provide very good performance predictions for heterogeneous, multi-component materials (oxygen carrier ores) for chemical-looping processes. These models were tested on unseen experimental and demonstrated their high level of accuracy and generality. The most optimal ANN model for the manganese ores reactivity predictions had a topology of 14-13-3 and was trained with the *trainbr* algorithm, which was able to achieve the highest R^2 (0.94) and lowest MAE (0.057).

ML is an effective approach to estimate the performance of oxygen-carrying materials for the chemical-looping process, and it improved as more datasets of oxygen-carrying materials were generated. These algorithms potentially offer new insights into historical research data on oxygen carriers in chemical-looping processes and could provide a rapid tool to predict the performance of oxygen-carrying materials without the need for significant further experimental investigation and reduce the testing time and cost to evaluate and develop new oxygen-carrier materials. We envisage that ML will accelerate the discovery, design, synthesis, and characterisation of oxygen-carrier materials for chemical-looping processes.

5.5 References

[1] Mattisson T, Lyngfelt A, Leion H. Chemical-looping with oxygen uncoupling for combustion of solid fuels. Int J Greenh Gas Control 2009;3:11–9. doi:10.1016/J.IJGGC.2008.06.002.

[2] Lyngfelt A, Leckner B, Mattisson T. A fluidized-bed combustion process with inherent CO_2 separation; application of chemical-looping combustion. Chem Eng Sci 2001;56:3101–13. doi:10.1016/S0009-2509(01)00007-0.

[3] Adanez J, Abad A, Garcia-Labiano F, Gayan P, de Diego LF. Progress in Chemical-Looping Combustion and Reforming technologies. Prog Energy Combust Sci 2012;38:215–82. doi:10.1016/J.PECS.2011.09.001.

[4] Rydén M, Lyngfelt A. Using steam reforming to produce hydrogen with carbon dioxide capture by chemical-looping combustion. Int J Hydrogen Energy 2006;31:1271–83. DOI:10.1016/J.IJHYDENE.2005.12.003.

[5] Mattisson T, Lyngfelt A. Applications of chemical-looping combustion with capture of CO_2. Control 2001:46–51.

[6] Fan L-S. Chemical Looping Partial Oxidation: Gasification, Reforming, and Chemical Syntheses. 2017. DOI: 10.1017/9781108157841.

[7] Guo Q, Cheng Y, Liu Y, Jia W, Ryu HJ. Coal chemical looping gasification for syngas generation using an iron-based oxygen carrier. Ind Eng Chem Res 2014;53:78–86. doi:10.1021/ie401568x.

[8] Rydén M, Hanning M, Corcoran A, Lind F. Oxygen Carrier Aided Combustion (OCAC) of Wood Chips in a Semi-Commercial Circulating Fluidized Bed Boiler Using Manganese Ore as Bed Material. Appl Sci 2016;6:347. doi:10.3390/app6110347.

[9] Thunman H, Lind F, Breitholtz C, Berguerand N, Seemann M. Using an oxygen-carrier as bed material for combustion of biomass in a 12-MWth circulating fluidized-bed boiler. Fuel 2013;113:300–9. doi:10.1016/j.fuel.2013.05.073.

[10] Imtiaz Q, Hosseini D, Müller CR. Review of Oxygen Carriers for Chemical Looping with Oxygen Uncoupling (CLOU): Thermodynamics, Material Development, and Synthesis. Energy Technol 2013;1:633–47. doi:10.1002/ente.201300099.

[11] Abanades JC, Arias B, Lyngfelt A, Mattisson T, Wiley DE, Li H, et al. Emerging CO_2 capture systems. Int J Greenh Gas Control 2015;40:126–66. doi:10.1016/j.ijggc.2015.04.018.

[12] Bui M, Adjiman CS, Bardow A, Anthony EJ, Boston A, Brown S, et al. Carbon capture and storage (CCS): The way forward. Energy Environ Sci 2018;11:1062–176. doi:10.1039/c7ee02342a.

[13] Lyngfelt A, Brink A, Langørgen Ø, Mattisson T, Rydén M, Linderholm C. 11,000 h of chemical-looping combustion operation—Where are we and where do we want to go? Int J Greenh Gas Control 2019;88:38–56. doi:10.1016/J.IJGGC.2019.05.023.

[14] Fennell P, Anthony B. Calcium and chemical looping technology for power generation and carbon dioxide (CO_2) capture. 2015.

[15] Fossdal A, Bakken E, Øye BA, Schøning C, Kaus I, Mokkelbost T, et al. Study of inexpensive oxygen carriers for chemical looping combustion. Int J Greenh Gas Control 2011;5:483–8. doi:10.1016/j.ijggc.2010.08.001.

[16] Lyngfelt A. Oxygen Carriers for Chemical Looping Combustion - 4000 h of Operational Experience. Oil Gas Sci Technol 2011;66:161–72. doi:10.2516/ogst/2010038.

[17] Hossain MM, de Lasa HI. Chemical-looping combustion (CLC) for inherent CO_2 separations—a review. Chem Eng Sci 2008;63:4433–51. doi:10.1016/J.CES.2008.05.028.

[18] Mattisson T. Materials for Chemical-Looping with Oxygen Uncoupling. ISRN Chem Eng 2013;2013:1–19. doi:10.1155/2013/526375.

[19] Leion H, Mattisson T, Lyngfelt A. Use of ores and industrial products as oxygen carriers in chemical-looping combustion. Energy and Fuels 2009;23:2307–15. doi:10.1021/ef8008629.

[20] Leion H, Lyngfelt A, Johansson M, Jerndal E, Mattisson T. The use of ilmenite as an oxygen carrier in chemical-looping combustion. Chem Eng Res Des 2008;86:1017–26. doi:10.1016/j.cherd.2008.03.019.

[21] Arjmand M, Leion H, Mattisson T, Lyngfelt A. Investigation of different manganese ores as oxygen carriers in chemical-looping combustion (CLC) for solid fuels. Appl Energy 2014;113:1883–94. doi:10.1016/j.apenergy.2013.06.015.

[22] Sundqvist S, Arjmand M, Mattisson T, Rydén M, Lyngfelt A. Screening of different manganese ores for chemical-looping combustion (CLC) and chemical-looping with oxygen uncoupling (CLOU). Int J Greenh Gas Control 2015;43:179–88. doi:10.1016/j.ijggc.2015.10.027.

[23] Sundqvist S, Khalilian N, Leion H, Mattisson T, Lyngfelt A. Manganese ores as oxygen carriers for chemical-looping combustion (CLC) and chemical-looping with oxygen uncoupling (CLOU). J Environ Chem Eng 2017;5:2552–63. doi:10.1016/j.jece.2017.05.007.

[24] Linderholm C, Schmitz M, Biermann M, Hanning M, Lyngfelt A. Chemical-looping combustion of solid fuel in a 100 kW unit using sintered manganese ore as oxygen carrier. Int J Greenh Gas Control 2017;65:170–81. doi:10.1016/J.IJGGC.2017.07.017.

[25] Schmitz M, Linderholm C, Hallberg P, Sundqvist S, Lyngfelt A. Chemical-Looping Combustion of Solid Fuels Using Manganese Ores as Oxygen Carriers. Energy and Fuels 2016;30:1204–16. doi:10.1021/acs.energyfuels.5b02440.

[26] Moldenhauer P, Rydén M, Mattisson T, Younes M, Lyngfelt A. The use of ilmenite as oxygen carrier with kerosene in a 300 W CLC laboratory reactor with continuous circulation. Appl Energy 2014;113:1846–54. doi:10.1016/J.APENERGY.2013.06.009.

[27] Moldenhauer P, Rydén M, Lyngfelt A. Testing of minerals and industrial by-products as oxygen carriers for chemical-looping combustion in a circulating fluidized-bed 300 W laboratory reactor. Fuel 2012;93:351–63. doi:10.1016/j.fuel.2011.11.009.

[28] Leion H, Jerndal E, Steenari BM, Hermansson S, Israelsson M, Jansson E, et al. Solid fuels in chemical-looping combustion using oxide scale and unprocessed iron ore as oxygen carriers. Fuel 2009;88:1945–54. doi:10.1016/j.fuel.2009.03.033.

[29] Song T, Wu J, Zhang H, Shen L. Characterization of an Australia hematite oxygen carrier in chemical looping combustion with coal. Int J Greenh Gas Control 2012;11:326–36. doi:10.1016/j.ijggc.2012.08.013.

[30] Shen L, Wu J, Xiao J, Song Q, Xiao R. Chemical-looping combustion of biomass in a 10 kWth reactor with iron oxide as an oxygen carrier. Energy and Fuels 2009;23:2498–505. doi:10.1021/ef900033n.

[31] Cuadrat A, Abad A, García-Labiano F, Gayán P, de Diego LF, Adánez J. The use of ilmenite as oxygen-carrier in a 500 Wth Chemical-Looping Coal Combustion unit. Int J Greenh Gas Control 2011;5:1630–42. doi:10.1016/j.ijggc.2011.09.010.

[32] Mohd Ali J, Hussain MA, Tade MO, Zhang J. Artificial Intelligence techniques applied as estimator in chemical process systems - A literature survey. Expert Syst Appl 2015;42:5915–31. doi:10.1016/j.eswa.2015.03.023.

[33] Panteleev J, Gao H, Jia L. Recent applications of machine learning in medicinal chemistry. Bioorganic Med Chem Lett 2018;28:2807–15. doi:10.1016/j.bmcl.2018.06.046.

[34] Kalogirou S. Applications of artificial neural networks in energy systems. Energy Convers Manag 1999;40:1073–87. doi:10.1016/S0196-8904(99)00012-6.

[35] Duchesne MA, MacChi A, Lu DY, Hughes RW, McCalden D, Anthony EJ. Artificial neural network model to predict slag viscosity over a broad range of temperatures and slag compositions. Fuel Process. Technol., vol. 91, Elsevier; 2010, p. 831–6. doi:10.1016/j.fuproc.2009.10.013.

[36] Kalogirou SA. Artificial neural networks in renewable energy systems applications: a review. Renew Sustain Energy Rev 2001;5:373–401. doi:10.1016/S1364-0321(01)00006-5.

[37] Hough BR, Beck DAC, Schwartz DT, Pfaendtner J. Application of machine learning to pyrolysis reaction networks: Reducing model solution time to enable process optimization. Comput Chem Eng 2017;104:56–63. doi:10.1016/j.compchemeng.2017.04.012.

[38] Sipöcz N, Tobiesen FA, Assadi M. The use of Artificial Neural Network models for CO_2 capture plants. Appl Energy 2011;88:2368–76. doi:10.1016/J.APENERGY.2011.01.013.

[39] Zhou Q, Wu Y, Chan CW, Tontiwachwuthikul P. Modeling of the carbon dioxide capture process system using machine intelligence approaches. Eng Appl Artif Intell 2011;24:673–85. doi:10.1016/j.engappai.2011.01.003.

[40] Fu K, Chen G, Sema T, Zhang X, Liang Z, Idem R, et al. Experimental study on mass transfer and prediction using artificial neural network for CO_2 absorption into aqueous DETA 2013. doi:10.1016/j.ces.2013.04.024.

[41] Li F, Zhang J, Oko E, Wang M. Modelling of a post-combustion CO_2 capture process using neural networks. Fuel 2015;151:156–63. doi:10.1016/j.fuel.2015.02.038.

[42] Dunstan MT, Jain A, Liu W, Ong SP, Liu T, Lee J, et al. Large scale computational screening and experimental discovery of novel materials for high temperature CO_2 capture. Energy Environ Sci 2016;9:1346–60. doi:10.1039/c5ee03253a.

[43] Lau CY, Dunstan MT, Hu W, Grey CP, Scott SA. Large scale in silico screening of materials for carbon capture through chemical looping. Energy Environ Sci 2017;10:818–31. doi:10.1039/c6ee02763f.

[44] Sundqvist S, Chalmers tekniska högskola. Department of Chemistry and Chemical Engineering. Manganese ores as oxygen carriers for chemical-looping combustion. Chalmers University of Technology; 2017.

[45] Butler KT, Davies DW, Cartwright H, Isayev O, Walsh A. Machine learning for molecular and materials science. Nature 2018;559:547–55. doi:10.1038/s41586-018-0337-2.

[46] Asadi-Eydivand M, Solati-Hashjin M, Farzadi A, Osman NAA. Artificial neural network approach to estimate the composition of chemically synthesized biphasic calcium phosphate powders. Ceram Int 2014;40:12439–48. doi:10.1016/j.ceramint.2014.04.095.

[47] Zhang J, Martin' EB, Morris AJ, Kiparissides C. Inferential Estimation of Polymer Quality Using Stacked Neural Networks. vol. 21. 1997.

[48] Joyce SJ, Osguthorpe DJ, Padgett JA, Price GJ. Neural network prediction of glass-transition temperatures from monomer structure. J Chem Soc Faraday Trans 1995;91:2491–6. doi:10.1039/FT9959102491.

[49] Yang H, Zhang Z, Zhang J, Zeng XC. Machine learning and artificial neural network prediction of interfacial thermal resistance between graphene and hexagonal boron nitride. Nanoscale 2018;10:19092–9. doi:10.1039/c8nr05703f.

[50] Sha W, Edwards KL. The use of artificial neural networks in materials science based research. Mater Des 2007;28:1747–52. doi:10.1016/j.matdes.2007.02.009.

[51] Hassan AM, Alrashdan A, Hayajneh MT, Mayyas AT. Prediction of density, porosity and hardness in aluminum-copper-based composite materials using artificial neural network. J Mater Process Technol 2009;209:894–9. doi:10.1016/j.jmatprotec.2008.02.066.

[52] Zhang Z, Yao JG, Boot-Handford ME, Fennell PS. Pressurised chemical-looping combustion of an iron-based oxygen carrier: Reduction kinetic measurements and modelling. Fuel Process Technol 2018;171:205–14. doi:10.1016/j.fuproc.2017.11.018.

[53] Mei D, Mendiara T, Abad A, De Diego LF, García-Labiano F, Gayán P, et al. Manganese Minerals as Oxygen Carriers for Chemical Looping Combustion of Coal. Ind Eng Chem Res 2016;55:6539–46. doi:10.1021/acs.iecr.6b00263.

[54] Zhang Y, Ling C. A strategy to apply machine learning to small datasets in materials science. Npj Comput Mater 2018;4:25. doi:10.1038/s41524-018-0081-z.

[55] Feng S, Zhou H, Dong H. Using deep neural network with small dataset to predict material defects. Mater Des 2019;162:300–10. doi:10.1016/j.matdes.2018.11.060.

[56] Pasini A. Artificial neural networks for small dataset analysis. J Thorac Dis 2015;7:953–60. doi:10.3978/j.issn.2072-1439.2015.04.61.

[57] Skoraczyñski G, DIttwald P, Miasojedow B, Szymkuc S, Gajewska EP, Grzybowski BA, et al. Predicting the outcomes of organic reactions via machine learning: Are current descriptors sufficient? Sci Rep 2017;7. doi:10.1038/s41598-017-02303-0.

6 Process Simulations of Blue Hydrogen Production by Upgraded Sorption Enhanced Steam Methane Reforming (SE-SMR) Processes

Yongliang Yan, Dhinesh Thanganadar, Peter T. Clough, Sanjay Mukherjee, Kumar Patchigolla Vasilije Manovic, Edward J. Anthony

Energy and Power Theme, School of Water, Energy and Environment, Cranfield University, Cranfield, Bedfordshire, MK43 0AL, UK.

DOI: https://doi.org/10.1016/j.enconman.2020.113144

Abstract

Clean and carbon-free hydrogen production is expected to play a vital role in future global energy transitions. In this work, six process arrangements for sorption enhanced steam methane reforming (SE-SMR) are proposed for blue H_2 production: 1) SE-SMR with an air fired calciner, 2) SE-SMR with a Pressure Swing Adsorption (PSA) unit, 3) SE-SMR thermally coupled with Chemical-Looping Combustion (CLC), 4) SE-SMR+PSA+CLC, 5) SE-SMR+PSA with an oxy-fired calciner, 6) SE-SMR+PSA and indirect firing H_2 combustion from the product stream recycle. The proposed process models with rigorous heat exchanger network design were simulated in Aspen Plus to understand the thermodynamic limitations in achieving the maximum CH_4 conversion, H_2 purity, CO_2 capture efficiency, cold gas efficiency and net operating efficiency. A sensitivity study was also performed for changes in the reformer temperature, pressure, and steam to carbon (S/C) ratio to explore the optimal operating space for each case. The SE-SMR+PSA+H_2 (Case 6) recycle process can achieve a maximum of 94.2% carbon capture with a trade-off in cold gas efficiency (51.3%), while a near 100% carbon capture with the maximum net efficiency of up to 76.3% is realisable by integrating CLC and PSA (Case 4) at 25 bar. Integration of oxy-fuel combustion lowered the net efficiency by 2.7% points due to the need for an air separation unit. In addition, the SE-SMR with the PSAOG process can be designed as a self-sustaining process without any additional fuel required to meet the process heat utility when the S/C ratio is ~3-3.5.

Keywords

Blue hydrogen production, sorption enhanced steam methane reforming, chemical-looping combustion, carbon capture.

6.1 Introduction

Hydrogen is widely used in oil refining, ammonia and other chemicals production and also draws significant attention because of its potential to tackle critical decarbonisation related challenges in the transport, and residential sectors, as well as industry and the power sectors. It also has the ability to serve as an energy storage medium for renewables, e.g. solar photovoltaics and wind energy [1]. Current global H_2 production is around 75 Mt per annum, of which 76% is produced from natural gas (205 Gm^3, or 6% of current global natural gas use) and 23% from coal (107 Mt, or 2% of global coal use), however, its production contributes about 830 Mt CO_2 emissions to the atmosphere per year (2% of global annual emissions) [1]. With the rapid growth rate in H_2 demand, CO_2 emissions from hydrogen production are predicted to increase significantly, if it is supplied from natural gas or coal without carbon capture and storage (CCS) technologies. These CO_2 emissions would limit our ability to use hydrogen as a means of achieving the 2 °C Paris Agreement goal and mitigating further climate change.

The two conventional ways of producing H_2 are Steam Methane Reforming (SMR) and Autothermal Reforming with a Gas Heated Reformer (ATR+GHR), both of which require an additional backend CO_2 capture process to decarbonise their processes. To meet climate change targets, it is imperative to develop low-carbon and cost-effective hydrogen production technologies to provide a clean, secure and affordable energy future that can compete with SMR and ATR+GHR coupled with backend CO_2 capture. Detailed techno-economic analysis and life cycle assessment of these two technologies with/without CO_2 capture are available elsewhere [2].

One innovative option is sorption enhanced steam reforming (SE-SMR), which involves an in-situ CO_2 capture process where the hydrocarbon fuel is reacted with steam in the presence of a CO_2 sorbent and a reforming catalyst to generate decarbonised, high purity H_2 [3]. The concept of SE-SMR is not new. Rostrup-Nielsen [4] reported that the concept of adding a CO_2 sorbent to a hydrocarbon-steam-reforming reactor was firstly described in 1868. Williams [5] published a patent for hydrogen production by steam methane reforming in the presence of a mixture of lime

and catalyst. Later on, Gorin and Retallick [6] patented a fluidised-bed process by reforming catalyst and CO_2 acceptor for hydrogen production. Then, a series of experimental investigation of the different sorbents with Ni catalyst under the multiple SE-SMR/regeneration cycles in a fluidised or packed bed was conducted and described elsewhere [7-11]. Recently, Ni-CaO combined sorbent-catalyst materials (CSCM, with Ni and CaO on a unique bifunctional kind of particles) have been investigated at industrially relevant conditions and demonstrated satisfactory performance over 100 SE-SMR/regeneration cycles [12,13]. More insights on the development of SE-SMR technology are available in the review papers by Harrison [14] and Di Giuliano and Gallucci [15].

Compared to the conventional processes, high yields of H_2 (~95%, dry basis) can be achieved at relatively low reaction temperatures (650 °C), without the need for multiple shift reactors and significant subsequent purification steps [16]. Although the in-situ CO_2 capture process of SE-SMR can remove the majority of the CO_2 from the process gas stream, CO_2 is still emitted in the process of supplying the heat for the regeneration of the CO_2 sorbent and generation of steam. Here too, this CO_2 production must be mitigated possibly through a high cost and energy-intensive processes like oxy-fuel combustion or post-combustion capture.

To reduce the cost and maximise the CO_2 capture from the SE-SMR technology for hydrogen production, various configurations integrated with SE-SMR have been proposed for low-carbon and high-purity hydrogen production. Ochoa-Fernández et al. [17] conducted a process simulation of the integration of SE-SMR and oxy-fuel combustion using HYSYS, and the results indicated that SE-SMR with oxy-fuel combustion offers advantages in terms of thermal efficiency, smaller pressure swing adsorption (PSA) unit, and CO_2 capture compared to conventional steam reforming with monoethanolamine (MEA) absorption. In addition, with the development of next-generation CO_2 capture processes, chemical-looping combustion (CLC) has been proposed for hydrogen production. CLC is a state-of-the-art method for heat and power generation with inherent CO_2 separation at low cost and with very low energy penalties compared to oxy-fuel combustion [18-21]. CLC is typically carried out in a dual fluidised-bed reactor system, where the oxygen is transported from an air reactor to a fuel reactor by utilising an oxygen carrier (OC) [22]. Rydén et al. [23] first proposed a novel process for the production of H_2 by SMR with inherent CO_2 capture by CLC.

Subsequently, Ortiz et al. [24] successfully tested the use of an iron-based waste product as an oxygen carrier burning a PSA off-gas in a 500 W_{th} unit under continuous operation and demonstrated that it is feasible to apply CLC in steam reforming with the inherent CO_2 separation. Recently, many studies [25-27] have carried out process simulations and thermodynamic analyses for the integration of CLC with SE-SMR and have shown some very promising results in terms of energy efficiency, H_2 purity and overall CO_2 capture efficiency. Besides indirect integration of CLC with SE-SMR, other novel concepts for Ca-Cu looping and sorption enhanced-chemical looping methane reforming for hydrogen production have also been intensively investigated [28-31]. The most recent achievements for the development of Ca-Cu looping technology were reviewed by Martínez et al.[32].

Although the concept of low-carbon hydrogen production by SE-SMR thermally coupling CLC has been simulated, the hydrogen product purity (92-98%) from previous CLC-SE-SMR investigation is still too low for some end-use applications such as fuel cells, electronics and polysilicon production. Thus, a hydrogen purification unit such as PSA or membrane separation must be installed to enhance the hydrogen purity, and the off-gas from the hydrogen purification unit can be recycled to the fuel reactor, which will reduce the additional fuel supply and improve the overall CO_2 capture. Also, these previous works have used a simplified modelling approach to model the heat network of SE-SMR with CLC process, which potentially results in less accurate values of process efficiency.

Moreover, past studies [25-27] evaluated the process simulation of the SE-SMR with CLC based on NiO/Ni oxygen carriers. Unfortunately, nickel oxides are among the most expensive oxygen carriers and have health, safety and environmental risks, as well as thermodynamic restrictions for fuel conversion, which mean that they are unlikely to be deployed in commercial CLC systems [33-35]. Therefore, low cost and less hazardous oxygen carriers such as iron-based oxygen carries must be investigated for this process.

The purpose of this work is to evaluate the potential performance and to provide a comprehensive investigation of six new process configurations of SE-SMR integrated with pressure swing adsorption, an iron-based CLC, and oxyfuel combustion for low-carbon and high-purity hydrogen production. In this work, six different SE-SMR

process models with a detailed heat exchanger network design are employed to understand the thermodynamic limitations of achieving the maximum cold gas efficiency and net efficiency whilst simultaneously capturing the greatest quantity of CO_2 from the production process. Sensitivity studies have also been performed for all six cases to better understand the influence of reformer pressure, temperature and steam to carbon molar ratio (S/C) on the CH_4 conversion, CO_2 capture efficiency, H_2 purity, cold gas efficiency and net efficiency.

6.2 Process Configuration and Simulation

6.2.1 Process Configuration

H_2 production by SE-SMR with a PSA unit, and integrated with CLC or an oxy-fired or a H_2-fired calciner has been proposed and simulated in Aspen Plus. The performance of the different cases has been evaluated on the basis of CH_4 conversion, H_2 purity, CO_2 capture efficiency, cold gas efficiency and net efficiency. **Figure 6-1** shows the simplified flow diagrams of the six simulated cases. Detailed flowsheets for each case can be found in **Appendix C**.

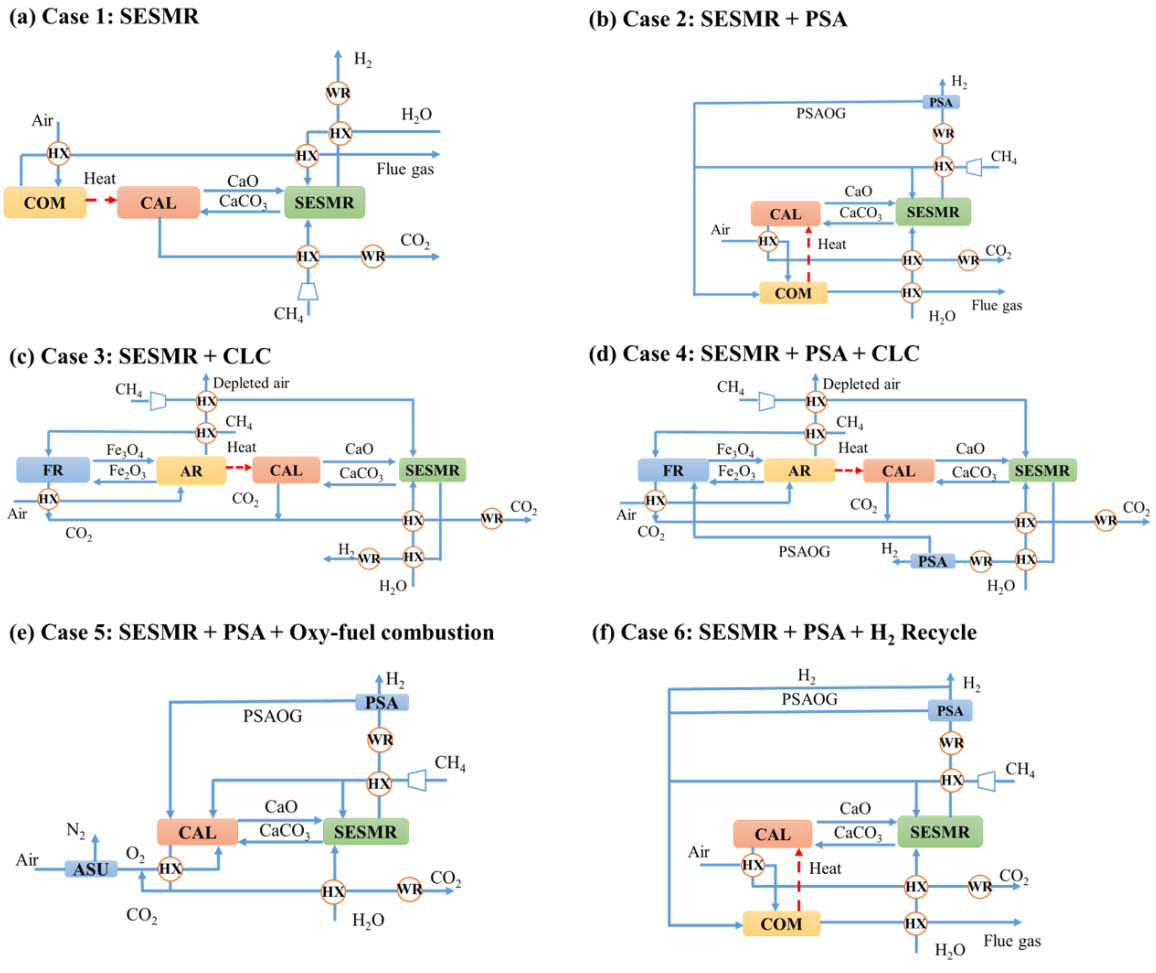

Figure 6-1 Flow diagrams of different simulated sorption enhanced steam methane reforming processes with CO_2 capture. CAL: sorbent regenerator (calciner), COM: combustor SE-SMR: sorption enhanced steam methane reformer, HX: heat exchanger, WR: water removal, PSA: pressure swing absorption unit, FR: fuel reactor, AR: air reactor, ASU: air separation unit.

6.2.1.1 Case 1: SE-SMR system

In the SE-SMR process, the compressed feed CH_4 is preheated by the heat from the CO_2 enriched gas from sorbent regenerator, and then mixed with CaO sorbent before entering the reformer with the high-temperature steam. Steam is produced from the waste heat of the reforming gas products and flue gas from an air-fired burner used for sorbent regeneration. The reformer in the SE-SMR process is a joint carbonator and reformer, which can achieve *in-situ* CO_2 separation in the presence of CaO or other CO_2 sorbents. The capture of CO_2 shifts the reforming and water-gas shift reactions in favour of more H_2 production according to Le Chatelier's principle. The produced $CaCO_3$ solids (if a CaO-based sorbents are used) are separated from gas stream and regenerated by an indirect air-fired methane calciner for a closed-loop operation. The gas product is further cooled via a cooler and water is condensed by a condenser, allowing an enriched H_2 product to be obtained. The overall SE-SMR reaction can be simplified to **Equation. (6-1)**.

$$\mathrm{CH_4} + 2\mathrm{H_2O} + \mathrm{CaO} \leftrightarrow \mathrm{CaCO_3} + 4\mathrm{H_2} \qquad \textbf{(6-1)}$$

The operating pressure of the reformer was set between 5 and 25 bar, which can be maintained by the feed pressure and adjusted by the back pressure controller of the reformer. There are two pressurised lock hoppers installed in the inlet and outlet of the calciner respectively, which can ensure the regeneration of CaO at atmospheric pressure.

6.2.1.2 Case 2: SE-SMR + PSA

In this case, the cooled and condensed H_2-enriched gas from the SE-SMR process is sent to the PSA unit at a feed pressure of 25 bar. A near pure H_2 stream is then produced from the separated product gas. The off-gas stream containing CH_4, CO, CO_2, H_2 and H_2O is sent to the air-fired burner to reduce the additional fuel requirement.

6.2.1.3 Case 3 and 4: SE-SMR +CLC without/with PSA

To avoid the release of CO_2 emissions from the calcination of $CaCO_3$, CLC has been integrated with the SE-SMR process (See **Figure 6-1**(c) and (d)). In previous work on process simulation of SE-SMR + CLC, only Ni-based oxygen carriers, which have a thermodynamic restriction in that they cannot convert fuels fully to CO_2 and H_2O, have been selected. Although the Ni-based oxygen carriers have a higher reactivity for CH_4, it is also among the most expensive of such materials and also has health, safety and environmental issues. In this work, a Fe_2O_3/Fe_3O_4 oxygen carrier supported by Al_2O_3 (15 wt %) and SiO_2 (15 wt %) has been chosen for the CLC process. Such iron based oxygen carriers have been successfully operated in different CLC pilot plants with coal, biomass, CH_4 and PSA off-gas [24,36-38]. A nickel-based CLC-SE-SMR process, is also investigated for the purpose of comparison.

The CLC unit is used to supply heat to the SE-SMR process. In Case 3, Fe_2O_3 reacts with the CH_4 in the fuel reactor (FR), and the reduced oxygen carrier – Fe_3O_4 is circulated to the air reactor (AR) and reoxidised. The reduction of Fe_2O_3 by CH_4 is endothermic (**Equation. (6-2)**), and the oxidation of Fe_3O_4 is an exothermic process (**Equation. (6-3)**). The released heat from the AR is utilised to provide the necessary heat for the calciner via a fluidised-bed heat exchanger [39] or heat pipes [40,41] as shown in **Figure 6-2**. Junk et al. [41] have conducted a technical and economical assessment of the indirectly heated carbonate looping by heat pipes, which indicates that the CO_2 avoidance costs of the indirectly heated carbonate looping by heat pipes is about € 22.6/t CO_2. This is much lower than that of oxy-fuel combustion or standard carbonate looping (€36 and €26/t CO_2). It is assumed 10% heat loss occurs during the heat transfer from the AR to the calciner, which is based on the recent testing of an indirectly heated calciner at a 300 kWth scale in Darmstadt [42,43]. The oxygen carriers and inert materials also carry the required amount of heat for CH_4 reduction in the FR as it is operated under adiabatic conditions. The heat from the depleted air from the AR and flue gas from the FR is used to preheat the CH_4 feed gas and to produce steam to the reformer. In Case 4, the PSA unit is installed after the reformer to generate high-purity H_2 and the PSA off-gas (PSAOG) is combined with CH_4, which is combusted in the FR as shown by **Equation. (6-2)**, **Equation. (6-4)** and **Equation. (6-5)**.

$$CH_4 + 12Fe_2O_3 \rightarrow CO_2 + 2H_2O + 8Fe_3O_4 \quad \textbf{(6-2)}$$

$$O_2 + 4Fe_3O_4 \rightarrow 6Fe_2O_3 \quad \textbf{(6-3)}$$

$$H_2 + 3Fe_2O_3 \rightarrow H_2O + 2Fe_3O_4 \quad \textbf{(6-4)}$$

$$CO + 3Fe_2O_3 \rightarrow CO_2 + 2Fe_3O_4 \quad \textbf{(6-5)}$$

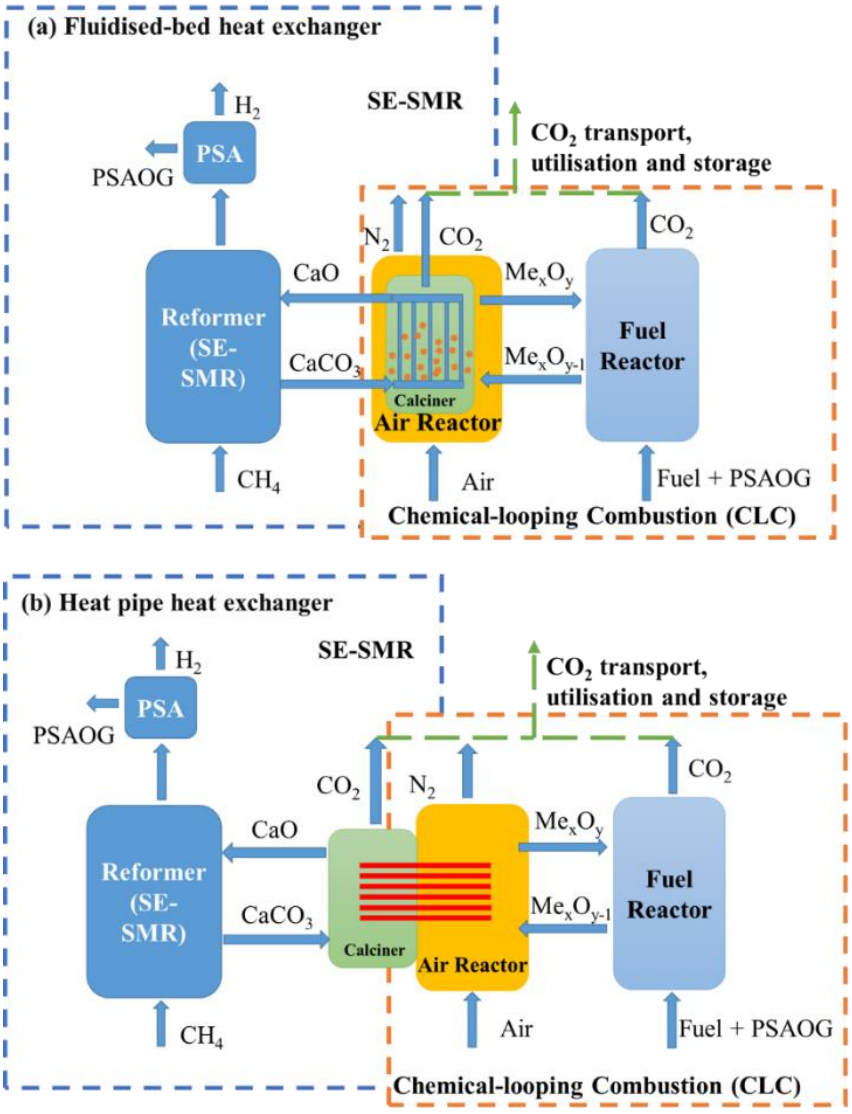

Figure 6-2 Options of heat integration between the air reactor and calciner

6.2.1.4 Case 5 and 6: SE-SMR + PSA + Oxy-fuel combustion and H_2 recycle

Due to the highly endothermic process of the CaO sorbents regeneration, i.e. calcination of $CaCO_3$, a large amount of heat is required by the calciner. To obtain high-purity CO_2 from the calciner, direct oxy-fuel combustion is used for the calcium-

looping process, which has been demonstrated at the pilot-plant scale [44,45]. In Case 5, CH_4 along with the PSAOG is introduced into the calciner and burnt in an O_2/CO_2 environment. Oxygen is produced in an Air Separation Unit (ASU) and the recirculated flue gas from the calciner is used to avoid superheated regions in the calciner, which operate at 900 °C. The high-temperature CO_2 rich gas stream leaving the calciner is utilised to preheat the fuel and steam. In Case 6, a new process integration of a H_2-fired calciner with SE-SMR is proposed to avoid the energy penalty and capital cost of the ASU. The heat from the burning of H_2 and PSAOG is transferred through the metallic walls or heat pipes or the hot solids circulating between the combustor and the calciner. The extracted heat from the flue gas of the H_2 combustor is used to preheat the steam to the reformer and the air to the combustor.

6.2.2 Process Simulation

The SE-SMR process was modelled in Aspen Plus under steady-state equilibrium conditions. The chemical equilibrium of the reformer and calciner were modelled using the RGibbs block, which minimises the Gibbs free energy of all the species. The Gibbs free energy minimisation method is based on the idea that the investigated chemical system is thermodynamically feasible when total Gibbs free energy has the lowest value and differential of Gibbs free energy is zero for current operation conditions [46,47]. Since the reformer is slightly endothermic (balanced by the exothermic carbonation reaction), the heat duty of this reactor is set to zero, therefore, the additional heat duty is nil (adiabatic). Consequently, the reformer outlet temperature is lower than the inlet. The reformer temperature reported in this paper refers to the reformer outlet temperature unless otherwise specified. **Table 6-1** shows all the thermodynamic modelling assumptions of the base model.

The heat exchanger networks are designed in order to ensure the maximum possible heat recovery, with the minimum number of heat exchangers. The steam generator is modelled with multiple zones to detect/avoid temperature crossover during the phase change. The fuel feed to the reformer is adjusted to ensure the flow rate of H_2 product is 1500 kg/h, equivalent to 50 MWth based on the lower heating value of hydrogen, for all cases. In addition, design specifications are also defined to ensure the S/C ratio is set to the desired values. The air mass flow to the air-CH_4 combustor is adjusted to ensure the excess O_2 in the flue gas stream is maintained at 5% molar basis. The flue-

gas is cooled to a minimum value of 50 °C (wherever possible) to estimate the maximum possible cold gas efficiency of the system. The carbonation efficiency of the CaO sorbent is enhanced under SE-SMR conditions (in the presence of steam and at elevated pressure), and acceptable mechanical stability of the sorbent can be achieved if the catalytic and sorbent particles are supported into combined sorbent-catalyst materials [12,48]. Based on recent long term cycling experimental results, it is estimated the average carbonation conversion of CaO sorbent during the SE-SMR process should be around 50% [12,16], this value dictates the ratio of Ca/C in the reformer and can be maintained by ensuring an effective make-up flow of the sorbent/combined particles. The pressures reported in this work are expressed as absolute pressure.

Table 6-1 Design assumptions used for developing the process flowsheet models in Aspen Plus

Parameters	Value	Unit
Reformer pressure	25	bar
Reformer temperature	600	°C
Reformer S/C	5	-
Calciner temperature	900	°C
CH_4 compressor efficiency	83	%
H_2 compressor efficiency	83	%
Water pump efficiency	83	%
Excess oxygen	5	%
Heat exchanger pinch	20	°C
Calciner heat loss	10	%
Calcination efficiency	100	%
Mechanical efficiency of pump and compressors	98	%
Fuel feed temperature	9	°C
Fuel feed pressure	1	bar

Feed water inlet temperature	20	°C
Feed water inlet pressure	1	bar
Air/oxygen temperature	25	°C
Air/oxygen pressure	1	bar

The H_2 purity of the conventional SE-SMR can be enhanced by adding a PSA unit downstream of the reformer. The off-gas from the PSA (PSAOG) contains H_2, CO, and CH_4 and is burned to partly meet the calciner heat duty. The carbon capture for the process can also be enhanced owing to the reduced fuel consumption needed to meet the heat utilities for the cycle. The PSAOG along with additional fuel (methane) is burned in air to meet the cycle utility requirement. A 95% separation efficiency for the PSA is considered reasonable. In addition, the inlet pressure to the PSA is always maintained higher than 25 bar, which is the typical operating pressure for PSA. When simulating the sensitivity study for different reformer pressures, an additional compressor is placed upstream of the PSA to match the pressure. The isentropic efficiency of the compressor is assumed to be 83% with a mechanical efficiency of 98%. The additional fuel is tuned to match the process heat utility requirement.

The SE-SMR model is integrated with CLC in Aspen Plus as shown in **Figure 6-1 (c)** and **(d)**. Both the fuel and air reactors are modelled using the RGibbs reactor. The Air Reactor (AR) supplies the calciner heat duty and the flue gas from the Fuel Reactor (FR) and AR are used to generate steam and preheat the fuel and air. Both FR and AR operate at ambient pressure. The air flow to the AR is controlled to meet 5% excess oxygen requirement at the AR outlet flue gas stream. The mass flow of the oxygen carrier is adjusted until all the hydrogen is completely burned in the FR outlet flue gas stream, and the heat load connected to them dictates the temperatures. The AR outlet temperature varies as the calciner heat-duty changes since the AR is directly coupled with the calciner and the outlet temperature of the AR flue gas is maintained higher than the calciner operating temperature (i.e. 900 °C). The fuel reactor is set as an adiabatic reactor (i.e. heat duty = 0), consequently, the FR temperature is dictated by the fuel and oxygen carrier inlet conditions. Additional methane is supplied as a fuel to the FR for this case. Since many different oxygen carriers are possible only two of the most common oxygen carriers are modelled here. Fe_2O_3 is used in all the

sensitivity studies and NiO is modelled separately to compare the performance difference to the iron-based oxygen carrier.

In Case 4, a PSA was added to the SE-SMR+CLC configuration and the PSAOG is connected to the FR to reduce the additional fuel requirement. In Case 5, SE-SMR+PSAOG configuration is integrated with oxy-combustion system to meet the heat duty of the calciner and steam generation. The 160 kWh/t of oxygen is assumed as the auxiliary power consumption of the air separator [49]. Here, 30% oxygen and 70% of CO_2 mole fraction gas is supplied to the oxy-fuel combustor. In Case 6, the SE-SMR is scaled-up in such a way that part of the product hydrogen together with the PSAOG can meet the heat utility requirement of the process. Therefore, no additional fuel is added to meet the heat utility requirement.

6.2.3 Performance Evaluation

The thermal performance of the six different cases were compared based on the five performance indexes: 1) CH_4 conversion 2) H_2 purity 3) cold gas efficiency 4) net efficiency 5) CO_2 capture efficiency. The methane conversion is calculated according to **Equation. (6-6)**, where $n_{CH4,in}$ and $n_{CH4,out}$ are the moles of methane flow at the inlet and outlet of the reformer respectively. The hydrogen purity was defined as the hydrogen mole fraction of the product stream from the plant, on a dry basis.

$$\mathrm{conv}_{\mathrm{CH_4}} = \left(1 - \frac{\mathrm{n}_{\mathrm{CH_4,out}}}{\mathrm{n}_{\mathrm{CH_4,in}}}\right) * 100\% \qquad \textbf{(6-6)}$$

The cold gas efficiency (η_{CG}) was calculated using **Equation. (6-7)** where $\dot{\mathrm{m}}_{\mathrm{H_2,product}}$, $\dot{\mathrm{m}}_{\mathrm{CH_4,feed}}$ and $\dot{\mathrm{m}}_{\mathrm{CH_4,additional}}$ are the mass flow rate of the product hydrogen, feed methane and additional methane required to meet the heat utility of the calciner and steam boiler, respectively. $\mathrm{LHV}_{\mathrm{H_2}}$ and $\mathrm{LHV}_{\mathrm{CH_4}}$ are the lower heating value of hydrogen (120 MJ/kg) and methane (50 MJ/kg), respectively.

$$\eta_{\mathrm{CG}} = \left(\frac{\dot{\mathrm{m}}_{\mathrm{H_2,product}} * \mathrm{LHV}_{\mathrm{H_2}}}{(\dot{\mathrm{m}}_{\mathrm{CH_4,feed}} + \dot{\mathrm{m}}_{\mathrm{CH_4,additional}}) * \mathrm{LHV}_{\mathrm{CH_4}}}\right) * 100\% \qquad \textbf{(6-7)}$$

The net efficiency (η_{net}) is calculated using **Equation. (6-8)**, where the electric utility ($\mathrm{P_e}$) requirement is also added to the cold gas efficiency equation. A thermal to electric conversion efficiency (η_{elect}) of 50% is utilised in this work.

$$\eta_{\text{net}} = \left(\frac{\dot{m}_{H_2,\text{product}} * \text{LHV}_{H_2}}{(\dot{m}_{CH_4,\text{feed}} + \dot{m}_{CH_4,\text{additional}}) * \text{LHV}_{CH_4} + \frac{P_e}{\eta_{\text{elect}}}} \right) * 100\% \quad \textbf{(6-8)}$$

The overall CO_2 capture efficiency is calculated using **Equation. (6-9)**, where $n_{CO_2,\text{captured}}$ is the moles of carbon capture.

$$CO_2 \text{ capture efficiency} = \left(\frac{n_{CO_2,\text{captured}}}{n_{CH_4,\text{feed}} + n_{CH_4,\text{additional}}} \right) * 100\% \quad \textbf{(6-9)}$$

6.3 Results and Discussion

6.3.1 Thermodynamic Analysis

In this section, a sensitivity analysis including the effects of reforming temperature, reforming pressure and S/C ratio (molar ratio of steam to carbon) on the performance of the above cases was conducted to investigate the optimal operating conditions and process configurations for the low-carbon and high-purity hydrogen production.

6.3.1.1 Effect of Reforming Temperature

The effect of the reformer temperature on the six different cases are plotted in **Figure 6-3**. Since the reformer is slightly endothermic, increasing the temperature also favours the forward reaction following Le Chatelier's principle. In the base case (Case 1), the methane conversion changes linearly from 83.7% at 500 °C to 87.1% at 700 °C. In addition, the hydrogen purity also increases slightly from 95.3% to 95.9% until 650 °C and then begins to drop at 700 °C by 0.1% points. Since the methane conversion increases with the reformer temperature, the fuel feed reduces linearly in order to achieve a 50 MWth plant output, reducing the fuel compressor power. This also implies that the steam flow rate reduces linearly in order to maintain the desired S/C ratio in the reformer inlet, lowering the pump power requirement. The reduction of the feed flow rate is roughly compensated by the increase in the methane conversion at a higher reformer temperature, consequently, the sorbent flow rate reduces by about only 0.5% when the reformer temperature increases from 500 °C to 650 °C. At 700 °C, the sorbent flow rate reduced by 1.5% in order to minimise the reformer Gibbs free energy. Furthermore, the calciner heat duty declines owing to the narrow temperature window at a higher reformer temperature. The additional methane required to meet the process heat utility is also reduced by about 1.6% at 700 °C reformer temperature owing to the reduced heat utility. The overall CO_2 capture

efficiency is driven by the efficiency of the in-situ reformer carbon capture and the carbon capture of the additional fuel firing. The latter is not captured in Case 1, therefore, the overall CO_2 capture efficiency is expected to increase with the increase in the reformer temperature owing to the reduction in the fuel inlet flow rate. However, the in-situ CO_2 capture efficiency of the reformer reduces significantly after 650 °C. Finally, the CO_2 capture efficiency increases from 57.6% to 58.6% when the reformer temperature increases from 500 °C to 650 °C and decreases to 58.1% at 700 °C owing to the reduction in the carbonation efficiency. The cold gas efficiency linearly increases with the reformer temperature owing to the increase of methane conversion, which subsequently reduces the feed flow, steam flow, the calciner heat duty. In addition, the net efficiency also linearly increased with the reformer temperature with the negative offset from the cold gas efficiency due to the natural gas compressor and water pump power consumption (1.6% points).

Adding a PSA (Case 2) increases the hydrogen purity close to 100% and utilising the PSAOG to provide the process heat improves the efficiency and the amount of CO_2 captured. The methane conversion in Case 2 follows the same trend as Case 1 since the reformer boundary conditions are unaffected. The heating value of the PSAOG depends on the methane conversion of the reformer. The in-situ carbon capture efficiency of the reformer follows a similar trend as Case 1, i.e. the CO_2 capture efficiency declines after 650 °C, with the positive offset of 9% points at 700 °C and 10.3% points at 500 °C. In addition, the cold gas efficiency is increased by 0.8% points due to the increase in PSAOG heating value as the methane conversion increases by 3.3% points. The difference between the cold gas efficiency and net efficiency is 2.1% points for all temperatures.

In Case 3, a CLC process is added in the additional fuel firing circuit but does not include a PSA in the overall plant layout. Therefore, the trend of methane conversion and hydrogen purity are the same as in Case 1 as the boundary conditions to the reformer are unaffected. The CO_2 capture efficiency is higher than both Case 1 and 2 as the CO_2 evolved from firing the additional fuel is also captured. The CO_2 capture efficiency trend is similar to Case 1 with a positive offset and it reached the maximum value of 90.2% at 650 °C and declined to 89.8% at 700 °C. Although the cold gas efficiency trend is similar to Case 1, the absolute values were lower by 0.6% points for all the temperatures. This is due to the inefficiency in handling the heat from both fuel

and air reactors as the heat network was optimised to extract heat from single flue gas stream from the combustor. Advanced heat exchanger network design could bridge this gap with additional capital cost. The same is also true for the net efficiency trend, which was negatively offset by 1% points for all the temperatures.

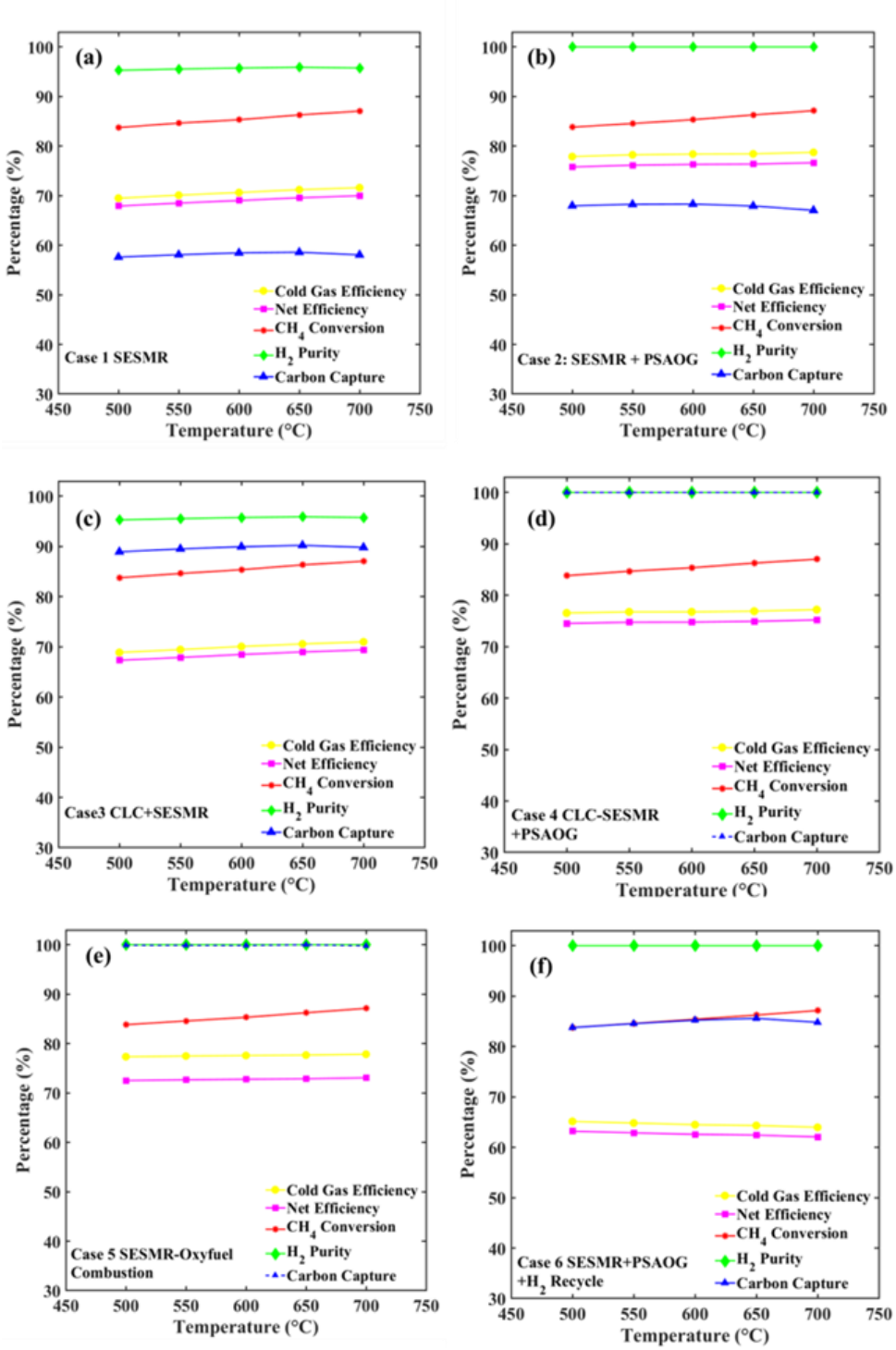

Figure 6-3 Process performance for different reforming temperatures. (a) Case 1 SE-SMR, (b) Case 2 SE-SMR+PSAOG, (c) Case 3 CLC+SE-SMR, (d) Case 4 CLC+SE-SMR+PSAOG, (e) Case 5 SE-SMR+Oxy-fuel combustion, (f) Case 6 SE-SMR+H_2 recycle

The performance trend of Case 4 is shown in **Figure 6-3 (d)** and it can be observed that the methane conversion is the same as Case 1 whilst the hydrogen purity is near 100% for all the temperatures due to the presence of PSA. The CO_2 capture efficiency is also close to 100% for all temperatures owing to the combination of PSAOG and CLC. The cold gas efficiency and the net efficiency trends are similar to Case 2 with the negative offset of 1.5% points. For the oxy-combustion with PSAOG scenario (Case 5), the carbon conversion is similar to Case 1 and the hydrogen purity reaches near 100% for all temperature. The carbon capture efficiency also reaches nearly 100% as shown in **Figure 6-3 (e)**. The cold gas efficiency is about the same as Case 2 whereas the net efficiency is lower by about 3.3% due to the auxiliary power consumption of air separation unit.

In Case 6, the methane conversion is similar to Case 2 and the hydrogen purity reaches ~100%. The CO_2 capture efficiency trend is similar to Case 2 with the positive offset. The increase in the CO_2 capture efficiency is due to the use of additional carbon free fuel (product hydrogen) to meet the heat requirement. However, the maximum carbon capture is 85.6% at a 650 °C reformer temperature. A further increase of reformer temperature to 700 °C reduced the CO_2 capture efficiency by 0.8% points. The CO_2 capture efficiency is limited by the methane conversion ratio and the in-situ carbon capture efficiency in the reformer. However, this increase in CO_2 capture efficiency comes at the expense of the process cold gas efficiency. Since the heat content of the product hydrogen from an SE-SMR is lower than the heat content of the feed methane by the factor related to its cold gas efficiency, switching the additional fuel (methane) to product hydrogen is associated with penalties in terms of the process efficiency of the same magnitude. The cold gas efficiency of Case 6 is lower than Case 2 by 12.7% at 500 °C and 14.8% at 700 °C. The fuel feed increases by 0.4% with the reformer temperature in order to maintain the fixed H_2 output, which is opposite to Case 2. Nevertheless, the calciner heat duty declines owing to the reduced temperature window at higher reformer temperatures.

6.3.1.2 Effect of Reforming Pressure

The sensitivity of reformer pressure was investigated for all six cases and the results are presented in **Figure 6-4**. For Case 1, the methane conversion declines with a pressure increase according to Le Chatelier's principle. This affects the hydrogen

purity, which reduces by 2.7% points with a pressure increase from 5 bar to 25 bar. The maximum hydrogen purity is 98.4% at 5 bar. The fuel feed increases with the reformer pressure by 11.5% from 5 bar to 25 bar to maintain the plant capacity at 50 MWth with the lower methane conversion. This also increases the steam flow by the same order to maintain the S/C ratio constant. Since the methane conversion is lower at higher pressure the methane mole fraction in the product stream increases from 1.2% to 4.1% when the reformer pressure increases from 5 bar to 25 bar. This together with the effect of increasing fuel inlet flow rate to meet the increased heat requirement reduces the CO_2 capture efficiency at higher pressures. Although the specific energy required to heat the water from 9 °C to 600 °C reduces at a higher pressure owing to the reduced latent heat, the increased steam flow rate dominates, thus increased the heat requirement. The cold gas efficiency decreases at higher pressure owing to the higher additional fuel requirement. The difference between cold gas efficiency and net efficiency increases from 0.8% points at 5 bar to 1.6% points at 25 bar, owing to the increase electrical power at higher pressures.

In Case 2, the methane conversion is the same as Case 1. The hydrogen purity is nearly 100% for all pressures. Since the separation efficiency of the PSA is 95%, the fuel feed in Case 2 is higher than that of Case 1 by the same factor. Because of the lower methane conversion ratio at a higher pressures, the PSAOG mass flow is higher and this reduces the fuel inlet flow rate by 28.8% when the reformer pressure is increased from 5 bar to 25 bar. On the other hand, the fuel feed is increased by 11.5% owing to the reduced methane conversion. As a result, the CO_2 capture efficiency reduces at higher pressures by 6.2% due to the reduced methane conversion. The cold gas efficiency roughly remains constant with pressure as the reduction in the additional fuel is compensated by the increased fuel feed. However, the net efficiency is penalised and reduced at lower pressures owing to the pressurisation of the PSA upstream fluid to 25 bar. At 25 bar, the difference between cold gas efficiency and net efficiency is 2% points which increases to 4% points at 5 bar. Therefore, a 25 bar pressure is preferred in this case as this also eliminates the compressor needed to achieve 25 bar for the PSA.

Adding a CLC to Case 1 (Case 3) does not appear to affect the trend of methane conversion and hydrogen purity, which are the same as Case 1. The CO_2 capture efficiency declines with increasing pressure and a maximum capture of 95.9% is

achieved at 5 bar. This is because the fuel supply required to meet the process utility is the smallest at lower pressure owing to the lower steam and fuel inlet flow rate at lower pressure. The cold gas efficiency is similar to Case 2 but lower by 0.5% points. This difference is due to the limitation of extracting heat with the current heat exchanger design and this could ideally be eliminated with the addition of heat exchangers. The difference between net efficiency and cold gas efficiency is 4% points at 5 bar, which reduces to 2% points at 25 bar. For Case 5, the methane conversion is similar to Case 2. The hydrogen purity and the CO_2 capture efficiency are nearly 100%. The cold gas efficiency is same as Case 2 for all pressures. However, the net efficiency is lower by 2.7% points than Case 2 for all pressures due to the auxiliary power consumption of an air separation unit.

In Case 6, the CO_2 capture efficiency reaches 94.2% at 5 bar which is an increase of 21.5% points from Case 2. The CO_2 capture efficiency reduces with increasing pressure owing to the increased PSAOG caused by the reduced methane conversion. Since this configuration does not add any additional infrastructure to capture the CO_2, the capital cost of this case is expected to be lower. However, the increased CO_2 capture efficiency comes with the trade-off in the net efficiency, which increases the operational cost. The cold gas efficiency is lower than Case 2 by 27.2% points at 5 bar whilst it is lower by 19.9% points at 25 bar. Therefore, a techno-economic assessment is essential to evaluate whether the increased CO_2 capture efficiency at a lower capital cost outweighs the increased operational cost.

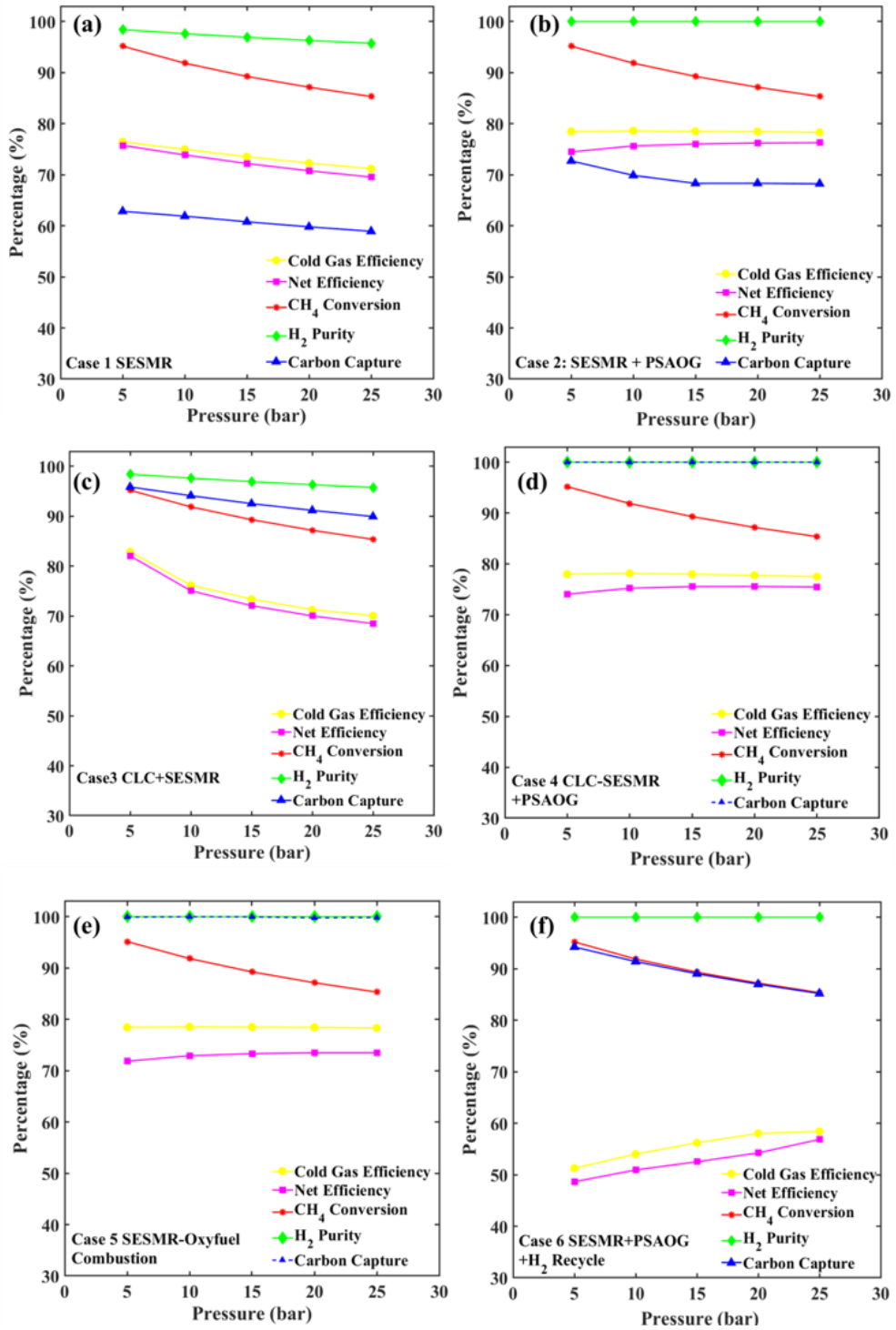

Figure 6-4 Process performance for different reforming pressures. (a) Case 1 SE-SMR, (b) Case 2 SE-SMR+PSAOG, (c) Case 3 CLC+SE-SMR, (d) Case 4 CLC+SE-SMR+PSAOG, (e) Case 5 SE-SMR+Oxy-fuel Combustion, (f) Case 6 SE-SMR+H_2 Recycle.

6.3.1.3 Effect of Steam to Carbon (S/C) Ratio

The effects of different S/C ratios on the process performance are shown in **Figure 6-5**. The increase in the reactant concentration favours the forward reaction according to Le Chatelier's principle in consequence increasing the methane conversion. The methane conversion increases from 67.3% to 85.3% for a corresponding increase in S/C ratio from 3 to 5 for all the cases when the reformer condition is 25 bar and 600 °C. The hydrogen purity of Case 1 increases from 89.1% to 95.7% with the S/C ratio. Since the methane conversion increases with the S/C ratio, the fuel feed to meet 50 MW_{th} plant capacity is reduced. However, the steam mass flow rate must increase to meet the increasing S/C ratio set point, which also increases the heat utility to the process, thereby raising the fuel supply by 3.3%. The number of carbon moles in the reformer outlet stream reduces with the increase in S/C ratio, owing to the increase in CH_4 conversion and subsequent capture of CO_2 by the sorbent. Since the reformer in-situ CO_2 capture efficiency remains the same, the overall carbon capture efficiency has to increase with the S/C ratio. On the other hand, the additional fuel input required to meet the process heat utility also increases with S/C ratio by 3.3%. However, the effect of the latter is minimal, consequently the CO_2 capture efficiency increases at a higher S/C ratio from 49.8% to 58.5%. In addition, the cold gas efficiency also increases from 60.2% to 70.6% owing to the higher methane conversion. The difference between cold gas efficiency and the net efficiency increases from 1.5% points to 1.6% points when the S/C increases from 3 to 5.

When the PSA is added to the system (Case 2), the hydrogen purity of the product stream reaches nearly 100%. The methane conversion is the same as Case 1, which increases by 18% points when the S/C ratio changes from 3 to 5. This also reduces the fuel feed by 21% in order to maintain the plant capacity, however, the steam flow increases by 31.5% to meet the higher S/C ratio target. Subsequently, the heat duty increases at higher S/C, which demands higher additional fuel use. The PSAOG itself can satisfy the heat utility of the process when the S/C ratio is 3 and 26% of the fuel feed is required as an additional fuel to meet the heat load when S/C ratio is 5. It is worth highlighting that the heat content of PSAOG is surplus to the process heat utility when S/C ratio is 3, therefore, the carbon capture (1% point) and the cold gas efficiency (1.1% point) are lower compared with the S/C ratio of 3.5. This also suggests that, at some S/C ratio between 3 and 3.5 the PSAOG can exactly satisfy the heat

utility of the process, offering slightly higher carbon capture and cold gas efficiency than the values presented for S/C ratio of 3.5. When the S/C ratio increases from 3.5 to 5, the CO_2 capture efficiency and cold gas efficiency reduce from 68.3% to 67.6% and from 78.4% to 77.6%, respectively. The difference between cold gas efficiency and net efficiency decreases with S/C ratio from 2.5% points (S/C=3) to 2% points (S/C=5) which is not significant therefore the efficiency can be considered to be insensitive to the changes in S/C. The cold gas efficiency of Case 2 is higher than Case 1 by 7% points with a CO_2 capture efficiency increase of 9.1% points when the S/C ratio is 5.

With the addition of CLC to Case 1 (Case 3), the carbon capture increases from 58.5% to 89.9% at S/C=5 without any impact on the hydrogen purity. The cold gas efficiency reduces by 0.6% points compared to Case 1 and is thus ensued by the current heat integration system. The penalty in the efficiency could theoretically be eliminated by increasing the number of heat exchangers and splitting the flow streams to minimise the exergy loss. The integration of CLC to Case 2 (Case 4) increases the carbon capture efficiency from 67.6% to nearly 100% and the hydrogen purity increased to nearly 100%. The cold gas efficiency trend is similar to Case 2 with the negative offset of 0.6% points caused by the limitation of the current heat exchanger network design. Integration of oxy-combustion to Case 2 (Case 5) for calciner heat duty was shown to achieve nearly 100% CO_2 capture efficiency and hydrogen purity. The cold gas efficiency is same as Case 2 whilst the net efficiency is negatively offset by 2.7% points due to the power consumption of air separation unit. It should be noted that the process is almost independent of S/C ratio when integrated with CLC+PSAOG (Case 4) and Oxy-combustion (Case 6).

In Case 6, the hydrogen purity is ~100% for all values of S/C ratio. Despite the increase of methane conversion at a higher S/C ratio, the fuel feed also increases by 7.8% when the S/C ratio increases from 3 to 5 to meet the plant capacity of 50 MWth by satisfying the heat utility. The steam flow rate increases with the S/C ratio by 79.9% thus the heat utility increases. The increase of the fuel feed at higher S/C ratio, where the methane conversion is higher, to meet the heat utility, also increases the sorbent flow given the calciner heat duty (36.8%). Here, 18.3 MWth (36.6% of the product hydrogen) is supplied as the additional fuel to meet the process heat demand for a S/C ratio of 5 which is 37.7% higher than the additional heat supplied to Case 2. In

consequence, the cold gas efficiency reduces by 13% points compared with Case 2 for a S/C ratio of 5. In addition, the cold gas efficiency reduces from 77.3% to 64.6% when the S/C ratio increases from 3 to 5. The carbon capture efficiency on the other hand increases from 67.3% to 85.3% as the methane conversion is higher and the product hydrogen is supplied as an additional fuel.

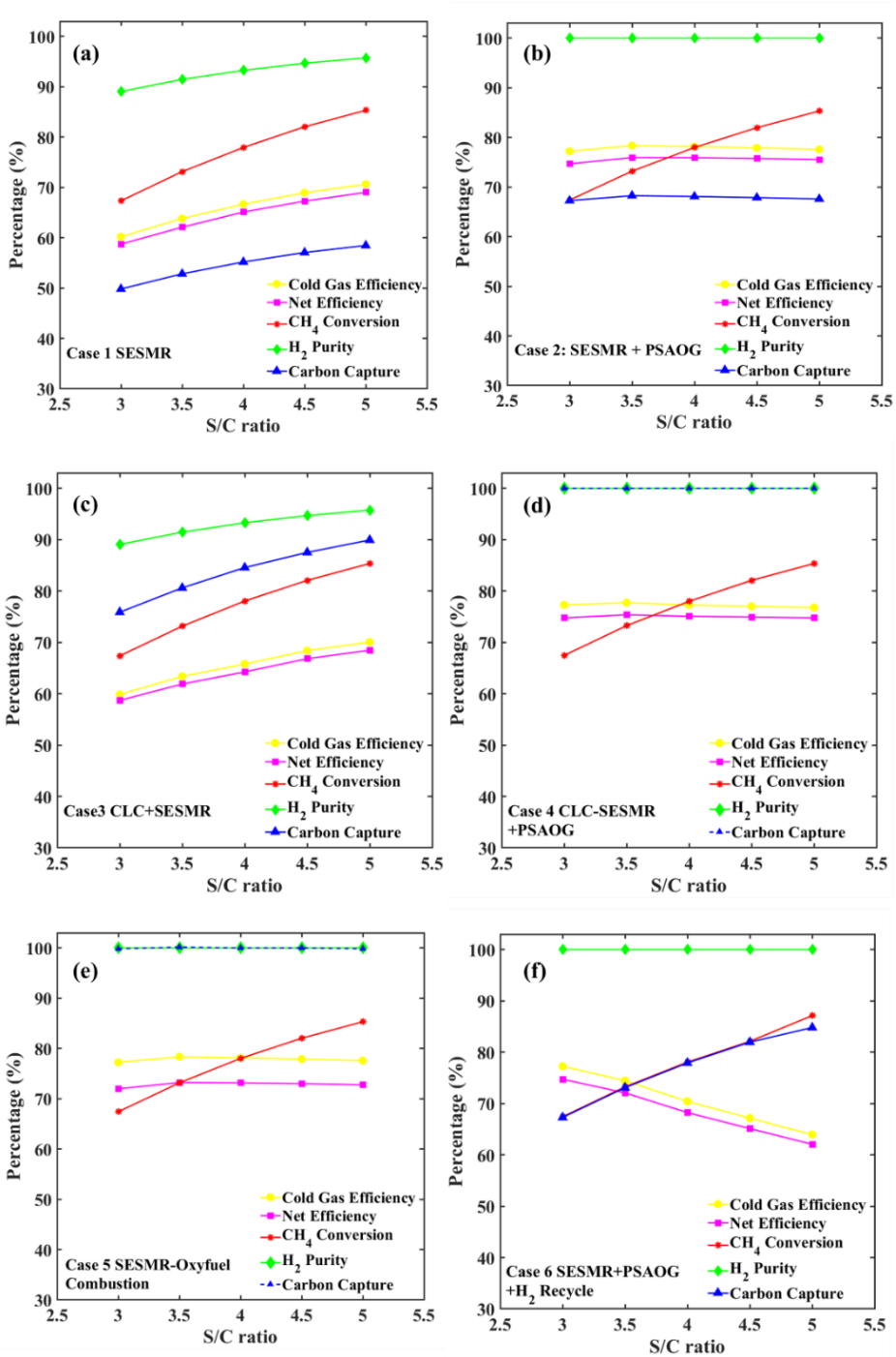

Figure 6-5 Process performance for different S/C ratios. (a) Case 1 SE-SMR, (b) Case 2 SE-SMR+PSAOG, (c) Case 3 CLC+SE-SMR, (d) Case 4 CLC+SE-SMR+PSAOG, (e) Case 5 SE-SMR+Oxy-fuel Combustion, (f) Case 6 SE-SMR+H_2 Recycle.

6.3.1.4 Effect of Oxygen Carriers

In Case 3 and 4, it is necessary to ensure the fuel is fully converted in the FR and the oxidation of reduced oxygen carriers in the AR can provide enough heat for calciner in the SE-SMR. A sensitivity analysis of the molar ratio of NiO and Fe_2O_3 with fuel (CH_4, CO and H_2) on the performance of Case 4 is investigated**. Figure 6-6** indicates the relationship between NiO and Fe_2O_3/fuel ratio and the performance of FR. The CO_2 concentration, carbon and hydrogen conversion of the FR increase with the increase of the both NiO and Fe_2O_3/fuel ratio. When the NiO and Fe_2O_3/fuel ratio reach the stoichiometric number of 4 and 9 respectively, the CO_2 concentration, carbon and hydrogen conversion of the FR remain stable and close to 100%.

Table 6-2 shows the performance of SE-SMR+PSA+CLC with NiO/Ni and Fe_2O_3/Fe_3O_4 at the conditions of reformer at 600 °C, 25 bar and S/C = 5. The CH_4 conversion of the reformer, cold gas efficiency and H_2 purity of both processes are the same. The main difference is the fuel conversion in the FR and total CO_2 capture. In the Ni-based oxygen carrier system, the maximum fuel conversion in the FR and total CO_2 capture are 98.6% and 99.4% respectively, while that of Fe-CLC+SE-SMR+PSA are 100.0% and 99.8% respectively. It is clear that the Fe-CLC+SE-SMR+PSA does not have the thermodynamic limitation of the fuel conversion and is able to capture the almost all of the CO_2 emissions from the CH_4 compared to a Ni-based process.

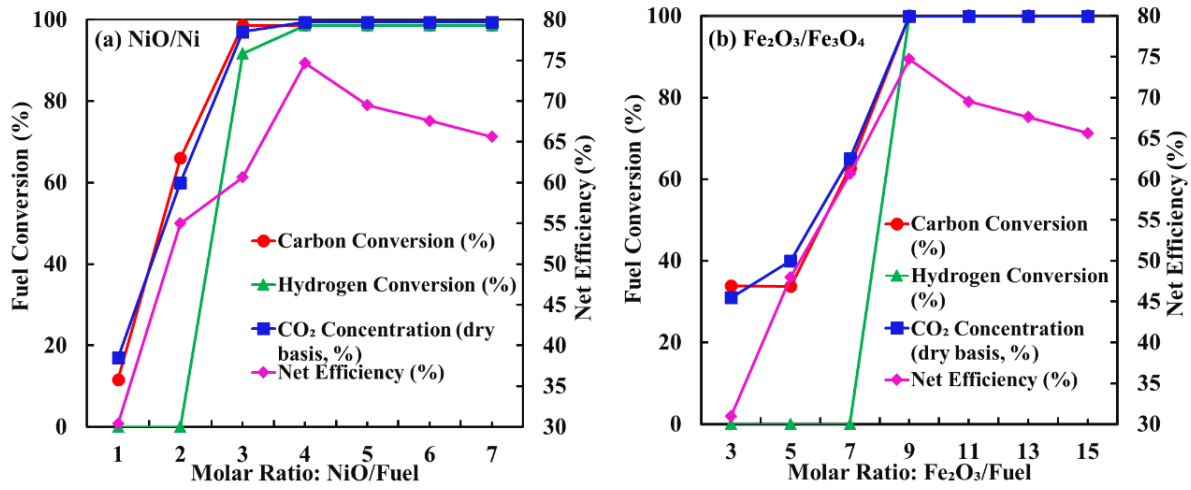

Figure 6-6 Effect of NiO and Fe_2O_3/fuel on performance of FR in Case 4.

Table 6-2 The performance of SE-SMR+PSA+CLC with different oxygen carriers. (Reformer operated at 600 °C, 25 bar and S/C = 5).

Performance	Ni-CLC+SE-SMR+PSA	Fe-CLC+SE-SMR+PSA
CH_4 conversion (%)	85.4	85.4
H_2 purity (%)	100	100
CO_2 capture (%)	99.4	99.8
Fuel conversion in FR (%)	98.6	100.0
Cold gas efficiency (%)	76.8	76.8
Net efficiency (%)	74.7	74.8
Mass flow rate of oxygen carriers to the FR (kg/s)	89.1	119.5

6.3.2 Discussion

In this work, we have proposed and compared six different SE-SMR systems for low-carbon and high-purity hydrogen production. The optimal operating conditions to achieve maximum CO_2 capture and H_2 purity from the parametric sensitivity analysis for each process is shown in **Table 6-3**. The conventional SE-SMR process (Case 1) can achieve a maximum CO_2 capture efficiency of 63% with a H_2 purity of 98% at 600 °C, 5 bar and S/C = 5. The H_2 purity in Case 1 suffices for gas turbines, refinery processes and industrial boilers, but it does not meet the requirements of high-purity H_2 applications such as fuel cells. The integration of a PSA with SE-SMR system can improve the H_2 purity from 98% (Case 1 and 3) to nearly 100% (Case 2 and 4), and increase the total CO_2 capture efficiency by 5-6%. However, only Case 4 (SE-SMR+PSA+CLC) and Case 5 (SE-SMR+PSA+Oxy-fuel combustion) can achieve the highest CO_2 capture efficiency (~100%) together with the highest H_2 purity, but the net efficiency of Case 5 drops by 2.7% points compared to Case 2. The combustion of recycled H_2 product with PSAOG to indirectly heat the calciner (Case 6) can generate a pure H_2 product with 94.2% CO_2 capture (5 bar, 600 °C and S/C = 5), but it has the lowest net efficiency, which increases the operational cost of the system. However, Case 6 does not have any additional components added for carbon capture, therefore

the capital cost could be significantly lower than other alternatives to achieve ~95% carbon capture efficiency. On the other hand, the thermodynamic optimal SE-SMR configuration for blue hydrogen production with ~100% CO_2 capture efficiency is the configuration combining an integrated CLC with SE-SMR + PSA (Case 4), which is 2.7% points higher in terms of net efficiency than that for Case 5. However, an economic study is needed to select the optimal configuration to achieve near 100% carbon capture efficiency.

Additionally, the best performance of Cases 2, 4, 5 and 6 is compared with literature results for SMR and SE-SMR processes integrated with CO_2 capture technologies in **Figure** 6-7**.** It can be observed that only the CLC+SMR+PSA, SE-SMR+PSA+Oxy-fuel (Case 5) and SE-SMR+PSA+CLC systems (Case 4) are capable of achieving blue hydrogen production without sacrificing the cold gas and net efficiency of conventional SMR technology. Compared to the above processes, the configuration of SMR+MEA+PSA can only capture 90 % CO_2 emission with the lower CH_4 conversion and cold gas efficiency. It is also worth noting that the SE-SMR has a joint reformer and water-gas shift reactor and its H_2 purity from the reformer to the PSA unit is much higher (98%) than that of SMR, which means lower operational expenditure and a reduced energy penalty from the PSA system [50].

Currently, the overall technology readiness level (TRL) for CLC is estimated as TRL 6, and a large number of materials have been successfully tested in continuous operation in CLC facilities from 0.3 kW_{th} to 1 MW_{th} worldwide [51]. The current TRL for SE-SMR is at 4, and it has been intensively investigated from the batch-scale to the lab-scale reactors [8,10,11,52]. A 1.5 MW_{th} SE-SMR pilot plant funded by UK Department for Business, Energy and Industrial Strategy's Energy Innovation Programme will be constructed at Cranfield University to identify pathways to accelerate the development of SE-SMR technology [53].

Table 6-3 Optimal design space for each SE-SMR process.

Case No.	Reforming temperature (°C)	Reforming pressure (bar)	S/C	CO_2 capture (%)	H_2 purity (%)	Net efficiency (%)
1	600-650	5	5	63	98	76
2	<650	5 (maximises CO_2 capture efficiency) 25 (maximises efficiency)	Independent	69	100	75
3	600-650	5	5	95	98	72
4	<650	25 (eliminates a compressor, efficiency change is negligible)	Independent	100	100	76
5	<650	25 (eliminates a compressor, efficiency change is negligible)	Independent	100	100	74

6	<650	5 (maximises CO_2 capture efficiency) 25 (maximises efficiency)	5 (maximises CO_2 capture efficiency) 3 (maximises efficiency)	87	100	62

Although the development in CLC and SE-SMR is promising, there are some obvious challenges with the concept of SE-SMR combined with CLC. Firstly, the heat transfer between the AR to the calciner through the fluidised-bed heat exchanger or heat pipes is at a very early stage. There are some undergoing projects, such as ANICA [58] and HyPER[59], are investigating the performance of indirectly heated calciner at pilot-scale. More work is required to design and test the feasibility of a calciner thermally coupled with the AR using tubes or pipes without influencing the fluidisation and circulation of sorbents and oxygen carriers. Secondly, the different lifetimes and performance of sorbents and oxygen carriers may increase the maintenance and add some operational challenges and costs. Moreover, while there are many economic evaluations of SMR with carbon capture technologies, there is no available information for the SE-SMR+PSA+CLC and SE-SMR+Oxy-fuel combustion systems. Thus, a detailed economic assessment is required to fully understand the potential of this concept at larger scales.

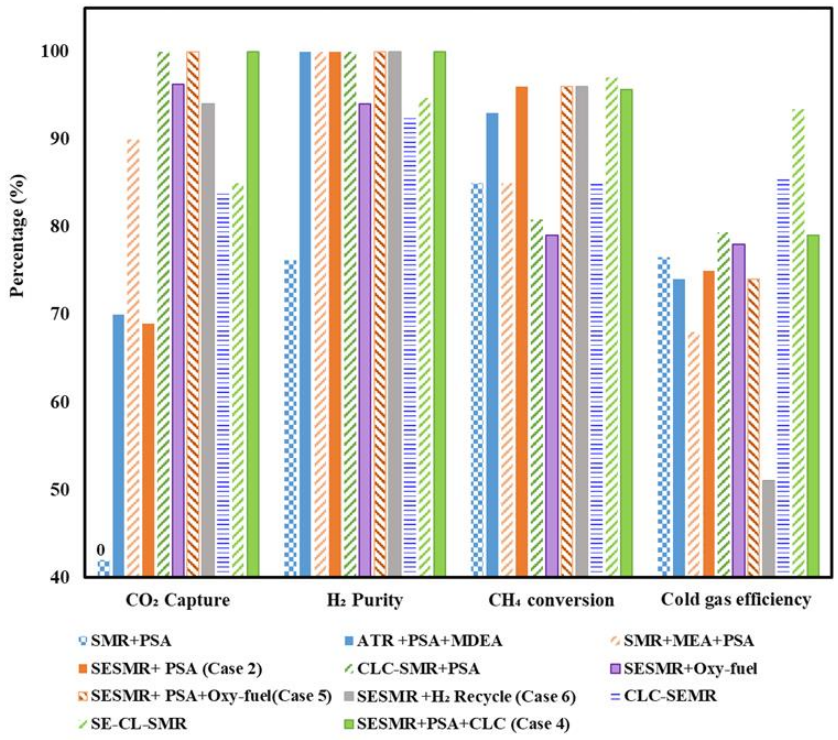

Figure 6-7 Comparison of proposed SE-SMR+PSA+CLC with the reported steam methane reforming processes in literature: SMR+PSA [17], ATR+PSA+MDEA [56,57], SMR+MEA+PSA [58], CLC+SMR+PSA [39], SE-SMR+Oxy-fuel [59], CLC+SE-SMR [26], SE-CL-SMR [60].

6.4 Conclusions

This work evaluates the competitiveness of six different sorption enhanced steam methane reforming (SE-SMR) configurations for clean hydrogen production. A thermodynamic analysis using Aspen Plus with a detailed heat exchanger modelling to recover the waste heat from the process respecting the second-law of thermodynamic, was used to evaluate the process performance of methane conversion, CO_2 capture efficiency, H_2 purity, maximum cold gas efficiency and net efficiency.

A parametric analysis was conducted to optimise operating process conditions considering the effects of reforming temperature, reforming pressure and S/C ratio on the process performance. The results indicate that the proposed cases in this work can provide flexible options for low-carbon hydrogen production based on the costs and demand of CO_2 reduction. The process of SE-SMR+PSA+CLC can realise nearly

100% CO_2 capture efficiency with the highest net efficiency of 75.5% in terms of near pure hydrogen production at a reformer temperature of 600 °C, a reformer pressure of 25 bar, and a S/C = 5, whilst the integration of oxy-combustion achieves the same CO_2 capture efficiency with nearly 100% hydrogen purity but with a 2.7% points penalty in the net efficiency. On the other hand, Case 6 where a proportion of the H_2 is recycled to provide heat for the calcination is able to achieve 94.2% carbon capture efficiency with a trade-off in the process efficiency.

In addition, utilisation of the PSAOG in Cases 2, 4 and 5 makes the CO_2 capture efficiency and cold gas efficiency independent of S/C, which could offer a large operational flexibility with a higher efficiency. The SE-SMR with the PSAOG case (Case 2) can be designed not to need additional fuel to meet the process heat utility when the S/C is between 3-3.5.

6.5 References

[1] IEA. The Future of Hydrogen. 2019. doi:10.1787/1e0514c4-en.

[2] Khojasteh Salkuyeh Y, Saville BA, MacLean HL. Techno-economic analysis and life cycle assessment of hydrogen production from natural gas using current and emerging technologies. Int. J. Hydrogen. Energy 2017;42:18894–909. doi:10.1016/j.ijhydene.2017.05.219.

[3] Clough PT, Boot-Handford ME, Zheng L, Zhang Z, Fennell PS. Hydrogen production by sorption enhanced steam reforming (SESR) of biomass in a fluidised-bed reactor using combined multifunctional particles. Materials (Basel) 2018;11. doi:10.3390/ma11050859.

[4] Rostrup-Nielsen JR. Catalytic Steam Reforming, 1984, p. 1–117. doi:10.1007/978-3-642-93247-2_1.

[5] Williams R. Hydrogen production. 1930. US1938202A

[6] Goria E, Gia P, Retaick WB. United States Patent Office 3,108,857 Method for the Production of Hydrogen. 1963.

[7] Ortiz AL, Harrison DP. Hydrogen production using sorption-enhanced reaction. Ind. Eng. Chem. Res., vol. 40, 2001, p. 5102–9. doi:10.1021/ie001009c.

[8] Johnsen K, Ryu HJ, Grace JR, Lim CJ. Sorption-enhanced steam reforming of methane in a fluidized bed reactor with dolomite as CO_2-acceptor. Chem Eng Sci 2006;61:1195–202. doi:10.1016/j.ces.2005.08.022.

[9] García-Lario AL, Aznar M, Martinez I, Grasa GS, Murillo R. Experimental study of the application of a NiO/$NiAl_2O_4$ catalyst and a CaO-based synthetic sorbent on the Sorption Enhanced Reforming process. Int. J. Hydrogen. Energy. 2015;40:219–32. doi:10.1016/j.ijhydene.2014.10.033.

[10] Arstad B, Prostak J, Blom R. Continuous hydrogen production by sorption enhanced steam methane reforming (SE-SMR) in a circulating fluidized bed reactor: Sorbent to catalyst ratio dependencies. Chem Eng J 2012;189–190:413–21. doi:10.1016/j.cej.2012.02.057.

[11] Li ZS, Cai NS, Yang JB. Continuous production of hydrogen from sorption-enhanced steam methane reforming in two parallel fixed-bed reactors operated in a cyclic manner. Ind Eng Chem Res 2006;45:8788–93. doi:10.1021/ie061010x.

[12] Di Giuliano A, Gallucci K, Kazi SS, Giancaterino F, Di Carlo A, Courson C, et al. Development of Ni- and CaO-based mono- and bi-functional catalyst and sorbent materials for Sorption Enhanced Steam Methane Reforming: Performance over 200 cycles and attrition tests. Fuel Process Technol 2019;195:106160. doi:10.1016/j.fuproc.2019.106160.

[13] Di Felice L, Kazi SS, Sørby MH, Martinez I, Grasa G, Maury D, et al. Combined sorbent and catalyst material for sorption enhanced reforming of methane under cyclic regeneration in presence of H_2O and CO_2. Fuel Process Technol 2019;183:35–47. doi:10.1016/j.fuproc.2018.10.012.

[14] Harrison DP. Sorption-enhanced hydrogen production: A review. Ind. Eng. Chem. Res., vol. 47, American Chemical Society; 2008, p. 6486–501. doi:10.1021/ie800298z.

[15] Di Giuliano A, Gallucci K. Sorption enhanced steam methane reforming based on nickel and calcium looping: a review. Chem Eng Process - Process Intensif 2018;130:240–52. doi:10.1016/j.cep.2018.06.021.

[16] Broda M, Manovic V, Imtiaz Q, Kierzkowska AM, Anthony EJ, Müller CR. High-purity hydrogen via the sorption-enhanced steam methane reforming reaction over a synthetic CaO-based sorbent and a Ni catalyst. Environ Sci Technol 2013;47:6007–14. doi:10.1021/es305113p.

[17] Ochoa-Fernández E, Haugen G, Zhao T, Rønning M, Aartun I, Børresen B, et al. Process design simulation of H_2 production by sorption enhanced steam methane reforming: evaluation of potential CO_2 acceptors. Green Chem 2007;9:654–62. doi:10.1039/B614270B.

[18] Mattisson T, Lyngfelt A, Leion H. Chemical-looping with oxygen uncoupling for combustion of solid fuels. Int J Greenh Gas Control 2009;3:11–9. doi:10.1016/J.IJGGC.2008.06.002.

[19] Mukherjee S, Kumar P, Yang A, Fennell P. Energy and exergy analysis of chemical looping combustion technology and comparison with pre-combustion and oxy-fuel combustion technologies for CO_2 capture. J Environ Chem Eng 2015;3:2104–14. doi:10.1016/J.JECE.2015.07.018.

[20] Bui M, Adjiman CS, Bardow A, Anthony EJ, Boston A, Brown S, et al. Carbon capture and storage (CCS): The way forward. Energy Environ Sci 2018;11:1062–176. doi:10.1039/c7ee02342a.

[21] Ishida M, Jin H. A new advanced power-generation system using chemical-looping combustion. Energy 1994;19:415–22. doi:10.1016/0360-5442(94)90120-1.

[22] Lyngfelt A, Leckner B, Mattisson T. A fluidized-bed combustion process with inherent CO_2 separation; application of chemical-looping combustion. Chem Eng Sci 2001;56:3101–13. doi:10.1016/S0009-2509(01)00007-0.

[23] Rydén M, Lyngfelt A. Using steam reforming to produce hydrogen with carbon dioxide capture by chemical-looping combustion. Int. J. Hydrogen. Energy. 2006;31:1271–83. doi:10.1016/J.IJHYDENE.2005.12.003.

[24] Ortiz M, Gayán P, De Diego LF, García-Labiano F, Abad A, Pans MA, et al. Hydrogen production with CO_2 capture by coupling steam reforming of methane and chemical-looping combustion: Use of an iron-based waste product as oxygen carrier

burning a PSA tail gas. J. Power Sources, vol. 196, Elsevier; 2011, p. 4370–81. doi:10.1016/j.jpowsour.2010.09.101.

[25] Zhu L, Fan J. Thermodynamic analysis of H_2 production from CaO sorption-enhanced methane steam reforming thermally coupled with chemical looping combustion as a novel technology. Int J Energy Res 2015;39:356–69. doi:10.1002/er.3248.

[26] Zhu L, Li L, Fan J. A modified process for overcoming the drawbacks of conventional steam methane reforming for hydrogen production: Thermodynamic investigation. Chem Eng Res Des 2015;104:792–806. doi:10.1016/j.cherd.2015.10.022.

[27] Alam S, Kumar JP, Rani KY, Sumana C. Self-sustained process scheme for high purity hydrogen production using sorption enhanced steam methane reforming coupled with chemical looping combustion. J Clean Prod 2017;162:687–701. doi:10.1016/j.jclepro.2017.05.136.

[28] Abanades JC, Murillo R, Fernandez JR, Grasa G, Martínez I. New CO_2 capture process for hydrogen production combining Ca and Cu chemical loops. Environ Sci Technol 2010;44:6901–4. doi:10.1021/es101707t.

[29] Antzara A, Heracleous E, Lemonidou AA. Energy efficient sorption enhanced-chemical looping methane reforming process for high-purity H_2 production: Experimental proof-of-concept. Appl Energy 2016;180:457–71. doi:10.1016/j.apenergy.2016.08.005.

[30] Ma J, Mei D, Peng W, Tian X, Ren D, Zhao H. On the high performance of a core-shell structured CaO-CuO/MgO@Al_2O_3 material in calcium looping integrated with chemical looping combustion (CaL-CLC). Chem. Eng. J. 2019;368:504–12. doi:10.1016/j.cej.2019.02.188.

[31] Martini M, van den Berg A, Gallucci F, van Sint Annaland M. Investigation of the process operability windows for Ca-Cu looping for hydrogen production with CO_2 capture. Chem Eng J 2016;303:73–88. doi:10.1016/j.cej.2016.05.135.

[32] Martínez I, Fernández JR, Martini M, Gallucci F, van Sint Annaland M, Romano MC, et al. Recent progress of the Ca-Cu technology for decarbonisation of power

plants and carbon intensive industries. Int. J. Greenh. Gas. Control. 2019;85:71–85. doi:10.1016/j.ijggc.2019.03.026.

[33] Lyngfelt A. Oxygen carriers for chemical-looping combustion. Elsevier; 2015. doi:10.1016/B978-0-85709-243-4.00011-2.

[34] Idziak K, Czakiert T, Krzywanski J, Zylka A, Kozlowska M, Nowak W. Safety and environmental reasons for the use of Ni-, Co-, Cu-, Mn- and Fe-based oxygen carriers in CLC/CLOU applications: An overview. Fuel 2020;268:117245. doi:10.1016/j.fuel.2020.117245.

[35] Mukherjee S, Kumar P, Yang A, Fennell P. A systematic investigation of the performance of copper-, cobalt-, iron-, manganese- and nickel-based oxygen carriers for chemical looping combustion technology through simulation models. Chem. Eng. Sci. 2015;130:79–91. doi:10.1016/j.ces.2015.03.009.

[36] Shen L, Wu J, Xiao J, Song Q, Xiao R. Chemical-looping combustion of biomass in a 10 kWth reactor with iron oxide as an oxygen carrier. Energy and Fuels 2009;23:2498–505. doi:10.1021/ef900033n.

[37] Tong A, Bayham S, Kathe M V., Zeng L, Luo S, Fan LS. Iron-based syngas chemical looping process and coal-direct chemical looping process development at Ohio State University. Appl Energy 2014;113:1836–45. doi:10.1016/j.apenergy.2013.05.024.

[38] Bidwe AR, Mayer F, Hawthorne C, Charitos A, Schuster A, Scheffknecht G. Use of ilmenite as an oxygen carrier in chemical looping combustion-batch and continuous dual fluidized bed investigation. Energy Procedia, vol. 4, Elsevier Ltd; 2011, p. 433–40. doi:10.1016/j.egypro.2011.01.072.

[39] Stenberg V, Rydén M, Mattisson T, Lyngfelt A. Exploring novel hydrogen production processes by integration of steam methane reforming with chemical-looping combustion (CLC-SMR) and oxygen carrier aided combustion (OCAC-SMR). Int. J. Greenh. Gas. Control. 2018;74:28–39. doi:10.1016/j.ijggc.2018.01.008.

[40] Reitza M, Junka M, Ströhlea J, Epplea B. Design and erection of a 300 kWth indirectly heated carbonate looping test facility. Energy Procedia, vol. 63, Elsevier Ltd; 2014, p. 2170–7. doi:10.1016/j.egypro.2014.11.236.

[41] Junk M, Reitz M, Ströhle J, Epple B. Technical and Economical Assessment of the Indirectly Heated Carbonate Looping Process. J. Energy. Resour. Technol. 2016;138. doi:10.1115/1.4033142.

[42] Hoeftberger D, Karl J. The indirectly heated carbonate looping process for CO2 capture A concept with heat pipe heat exchanger. J. Energy. Resour. Technol. Trans. ASME 2016;138. doi:10.1115/1.4033302.

[43] Reitz M, Junk M, Ströhle J, Epple B. Design and operation of a 300 kWth indirectly heated carbonate looping pilot plant. Int. J. Greenh. Gas. Control. 2016;54:272–81. doi:10.1016/j.ijggc.2016.09.016.

[44] Arias B, Diego ME, Abanades JC, Lorenzo M, Diaz L, Martínez D, et al. Demonstration of steady state CO_2 capture in a 1.7 MWth calcium looping pilot. Int. J. Greenh. Gas. Control. 2013;18:237–45. doi:10.1016/j.ijggc.2013.07.014.

[45] Arias B, Diego ME, Méndez A, Alonso M, Abanades JC. Calcium looping performance under extreme oxy-fuel combustion conditions in the calciner. Fuel 2018;222:711–7. doi:10.1016/j.fuel.2018.02.163.

[46] Pashchenko D. Thermodynamic equilibrium analysis of combined dry and steam reforming of propane for thermochemical waste-heat recuperation. Int. J. Hydrogen. Energy. 2017;42:14926–35. doi:10.1016/j.ijhydene.2017.04.284.

[47] Pashchenko D. Experimental study of methane reforming with products of complete methane combustion in a reformer filled with a nickel-based catalyst. Energy Convers Manag 2019;183:159–66. doi:10.1016/j.enconman.2018.12.102.

[48] Fan Y, Yao JG, Zhang Z, Sceats M, Zhuo Y, Li L, et al. Pressurized calcium looping in the presence of steam in a spout-fluidized-bed reactor with DFT analysis. Fuel Process Technol 2018;169:24–41. doi:10.1016/j.fuproc.2017.09.006.

[49] Tranier J-P, Dubettier R, Perrin N, Air Liquide. Air Separation Unit for Oxy-Coal Combustion Systems. 1st Int. Oxyfuel Combust. Conf., 2009.

[50] Waldron WE, Sircar S. Parametric Study of a Pressure Swing Adsorption Process. vol. 6. 2000.

[51] Yan Y, Mattisson T, Moldenhauer P, Anthony EJ, Clough PT. Applying machine learning algorithms in estimating the performance of heterogeneous, multi-component materials as oxygen carriers for chemical-looping processes. Chem. Eng. J. 2020;387:124072. doi:10.1016/j.cej.2020.124072.

[52] Mays J. One Step Hydrogen Generation Through Sorption Enhanced Reforming. Golden, CO (United States): 2015. doi:10.2172/1373949.

[53] Low-carbon hydrogen - international project examines new technology https://www.cranfield.ac.uk/press/news-2020/low-carbon-hydrogen-international-project-examines-new-technology (accessed March 31, 2020).

[54] ANICA — ACT. http://www.act-ccs.eu/anica (accessed June 17, 2020).

[55] Phase 1 SBRI Hydrogen Supply Competition Bulk Hydrogen Production by Sorbent Enhanced Steam Reforming (HyPER) Project Executive Summary- https://assets.publishing.service.gov.uk/government/uploads/system/uploads/attachment_data/file/866373/Phase_1_-_Cranfield_-_HyPER.pdf

[56] Halabi MH, de Croon MHJM, van der Schaaf J, Cobden PD, Schouten JC. Modelling and analysis of autothermal reforming of methane to hydrogen in a fixed bed reformer. Chem Eng J 2008;137:568–78. doi:10.1016/j.cej.2007.05.019.

[57] Editors G, Walmsley TG, Su R, Cormos A-M, Szima S, Fogarasi S, et al. Economic Assessments of Hydrogen Production Processes Based on Natural Gas Reforming with Carbon Capture. vol. 70, 2018. doi:10.3303/CET1870206.

[58] Tarun CB, Croiset E, Douglas PL, Gupta M, Chowdhury MHM. Techno-economic study of CO_2 capture from natural gas based hydrogen plants. Int. J. Greenh. Gas. Control. 2007;1:55–61. doi:10.1016/S1750-5836(07)00036-9.

[59] Tzanetis KF, Martavaltzi CS, Lemonidou AA. Comparative exergy analysis of sorption enhanced and conventional methane steam reforming. Int. J. Hydrogen. Energy, vol. 37, 2012, p. 16308–20. doi:10.1016/j.ijhydene.2012.02.191.

[60] Antzara A, Heracleous E, Bukur DB, Lemonidou AA. Thermodynamic analysis of hydrogen production via chemical looping steam methane reforming coupled with in situ CO_2 capture. Energy Procedia 2014;63:6576–89. doi:10.1016/j.egypro.2014.11.694

7 Techno-economic Analysis of Low-carbon Hydrogen Production by Sorption Enhanced Steam Methane Reforming (SE-SMR) Processes

Yongliang Yan, Vasilije Manovic, Edward J. Anthony, Peter T. Clough*

Energy and Power Theme, School of Water, Energy and Environment, Cranfield University, Cranfield, Bedfordshire, MK43 0AL, UK.

* Corresponding author: Peter T. Clough, Email: P.T.Clough@cranfield.ac.uk, Phone: +44(0)1234 754 873

Submitted to the Energy Conversion and Management, under review.

Abstract

Hydrogen is an attractive energy carrier that will play a key role in future global energy transitions. This work investigates the techno-economic performance of six different sorption enhanced steam methane reforming (SE-SMR) configurations integrated with an indirect natural gas or biomass-fired calciner, oxy-fuel combustion and chemical-looping combustion for large-scale blue and carbon-negative hydrogen production. The techno-economic performance of the proposed cases were evaluated by their net efficiency, CO_2 capture efficiency, levelised cost of hydrogen (LCOH), and costs of CO_2 avoided and removal. A sensitivity analysis was also conducted to evaluate the key parameters and explore existing uncertainties that can affect the economic performance of the proposed SE-SMR processes. The results revealed that the proposed systems were comparable with conventional steam methane reforming (SMR) with carbon capture and storage (CCS). The LCOH of the proposed SE-SMR plants ranged from £1.90-2.80/kg, and the costs of CO_2 avoided and removal ranged from £33-69/tonne and £58-107/tonne, respectively. By applying a carbon price (£16/tonne CO_2), the costs of CO_2 avoided and removal for the proposed SE-SMR processes could be significantly reduced. The results of cumulative discounted cash

flow of SE-SMR plants at a hydrogen selling price of £3.00/kg indicated that all the investment of the proposed cases could be paid back after eight years, even if carbon tax is zero.

Keywords

Blue hydrogen production, Sorption enhanced steam methane reforming, Carbon capture, Techno-economic analysis

7.1 Introduction

Hydrogen is a versatile feedstock that is widely used in oil refining, ammonia synthesis and the production of many other chemicals. Using low-carbon hydrogen as an energy carrier is attracting increasing attention due to its potential to replace carbon-intensive fossil fuels, which enables end-users to solve critical decarbonisation related issues in the transport, residential, and power sectors. Globally, approximately 70 Mt of dedicated hydrogen was produced in 2019, 76% from natural gas, 23% from coal and the rest from oil and electricity, which resulted in the emission of approx. 830 Mt CO_2 (2.6% of global CO_2 emissions in 2019) [1]. Looking at the annual CO_2 emissions from hydrogen production in 2014 (550 Mt), it has increased by 51% points in 2019. Moreover, if hydrogen is mainly produced from natural gas and coal without employing carbon capture and storage (CCS) technologies, then CO_2 emissions from hydrogen production will increase significantly with the rapid growth rate of H_2 demand. Despite efforts to drive down the costs of green hydrogen production by solar, wind and biomass energy, natural gas reforming remains the most economic pathway for large-scale hydrogen production in the foreseeable future. Therefore, there is an urgent need to develop low-carbon hydrogen production technologies that enable us to use hydrogen in the energy transition while achieving the 2 °C Paris Agreement goal and mitigating further climate change.

To reduce the CO_2 emissions of hydrogen production by Steam Methane Reforming (SMR), Autothermal Reforming (ATR) with gas heated reformer (GHR), coal and biomass gasification, different options such as adsorption, absorption, membranes and cryogenic separation can be adopted. Detailed reviews of different hydrogen production technologies integrated with CO_2 capture are available in the literature [2-5]. Among them, one novel and promising technology is sorption enhanced steam

methane reforming (SE-SMR), which can produce low-carbon and high purity H_2 through an in-situ CO_2 capture process where the hydrocarbon fuel is reacted with steam in the presence of a CO_2 sorbent and a reforming catalyst. Compared to the current available SMR technologies with aqueous solutions of amines such as MEA, TEA and MDEA for decarbonised hydrogen production, the SE-SMR approach has the advantages of high yields of H_2, high conversion of methane, low reforming temperature, without the requirement of multiple shift reactors and subsequent purification steps. Recently, extensive research has been carried out to develop high-performance CO_2 sorbents for multiple SE-SMR/regeneration cycles [6-11], and to investigate the thermodynamic performance of different integrations of SE-SMR process for hydrogen production [12-17]. The main drawback of the SE-SMR technology is that to produce the calcination heat demand without emitting CO_2 to the atmosphere requires energy-intensive processes like oxy-fuel combustion or the use of an indirectly heated calciner.

To reduce the energy penalties and CO_2 emissions from the regeneration of CO_2 sorbent during the SE-SMR process, different integrations have been proposed for decarbonised and high-purity hydrogen production. Ochoa-Fernández et al. [12] investigated the process simulation performance of SE-SMR integrated with oxy-fuel combustion with CaO and other novel CO_2 acceptors (Li_2ZrO_3, K-doped Li_2ZrO_3, Na_2ZrO_3 and $LiSiO_4$). Their results indicated that the use of CaO as the CO_2 acceptor integrated with oxy-fuel combustion had better performance in terms of net efficiency, CO_2 capture efficiency, and required smaller pressure swing adsorption (PSA) unit for hydrogen purification compared to that of SMR with MEA. Abanades et al. [18] proposed the integrated Ca-Cu looping process for hydrogen production, which utilised the heat of reduction of CuO with a fuel gas for calcination of $CaCO_3$. Later on, this concept was further investigated by means of experiments and process simulations [19-21].

Besides applying the oxy-fuel combustion and Ca-Cu looping for calcination of $CaCO_3$, indirectly heated calcination process through the use of heat pipes and heat transfer walls has been intensively investigated [22-24] and successfully demonstrated with a 300 kWth carbonate looping pilot. Zhu et al. [13] proposed a novel SE-SMR process thermally coupled with chemical-looping combustion (CLC) to supply the necessary heat for calcination of $CaCO_3$. The results of thermodynamic analysis showed that the

overall exergy efficiency of SE-SMR integrated with CLC increased by 14.39% points compared to SMR without CCS. Yan et al. [17] evaluated the process performance of different SE-SMR configurations, which consisted of process integrations with PSA, CLC, oxy-fuel combustion or H_2-fired calciner, and their results indicated that the upgraded SE-SMR processes could provide flexible options for low-carbon hydrogen production based on the costs and demand of CO_2 reduction.

Although, different SE-SMR configurations have given promising results in experimental investigations and by thermodynamic analysis, there is a limited work on economic assessment to fully understand the potential of SE-SMR at large scales. Diglio et al. conducted a techno-economic assessment of SE-SMR in a fixed bed reactor network integrated with fuel cells and calculated the cost of CO_2 avoided was £33.43/kg CO_2, which was lower than that of SMR with CO_2 capture and chemical-looping reforming (CLR). However, there is no further published work on the economic performance of SE-SMR or SE-SMR integrated with other process options to achieve near-zero and negative CO_2 emissions (oxy-fuel combustion, chemical-looping combustion or biomass-fired calciner).

A series of studies have been conducted to evaluate the economic performance of current and emerging technologies for low-carbon hydrogen production such as SMR with amine scrubbing [25], SMR with CLC [26], ATR with CCS [26], CLR [25,26], membrane assisted fluidised-bed reactors [27] and gas switching reforming [28], and the levelised cost of hydrogen (LCOH) of these technologies was reported to be in the range of £1.42-2.84/kg H_2. To compare the economic performance of SE-SMR with the above low-carbon hydrogen production technologies and promote the scale-up of the SE-SMR technology, techno-economic assessments of various SE-SMR configurations for hydrogen production are required.

The objectives of this study are to evaluate the techno-economic feasibility of the SE-SMR process integrated with oxy-fuel combustion, chemical-looping combustion and biomass-fired calciner for low-carbon (blue) and carbon-negative hydrogen production. The operating and economic performance of the proposed cases is evaluated in terms of the net efficiency, CO_2 capture efficiency, LCOH, CO_2 avoided and removal cost, and is compared with that of SMR and CLR with CCS. In addition,

a detailed sensitivity analysis is performed to explore the influence of uncertainty in the input variables on the key economic performance indicators.

7.2 Methodology

7.2.1 Process Description of Different SE-SMR Configurations

In our previous work [17], we have investigated thermodynamic performance and operating window of six upgraded SE-SMR process for blue hydrogen production: 1) SE-SMR with an air fired calciner, 2) SE-SMR with a Pressure Swing Adsorption (PSA) unit, 3) SE-SMR thermally coupled with Chemical-Looping Combustion (CLC), 4) SE-SMR+PSA+CLC, 5) SE-SMR+PSA with an oxy-fired calciner, 6) SE-SMR+PSA with an indirect H_2 -fired calciner. Only natural gas was used as a feedstock in the previous process simulations. Within this paper we investigate the economic performance of the proposed SE-SMR processes and calculate the impact of switching fuel supplies from natural gas to biomass. Hence, the following SE-SMR configurations are studied in this manuscript.

Case 1A: SE-SMR with indirect air-natural gas combustion calciner

Case 1B: SE-SMR with indirect air-biomass combustion calciner

Case 2A: SE-SMR with indirect oxy-natural gas combustion calciner

Case 2B: SE-SMR with indirect oxy-biomass combustion calciner

Case 3A: SE-SMR with indirect chemical-looping combustion of natural gas calciner

Case 3B: SE-SMR with indirect chemical-looping combustion of biomass calciner

Figure 7-1 illustrates the process for case 1A and case 1B. The natural gas feed to the reformer is compressed to 25 bar by the fuel compressor and preheated by the heat from the CO_2 enriched gas from the calciner. Here, the feed water is supplied by a high-pressure pump goes through two heat exchangers heated by the hot syngas after the reformer and the flue gas from the air-fired combustor to produce the high temperature steam. Then the mixture of natural gas, steam and CaO sorbent enters the fluidised bed reformer. The reformer in the SE-SMR process is operated as a joint carbonator and reformer, which can realise *in-situ* CO_2 capture in the presence of CaO or other CO_2 sorbents. The *in-situ* CO_2 capture in the reformer shifts the reforming and

water-gas shift reaction in the direction of increasing hydrogen production based on Le Chatelier's principle. The total SE-SMR reaction can be simplified as shown by **Equation. (7-1)**. The reformer in the SE-SMR process is typically operated in the temperature range of 550 to 650 °C and elevated pressure (~25 bar) to reduce the energy penalty of H_2 compression. The cooled syngas after the reformer is sent to the PSA unit to recover the H_2 product and the off-gas which contains CH_4, CO, CO_2, H_2 and H_2O is sent to the air-fired burner to reduce the additional fuel requirement. The calciner is operated at ambient pressure and indirectly heated by the combustion of natural gas and PSA off-gas with air. The air and fuel inlet of the burner are preheated by the remaining heat of the flue gas and CO_2 product gas, respectively. The used sorbent is transported from the high-pressure reformer to the calciner via a depressurised lock hopper and the regenerated sorbent carried by the steam or CO_2 is returned to the reformer through the pressurised lock hopper. Finally, the cooled CO_2 from the calciner is compressed to 110 bar and cooled to room temperature in the form of a dense liquid suitable for transportation and storage. For the case 1B, woody biomass together with the PSA off-gas is used as the fuel for the air-fired burner to provide the heat for the sorbent regeneration and steam generation. A gas cleaning unit is installed after the biomass combustor to remove the SO_x and NO_x in the flue gas.

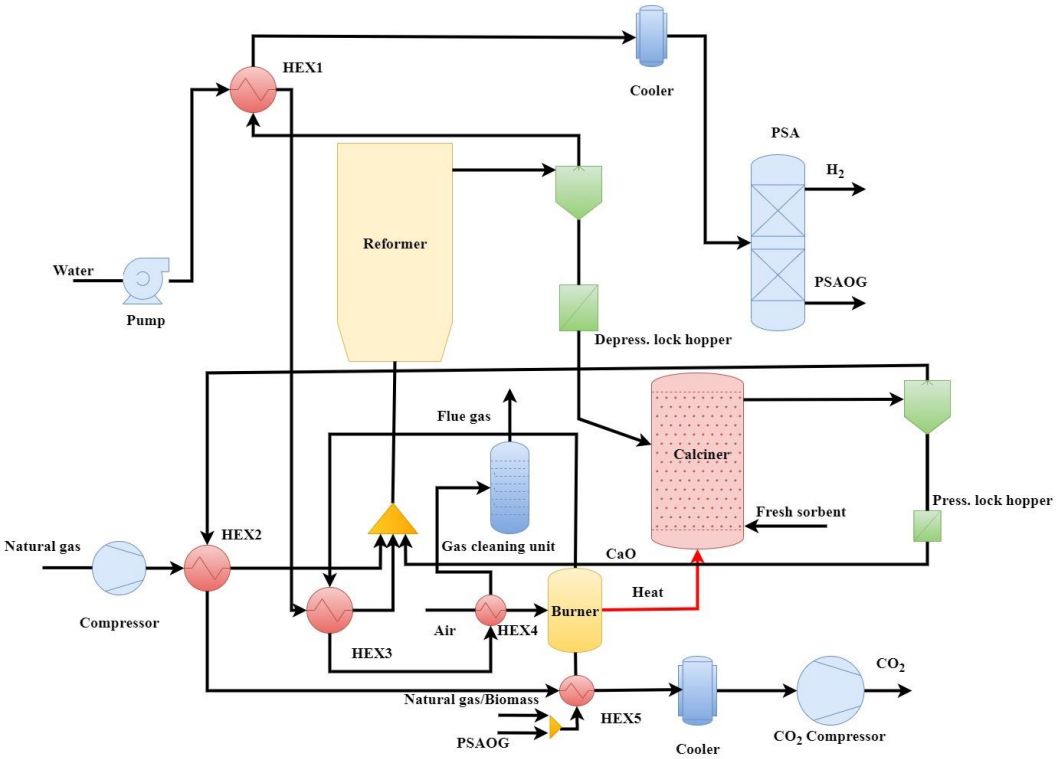

Figure 7-1 Simplified process flow diagram of case 1A and B

$$CH_4 + 2H_2O + CaO \leftrightarrow CaCO_3 + 4H_2 \quad \textbf{(7-1)}$$

To avoid the CO_2 emissions from the indirectly air-fired calciner, an oxy-fuel burner has been coupled to the calciner to facilitate CO_2 separation by providing the heat for sorbent regeneration and steam generation in cases 2A and 2B as **Figure 7-2** shown. Compared to the use of a direct oxy-fired calciner, the indirect oxy-fuel burner has the major advantage of providing an almost pure CO_2 stream from the calciner, which minimises the energy for CO_2 purification, and reduces sorbent make-up flow due to minimal impurities in the gas stream. To avoid superheated regions in the oxy-fuel burner, oxygen produced by the Air Separation Unit (ASU) is always mixed with the recirculated flue gas. Here, only small amount of the CO_2 enriched gas needs to be purified by the gas cleaning unit and then combined with the CO_2 stream from the calciner for compression and storage.

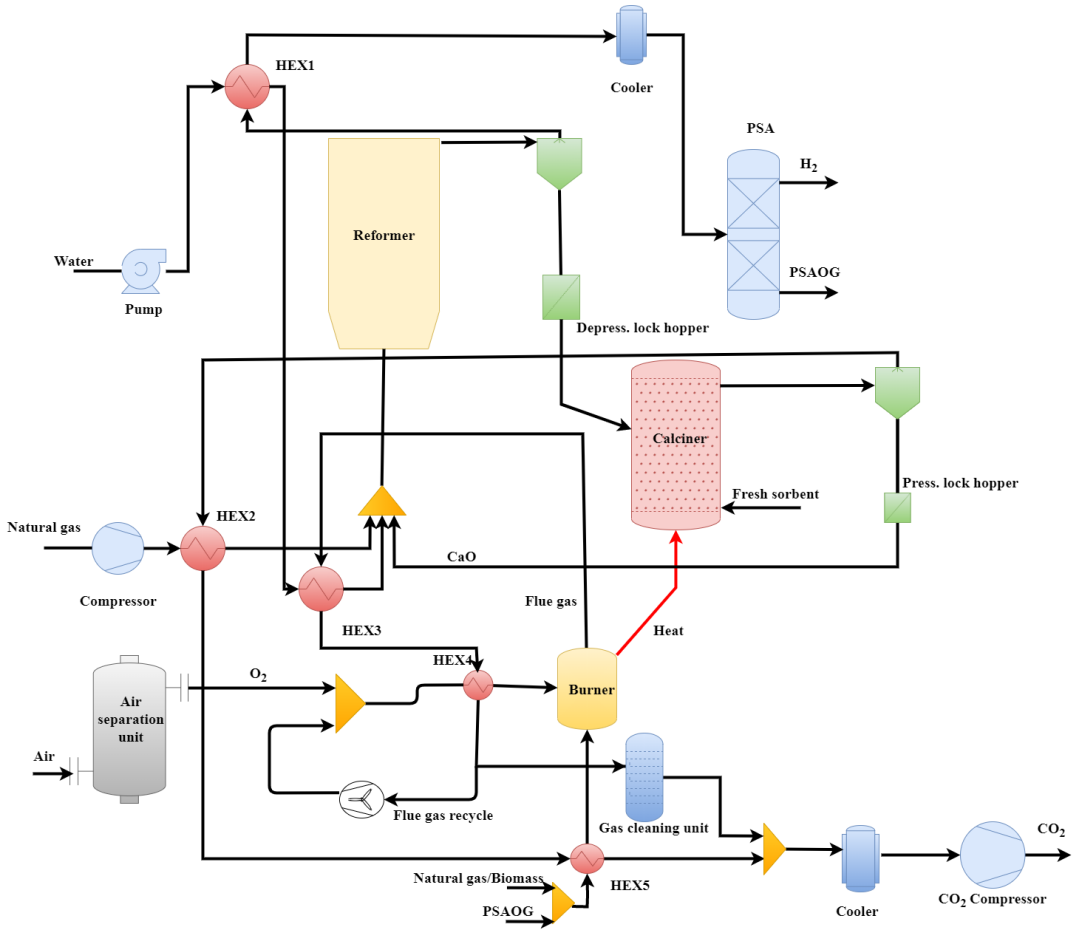

Figure 7-2 Simplified process flow diagram of case 2A & B

Another novel configuration for SE-SMR is thermally coupled chemical-looping combustion (CLC) for blue hydrogen production, which has been shown to be more

efficient than SMR with CCS and SE-SMR with oxy-fuel combustion [60]. In the case 3A and 3B (described in **Figure 7-3**), chemical-looping combustion of natural gas and biomass with PSA off-gas is employed to provide the necessary heat for SE-SMR, simultaneously realising inherent separation of CO_2 without addition energy consumed. Iron oxide supported with Al_2O_3 (15 wt %) and SiO_2 (15 wt %) was selected as the oxygen carrier of the CLC process due to its low-cost and its acceptable albeit moderate reactivity with fuels [16]. In the air reactor, the exothermic process in oxidation of Fe_3O_4 by air (**Equation. ((7-2)**) provides enough heat to the calciner via heat pipe exchangers. The heat from the depleted air is extracted for steam generation and preheating the air inlet. The oxidised oxygen carriers (Fe_2O_3) are transported from the air reactor to react with natural gas (case 3A) or biomass (case 3B) and PSA off-gas in the fuel reactor, the resulting emissions consist of only CO_2 and steam. The reactions in fuel reactor for case 3A is described by **Equation. (7-3)** to **(7-5)**. For case 3B, chemical-looping combustion of biomass is a very complex process, it involves fuel devolatilisation (**Equation. (7-6)**) and char gasification (**Equation. (7-7)** and **(7-8)**) and their gaseous products react with the oxygen carriers as shown in **Equation. (7-3)** to **(7-5).** The CO_2 enriched stream after the fuel reactor is combined with the CO_2 stream from the calciner, and the heat is used to preheat the fuel feed. After that, the CO_2 stream is purified and condensed for compression.

$$O_2 + 4Fe_3O_4 \rightarrow 6Fe_2O_3 \quad \textbf{(7-2)}$$

$$CH_4 + 12Fe_2O_3 \rightarrow CO_2 + 2H_2O + 8Fe_3O_4 \quad \textbf{(7-3)}$$

$$H_2 + 3Fe_2O_3 \rightarrow H_2O + 2Fe_3O_4 \quad \textbf{(7-4)}$$

$$CO + 3Fe_2O_3 \rightarrow CO_2 + 2Fe_3O_4 \quad \textbf{(7-5)}$$

$$\text{Biomass} \xrightarrow{\text{devolatilisation}} \text{Volatiles} + C \quad \textbf{(7-6)}$$

$$C + CO_2 \rightarrow 2CO \quad \textbf{(7-7)}$$

$$C + H_2O \rightarrow CO + H_2 \quad \textbf{(7-8)}$$

7.2.2 Process Simulation

The process simulation and mass-energy balance calculations used for the techno-economic analysis were performed by Aspen Plus V10. **Table 7-1** shows the main parameters and assumptions used for the process simulation. Natural gas (see **Table 7-1** for its composition) was used as a feedstock for the reformer for all cases. Only in case 1B, 2B and 3B is biomass employed as fuel to provide the heat of calcination for sorbent and steam generation. The proximate and ultimate analyses of the woody biomass reported by Yan et al. [29] were used in this work. The SRK (Soave–Redlich–Kwong) equation of state, which has shown good performance in simulations of hydrocarbon processing [30], was used for the process simulation of all cases. The mass flow rate of H_2 product for all cases is set to 19.5 tonne/h, equivalent to 650 MW_{th} based on the lower heating value of H_2. The SE-SMR H_2 production plants are assumed to be located in Tees Valley, UK. This location is chosen because it produces over 50% of the total UK H_2 production for the chemicals industry, operates a liquid natural gas (LNG) receiving facility, and has a unique set of H_2 distribution pipes, plus salt caverns for large volume storage of H_2 and the potential for offshore CO_2 storage [31-33].

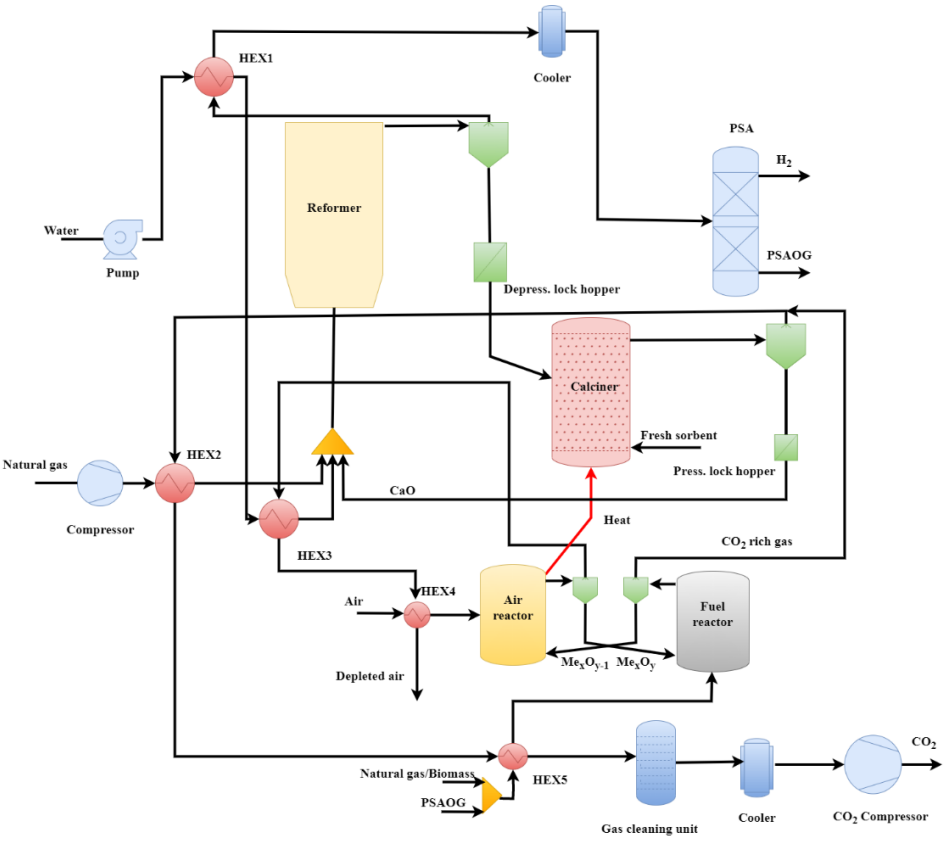

Figure 7-3 Simplified process flow diagram of case 3A and B

The SE-SMR process was simulated in Aspen Plus under steady-state equilibrium conditions. The RGibbs block, which calculates the chemical and phase equilibrium by minimising the Gibbs free energy of all components to achieve equilibrium, was used to model the reformer, calciner and combustor. To separate solid phase from gas phase, Sep model with 100% separation efficiency was used to simulate the cyclone of reformer and calciner. The calciner was operated at ambient pressure and the reformer was operated at 25 bar. It requires a depressurised lock hopper after the cyclone of reformer and a pressurised locker hopper after the cyclone of calciner to ensure the sorbent transported between the reformer and calciner under practical conditions. The pressures reported in this work are expressed as absolute pressure. The effective CaO conversion is in the range of 0.07-0.82, which is strongly affected by the process conditions and the CaO precursors used [34]. According to experimental investigations [9,10], it is reasonable to estimate that the average carbonation conversion of CaO sorbent under this SE-SMR conditions can achieve 50%, which can be maintained by ensuring an effective make-up flow of the sorbent/composite particles.

The natural gas feed to the reformer is adjusted to ensure the mass flow rate of H_2 product is 19.5 tonne/h for all cases with the S/C=5. The pure hydrogen is recovered from the water-condensed H_2 enriched gas using a pressure swing adsorption (PSA) unit with 95% recovery efficiency [35], which was simulated by the Sep model in Aspen Plus. The inlet pressure of condensed H_2 enriched gas to the PSA unit is maintained over 25 bar, which is the common operating pressure for PSA. Then, the pressurised H_2 product at room temperature can be stored or distributed. The off-gas from the PSA unit, which contains H_2, CO, and CH_4, can be burned with natural gas or biomass to help meet the calciner heat duty.

The MHeatX model was selected to simulate the heat exchangers and heat recovery steam generator (HRSG) for all the cases. The goal of heat exchanger networks design is to obtain the maximum heat recovery with the minimum number of heat exchangers. The steam generator was simulated with multiple zones to detect and avoid temperature crossover during the phase transition.

The process of biomass combustion was simulated by the modified models shown elsewhere [36]. Firstly, raw biomass was dried by the primary air in the RStoic block,

and the moisture was removed by the Flash2 block. Then, the decomposition of dried biomass occurs in the RYield block, and a calculator block is used to calculate the actual yield distribution from the component attributes of biomass. Next, the products were sent to the RGibbs block to complete the simulation of combustion process. A heat stream was used to carry the heat from the RYield block to the RGibbs block in the biomass combustion process, and another heat stream was added from the RGibbs block in the biomass combustion process to the calciner to simulate the heat transfer from the combustor to the calciner in the case 1B and 2B. For the case 1B, air was used as an oxidant for the inlet of RGibbs block. For the case 2B, a mixture of O_2 and recirculated flue gas were used as an oxidant for the inlet of RGibbs block. For the case 3B, Fe_2O_3 were used as an oxidant for the inlet of RGibbs block. Finally, the SSplit model was used as a cyclone to separate the combustion gases from ash, and the heat of the combustion gases could be further extracted by the heat exchangers. For the case 2A and 2B, the ASU was not modelled, but the specific energy of oxygen separation was set to 160 kWh/tonne [37] O_2 for the techno-economic analysis. The mass flow rate of recirculated flue gas was adjusted to maintain the O_2 volume concentration at 30% in the oxy-fuel combustor to control flame temperature [38].

In the case 3A and 3B, an RGibbs block was selected to model both the air reactor (AR) and fuel reactor (FR). A heat stream was used to carry the heat from oxidation of Fe_3O_4 in the air reactor (AR) to meet the heat duty of calciner. It was assumed 10% heat loss during the heat transfer from the AR to the calciner. The outlet temperature of the AR varied as the change in heat duty of calciner, but it was always maintained higher than the calciner operating temperature (900 °C). The FR was set to an adiabatic reactor and its temperate was decided by the inlet conditions of fuel and oxygen carriers. The mass flow of oxygen carriers to the FR was determined by the all hydrogen was completely combusted in the outlet flue gas of the FR. The heat of depleted air from the AR and CO_2 enriched gas from the FR were used to generate steam and preheat the air and fuel. Both the AR and FR were operated at ambient pressure.

Table 7-1 Main parameters and assumptions for process simulation in Aspen plus

Parameters	Value	Unit
Reformer pressure	25	bar
Reformer temperature	600	°C
Steam to carbon (S/C) ratio	5	-
Calciner temperature	900	°C
Isentropic efficiency of natural gas and CO_2 compressor	83	%
Water pump efficiency	83	%
Excess oxygen	10	%
Calciner heat loss	10	%
Calcination efficiency	100	%
Mechanical efficiency of pump and compressors	98	%
Fuel feed temperature	9	°C
Fuel feed pressure	1	bar
Feed water inlet temperature	10	°C
Feed water inlet pressure	1	bar
Air/oxygen temperature	20	°C
Air/oxygen pressure	1	bar
Stack temperature of flue gas	120	°C
Lower heating value of H_2	120	MJ/kg
Lower heating value of biomass	16.30	MJ/kg
Natural gas composition (mol. %)	[61]	
CH_4 92.03	C_2H_6	5.75
C_3H_8 1.31	C_{4+}	0.45
N_2 0.46	Lower heating value (MJ/kg)	46.02

The key performance indicators to evaluate the thermodynamic performance of different SE-SMR processes are cold gas efficiency, net efficiency and CO_2 capture efficiency. Because the PSA unit has been installed and the off-gas of PSA unit (PSAOG) has been utilised in all cases, the H_2 purity and total natural gas conversion for all the cases are assumed to be a hundred percent.

The cold gas efficiency (η_{CG}) is calculated by **Equation. (7-9)**.

$$\eta_{\mathrm{CG}} = \left(\frac{\dot{\mathrm{m}}_{\mathrm{H_2,product}} * \mathrm{LHV}_{\mathrm{H_2}}}{\dot{\mathrm{m}}_{\mathrm{NG,feed}} * \mathrm{LHV}_{\mathrm{NG}} + \dot{\mathrm{m}}_{\mathrm{NG/Biomass,additional}} * \mathrm{LHV}_{\mathrm{NG/Biomass}}}\right) * 100\% \qquad \textbf{(7-9)}$$

Where $\dot{\mathrm{m}}_{\mathrm{H_2,product}}$, $\dot{\mathrm{m}}_{\mathrm{NG,feed}}$ and $\dot{\mathrm{m}}_{\mathrm{NG/Biomass,additional}}$ are the mass flow rate of the hydrogen product, natural gas feed and additional natural gas or biomass required to meet the heat utility of the calciner and steam boiler, respectively, $\mathrm{LHV}_{\mathrm{H_2}}$ and $\mathrm{LHV}_{\mathrm{NG/Biomass}}$ are the lower heating value of hydrogen and natural gas or biomass, respectively.

The net efficiency (η_{net}) is calculated as shown in **Equation. (7-10)**, where the electric utility ($\mathrm{P_e}$) requirement is also added to the cold gas efficiency equation. A thermal to electrical conversion efficiency (η_{elect}) of 50% is utilised in this work.

$$\eta_{net} = \left(\frac{\dot{\mathrm{m}}_{\mathrm{H_2,product}} * \mathrm{LHV}_{\mathrm{H_2}}}{(\dot{\mathrm{m}}_{\mathrm{NG,feed}} + \dot{\mathrm{m}}_{\mathrm{NG/Biomass,additional}}) * \mathrm{LHV}_{\mathrm{CH_4}} + \dfrac{\mathrm{P_e}}{\eta_{\mathrm{elect}}}}\right) * 100\% \qquad \textbf{(7-10)}$$

The overall CO_2 capture efficiency is calculated using **Equation. (7-11)**. In this work, only the CO_2 emissions of SE-SMR plants are considered and biomass is considered to be a carbon-neutral fuel.

$$\mathrm{CO_2\ capture\ efficiency} = \left(\frac{\mathrm{n}_{\mathrm{CO_2,captured}}}{\mathrm{n}_{\mathrm{NG,feed}} + \mathrm{n}_{\mathrm{NG/Biomass,additional}}}\right) * 100\% \qquad \textbf{(7-11)}$$

Herein, $\mathrm{n}_{\mathrm{CO_2,captured}}$ is the moles of carbon capture, $\mathrm{n}_{\mathrm{NG,feed}}$ is the moles of carbon in natural gas feed to the reformer, and $\mathrm{n}_{\mathrm{NG/Biomass,additional}}$ is the moles of carbon in natural gas or biomass feed to the combustor or FR.

7.2.3 Economic Evaluation

A detailed cost estimation of the above different SE-SMR configurations is conducted to compare their economic performance. A chemical plant cost estimation

methodology developed by Sinnott et al. [40] for calculating the capital and operating costs is employed. The capital cost consists of direct capital costs of the major equipment, such as the reformer, calciner, heat recovery steam generator (HRSG), pressure swing adsorption (PSA) unit, chemical-looping combustion (CLC) unit and CO_2 compressor, and indirect capital costs. The direct capital costs of the major equipment are based on estimation of corresponding units from the literature, and corrected to a consistent baseline year (2019) by employing chemical engineering plant cost index factors and equipment scaling exponents as **Equation. (7-12)** shown.

$$C_A = \left(\frac{CI_A}{CI_B}\right) * C_B * \left(\frac{S_A}{S_B}\right)^x \quad \textbf{(7-12)}$$

Where C_A is the new scaled equipment cost, C_B is the base equipment cost, CI_A and CI_B are the annual chemical engineering plant cost index factor in the year A and B respectively, S_A is the new equipment's capacity, S_B is the base equipment's capacity, and x is the scaling exponent for the equipment, which is taken as 0.6 in this work, as known as the six-tenths rule.

The operating cost is made up of the fixed costs, variable costs and fuel costs. The price of the raw materials and fuel is obtained from the quotations of the potential suppliers and literature. Parameters and assumptions for the capital and operating costs are described in **Table 7-2.** The costs of shipping and distributing H_2 product are not considered in this work. It is assumed that the proposed cases are the central hydrogen production plants, and that a distribution network is available.

The key economic performance indicators used in this analysis are the levelised cost of hydrogen (LCOH), cost of CO_2 avoided (CCA) and removal (CCR). These costs are calculated by the following equations:

$$\mathrm{LCOH} = \frac{(\mathrm{TOC} * \mathrm{FCF} + \mathrm{FOM})}{(\mathrm{CF} * 8760)} + (\mathrm{FC} * \mathrm{HR}) + \mathrm{VOM} \quad \textbf{(7-13)}$$

$$\mathrm{CCA} = \frac{\mathrm{LCOH}_{\mathrm{SE-SMR}} - \mathrm{LCOH}_{\mathrm{Non\ CCS}}}{\mathrm{CO_2\ Emissions}_{\mathrm{Non\ CCS}} - \mathrm{CO_2\ Emissions}_{\mathrm{SE-SMR}}} \quad \textbf{(7-14)}$$

$$\mathrm{CCR} = \frac{\mathrm{LCOH}_{\mathrm{SE-SMR}} - \mathrm{LCOH}_{\mathrm{Non\ CCS}}}{\mathrm{CO_2\ Removed}_{\mathrm{SE-SMR}}} \quad \textbf{(7-15)}$$

Where TOC is the total overnight capital cost, FOM is the fixed operating and maintenance costs, VOM is the variable operating and maintenance costs, FC is the

fuel costs, CF is the capacity factor, HR is the net heat rate of the plant, and FCF is the fixed charge factor as defined in **Equation. (**7-16**)**.

$$\mathrm{FCF} = \frac{\mathrm{r}(1+\mathrm{r})^{\mathrm{t}}}{(1+\mathrm{r})^{\mathrm{t}}-1} \quad \textbf{(7-16)}$$

Herein, *t* is the economic lifetime of the plant relative to its base year, and *r* is the discount rate. In this study, a plant lifetime of 30 years and a discount rate of 12% obtained from the report of discount rates for low-carbon and renewable generation technologies in the UK [41] are used.

The value of LCOH with and without carbon price (£16/tonne [42]) of an SMR plant ($LCOH_{Non\ CCS}$) is £2.17 and £1.33/kg H_2 [43], and the CO_2 emissions of SMR plant without carbon capture (CO_2 $Emissions_{Non\ CCS}$) is assumed to be 10 kg/kg H_2 [26].

Table 7-2 Parameters and assumptions for economic analysis

Parameter	Value	Reference
Specific cost of reformer (£/kW_{th})	55.3	[15]
Specific cost of calciner (£/kW_{th})	171.5	[62]
Specific cost of CLC unit (£/kW_{th})	178.8	[63]
Specific cost of heat recovery steam generator (£/kW_{th})	112.8	[64]
Specific cost of Sulphur removal unit (£/kW_{th})	38.3	[65]
Cost of PSA unit (£m)	90.3	[15]
Cost of ASU (£m)	32.0	[15]
Cost of CO_2 compressor (£m)	37.7	[66]
Cost of CO_2 storage (£/tonne)	19	[67]
Heat pipe (£/pipe)	179.3	[68]
Natural gas price (£/MWh)	15.4	[69]
Biomass price (£/MWh)	19.0	[69]

Electricity price (£/kWh)	0.16	[70]
Process water (Including waste water treatment, £/m^3)	3.1	[71]
Ni catalyst (£/kg, life span: 5 years)	24.5	[72]
Fe_2O_3 oxygen carriers (Including disposal cost, £/kg, life span: 3000 h)	1.5	[15]
Limestone (£/tonne, life span: 500 h)	85	[73]
Solid inventory of $CaCO_3$ (kg/m^2)	1000	[74]
Solid inventory of the fuel reactor (kg/MW_{th})	500	[75]
Solid inventory of the air reactor (kg/MW_{th})	250	[75]
Industrial land value (Tees Valley, £m/hectare)	0.32	[76]
Chemical Engineering Plant Cost Index (CEPCI) 2019	607.5	[77]
Plant staff	35	
Burdened labour cost (Including the overheads, £/man-hr)	25	
Plant life (year)	30	
Capacity factor	0.95	
Design and engineering	20% of total direct capital costs of equipment	
Contractor's fee	5% of total direct capital costs of equipment	
Contingency allowance	5% of total direct capital costs of equipment	
Maintenance	10% of total capital costs	

Miscellaneous materials	10% of maintenance cost
Insurance	1% of total capital costs per year
Local taxes	1% of total capital costs per year
Supervision	10% of the operating labour costs
Laboratory costs	20% of the operating labour costs
Plant overheads	60% of the operating labour costs

7.3 Results and Discussion

7.3.1 Technical Performance

The detailed technical performance of six different SE-SMR plants are shown in **Table 7-3**. Case 2A has the highest cold gas efficiency (82.59%), but its net efficiency is 3.24% and 0.9% points respectively lower than those of case 1A (76.96%) and 3A (74.10%) due to the high electricity consumption of the ASU. Case 1A has the highest net efficiency (76.96%), but the lowest CO_2 capture efficiency (60.08%), because only the CO_2 from the reformer has been captured by CaO sorbent, and the CO_2 from the indirect-air natural gas combustion calciner is released directly to the atmosphere. When biomass is used as the fuel to meet the heat duty of calciner and steam generation (case 1B) the system can achieve the highest net efficiency (70.52%) with overall CO_2 capture efficiency of 86.08%. While, Case 2B and 3B can realise nearly 100% overall CO_2 capture efficiency with a 4.19% and 1.2% drop in net efficiency compared to the Case 1A. In addition, another advantage of case 2B and 3B is negative CO_2 emissions for hydrogen production, which can remove 5.4 and 5.5 kg CO_2 respectively from the atmosphere per kg of hydrogen produced. It is also worth noting that the replacement of natural gas for biomass in the calciner significantly decreases both the cold gas and net efficiencies by ~5-7% points for these cases, although the CO_2 emissions for hydrogen production decreases. The NO_x and SO_x

emissions increase significantly when natural gas is replaced by biomass to meet the heat duty of calciner and steam generation. But the NO_x emissions of case 1B, 2B and 3B are well below the EU directive on industrial NO_x emissions of biomass combustion (250 mg/Nm^3). For SO_x emissions, only in the case 3B is the value (308 mg/Nm^3) over the limitation for industrial SO_x emissions for biomass combustion (250 mg/Nm^3). It would be necessary to add a gas cleaning unit to further purify the CO_2 stream before the CO_2 compression in cases 2B and 3B, to avoid the risk of corrosion throughout transport pipelines and plant components.

Table 7-3 Technical performance indicators of SE-SMR H_2 production plants

Cases	Units	Case 1A	Case 1B	Case 2A	Case 2B	Case 3A	Case 3B
Natural gas	tonne/h	62.8	48.4	61.6	48.4	64.3	48.4
Biomass	tonne/h	0.0	57.6	0.0	55.0	0.0	56.5
Boiler feed water	tonne/h	273.0	273.0	281.9	273.0	272.8	300.7
Fuel compressor	MW_{th}	10.3	10.3	10.3	10.3	10.3	10.3
Water pump	MW_{th}	0.2	0.2	0.2	0.2	0.2	0.2
CO_2 compressor	MW_{th}	10.8	10.8	16.0	20.7	17.2	20.9
Air separation unit	MW_{th}	0.0	0.0	20.7	25.1	0.0	0.0
Calciner	MW_{th}	160.9	160.9	166.1	160.8	160.5	160.5
Combustor/CLC unit	MW_{th}	274.5	311.4	269.6	299.5	291.00	374.6
H_2 product flowrate	tonne/h	19.5	19.5	19.5	19.5	19.5	19.5
H_2 product (LHV)	MW_{th}	650	650	650	650	650	650
Cold gas efficiency	%	81.0	73.9	82.6	74.9	79.1	74.4
Net efficiency	%	77.0	70.5	73.7	66.3	74.1	69.4
CO_2 capture efficiency	%	60.1	86.1	100.0	100.0	100.0	99.7
CO_2 captured	(kg/kg H_2)	5.88	5.88	8.69	11.29	9.08	11.40

CO_2 emissions	(g/kg H_2)	2980	0.49	0.34	-5410	0.43	-5520
NO_x emissions	mg/Nm³	2.21	59.67	0.01	3.56	0.02	0.01
SO_x emissions	mg/Nm³	0.00	58.21	0.00	93.9	0.00	308.00

7.3.2 Economic Analysis

7.3.2.1 Economic Performance

Table 7-4 presents the detailed results of economic analysis of the different SE-SMR processes. The integration of SE-SMR with oxy-biomass combustion calciner (case 2B) has the highest total capital and operating costs (£293m and £329m, respectively) compared to that of the other cases. The replacement of oxy-fuel combustion unit by the CLC unit in case 3B decreased the total capital and operating costs relative to case 2B by 2.76% points and 9.36% points respectively. While, the total capital and operating costs of case 3A has increased by 6.21% points and 3.04% points compared to the case 3A, which is due to the increase in the capacity of CO_2 compression unit in case 3A. Case 1A has the lowest total capital and operating costs (£189m and £238m) but with the lowest CO_2 capture efficiency (60.08%). The total capital and operating costs of case 1A are increased by 2.47% points and 6.48% points when biomass replaces the natural gas as the feed of the indirect calciner (case 1B), but the CO_2 capture efficiency is increased by 30.2% points.

Table 7-4 Main results of economic analysis of SE-SMR hydrogen plants

Cases	Units	Case 1A	Case 1B	Case 2A	Case 2B	Case 3A	Case 3B
Direct capital costs							
Reformer	£m	34.2	34.2	34.2	34.2	34.2	34.2
Calciner &combustor	£m	27.6	27.6	28.5	27.6	27.5	27.5
PSA	£m	39.5	39.5	39.5	39.5	39.5	39.5
CLC unit	£m	0.0	0.0	0.0	0.0	36.4	45.9

ASU	£m	0.0	0.0	37.9	63.4	0.0	0.0
CO_2 compressor	£m	13.5	13.5	20.2	26.1	26.1	26.4
Gas cleaning unit	£m	0.0	3.3	0.0	3.3	0.0	3.3
HRSG & Heat exchangers	£m	27.9	27.9	27.9	27.9	29.8	29.8
Indirect capital cost							
Design and engineering	£m	28.5	29.2	37.6	44.4	40.2	43.2
Contractor's fees	£m	7.1	7.3	9.4	11.1	10.0	10.8
Contingency allowance	£m	7.1	7.3	9.4	11.1	10.0	10.8
Non-Depreciable Capital Costs							
Land	£m	3.2	3.7	3.8	4.4	3.8	4.4
Total capital costs	£m	188.7	193.5	248.4	293.0	264.9	284.9
Operating costs							
Fixed operating costs							
Maintenance	£m	18.9	19.4	24.8	29.3	26.5	28.5
Operating labour cost	£m	1.82	1.82	1.82	1.82	1.82	1.82
Laboratory costs	£m	0.36	0.36	0.36	0.36	0.36	0.36
Supervision	£m	0.18	0.18	0.18	0.18	0.18	0.18
Plant overheads	£m	1.09	1.09	1.09	1.09	1.09	1.09
Local taxes	£m	1.89	1.93	2.48	2.93	2.65	2.85

Insurance rate	£m	1.89	1.93	2.48	2.93	2.65	2.85
Variable operating costs							
Limestone	£m	0.13	0.13	0.13	0.13	0.13	0.13
Ni Catalyst	£m	0.54	0.54	0.54	0.54	0.54	0.54
Fe_2O_3 oxygen carriers	£m	0.00	0.00	0.00	0.00	0.69	1.30
CO_2 storage cost	£m	19.0	19.0	28.3	36.7	36.7	37.1
Boiler feed water	£m	3.14	3.14	3.24	3.14	3.14	3.46
Electricity	£m	27.6	27.6	61.9	73.4	36.2	41.0
Miscellaneous materials	£m	1.82	2.16	2.43	3.25	2.31	2.49
Fuel costs							
Natural gas	£m	159.1	122.8	156.1	122.7	163.0	122.6
Biomass	£m	0.0	51.1	0.0	51.7	0.0	53.1
Total operating costs	£m	237.5	252.9	286.0	329.8	277.5	299.0
LCOH (without CO_2 storage)	£/kg	1.78	2.04	2.12	2.58	2.03	2.31
LCOH (with CO_2 storage)	£/kg	1.90	2.15	2.30	2.80	2.26	2.53
Cost of CO_2 avoided (zero carbon price)	£/tonne	33.0	45.7	57.3	68.6	54.4	52.9
Cost of CO_2 avoided (with carbon price)	£/tonne	-24.7	0.3	10.6	36.2	7.7	20.8

Cost of CO_2 removal (zero carbon price)	£/tonne	57.7	96.9	80.0	106.5	72.7	81.9
Cost of CO_2 removal (with carbon price £16/tonne CO_2)	£/tonne	-38.7	0.5	14.8	56.3	10.2	32.2

Figure 7-4 shows the breakdown of total capital costs of different SE-SMR configurations. The direct capital costs of reformer and calciner are the major share of the SE-SMR process, accounting for 32% to 43% of the total capital costs for each case. The direct capital costs of PSA unit and heat exchangers serve as the second and third largest share of the total capital costs, which constitute values of 13% to 21% and 9% to 15% respectively.

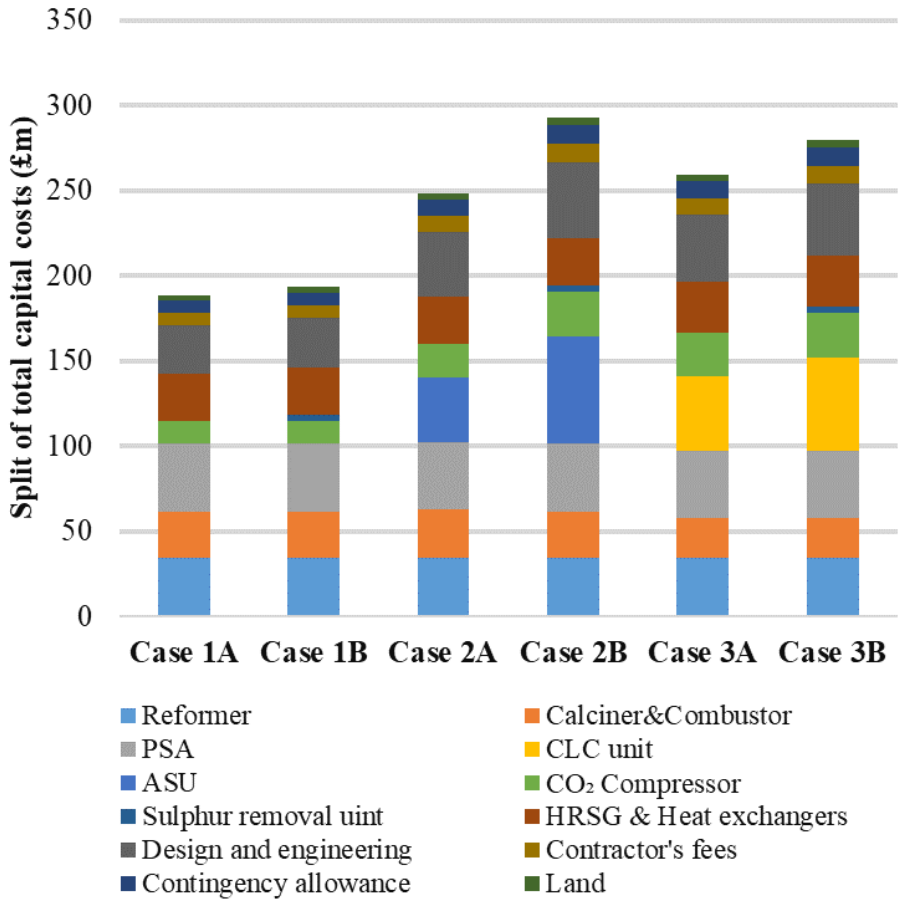

Figure 7-4 Split of total capital costs of SE-SMR hydrogen plants

The breakdown of variable operating costs of different SE-SMR hydrogen plants are shown in **Figure 7-5**. It can be concluded that the CO_2 storage and electricity costs make up the majority of variable operating costs of different SE-SMR hydrogen plants (>88%). Here case 2A and 2B have the greatest share of electricity cost (64.07% and 62.83%), which is due to the installation of an ASU for oxygen production. Although, there is a concern about the decay of the natural CaO sorbent during the CO_2 capture process, the costs of limestone only contribute 0.11% to 0.25% to the total variable operating costs of different SE-SMR configurations based on the lifetime of 500 h. Also, the end use of lime-based sorbents from calcium looping process has been proved successfully for cement production[78], which offers the potential to offset the costs of limestone consumption during the SE-SMR process.

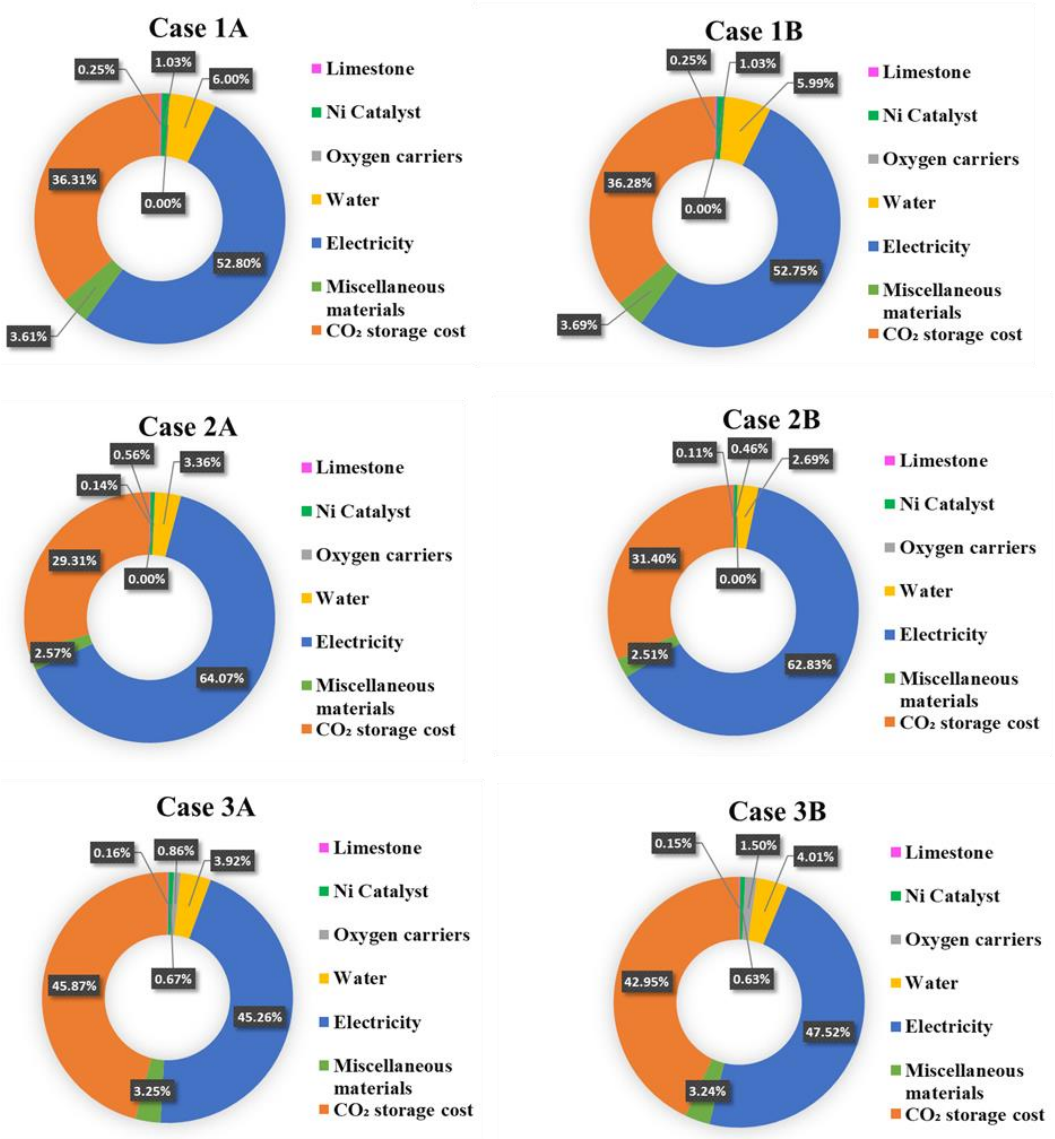

Figure 7-5 Split of the variable operating costs of SE-SMR hydrogen plants

Figure 7-6 presents the levelised cost of hydrogen (LCOH) and distribution of its different components of different SE-SMR hydrogen plants with CO_2 transport and storage. Case 1A has the lowest LCOH (£1.90/kg H_2) among others but the lowest overall CO_2 capture efficiency (60.08%). The LCOH of case 3A is £2.26/kg H_2, which is 18.95% points greater than that of case A and 5.12% points than that of case 1B, but is the most economic pathway for nearly whole CO_2 capture compared that of case 2A, 2B and 3B (£2.30, £2.80 and £2.53/kg H_2). The LCOH of proposed SE-SMR processes in this study is comparable with the LCOH of SMR, ATR and coal with CCS (£1.76 and £2.08/kg H_2), and is more competitive than that of biomass with CCS (£2.8/kg H_2) and electrolysis with renewable energy (£6.38-11.55/kg H_2) [60].

The cost of CO_2 avoided and removal of different SE-SMR processes with/without a carbon price are shown in **Table 7-4**. Interestingly, the cost of CO_2 avoided and removal decreases dramatically by applying a carbon price of £16/tonne CO_2. The calculated cost of CO_2 avoided of different SE-SMR processes proposed in this work is in the range of £32.97 to £68.55/tonne CO_2, which is lower than that of SMR with MDEA (£104.92/tonne CO_2), CLR (£78.10/tonne CO_2) [25] and ATR (£64.31/tonne CO_2, excluding case 2B) [26]. The estimated cost of CO_2 removal for carbon-negative hydrogen production in the case 2B and 3B is £106.50/tonne CO_2 and £81.91/tonne CO_2 respectively, which is significantly lower than that of biomass-derived hydrogen with carbon capture and storage (BHCCS)- £149/tonne CO_2 reported in [61].

The costs of integration of SMR with CCS technologies have been extensively investigated over the past two decades. The cost of hydrogen from these studies varies from £0.95-2.18/kg H_2 for capture rates from 60-90%, and their cost of CO_2 avoided ranges from £13-106/tonne CO_2 [60]. Compared with the economic performance of the cases presented in this work, it can be concluded that the economic performance of different SE-SMR configurations proposed in this work is promising and comparable with that of currently available SMR with CCS technology. Furthermore, the case 2B and 3B can achieve negative CO_2 emissions from H_2 production with a moderate LCOH (£2.80 and £2.53/kg H_2) and cost of CO_2 avoided (£68.55 and £52.90/tonne CO_2). When the carbon price of £16/tonne CO_2 is employed, it further reduces their cost of CO_2 avoided to £36.24 and £20.79/tonne CO_2 respectively.

Notably, the estimated production cost of hydrogen from natural gas and cost of CO_2 avoided are influenced by various technical and economic factors, for instance, the complexity and accuracy of the techno-economic models and uncertainty of the input variables (e.g. natural gas price, capital costs of equipment, CO_2 storage cost and carbon price). In the next section, the impacts of uncertainty in the input variables on the levelised cost of hydrogen for different SE-SMR configurations are discussed.

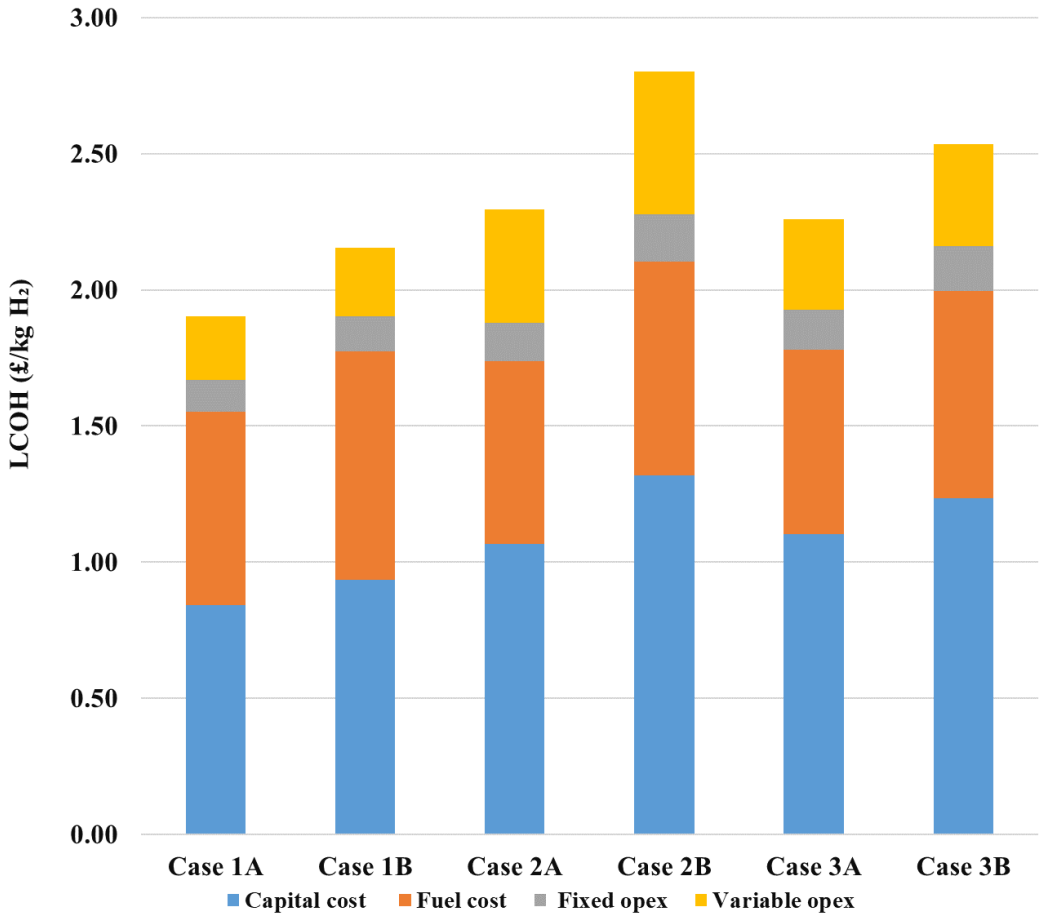

Figure 7-6 Distribution of different costs of levelised cost of hydrogen for different SE-SMR processes

7.3.2.2 Sensitivity Analysis

The LCOH is one of the key economic performance indicators for SE-SMR hydrogen plants, which is affected by different technical and economic factors. A sensitivity analysis including the effects of uncertainty in the total direct capital costs (TDCC), discount rate, fuel costs, CO_2 storage cost, operating capacity factor and net efficiency on the LCOH of the different SE-SMR processes was conducted to investigate the economic performance of SE-SMR plants in the presence of uncertainty.

The SE-SMR processes are highly sensitive to the fuel costs as seen in **Figure 7-7 (c)**. The reference price of natural gas and biomass is £15.41/MWh and £19.00/MWh respectively, and a change in their price by ±30% points affects the LCOH for SE-SMR plants by an average of -12.46-18.69% points. Due to the low TRL of the SE-SMR process and lack of published data on the capital cost of commercial scale SE-SMR hydrogen plant, ±30% change is considered to investigate the impacts on the LCOH for different SE-SMR processes and the results are shown in **Figure 7-7 (a)**. This changes the LCOH for SE-SMR plants by an average of ±4.67% points compared that of reference cases.

Discount rates for low-carbon and renewable generation technologies are significantly influenced by the maturity of technology, systematic and policy risk. In this study, a discount rate of 12% has been applied to the base cases of SE-SMR processes, and it is reasonable to estimate it will fluctuate in the range of 6 to 14% according to [41]. **Figure 7-7 (b)** illustrates the increase of discount rate from 6% to 14% rises the LCOH of SE-SMR processes by an average of 3.58% points. A ±30% change in the CO_2 storage cost in the base cases acts the average of -1.54% to 2.31% points on the LCOH of base SE-SMR processes as **Figure 7-7 (d)** shown. The increase of operating capacity factor from 80% to 100% reduces the LCOH by an average of 3.83% points (**Figure 7-7 (e)**). In the **Figure 7-7 (d)**, when the net efficiency of base cases decreases by 10% points, the LCOH rises by an average of 6.92% points. On the other hand, with an increase of the net efficiency in the base cases by 10% points, the LCOH declines by an average of 5.66%.

Based on the sensitivity analysis, it is clear that the economic performance of SE-SMR processes proposed in this work is mainly affected by the fuel costs of natural gas and biomass, followed by the net efficiency, TDCC, discount rate and CO_2 storage cost. This generally agrees well with other techno-economic assessment work on SMR with/without CCS or SE-SMR for hydrogen production in [1,16].

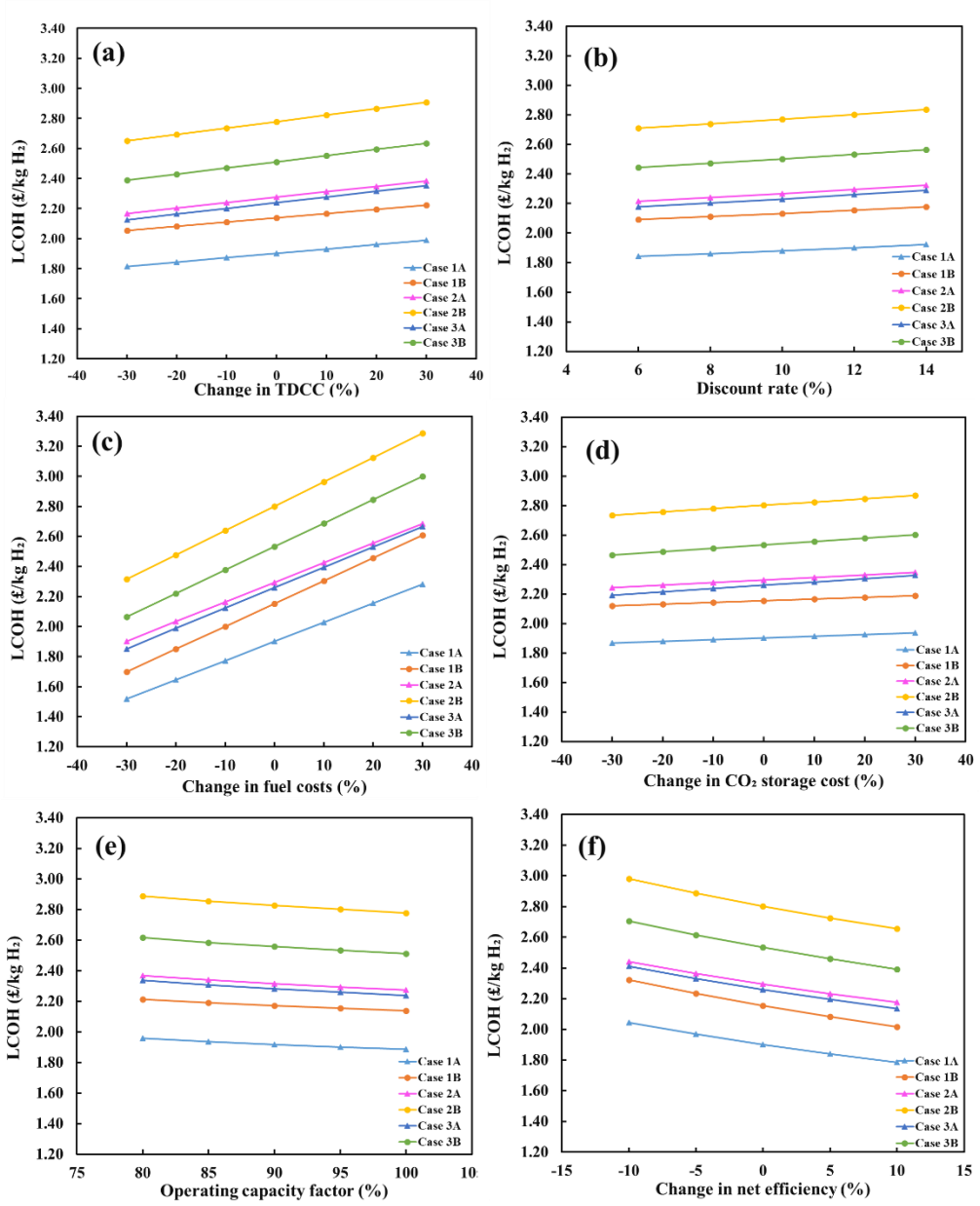

Figure 7-7 Sensitivity analyses a) TDCC vs LCOH, b) Discount rate vs LCOH, c) Fuel costs vs LCOH, d) CO_2 storage costs vs LCOH, e) Operating capacity factor vs LCOH, f) Net efficiency vs LCOH.

Discounted cash flow analysis is an important technique for translating the net future cash flows of the project to the net present value (NPV), which gives a clear indication of the resources required for a project and the timing of earning. **Figure 7-8** presents the cumulative discounted cash flow of proposed SE-SMR processes in this work with hydrogen selling price of £2.20, £2.60 and £3.00/kg H_2. Here case 2B and 3B cannot make any revenue when the hydrogen selling price is assumed to be less than £2.20/kg. When the hydrogen price is increased from £2.20/kg to £2.60/kg, all the proposed SE-SMR processes can make profits after the 13th year of the project. At a

hydrogen selling price of £3.00/kg, the payback time of case 1A and 1B is 5 years, followed by 6 years for cases 2A and 3A, 7 years for case 3B, and 8 years for case 2B.

Notably, the hydrogen selling price play a crucial role in the economic performance of hydrogen production plants. Although the current hydrogen selling price is approximately £7.50/kg H_2 at hydrogen vehicle refuelling stations in the UK [62] and the transaction prices of hydrogen are in the range of £1.40/kg to £3.60/kg in terms of scale and purity [63], the proposed SE-SMR processes in this study shows that blue and carbon negative hydrogen are able to achieve significant economic gains with a hydrogen selling price of only from £2.20 to 3.00/kg H_2.

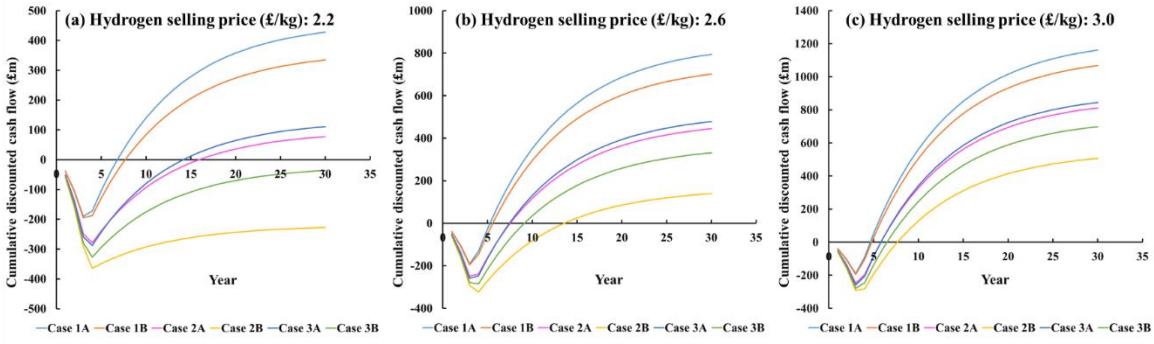

Figure 7-8 Cumulative discounted cash flow of SE-SMR plants under different hydrogen selling price

7.4 Conclusions

This work presents a detailed techno-economic assessment of six SE-SMR configurations for large-scale blue and carbon-negative hydrogen production. The impact of incorporating oxy-fuel combustion, chemical-looping combustion and CO_2 compression unit, and using biomass as the feedstock for providing combustion heat to the calciner on the net efficiency, CO_2 capture efficiency, levelised cost of hydrogen, CO_2 avoided and removal cost of the proposed cases were also evaluated. Results indicated that the retrofitted SE-SMR processes could provide flexible options for low-carbon hydrogen production based on the costs and demand of CO_2 reduction and were comparable with SMR with CCS technologies.

The replacement of natural gas by biomass in the calciner has improved the CO_2 captured for all the cases, but reduced their net efficiency by an average of 8.25%

points. SE-SMR with indirect air-natural gas combustion calciner (case 1A) has the highest net efficiency (76.96%) and the lowest LCOH (£1.90/kg H_2), but only 60.06% CO_2 is captured. The replacement of natural gas by biomass in the calciner (case 1B) can increase the CO_2 capture efficiency to 86.08% with the LCOH of £2.15/kg H_2. In case 2A (SE-SMR with indirect oxy-natural gas combustion calciner) and case 3A (SE-SMR with indirect calciner heated by chemical-looping combustion with natural gas) can realise almost complete CO_2 capture and pure hydrogen production, but case 3A is more economically favourable than case 2A in terms of LCOH and costs of CO_2 avoided and removal. With the use of biomass in case 2B and case 3B, this can achieve carbon-negative hydrogen production, which removes 5.42 kg and 5.52 kg of CO_2 respectively from the atmosphere per kg hydrogen produced but with the highest LCOH and costs of CO_2 avoided and removal. By applying a carbon price (£16/tonne CO_2) it is possible to reduce the costs of CO_2 avoided and removal significantly.

The results of sensitivity analyses indicated that fuel costs of natural gas and biomass are the major factor affecting the economic performance of proposed SE-SMR processes, followed by net efficiency, total direct capital costs of equipment and CO_2 storage costs. Cumulative discounted cash flow of the proposed SE-SMR plants with hydrogen selling price from £2.20-3.00 was calculated to analyse the profitability and payback time. With a hydrogen selling price of £3.00/kg, investment in any of the proposed SE-SMR plants can be paid back after eight years without employing a carbon price.

7.5 References

[1] IEA. The Future of Hydrogen. 2019. doi:10.1787/1e0514c4-en.

[2] Voldsund M, Jordal K, Anantharaman R. Hydrogen production with CO_2 capture. Int J Hydrogen Energy 2016;41:4969–92. doi:10.1016/j.ijhydene.2016.01.009.

[3] Ji G, Yao JG, Clough PT, Da Costa JCD, Anthony EJ, Fennell PS, et al. Enhanced hydrogen production from thermochemical processes. Energy Environ Sci 2018;11:2647–72. doi:10.1039/c8ee01393d.

[4] Muradov N. Low to near-zero CO_2 production of hydrogen from fossil fuels: Status and perspectives. Int J Hydrogen Energy 2017;42:14058–88. doi:10.1016/j.ijhydene.2017.04.101.

[5] Cormos CC, Petrescu L, Cormos AM. Assessment of hydrogen production systems based on natural gas conversion with carbon capture and storage. Comput. Aided Chem. Eng., vol. 33, Elsevier B.V.; 2014, p. 1081–6. doi:10.1016/B978-0-444-63455-9.50015-5.

[6] Johnsen K, Ryu HJ, Grace JR, Lim CJ. Sorption-enhanced steam reforming of methane in a fluidized bed reactor with dolomite as CO_2-acceptor. Chem Eng Sci 2006;61:1195–202. doi:10.1016/j.ces.2005.08.022.

[7] García-Lario AL, Aznar M, Martinez I, Grasa GS, Murillo R. Experimental study of the application of a NiO/NiAl2O4 catalyst and a CaO-based synthetic sorbent on the Sorption Enhanced Reforming process. Int J Hydrogen Energy 2015;40:219–32. doi:10.1016/j.ijhydene.2014.10.033.

[8] Arstad B, Prostak J, Blom R. Continuous hydrogen production by sorption enhanced steam methane reforming (SE-SMR) in a circulating fluidized bed reactor: Sorbent to catalyst ratio dependencies. Chem Eng J 2012;189–190:413–21. doi:10.1016/j.cej.2012.02.057.

[9] Di Giuliano A, Gallucci K, Kazi SS, Giancaterino F, Di Carlo A, Courson C, et al. Development of Ni- and CaO-based mono- and bi-functional catalyst and sorbent materials for Sorption Enhanced Steam Methane Reforming: Performance over 200 cycles and attrition tests. Fuel Process Technol 2019;195:106160. doi:10.1016/j.fuproc.2019.106160.

[10] Broda M, Manovic V, Imtiaz Q, Kierzkowska AM, Anthony EJ, Müller CR. High-purity hydrogen via the sorption-enhanced steam methane reforming reaction over a synthetic CaO-based sorbent and a Ni catalyst. Environ Sci Technol 2013;47:6007–14. doi:10.1021/es305113p.

[11] Chen J, Donat F, Duan L, Kierzkowska AM, Min Kim S, Xu Y, et al. Metal-oxide stabilized CaO/CuO Composites for the Integrated Ca/Cu Looping Process. Chem Eng J 2020;403:126330. doi:10.1016/j.cej.2020.126330.

[12] Ochoa-Fernández E, Haugen G, Zhao T, Rønning M, Aartun I, Børresen B, et al. Process design simulation of H_2 production by sorption enhanced steam methane reforming: Evaluation of potential CO_2 acceptors. Green Chem., vol. 9, Royal Society of Chemistry; 2007, p. 654–62. doi:10.1039/b614270b.

[13] Zhu L, Li L, Fan J. A modified process for overcoming the drawbacks of conventional steam methane reforming for hydrogen production: Thermodynamic investigation. Chem Eng Res Des 2015;104:792–806. doi:10.1016/j.cherd.2015.10.022.

[14] Alam S, Kumar JP, Rani KY, Sumana C. Self-sustained process scheme for high purity hydrogen production using sorption enhanced steam methane reforming coupled with chemical looping combustion. J Clean Prod 2017;162:687–701. doi:10.1016/j.jclepro.2017.05.136.

[15] Abanades JC, Murillo R, Fernandez JR, Grasa G, Martínez I. New CO_2 capture process for hydrogen production combining Ca and Cu chemical loops. Environ Sci Technol 2010;44:6901–4. doi:10.1021/es101707t.

[16] Diglio G, Hanak DP, Bareschino P, Mancusi E, Pepe F, Montagnaro F, et al. Techno-economic analysis of sorption-enhanced steam methane reforming in a fixed bed reactor network integrated with fuel cell. J Power Sources 2017;364:41–51. doi:10.1016/j.jpowsour.2017.08.005.

[17] Yan Y, Thanganadar D, Clough PT, Mukherjee S, Patchigolla K, Manovic V, et al. Process simulations of blue hydrogen production by upgraded sorption enhanced steam methane reforming (SE-SMR) processes. Energy Convers Manag 2020;222:113144. doi:10.1016/j.enconman.2020.113144.

[18] Abanades JC, Murillo R, Fernandez JR, Grasa G, Martínez I. New CO_2 capture process for hydrogen production combining Ca and Cu chemical loops. Environ Sci Technol 2010;44:6901–4. doi:10.1021/es101707t.

[19] Antzara A, Heracleous E, Lemonidou AA. Energy efficient sorption enhanced-chemical looping methane reforming process for high-purity H_2 production: Experimental proof-of-concept. Appl Energy 2016;180:457–71. doi:10.1016/j.apenergy.2016.08.005.

[20] Martini M, van den Berg A, Gallucci F, van Sint Annaland M. Investigation of the process operability windows for Ca-Cu looping for hydrogen production with CO_2 capture. Chem Eng J 2016;303:73–88. doi:10.1016/j.cej.2016.05.135.

[21] Fernandez JR, Abanades JC, Grasa G. Modeling of sorption enhanced steam methane reforming-Part II: Simulation within a novel Ca/Cu chemical loop process for hydrogen production. Chem Eng Sci 2012;84:12–20. doi:10.1016/j.ces.2012.07.050.

[22] Reitza M, Junka M, Ströhlea J, Epplea B. Design and erection of a 300 kWth indirectly heated carbonate looping test facility. Energy Procedia, vol. 63, Elsevier Ltd; 2014, p. 2170–7. doi:10.1016/j.egypro.2014.11.236.

[23] Reitz M, Junk M, Ströhle J, Epple B. Design and operation of a 300 kWth indirectly heated carbonate looping pilot plant. Int J Greenh Gas Control 2016;54:272–81. doi:10.1016/j.ijggc.2016.09.016.

[24] Junk M, Reitz M, Strohle J, Epple B. Technical and economical assessment of the indirectly heated carbonate looping process. J Energy Resour Technol Trans ASME 2016;138. doi:10.1115/1.4033142.

[25] Spallina V, Shams A, Battistella A, Gallucci F, Annaland MVS. Chemical Looping Technologies for H_2 Production with CO_2 Capture: Thermodynamic Assessment and Economic Comparison. Energy Procedia, vol. 114, Elsevier Ltd; 2017, p. 419–28. doi:10.1016/j.egypro.2017.03.1184.

[26] Khojasteh Salkuyeh Y, Saville BA, MacLean HL. Techno-economic analysis and life cycle assessment of hydrogen production from natural gas using current and emerging technologies. Int J Hydrogen Energy 2017;42:18894–909. doi:10.1016/j.ijhydene.2017.05.219.

[27] Spallina V, Pandolfo D, Battistella A, Romano MC, Van Sint Annaland M, Gallucci F. Techno-economic assessment of membrane assisted fluidized bed reactors for pure H_2 production with CO_2 capture. Energy Convers Manag 2016;120:257–73. doi:10.1016/j.enconman.2016.04.073.

[28] Nazir SM, Cloete JH, Cloete S, Amini S. Pathways to low-cost clean hydrogen production with gas switching reforming. Int J Hydrogen Energy 2020. doi:10.1016/j.ijhydene.2020.01.234.

[29] Yan Y, Clough PT, Anthony EJ. Investigation of the apparent kinetics of air and oxy-fuel biomass combustion in a spout fluidised-bed reactor. Chem Eng Res Des 2020;153:276–83. doi:10.1016/j.cherd.2019.10.043.

[30] Aspen Technology. Aspen Physical Property Methods. 2013.

[31] Element Energy. Hydrogen supply chain evidence base. 2018.

[32] Global CCS Institute. CCS: A Critical Technology for Saving our Environment 2017. https://www.globalccsinstitute.com/wp-content/uploads/2018/12/2017-Global-Status-Report.pdf.

[33] Tees Valley Mayor. Hydrogen & the Tees Valley. https://ukccsrc.ac.uk/wp-content/uploads/2020/07/Tees-Valley-16072020.pdf.

[34] Ortiz C, Valverde JM, Chacartegui R, Perez-Maqueda LA, Giménez P. The Calcium-Looping ($CaCO_3$/CaO) process for thermochemical energy storage in Concentrating Solar Power plants. Renew Sustain Energy Rev 2019;113:109252. doi:10.1016/j.rser.2019.109252.

[35] Ortiz M, Gayán P, De Diego LF, García-Labiano F, Abad A, Pans MA, et al. Hydrogen production with CO_2 capture by coupling steam reforming of methane and chemical-looping combustion: Use of an iron-based waste product as oxygen carrier burning a PSA tail gas. J. Power Sources, vol. 196, Elsevier; 2011, p. 4370–81. doi:10.1016/j.jpowsour.2010.09.101.

[36] Inc AT. Aspen Plus: Getting Started Modeling Processes with Solids 2009:1–96.

[37] Tranier J-P, Dubettier R, Perrin N, Air Liquide. Air Separation Unit for Oxy-Coal Combustion Systems. 1st Int. Oxyfuel Combust. Conf., 2009.

[38] Wall T, Liu Y, Spero C, Elliott L, Khare S, Rathnam R, et al. An overview on oxyfuel coal combustion-State of the art research and technology development. Chem Eng Res Des 2009;87:1003–16. doi:10.1016/j.cherd.2009.02.005.

[39] Denys F, De Vries W. Gas Composition Transition Agency Report 2013 The status of the transition to high-calorific-value gas Date 1 August 2013 Status Final for publication.

[40] R. K. Sinnott, J. M. Coulson JFR. Coulson and Richardson's Chemical Engineering Volume 6 - Chemical Engineering Design (4th Edition). 2005. doi:10.1016/b978-0-08-041865-0.50014-3.

[41] Oxera. Discount rates for low-carbon and renewable generation technologies Prepared for the Committee on Climate Change. 2011.

[42] HM Revenue & Customs. Policy paper: Carbon Emissions Tax. Policy Pap 2018. https://www.gov.uk/government/publications/carbon-emmisions-tax/carbon-emmisions-tax (accessed August 19, 2020).

[43] Kew Projects Ltd. Kew H2: Zero-Carbon Bulk Supply. 2019.

[44] MacKenzie A, Granatstein DL, Anthony EJ, Abanades JC. Economics of CO_2 capture using the calcium cycle with a pressurized fluidized bed combustor. Energy and Fuels 2007;21:920–6. doi:10.1021/ef0603378.

[45] Porrazzo R, White G, Ocone R. Techno-economic investigation of a chemical looping combustion based power plant 2016. doi:10.1039/c6fd00033a.

[46] Nadir M, Ghenaiet A, Carcasci C. Thermo-economic optimization of heat recovery steam generator for a range of gas turbine exhaust temperatures. Appl Therm Eng 2016;106:811–26. doi:10.1016/j.applthermaleng.2016.06.035.

[47] Cormos CC. Economic evaluations of coal-based combustion and gasification power plants with post-combustion CO_2 capture using calcium looping cycle. Energy 2014;78:665–73. doi:10.1016/j.energy.2014.10.054.

[48] Porter RTJ, Fairweather M, Kolster C, Dowell N Mac, Shah N, Woolley RM. Cost and performance of some carbon capture technology options for producing different quality CO_2 product streams.

[49] Maas W. The post-2020 Cost-Competitiveness of CCS Cost of Storage.

[50] Wood. Hydrogen Supply Programme – Novel Steam Methane / Gas Heated Reformer 2020:1–22.

[51] United Kingdom electricity prices, September 2019| GlobalPetrolPrices.com https://www.globalpetrolprices.com/United-Kingdom/electricity_prices/ (accessed June 12, 2020).

[52] Standard rates | Anglian Water Services https://www.anglianwater.co.uk/account-and-bill/tariffs-and-charges/standard-rates/ (accessed June 12, 2020).

[53] Nickel Catalyst / Z111 Series Primary Steam-reforming Catalysts - Buy Nickel Catalyst,Primary Steam-reforming Catalysts,Nickel Catalyst Manufacturer Product on Alibaba.com n.d. https://www.alibaba.com/product-detail/Nickel-catalyst-Z111-series-primary-steam_62339979053.html?spm=a2700.galleryofferlist.0.0.11215a45D0GM56&bypass=true (accessed June 12, 2020).

[54] Longcliffe. https://www.longcliffe.co.uk/ (accessed June 12, 2020).

[55] Diego ME, Arias B, Abanades JC. Modeling the solids circulation rates and solids inventories of an interconnected circulating fluidized bed reactor system for CO_2 capture by calcium looping. Chem Eng J 2012;198–199:228–35. doi:10.1016/j.cej.2012.05.099.

[56] Lyngfelt A, Leckner B. A 1000 MWth boiler for chemical-looping combustion of solid fuels – Discussion of design and costs. Appl Energy 2015;157:475–87. doi:10.1016/j.apenergy.2015.04.057.

[57] Land Value Estimates for Policy Appraisal : May 2017 Values.

[58] 2019 Chemical Engineering Plant Cost Index Annual Average - Chemical Engineering | Page 1 https://www.chemengonline.com/2019-chemical-engineering-plant-cost-index-annual-average/ (accessed June 12, 2020).

[59] Erans M, Jeremias M, Zheng L, Yao JG, Blamey J, Manovic V, et al. Pilot testing of enhanced sorbents for calcium looping with cement production. Appl Energy 2018;225:392–401. doi:10.1016/j.apenergy.2018.05.039.

[60] Parkinson B, Balcombe P, Speirs JF, Hawkes AD, Hellgardt K. Levelized cost of CO_2 mitigation from hydrogen production routes. Energy Environ Sci 2019;12:19–40. doi:10.1039/c8ee02079e.

[61] Bui M, Fajardy M, Zhang D, Mac Dowell N. Delivering negative emissions from biomass derived hydrogen 2020:1–81.

[62] London: a capital for hydrogen and fuel cell technologies. 2016.

[63] Glenk G, Reichelstein S. Economics of converting renewable power to hydrogen. Nat Energy 2019;4:216–22. doi:10.1038/s41560-019-0326-1.

8 Conclusions and Recommendations for Future Work

8.1 General Conclusions

Carbon capture and storage (CCS) is well recognised technology that can significantly reduce the global greenhouse gas (GHG) emissions to deliver a 2 °C climate goal, but which has not been widely deployed. Currently, COVID-19 has provided a timely warning of what happens when the relationship between human and nature is broke down. This lesson can also be applied to climate change and global warming. It is a good opportunity for us to awareness the serious situations of the climate change and global warming, and work together to solve these challenges. This thesis is focused on solving the key issues and barriers related to scale-up oxy-fuel and chemical-looping combustion, and low-carbon hydrogen production via sorption enhanced steam methane reforming (SE-SMR).

Firstly, a lab-scale fluidised-bed reactor that can be operated at flexible temperature, gas mixtures and pressure has been built and retrofitted during this PhD study to investigate the reaction kinetics of woody biomass and its char under the air and oxy-fuel combustion conditions. The detailed design and standard operation procedure of this reactor can be found in Chapter 3 and 4. Compared to the traditional TGA for kinetic measurement, the combustion kinetics measured by the fluidised-bed reactor is more close to the realistic conditions with the advantages of high heating rates and minimised heat and mass transfer resistances. In Chapter 3, the air and oxy-fuel combustion reactions of raw woody biomass have been investigated in a bench-scale, spouted fluidised-bed reactor. Combustion experiments were conducted under the different oxygen concentrations (20-35 vol%), and across a range of bed temperatures (923-1073 K). The shrinking core model was fitted to the carbon conversion data and well represented the reaction kinetics observed, with the largest deviation occurring in the initial stages of combustion. It is found that the measured rate of oxy-fuel combustion is higher (~37.5%) than that of air combustion under the same conditions. The apparent orders of reaction for air and oxy-fuel combustion of biomass in the spouted fluidised-bed reactor were found to be approximately zero. The activation energies for air and oxy-fuel combustion of biomass were found to be 18.95 kJ/mol and 26.93 kJ/mol, respectively. It should be noted that this work measured the apparent kinetics of woody biomass in the fluidised-bed reactor under the air and oxy-fuel combustion conditions, which represents the averaged kinetics of multi-stages of

woody combustion (devolatilisation and volatile combustion of woody biomass and char combustion). In order to obtain the intrinsic air and oxy-fuel combustion kinetics of wood char, char produced from the devolatilisation of woody biomass under N_2 and CO_2 was used for char combustion tests in a bubbling fluidised-bed reactor (retrofitted from the spouted fluidised-bed reactor reported in Chapter 3). The experimental results indicate that the corrected rates of char combustion in O_2/CO_2 are about 13% points higher than that in O_2/N_2 at the same conditions. The apparent order of reaction is 0.41 (R^2= 0.84) for char combustion under O_2/N_2 and 0.44 (R^2= 0.95) for char combustion under O_2/CO_2. The activation energies for char combustion under O_2/N_2 and O_2/CO_2 at the oxygen concentration of 20% were calculated to be 20.03 (R^2= 0.90) and 26.58 (R^2= 0.91) kJ/mol, respectively. There is more CO generated during the char combustion in O_2/CO_2 than that in O_2/N_2. Hence, the impact of char-CO_2 gasification should be taken into account for the retrofit of current fluidised-bed biomass boilers as well as design of new oxy-fuel biomass combustion fluidised-bed boilers.

In Chapter 5, the author was first to propose to harness the power of machine learning in screening the oxygen carrying materials for chemical-looping process. This novel method is envisaged to play a crucial role in developing suitable oxygen carriers for chemical-looping processes, especially for the low-cost, heterogeneous and multi-component ores and industrial byproduct. This idea was demonstrated by using machine learning algorithms named artificial neural networks (ANNs) to predict the reactivity of manganese ores as oxygen-carrying materials in chemical-looping processes. It indicated that trained ANNs can provide very good performance predictions for heterogeneous, multi-component materials (oxygen carrier ores) for chemical-looping processes. These models were tested on unseen experimental and their high level of accuracy and generality were demonstrated. The most optimal ANN model for the manganese ores reactivity predictions had a topology of 14-13-3 and was trained with the trainbr algorithm, which was able to achieve the highest R^2 (0.94) and lowest MAE (0.057).

H_2 is versatile and also has the potential to act as a clean energy carrier to tackle various critical energy challenges. But the current H_2 production is also a CO_2 intensive process based on steam methane reforming or coal gasification. SE-SMR as an emerging blue hydrogen technology can produce the decarbonised H_2 at low costs

and high efficiency, but there is lack of work in investigating the further CO_2 emissions reduction from its calciner and steam generator. Oxy-fuel and chemical-looping combustion are promising carbon capture technologies, which are also feasible to be integrated with SE-SMR to solve these issues. In Chapter 6, six process arrangements for sorption enhanced steam methane reforming (SE-SMR) were proposed for blue H_2 production: 1) SE-SMR with an air fired calciner, 2) SE-SMR with a Pressure Swing Adsorption (PSA) unit, 3) SE-SMR thermally coupled with Chemical-Looping Combustion (CLC), 4) SE-SMR+PSA+CLC, 5) SE-SMR+PSA with an oxy-fired calciner, 6) SE-SMR+PSA and indirect firing H_2 combustion from the product stream recycle. A thermodynamic analysis using Aspen Plus with a detailed heat exchanger modelling to recover the waste heat from the process was conducted to evaluate the process performance in terms of methane conversion, CO_2 capture efficiency, H_2 purity, maximum cold gas efficiency and net efficiency. The results indicated that the proposed cases can provide flexible options for low-carbon hydrogen production based on the costs and demand of CO_2 reduction. The process of SE-SMR+PSA+CLC can realise nearly 100% CO_2 capture efficiency with the highest net efficiency of 75.5% in terms of near pure hydrogen production at a reformer temperature of 600 °C, a reformer pressure of 25 bar, and a S/C = 5, whilst the integration of oxy-combustion achieves the same CO_2 capture efficiency with nearly 100% hydrogen purity but with a 2.7% points penalty in the net efficiency. On the other hand, Case 6 where a proportion of the H_2 is recycled to provide heat for the calcination is able to achieve 94.2% carbon capture efficiency with a trade-off in the process efficiency.

Upon the thermodynamic analysis of the above different SE-SMR processes, it is also necessary to evaluate their economic performance to explore their feasibility to be deployed in the large-scale. In Chapter 7, a detailed techno-economic assessment of six SE-SMR configurations for large-scale low-carbon hydrogen production is presented. The impact of incorporating oxy-fuel combustion, chemical-looping combustion and CO_2 compression unit, and using biomass as the feedstock for providing combustion heat to the calciner on the net efficiency, CO_2 capture efficiency, levelised cost of hydrogen, CO_2 avoided and removal cost of the proposed cases were also evaluated. The replacement of natural gas by biomass in the calciner has improved the CO_2 capture efficiency for all the cases, but reduced their net efficiency by an average of 8.25% points. SE-SMR with indirect air-natural gas heated calciner

(case 1A) has the highest net efficiency (76.96%) and the lowest LCOH (£1.90/kg H_2), but only 60.06% CO_2 is captured. The replacement of natural gas by biomass in the calciner (case 1B) can increase the CO_2 capture efficiency to 86.08% with the LCOH of £2.15/kg H_2. The LCOH of the proposed SE-SMR plants ranged from £1.90-2.80/kg, and the costs of CO_2 avoided and removal ranged from £33-69/tonne and £58-107/tonne, respectively. By applying a carbon price (£16/tonne CO_2), the costs of CO_2 avoided and removal for the proposed SE-SMR processes could be significantly reduced. The results of cumulative discounted cash flow of SE-SMR plants at a hydrogen selling price of £3.00/kg indicated that all the investment of the proposed cases could be paid back after eight years, even if carbon tax is zero. The sensitivity analysis indicated that fuel costs of natural gas and biomass are the major factor affecting the economic performance of proposed SE-SMR processes, followed by net efficiency, total direct capital costs of equipment and CO_2 storage costs.

In conclusion, this PhD project addressed some of the key challenges of deploying oxy-fuel and chemical-looping combustion technologies. Combustion kinetics and suitable oxygen carries are one of the key factors to accelerate the development of oxy-fuel and chemical-looping combustion. The measured air and oxy-fuel combustion kinetics of biomass combustion from the fluidised-bed reactor can provide useful information for retrofit the current boilers as well as design of new boilers. The use of machine learning for oxygen carriers can accelerate the finding and designing cost-effective oxygen carriers for large-scale CLC. In addition, this project also explore the feasibility of the integration of oxy-fuel combustion and CLC with SE-SMR for large-scale low-carbon hydrogen production. The findings indicate that oxy-fuel combustion and CLC are promising to be integrated with SE-SMR in a large-scale, which has a competitive price.

8.2 Recommendations for Future Work

The work presented in this thesis dealt with the key challenges across reaction kinetics of oxy-fuel combustion of biomass, applications of machine learning in oxygen carriers and techno-economic performance of SE-SMR process. It can be further extended through a series future work to have a better understanding these research fields and accelerate the deployment of these low-carbon technologies to tackle the climate change.

Some potential areas and research directions of future work include:

1. The effects of pressure on air and oxy-fuel combustion kinetics of biomass are not investigated in this work. Future researchers can measure and compare the combustion kinetics of different solid fuels in a lab-scale fluidised-bed reactor, which will provide more useful information for scale-up pressurised air and oxy-fuel combustion of biomass.
2. The batch fuel feeding system in this work can be retrofitted to an automatic feeding valve to reduce the preparing work and feeding time for the test. This will need to install a pressurised cylinder with several electronic valves on the current feeding system, as well as the code in VEE programme.
3. The success in applying machine learning for oxygen carriers suggests it is also feasible to apply machine learning for CO_2 sorbents, such as lime-based sorbents. It is potential to use machine learning to predict their CO_2 capacity and cyclic performance or develop optimal synthesis methods to reduce the experimental time and costs.
4. It was noted that the collection of experimental data of oxygen carriers from different research groups to create the training data for the machine learning models was hard and time consuming, because the difference in data and performance evaluation as well as the lack of data. It is recommended that future researchers can use online materials database such as materials project to obtain sufficient data for machine learning to screen suitable oxygen carrying materials.
5. Finally, since the research shows a very promising techno-economic performance of the SE-SMR integrated with indirectly heated calciner or CLC processes. It is recommended that a pilot-scale of these processes can be constructed to further improve their technology readiness level. Here too, machine learning is envisaged to play a vital role in design and screening of suitable sorbents and catalysts during this process.

Appendices

Appendix A Biomass Combustion Kinetics Measurement using a Fluidised-bed Reactor

A.1 Operation Conditions

Table_Apx A-1 Operating conditions used in tests

Combustion Mode	Bed Temperature (K)	O_2 Concentration (vol.%)	CO_2 Concentration (vol.%)	N_2 Concentration (vol.%)	Total flow rate (mL/s)
Air Combustion	923	20	0	80	50.19
	973	25	0	75	50.19
	1023	30	0	70	50.19
	1073	35	0	60	50.19
Oxy-fuel Combustion	923	20	75	5	50.33
	973	25	70	5	50.33
	1023	30	65	5	50.33
	1073	35	60	5	50.33

A.2 Validation of Well-mixed Assumption

To validate that the fluidised bed reactor is a well-mixed system, the cross-flow factor was experimentally determined using a method published elsewhere [1,2]. The measured ratio CO_{2out}/CO_{2in} was plotted against the varied mass of fuel samples added to the reactor at a bed temperature of 923 K in **Figure_Apx A-1**. The best-fit values for the cross-flow factor, *Xf,* was calculated to be 39.23, which indicated a high degree of mixing within the bed and a similar concentration of gases within the particulate and bubble phases of the fluidized bed.

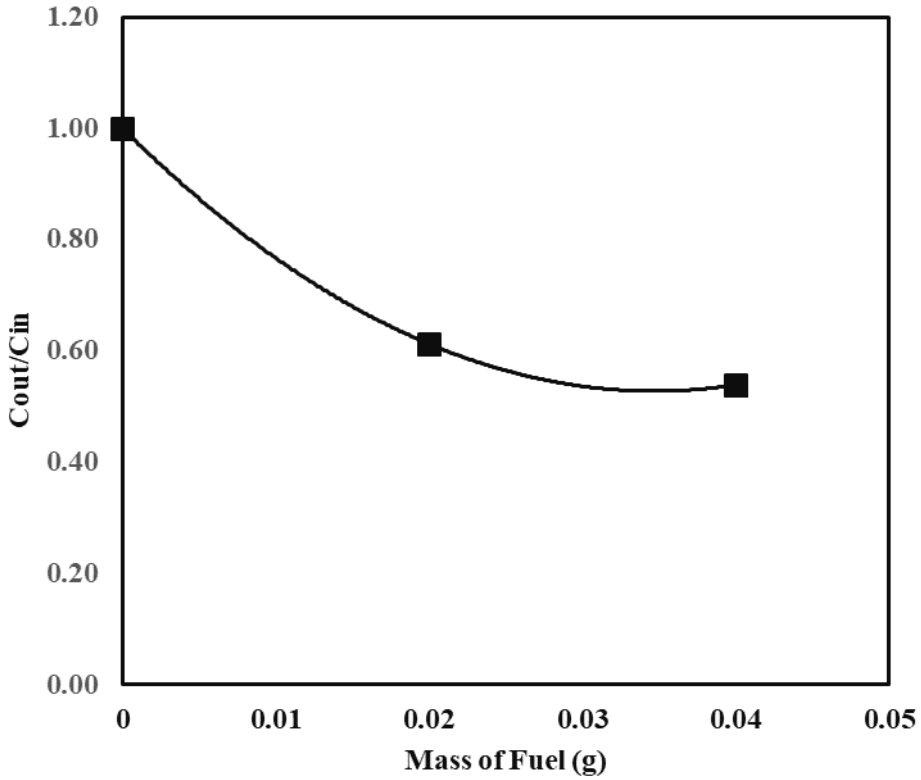

Figure_Apx A-1 The ratio of oxygen outlet and inlet concentrations plotted against the mass of fuel at conditions of 923K, 25 vol% O_2/75 vol% N_2, U/U_{mf} = 3, and 1 bar (a).

A.3 Deconvolution and adjustment of analyser signal

To achieve the real-time measured gas concentration, it is necessary to consider the response time of the test rig. In this work we used the deconvolution of the measured gas concentration following a published method in [3].

To characterise response time, three 'step' CO_2 increases were simulated in the gas fluidising bed at 293K and 1023K, U/U_{mf} = 3 and 1 bar(a) by the process control system, as shown in **Figure_Apx A-2**. This process was assumed as a continuous stirred-tank reactor (CSTR), and the instantaneous concentration of CO_2 can be calculated by **Equation. (A-1).**

$$\boldsymbol{C_{tCO_2} = C_{mCO_2} + \tau_{bed} \frac{dC_{mCO_2}}{dt}} \qquad \textbf{(A-1)}$$

where C_{tCO_2} is the instantaneous concentration of CO_2, C_{mCO_2} is the measured concentration of CO_2 and τ_{bed} is the response time of the bed. The τ_{bed} was calculated by $\tau_{bed} = \tau_m - \tau_r$, where τ_m and τ_r are the measured response time and the rise of CO_2 concentration (~0.3 s), respectively. The slope of ln (1-C_{mCO_2}/C_{iCO_2})/t

(shown in **Figure_Apx A-3**) gave the value of $1/\tau_m$, and thus the τ_{bed} was calculated. The response time of this test rig was calculated to be about 2.29 s.

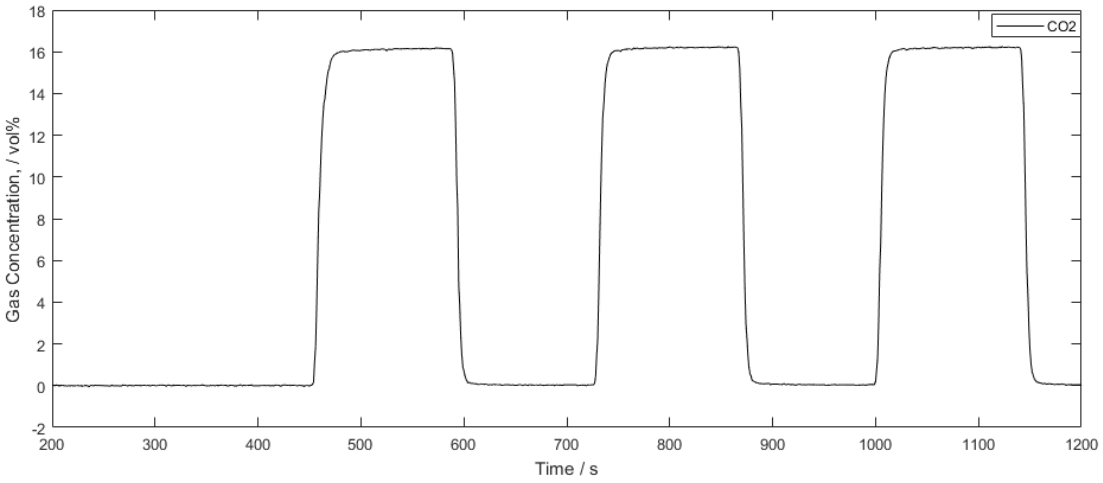

Figure_Apx A-2 'Step' increases of CO_2 concentration.

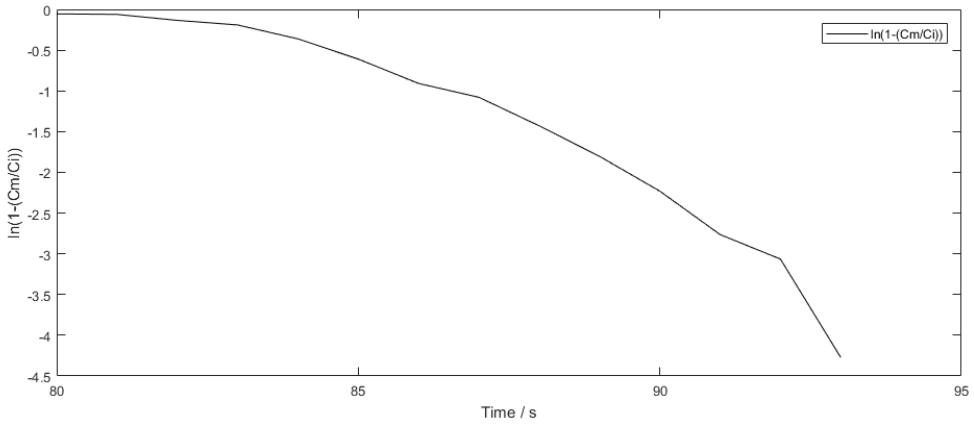

Figure_Apx A-3 Measured response for 'step' increases of CO_2.

The pressurised feeding system relied on a small amount (12.66 cm^3 at 0.15 bar(a)) of N_2 or CO_2, depending on whether the test was air or oxy-fuel combustion, which was utilised to carry the biomass sample into the reactor. This additional gas altered the concentration of the baseline within the reactor (as can be seen in **Figure_Apx A-4**) and, therefore, was accounted and corrected for. Two blank tests were carried out per sample, once before and once after sample injection; the post-sample blank test was utilised to check if the sample was completely injected.

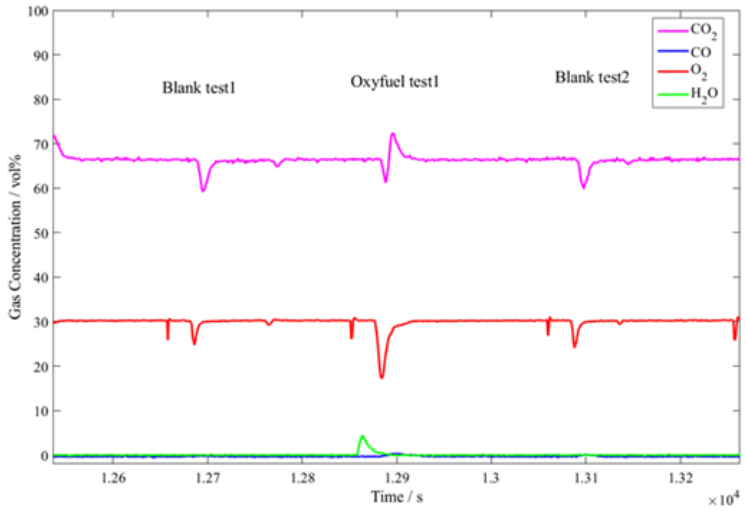

Figure_Apx A-4 Measured gas concentrations during the blank tests and an oxy-fuel test. At conditions of 973 K; 30 vol.% O_2/65 vol.% CO_2/5 vol% N_2, U/U_{mf} = 3, 0.02 g (±2%) biomass and 1 bar(a).

A MATLAB script was developed to correct for this additional gas injection and to determine the true response in gas concentration during the combustion tests; this script worked by subtracting the gas concentration response for the blank test from the sample response. The corrected CO_2 response, relative to the measured response can be seen in **Figure_Apx A-5**. As moisture was removed from the gas stream prior to the gas entering the multi-gas analyser (where the dry gas concentrations were measured), it was necessary to back-calculate the wet gas concentrations.

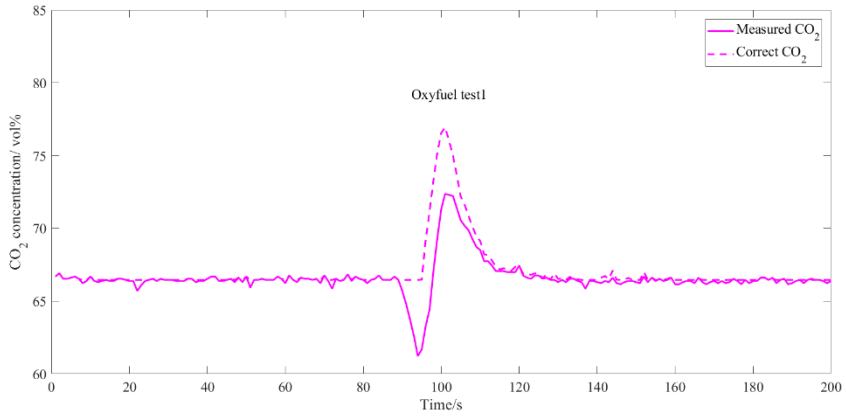

Figure_Apx A-5 Measured and corrected CO_2 concentration from oxy-fuel combustion. At conditions of 973 K, 30 vol% O_2/65 vol% CO_2/5 vol% N_2, U/U_{mf} = 3, 0.02 g (±2%) biomass and 1 bar(a).

Due to the order of the gas sensors inside the gas analyser and along the gas path, the steam concentration was measured first by the RH probe close to the gas exit from the reactor, then the concentrations of O_2, CO and CO_2 were measured in that order within the analyser. Thus, it was necessary to apply a time shifting function to the data so that the starting point of the reaction was the same for each gas measurement, as shown in **Figure_Apx A-6**.

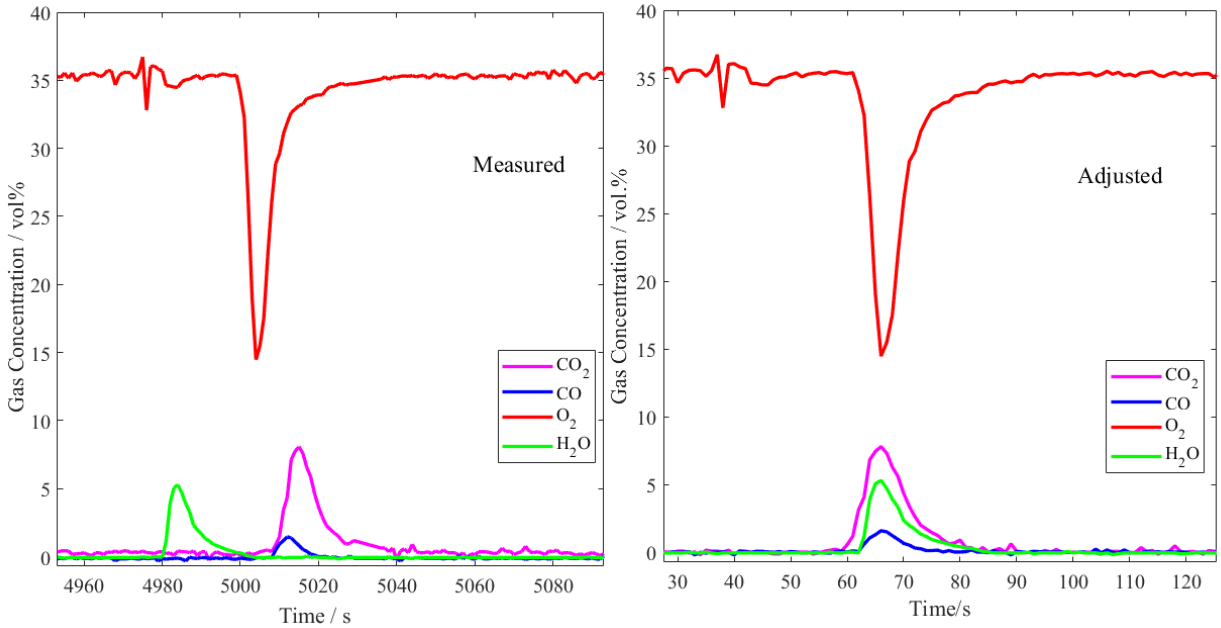

Figure_Apx A-6 Raw measured data (left) and time-shifted data (right) of direct-measured gas concentration. At conditions of 1023 K, 35 vol% O_2/65 vol% N_2, U/U_{mf} = 3, 0.02 g (±2%) biomass, and 1 bar(a).

Table_Apx A-2 Overview of measured rates of air and oxy-fuel combustion of biomass and measured recovery of carbon. Here the average rate of CO_2 production is used as a proxy for the rate of combustion.

	Temperature (K)	O_2 concentration (vol%)	Average rate of CO_2 production ($\times 10^{-3}$ mol/g s)	Standard deviation of rate $\sigma(r)$ (%)	Average carbon balance (%)	Standard deviation of recovery σ (%)
Air combustion	923	20	1.48	1.37	74.4	3.3
		25	1.56	0.73	79.9	4.7
		30	1.72	0.66	86.2	4.4
		35	1.61	0.66	80.3	2.2
	973	20	2.03	0.26	56.5	5.1
		25	2.18	0.28	67.7	1.4
		30	2.31	0.68	73.3	5.2
		35	2.15	1.32	55.2	8.5
	1023	20	2.07	0.97	64.3	5.2
		25	2.10	0.37	59.5	5.7
		30	2.11	0.95	59.5	5.7
		35	2.13	1.88	60.4	5.2
	1073	20	2.40	1.48	71.8	2.2
		25	2.29	1.58	69.7	4.9
		30	2.39	0.96	72.6	4.2
		35	2.28	1.40	75.0	2.7
Oxy-fuel combustion	923	20	2.00	3.96	55.0	14.6
		25	1.87	2.20	56.3	7.8
		30	1.88	2.30	61.1	19.4
		35	2.31	0.92	89.3	19.3
	973	20	3.00	2.83	92.3	7.4
		25	2.49	3.91	88.7	10.3
		30	2.72	1.33	111.0	12.3
		35	2.83	0.18	94.7	0.3
	1023	20	3.73	1.51	106.6	12.0
		25	3.49	4.96	108.4	4.0
		30	2.76	1.77	76.8	18.7
		35	2.95	1.66	67.9	9.7
	1073	20	3.55	1.19	94.7	9.5
		25	3.52	2.33	99.1	4.9
		30	3.22	3.42	129.0	10.3
		35	2.81	0.53	69.4	12.2

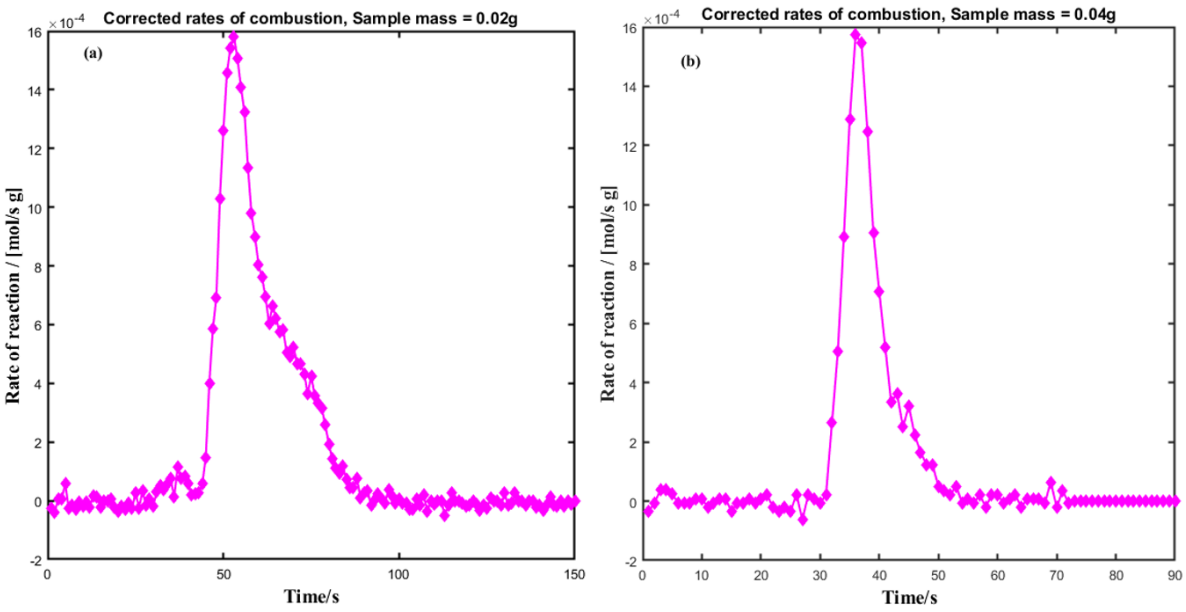

Figure_Apx A-7 Compensation of the effects of mass added on measured rate of reaction. At conditions of 923K, 25 vol% O_2/75 vol% N_2, U/U_{mf} = 3, and 1 bar(a).

A.4 Effects of external mass transfer

To identify if the combusting fuel in this work was controlled by kinetics or external mass transfer, the mass transfer rate, r_m, of oxygen to the exterior of the fuel particle is calculated by the following equations [41]:

$$r_m = k_g \pi d^2 [O_2]_m \quad \textbf{(A-2)}$$

$$\boldsymbol{k_g = sh\frac{D}{d}} \quad \textbf{(A-3)}$$

Where the Sherwood number, *sh*, was estimated to be 2, *D* is the bulk diffusivity of O_2 in N_2 at a bed temperature of 923 K, according to the Chapman–Enskog theory, is 2 $\times 10^{-5}$ m^2/s. Then the external mass transfer rate of O_2 can be calculated as 4.5×10^{-7} mol/g s, which is far less that the value of the reaction rate (the lowest rate of reaction measured was ~1.5×10^{-3} mol/g s). We are therefore able to conclude that the rate of reaction measured was indeed a kinetic rate and not a mass transfer rate, and that the diffusion of oxygen to the surface of the particles was sufficiently fast.

A.5 References

[1] Fan Y, Yao JG, Zhang Z, Sceats M, Zhuo Y, Li L, et al. Pressurized calcium looping in the presence of steam in a spout-fluidized-bed reactor with DFT analysis. Fuel Process Technol 2018; 169: 24–41. doi:10.1016/j.fuproc.2017.09.006.

[2] Zhang Z, Hills TP, Scott SA, Fennell PS. Spouted bed reactor for kinetic measurements of reduction of Fe_2O_3 in a CO_2/CO atmosphere Part I: Atmospheric pressure measurements and equipment commissioning. Chem Eng Res Des 2016; 114: 307–20. doi:10.1016/J.CHERD.2016.06.028.

[3] Fennell PS, Dennis JS, Hayhurst AN. The order with respect to oxygen and the activation energy for the burning of an anthracitic char in O_2 in a fluidised bed, as measured using a rapid analyser for CO and CO_2. Proc Combust Inst 2009; 32 II:2051–8. doi:10.1016/j.proci.2008.06.097.

Appendix B Applying Machine Learning Algorithms in Estimating the Performance of Heterogeneous, Multi-component Materials as Oxygen Carriers for Chemical-looping Processes

B.1 Supplementary Materials

Table_Apx B-1. Name of the manganese ores investigated in this work

Abbreviation	Name
EB	Elwaleed Grade B
EC	Elwaleed Grade C
AN	Autlan Nodules
AC	Autlan Carbonate
SB	Sibelco Braunite
SA	SinAus
GZ	Guizhou
SC	Sibelco Calcined
BR	Brazilian (Buritirama)
EG	Egyptain
GL	Gloria
MT	Metmin
NCH	Nchwaning
SL	Slovakian
SAB	South Africa B
SAA	South Africa A
UMK	United Manganese of Kalahari

TS	Tshipi
HM	Eramet HM

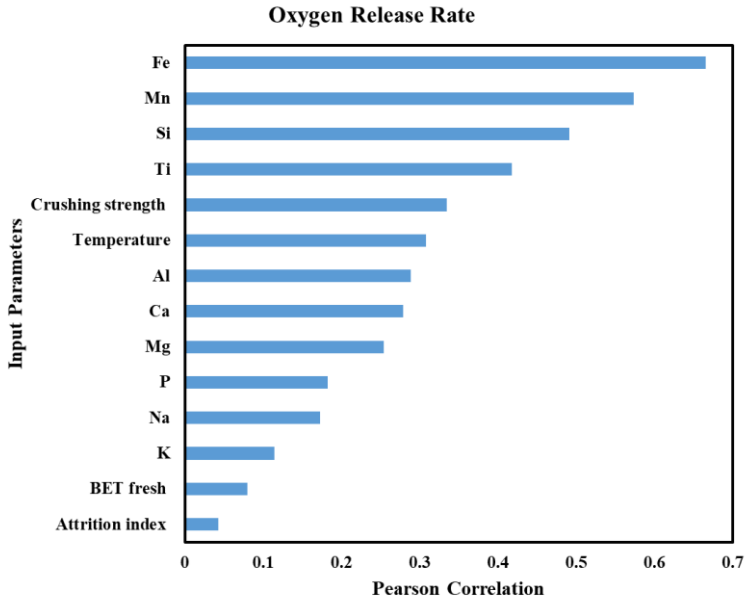

Figure_Apx B-1. Pearson linear correlation factor of each inputs to the O_2 release rate of manganese ores

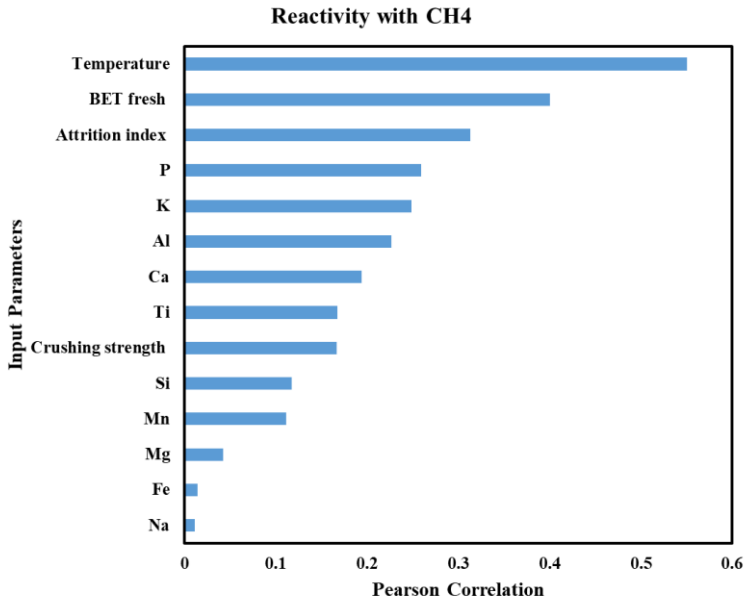

Figure_Apx B-2 Pearson linear correlation factor of each inputs to the reactivity with CH_4 of manganese ores

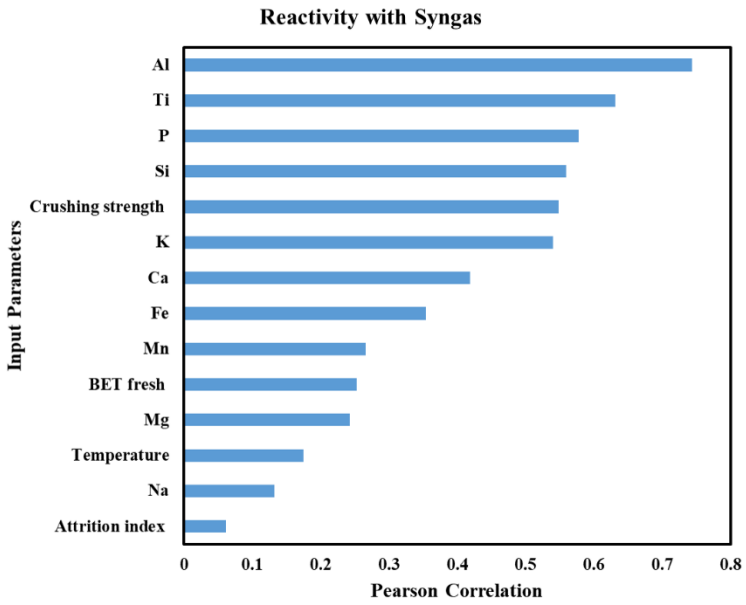

Figure_Apx B-3 Pearson linear correlation factor of each inputs to the reactivity with syngas of manganese ores

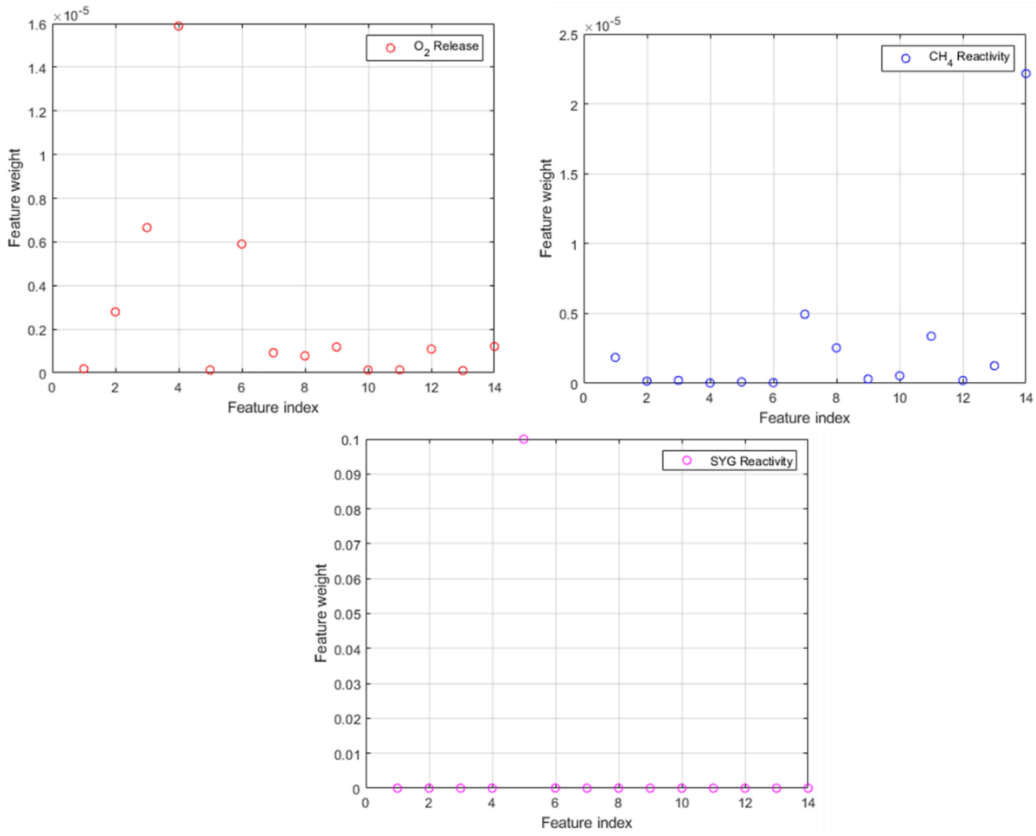

Figure_Apx B-4 Feature selection using neighbourhood component analysis for regression for reducing the inputs of ANNs

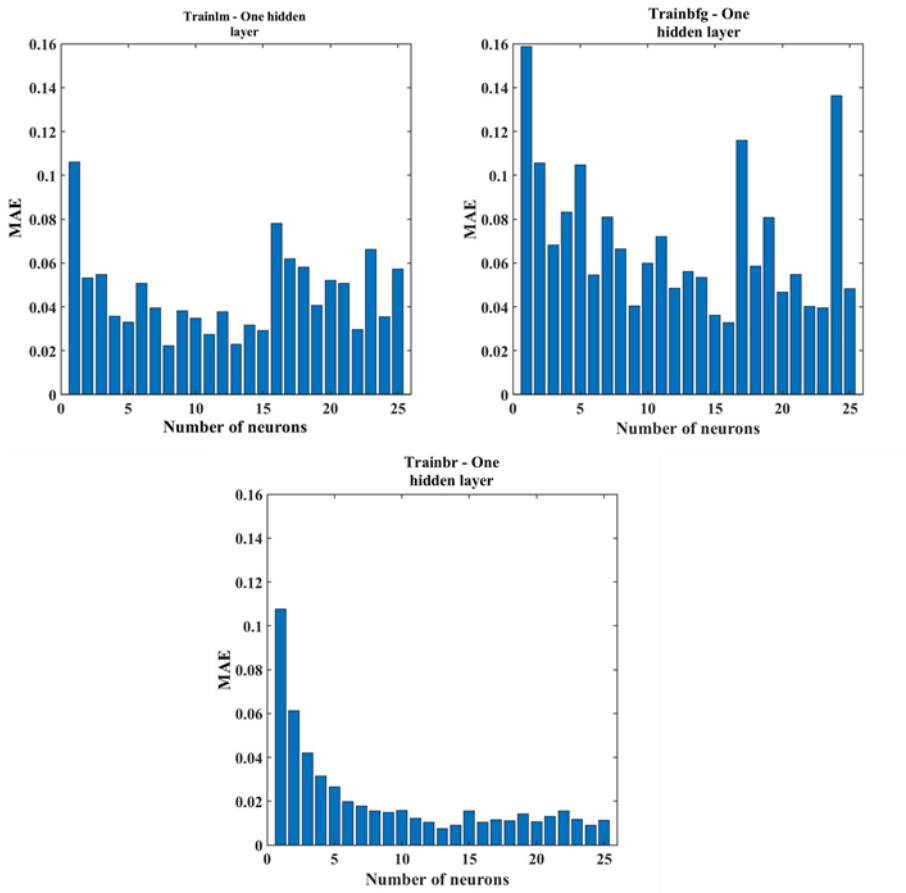

Figure_Apx B-5 Mean absolute error (MAE) of single hidden layer neural networks (14 inputs) with different number of neurons and trained with three different learning algorithms, trainlm, trainbr and trainbfg.

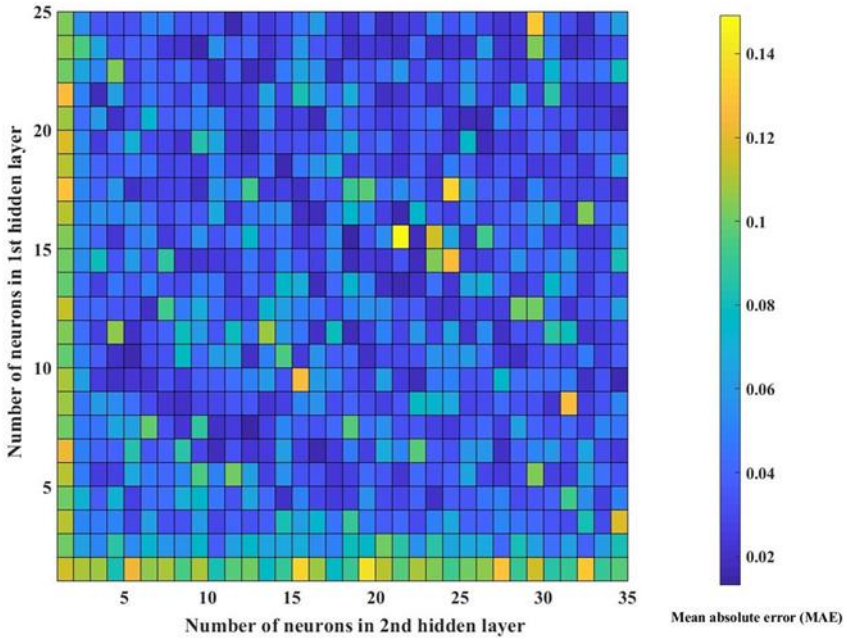

Figure_Apx B-6 Mean absolute error (MAE) of two-hidden layers neural networks (14 inputs) with different number of neurons using the algorithm *trainlm*.

Table_Apx B-2. Topology and performance of the trained neural networks with all 14 inputs.

Number of hidden layers	Training Function	Optimal ANN architecture†	RMSE (Trained ANN)	MAE (Trained ANN)	R^2 (Trained ANN)	RMSE* (Trained ANN)	MAE* (Trained ANN)	R^{2*} (Trained ANN)	RMSE* (Stacked ANNs)	MAE* (Stacked ANNs)	R^{2*} (Stacked ANNs)
Single hidden layer	trainlm	14-8-3	0.045	0.022	0.97	0.361	0.250	0.77	0.077	0.075	0.89
	trainbfg	14-21-3	0.055	0.033	0.95	0.374	0.273	0.88	0.095	0.088	0.85
	trainbr	14-13-3	0.023	0.008	1.00	--	--	--	0.071	0.057	0.94
Two hidden layers	trainlm	14-7-12-3	0.026	0.013	0.99	0.346	0.273	0.85	0.089	0.073	0.91
	trainbfg	14-9-35-3	0.031	0.018	0.98	0.374	0.250	0.85	0.114	0.091	0.83
	trainbr	14-5-21-3	0.023	0.008	0.99	--	--	--	0.195	0.157	0.93

*Unseen data †Number of neurons in each layer

Table_Apx B-3 Topology and performance of the reduced 7-input trained neural networks

Predicted Properties	Number of hidden layers	Training Function	Optimal ANN architecture†	RMSE (Trained ANN)	MAE (Trained ANN)	R^2 (Trained ANN)	RMSE* (Trained ANN)	MAE* (Trained ANN)	R^{2*} (Trained ANN)	RMSE* (Stacked ANNs)	MAE* (Stacked ANNs)	R^{2*} (Stacked ANNs)
CH_4 and Syngas	Single hidden layer	trainlm	7 -7-2	0.026	0.016	0.99	0.373	0.277	0.83	0.106	0.090	0.82
		trainbfg	7-13-2	0.088	0.061	0.89	0.391	0.304	0.79	0.149	0.120	0.64
		trainbr	7-24-2	0.024	0.008	0.99	--	--	--	0.078	0.064	0.92
	Two hidden layers	trainlm	7-4-9-2	0.033	0.018	0.98	0.339	0.264	0.83	0.132	0.108	0.79
		trainbfg	7-13-29-2	0.062	0.034	095	0.295	0.259	0.82	0.132	0.110	0.71
		trainbr	7-5-35-2	0.026	0.008	0.99	--	--	--	0.082	0.070	0.94
O_2 Releasing	Single hidden layer	trainlm	4-8-1	0.0404	0.029	0.95	--	--	--	--	--	--
		trainbfg	4-10-1	0.0878	0.063	0.76	--	--	--	--	--	--

	trainbr	4-25-1	0.0270	0.017	0.98	--	--	--	--	--	--
Two hidden layers	trainlm	4-19-30-1	0.0049	0.019	0.93	--	--	--	--	--	--
	trainbfg	4-25-21-1	0.0639	0.034	0.88	--	--	--	--	--	--
	trainbr	4-6-6-1	0.0413	0.021	0.95	--	--	--	--	--	--

*Unseen data †Number of neurons in each layer

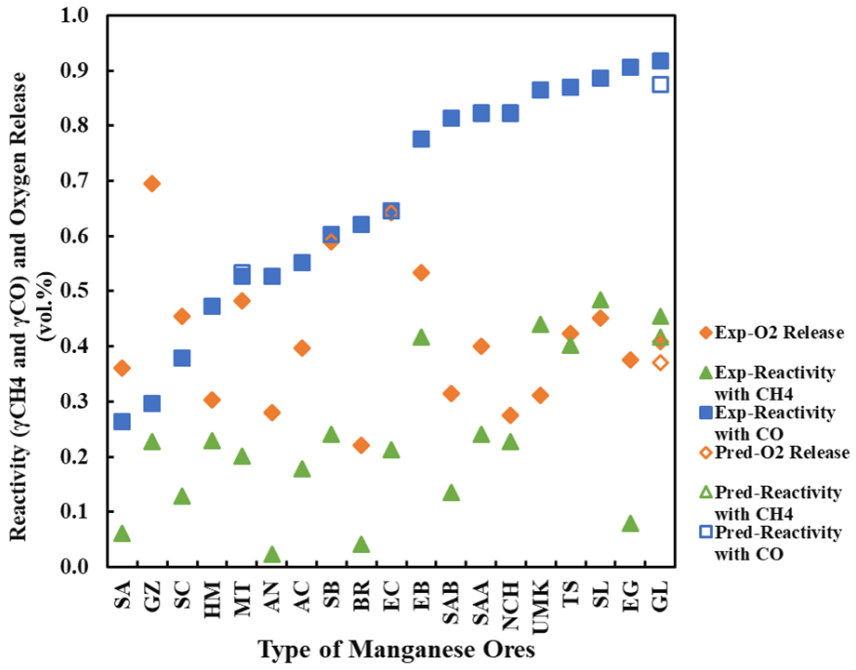

Figure_Apx B-7 Experimental and predicted reactivity and O_2 release of manganese

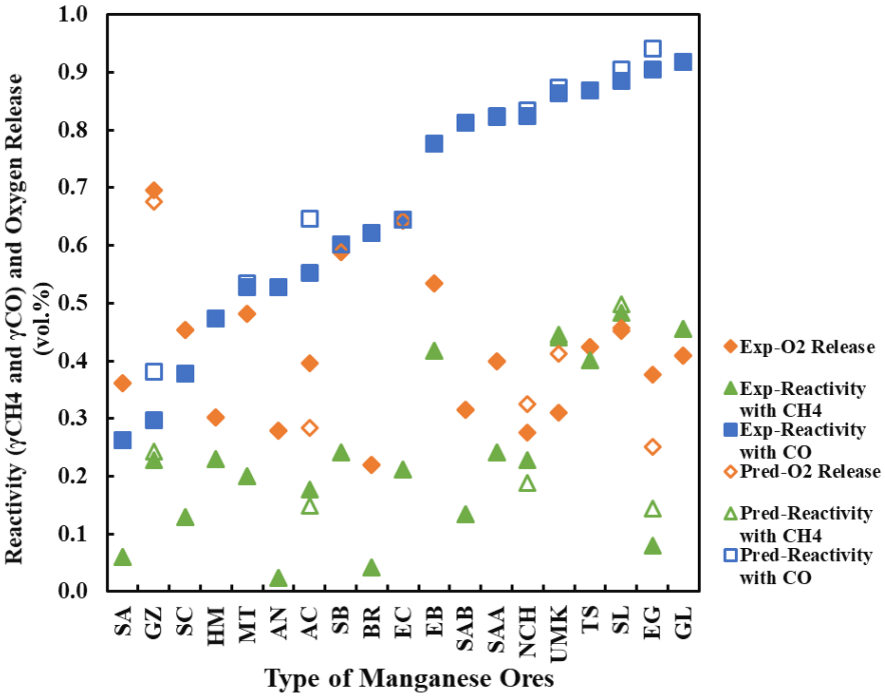

ores as oxygen carriers (*trainbr* single hidden-layer) at bed temperature 900 °C.

Figure_Apx B-8 Experimental and predicted reactivity and O_2 release of manganese ores as oxygen carriers (*trainbr* two hidden-layer) at bed temperature 900 °C.

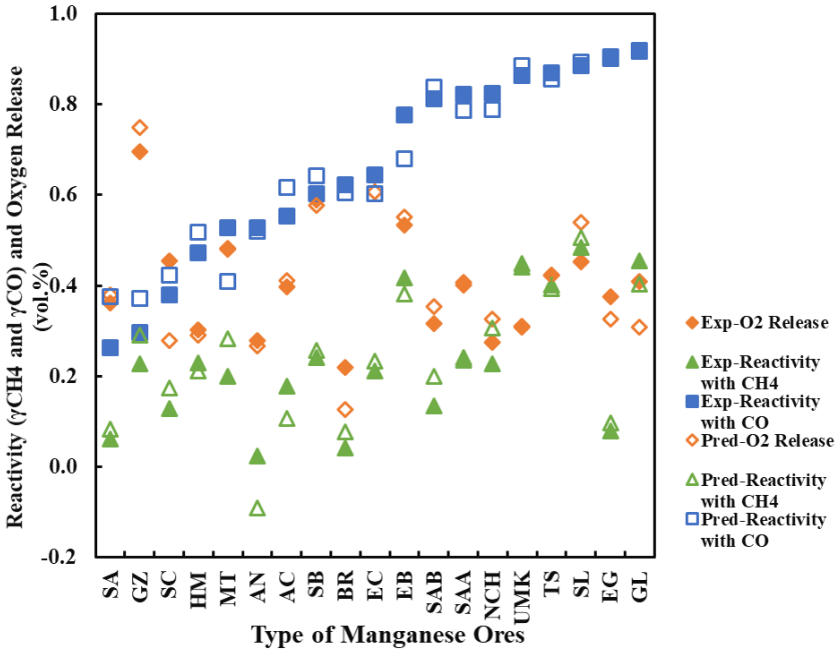

Figure_Apx B-9 Experimental and predicted reactivity and O_2 release of manganese ores as oxygen carriers (*trainbfg* single hidden-layer) at bed temperature 900 °C.

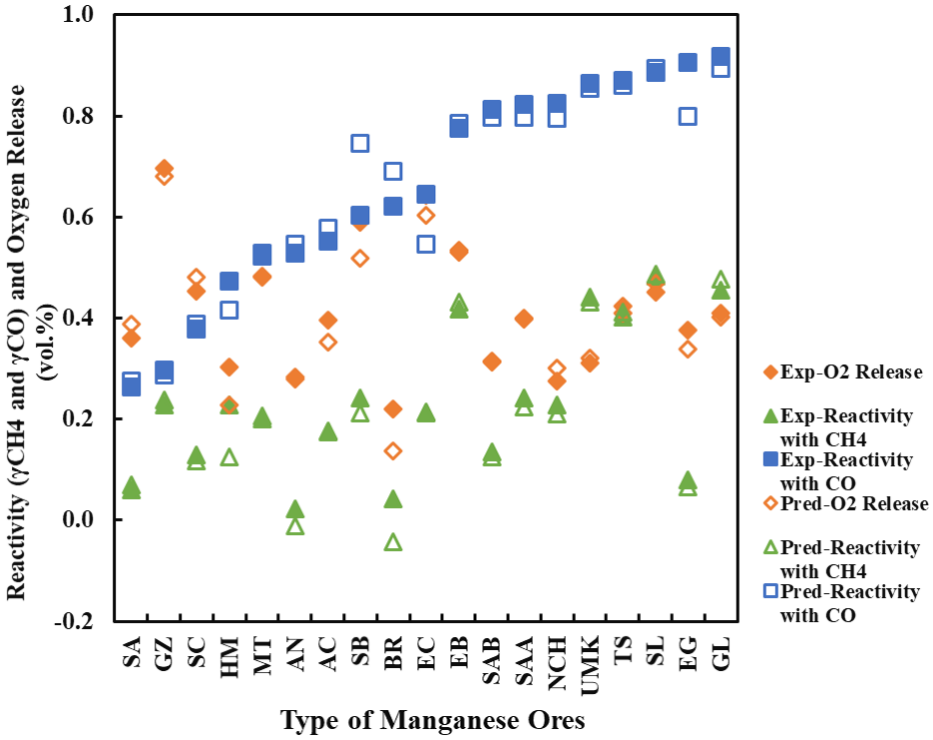

Figure_Apx B-10 Experimental and predicted reactivity and O_2 release of manganese ores as oxygen carriers (*trainbfg* two hidden-layer) at bed temperature 900 °C.

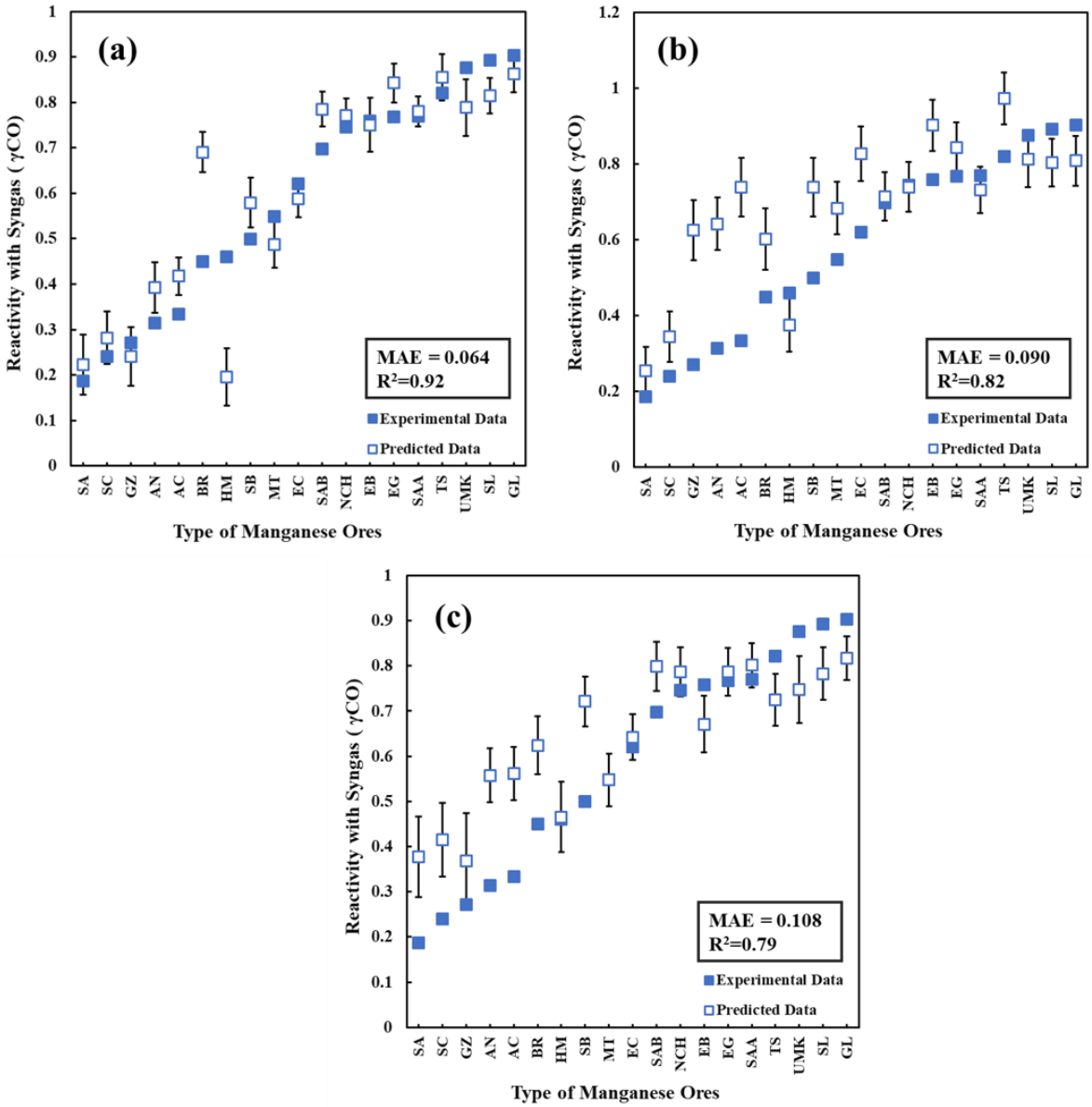

Figure_Apx B-11 (a) Predictions of stacked neural network (7-24-2) trained with *trainbr* with 95% confidence intervals on unseen data; (b) Predictions of stacked neural network (7-7-2) trained with *trainlm* with 95% confidence intervals on unseen data; (c) Predictions of stacked neural network (7-4-9-2) trained with *trainlm* with 95% confidence intervals on unseen data.

Appendix C Process Simulations of Blue Hydrogen Production by Upgraded Sorption Enhanced Steam Methane Reforming (SE-SMR) Processes

C.1 Flowsheet of different SE-SMR configurations

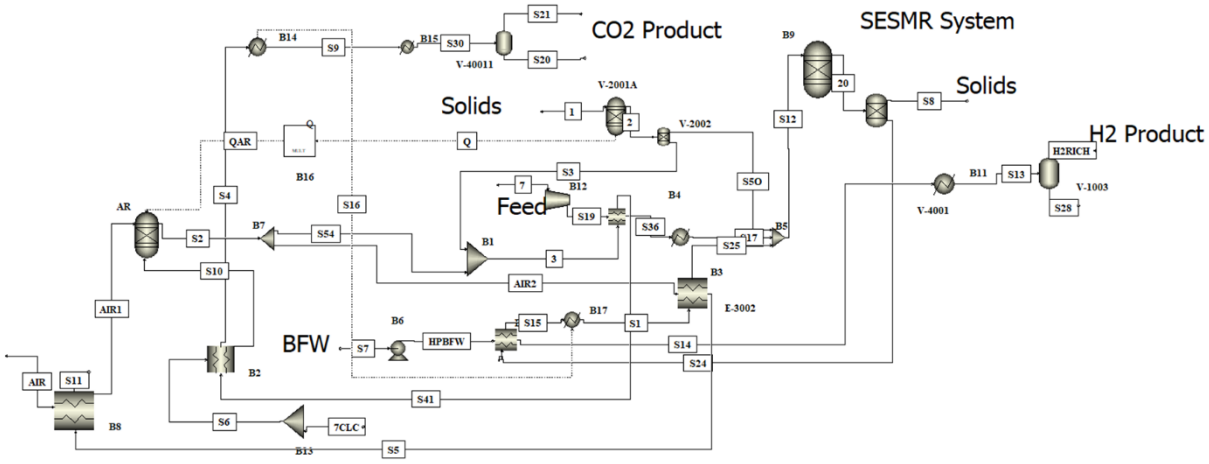

Figure_Apx C-1. Flowsheet of SE-SMR

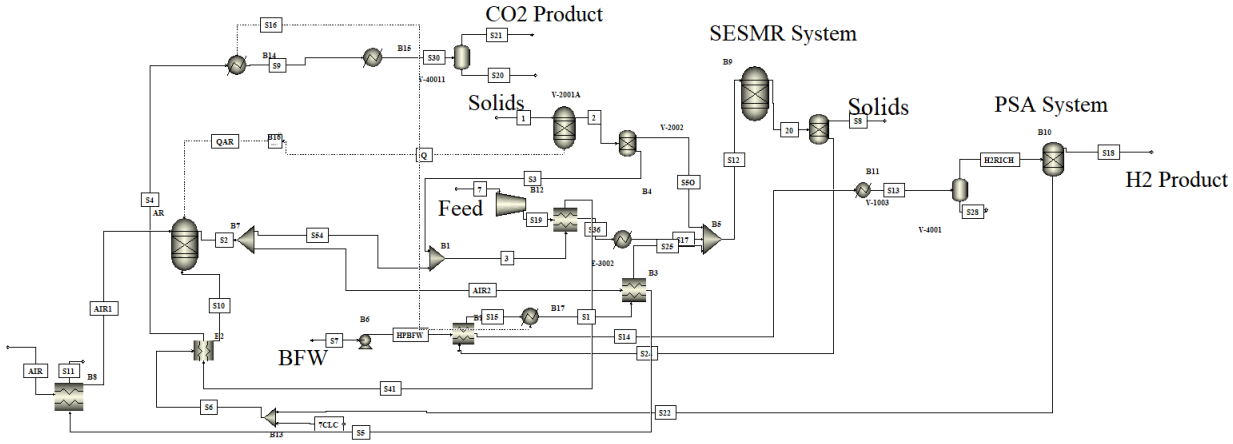

Figure_Apx C-2 Flowsheet of SE-SMR+PSA

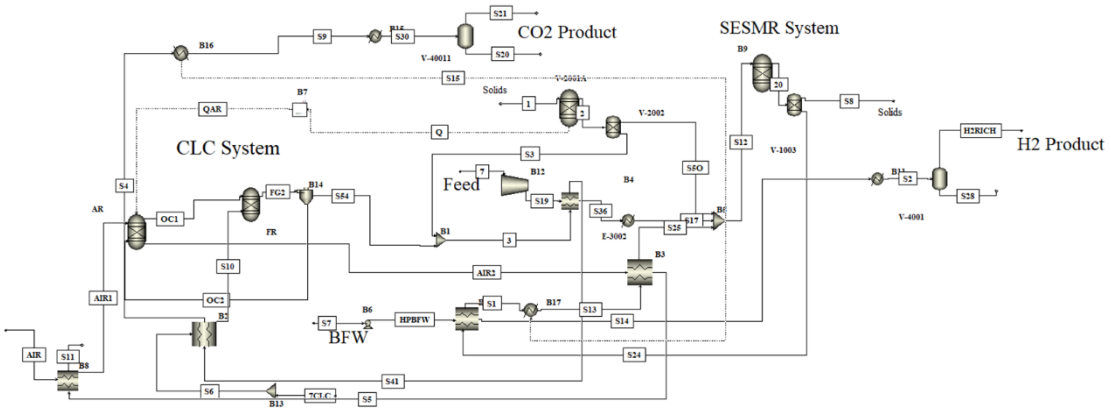

Figure_Apx C-3 Flowsheet of SE-SMR+CLC

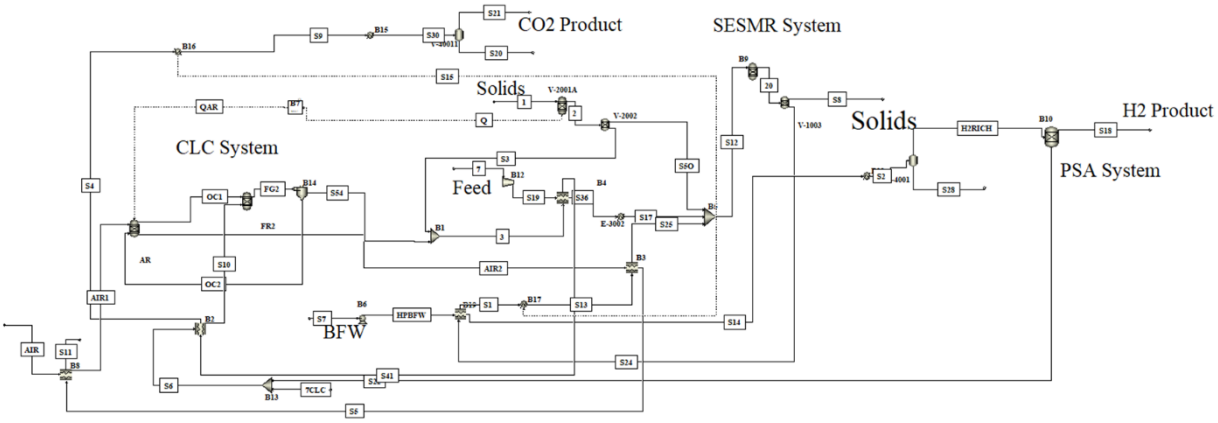

Figure_Apx C-4 Flowsheet of SE-SMR+PSA+CLC

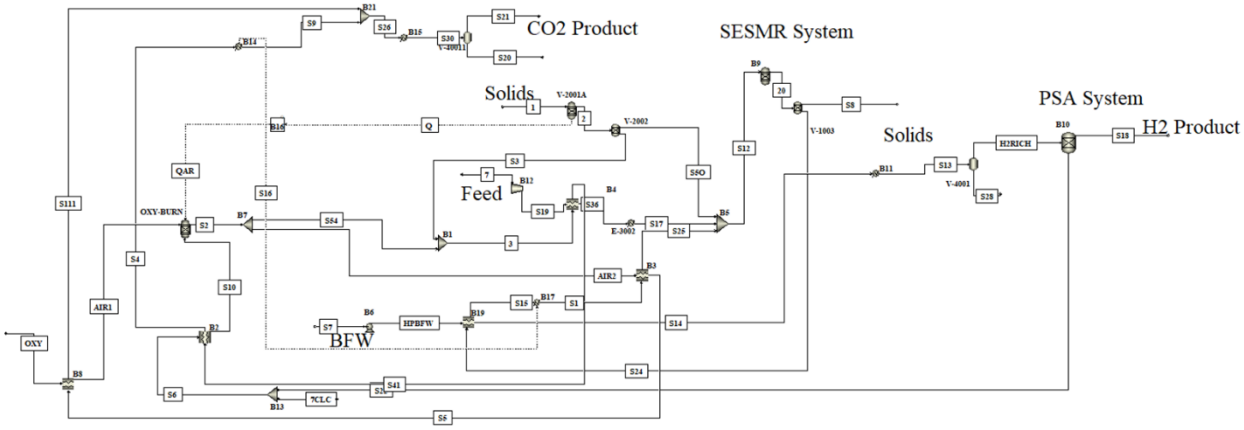

Figure_Apx C-5 Flowsheet of SE-SMR+Oxy-fuel combustion

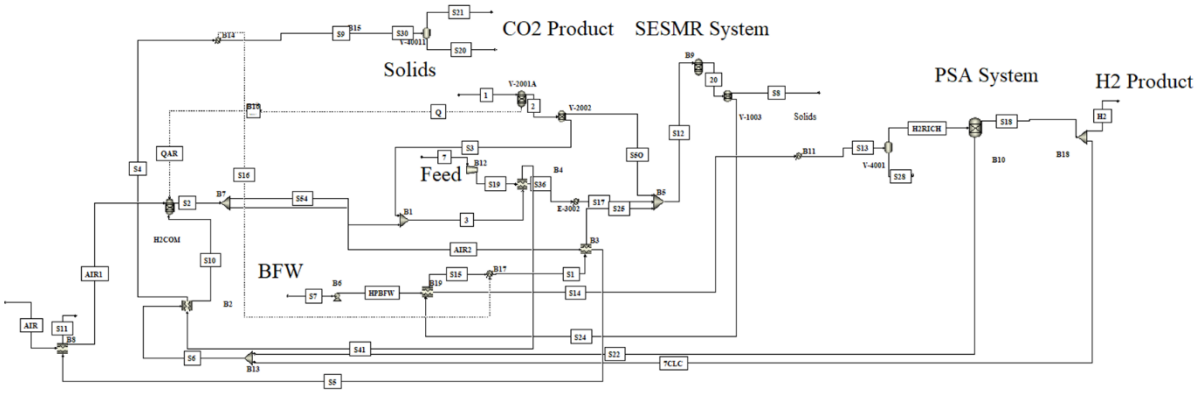

Figure_Apx C-6 Flowsheet of SE-SMR+H_2 recycle